UNIVERSITAT ROVIRA I VIRGILI
DESIGN, FABRICATION AND CHARACTERIZATION OF POROUS SILICON MULTILAYER OPTICAL DEVICES
Elisabet Xifré Pérez
ISBN: 978-84-691-0362-3/DL: T.2181-2007

Chapter 3

Simulation programs for the analysis of multilayer media

In this chapter, we present the software realized for the mathematical study and design of multilayers. Although different methods exist for the simulation of these structures, all the programs presented here are based on the transfer matrix method. Firstly, the transfer matrix method is explained in detail and its mathematical bases are presented. This method is compared with two other ones that can be also used for this purpose. After that, the realized simulation programs based on the transfer matrix method are explained in detail. Their selectable variables and the optical properties calculated with each one are presented. Finally, the performance of the programs is evaluated by comparing the simulated optical responses of widely reported multilayer structures (Distributed Bragg Reflectors and microcavities) with the ones obtained in the literature.

UNIVERSITAT ROVIRA I VIRGILI
DESIGN, FABRICATION AND CHARACTERIZATION OF POROUS SILICON MULTILAYER OPTICAL DEVICES
Elisabet Xifré Pérez
ISBN: 978-84-691-0362-3/DL: T.2181-2007

3.1. Mathematical methods for the analysis and simulation of multilayers

The development of methods for analyzing the multilayers is essential, if we want to understand their fundamental properties. Any experimental exploration of the multilayers must be accompanied by a quantitative theoretical analysis so that the most interesting cases can be identified, the experimental measurements interpreted, and stable designs for successfully operating devices be found. This section provides an outline of the most widely used numerical techniques that make it possible to determine the optical properties of multilayers. The first, the Transfer Matrix method is the method used for the analysis of the multilayers presented in this work, for this reason it is presented in detail whereas the rest of methods are briefly explained.

3.1.1. Transfer Matrix Method (TMM)

This is the most widely used method for the mathematical study of wave transmission in one-dimensional structures because it allows the calculation of band diagrams [149], reflectivity and transmission spectra [150], emission spectra [44], guided modes [126] and the modelization of porosity and thickness gradients [85].

To study the reflection and the transmission of electromagnetic radiation through a multilayer with the TMM method, we consider a one-dimensional structure consisting of alternating porous silicon layers of different refractive indices coupled to a homogeneous medium characterized by refractive index n_0 at the interface. Fig. 3.1 shows this structure, where n_1 and n_2 are the layers refractive index, h_1 and h_2 are the thicknesses of the respective layers and Λ is the period of the structure ($\Lambda = h_1 + h_2$).

ISBN: 978-84-691-0362-3/DL: T.2181-2007

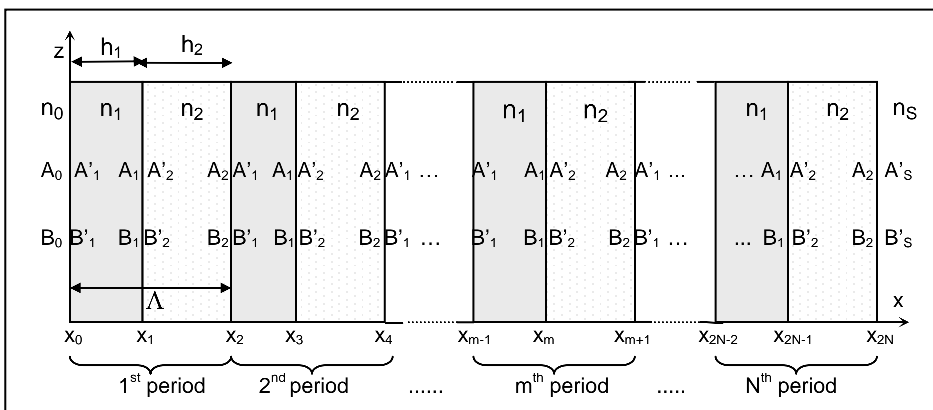

Fig. 3.1. Schematic of a multilayer system. A(x) represent the amplitude of the right-traveling-wave and B(x) that of the left-traveling one. Note that A(x) and B(x) are not continuous at the interfaces. It is a periodic structure made of two layers, 1 and 2. The thickness of each layer is h_m, n_m is the refractive index and Λ is the period. The structure is coupled to a homogeneous medium characterized by n_0 (initial medium) and n_S (final medium).

The dielectric structure is defined by

$$n(x) = \begin{cases} n_0, & x < x_0 \\ n_1, & x_0 < x < x_1 \quad with\ x_1 = x_0 + h_1 \\ n_2, & x_1 < x < x_2 \quad with\ x_2 = x_0 + \Lambda = x_1 + h_2 \\ \vdots & \\ n_S, & x_{2N} < x \quad with\ x_{2N} = x_0 + N\Lambda = x_{2N-1} + h_2 \end{cases} \tag{3.1}$$

with n(x)=n(x+Λ). n_s is the substrate refractive index, n_0 is that of the incident medium and n_m is the refractive index of the m layer. Layer thicknesses are related to x_m by $h_m=x_m-x_{m-1}$ (m=1..2N).

The electric field of a general plane-wave solution can be written as $E=E(x)e^{i(\omega t-\beta z)}$, where the electric field distribution E(x) can be written as

UNIVERSITAT ROVIRA I VIRGILI
DESIGN, FABRICATION AND CHARACTERIZATION OF POROUS SILICON MULTILAYER OPTICAL DEVICES
Elisabet Xifré Pérez
ISBN: 978-84-691-0362-3/DL: T.2181-2007

$$E(x) = \begin{cases} A_0 e^{-ik_{0x}(x-xo)} + B_0 e^{ik_{0x}(x-xo)}, & x < x_0 \\ A_m e^{-ik_{mx}(x-x_m)} + B_m e^{ik_{mx}(x-x_m)}, & x_{m-1} < x < x_m, \\ A'_S\, e^{-ik_{Sx}(x-x_{2N})} + B'_S\, e^{ik_{Sx}(x-x_{2N})}, & x_{2N} < x \end{cases} \tag{3.2}$$

where k_{mx} is the x component of the wave vectors $k_{mx} = \omega n_m \cos\theta_m/c$ and θ_m is the ray angle in each layer. A_m and B_m represent the amplitude of the plane waves at interface $x=x_m$ (see Fig. 3.1).

If the two general amplitudes of E(x) are represented as column vectors, the plane waves at different layers can be related by

$$\begin{pmatrix} A_{m-1} \\ B_{m-1} \end{pmatrix} = D_{m-1}^{-1} D_m \begin{pmatrix} A'_m \\ B'_m \end{pmatrix} = D_{m-1}^{-1} D_m P_m \begin{pmatrix} A_m \\ B_m \end{pmatrix} \quad \text{m=1,2,...,2N+1} \tag{3.3}$$

where matrices D_m are the dynamical matrices given by

$$D_m = \begin{cases} \begin{pmatrix} 1 & 1 \\ n_m \cos\theta_m & -n_m \cos\theta_m \end{pmatrix} & \textit{for TE wave} \\ \begin{pmatrix} \cos\theta_m & \cos\theta_m \\ n_m & -n_m \end{pmatrix} & \textit{for TM wave} \end{cases} \tag{3.4}$$

and P_m is the propagation matrix, that can be written as

$$P_m = \begin{pmatrix} e^{ik_{mx}h_m} & 0 \\ 0 & e^{-ik_{mx}h_m} \end{pmatrix} \tag{3.5}$$

The relation between A_0, B_0 and A_s', B_s' can thus be written as

$$\begin{pmatrix} A_0 \\ B_0 \end{pmatrix} = D_0^{-1} \left[D_1 P_1 D_1^{-1} D_2 P_2 D_2^{-1} \right]^N D_S = \begin{pmatrix} M_{11} & M_{12} \\ M_{21} & M_{22} \end{pmatrix} \begin{pmatrix} A'_S \\ B'_S \end{pmatrix} \tag{3.6}$$

where N is the number of periods in the structure.

ISBN: 978-84-691-0362-3/DL: T.2181-2007

3.1.1.1. Reflectance and transmittance of the multilayer

The reflectance and transmittance of monochromatic plane waves through the multilayer structure are calculated from the matrix elements.

If the light is incident from medium 0, the reflection and transmission coefficients are defined as

$$r = \left(\frac{B_0}{A_0}\right)_{B_S=0} \qquad t = \left(\frac{A_S}{A_0}\right)_{B_S=0} \tag{3.7}$$

Using the matrix equation (3.6) and following the definitions in Eq. (3.7), we obtain

$$r = \frac{M_{21}}{M_{11}} \qquad t = \frac{1}{M_{11}} \tag{3.8}$$

Reflectance is given by

$$R = |r^2| = \left|\frac{M_{21}}{M_{11}}\right|^2 \tag{3.9}$$

provided medium 0 is lossless.

If the bounding media (0,*s*) are both pure dielectric with real n_s and n_0, transmittance T is given by

$$T = \frac{n_s \cos\theta_s}{n_0 \cos\theta_0}|t|^2 = \frac{n_s \cos\theta_s}{n_0 \cos\theta_0}\left|\frac{1}{M_{11}}\right|^2 \tag{3.10}$$

ISBN: 978-84-691-0362-3/DL: T.2181-2007

3.1.1.2. Bloch waves and band structures

Wave propagation in periodic media is very similar to the motion of electrons in crystalline solid. In fact, formulation of the Kroning Penny model used in elementary band theory of solids is mathematically identical to that of the electromagnetic radiation in periodic layered media. Thus, some of the physical concepts used in solid-state physics such as Bloch waves, Brillouin zones and forbidden bands can also be used here. A periodic layered medium is equivalent to a one-dimensional lattice that is invariant under lattice translation. In other words $n^2(x+\Lambda)= n^2(x)$, where Λ is the period

According to the Floquet theorem, solutions of wave equations for a periodic medium are of the form [151] $E_K(x,z)= E_K(x)e^{-i\beta z}\ e^{-iKx}$, where $E_K(x+\Lambda)= E_K(x)$. The subscript K indicates that the function $E_K(x)$ depends on K. The constant K is known as the Bloch wave number. The problem is thus that of determining K and $E_K(x)$.

In term of our column vector representation and from Eq. (3.2), the periodic condition $E_K(x+\Lambda)= E_K(x)$ for the Bloch wave is simply

$$\begin{pmatrix} A_1 \\ B_1 \end{pmatrix}_{n\ period} = e^{-iK\Lambda} \begin{pmatrix} A_1 \\ B_1 \end{pmatrix}_{n-1\ period} \tag{3.11}$$

From the matrix expression (3.3), the unit cell of the periodic multilayer can be defined as

$$\begin{pmatrix} A_1 \\ B_1 \end{pmatrix}_{n-1\ period} = D_1^{-1} D_2 P_2 D_2^{-1} D_1 P_1 \begin{pmatrix} A_1 \\ B_1 \end{pmatrix}_{n\ period} = \begin{pmatrix} S & T \\ U & V \end{pmatrix} \begin{pmatrix} A_1 \\ B_1 \end{pmatrix}_{n\ period} \tag{3.12}$$

It follows from this equation and Eq. (3.11) that the column vector of the Bloch wave satisfies the following eigenvalue problem:

$$\begin{pmatrix} S & T \\ U & V \end{pmatrix} \begin{pmatrix} A_1 \\ B_1 \end{pmatrix} = e^{iK\Lambda} \begin{pmatrix} A_1 \\ B_1 \end{pmatrix} \tag{3.13}$$

ISBN: 978-84-691-0362-3/DL: T.2181-2007

The phase vector $e^{iK\Lambda}$ is thus the eigenvalue of the translation matrix (S,T,U,V) and is given by

$$e^{iK\Lambda}= (1/2)(S+V) \pm \{[(1/2)(S+V)]^2-1\}^{1/2} \qquad (3.14)$$

The eigenvectors corresponding to this eigenvalues are obtained from Eq. (3.13) and are

$$\begin{pmatrix} A_0 \\ B_0 \end{pmatrix} = \begin{pmatrix} T \\ e^{jK\Lambda} - S \end{pmatrix} \qquad (3.15)$$

times the arbitrary constant. The Bloch waves that result from Eq. (3.15) can be considered as the eigenvectors of the translation matrix with eigenvalues $e^{\pm iK\Lambda}$ given by Eq. (3.14). The two eigenvalues in Eq. (3.14) are the inverse of each other since the translation matrix is unimodular. Eq. (3.14) gives the dispersion relation between ω, β and K for the Bloch function,

$$K(\beta,\omega)= (1/\Lambda) \cos^{-1}[(1/2)(S+V)] \qquad (16)$$

Regimes where /(1/2)(S+V)/<1 correspond to real K and thus to propagation Bloch waves; when /(1/2)(S+V)/>1, however, $K=m\pi/\Lambda+iK_i$ which has an imaginary part K_i so that the Bloch wave is evanescent. These are the so-called forbidden bands of the periodic medium. The band edges are the regimes where /(1/2)(S+V)/=1.

The dispersion relation can be also written as

$$\cos K\Lambda = \frac{1}{2}(S+V) = \cos k_1 d_1 \cos k_2 d_2 - \frac{1}{2}\varphi \sin k_1 d_1 \sin k_2 d_2 \qquad (3.17)$$

where $\varphi=\frac{k_{2x}}{k_{1x}}+\frac{k_{1x}}{k_{2x}}$ for TE waves and $\varphi=\frac{n_2^2 k_{1x}}{n_1^2 k_{2x}}+\frac{n_1^2 k_{2x}}{n_2^2 k_{1x}}$ for TM waves, and $\beta=\omega n_m \sin\theta/c$.

In order to study the omnidirectional band gap of a multilayer, the dispersion relation is calculated for all incidence angles, obtaining the projected band structure (PBS).

UNIVERSITAT ROVIRA I VIRGILI
DESIGN, FABRICATION AND CHARACTERIZATION OF POROUS SILICON MULTILAYER OPTICAL DEVICES
Elisabet Xifré Pérez
ISBN: 978-84-691-0362-3/DL: T.2181-2007

3.1.1.3. Advantages and drawbacks of the TMM

The TMM has many advantages. It is a very useful algorithm, very appropriate for reflectivity and transmission calculations of multilayer structures. It can take in values for the refractive index that are either real or complex. A real refractive index represents a lossless material whereas a complex refractive index can represent either one of two types of materials. If the imaginary part of the complex refractive index is negative then the material is absorptive. If it is positive then this is an indication of having a gain medium.

The TMM can also handle any number of layers in a multilayer structure. In addition, these layers can be ordered in any manner and there is no requirement that they should be periodic. Even if they are periodic, the unit cell that is repeated does not have to be composed of two layers only, but any number of layers. There is also no restriction on the thickness of any layer. The thickness and the refractive index of each layer can be defined independently. This makes the TMM most suitable for modelling structures formed by different periodic multilayers stacked together, since they are not fully periodic.

The TMM can handle structures having a high index contrast between their two composite materials contrast material systems. This makes the TMM suitable for modelling multilayer structures, which usually have a high index contrast between their composite materials.

The TMM has also some drawbacks. For example, it assumes that the plane perpendicular to the direction of propagation is infinite, meaning that each layer in a multilayer structure extends infinitely in both of its dimensions. Of course, this is unrealistic, so the layers that are modelled have to be wide enough to avoid errors from this assumption. The TMM calculates the field throughout the structure by propagating it from one layer to the other by matrix relations. As such, it depends greatly on the computational speed and is therefore limited by it. It lacks a mathematical expression that can relate the field between multiple layers, which would reduce the mathematical calculations required and consequently the computational time.

Another drawback of the TMM is that it is limited to continuous wave propagation and cannot handle pulse propagation. To model pulses, the TMM

UNIVERSITAT ROVIRA I VIRGILI
DESIGN, FABRICATION AND CHARACTERIZATION OF POROUS SILICON MULTILAYER OPTICAL DEVICES
Elisabet Xifré Pérez
ISBN: 978-84-691-0362-3/DL: T.2181-2007

must be combined with the Fourier Transform. Pulses are better modelled with other techniques such as the Finite Difference Time Domain method.

3.1.2. Plane Wave Method

Another way to calculate photonic band structures is to adapt the methods of electronic band structure calculations to the case of photonic crystals. The plane wave expansion method can be classified as one of the numerical techniques borrowed from solid state physics. However, it had to undergo various adjustments before it could be carried over to the photonic case. These adjustments reflect the differences between photonic and conventional crystals, such as the fact that the electromagnetic field is inherently vectorial by nature or that the "scattering potentials" of photonic atoms are known beforehand and do not have to be determined self-consistently.

The plane wave method is used to solve periodic electromagnetic problems, among them the modelization of periodic structures, because accurate and reliable results are obtained [152]. It is widely used to find the Bloch frequencies of infinite periodic structures [125,153,154].

This method uses the Fourier expansion in terms of harmonic functions (modes), defined by the reciprocal space vectors. By applying the Fourier expansion in terms of Bloch waves $\mathrm{H_k(r) = u_k(r)e^{ikr}}$, the Maxwell's equations are converted to an eigenvalue and eigenvector problem:

$$\Theta H(r) = \left(\frac{\omega}{c}\right)^2 H(r) \tag{3.18}$$

where $\Theta = \nabla \times \left(\frac{1}{\varepsilon(r)}\right)\nabla \times$ is the Maxwell's operator. The $u_k(k)$ function is a periodic function that follows the structure periodicity.

The plane wave method is one of the first methods used, because it is easy to understand and computationally very straightforward to implement. It can be used to solve periodic problems in one, two and three dimensions. However, it has some serious limitations which restrict its usefulness. First, the

UNIVERSITAT ROVIRA I VIRGILI
DESIGN, FABRICATION AND CHARACTERIZATION OF POROUS SILICON MULTILAYER OPTICAL DEVICES
Elisabet Xifré Pérez
ISBN: 978-84-691-0362-3/DL: T.2181-2007

method fixes the wave vector $\vec{k}$ and then determines the eigenfrequencies for this $\vec{k}$, so the method runs into difficulties if the dielectric constant is itself a function of frequency. Hence, structures that include metallic or other dispersive materials are beyond the scope of the plane wave method. Second, the key step in the method is the matrix diagonalization, so the computer time required scales like N^3, where N is the number of plane waves used in the expansion. This scaling law is inefficient and renders the calculations impossibly time consuming when a large number of plane waves is required for more complex structures [155].

3.1.3. Finite Difference Time Domain

The finite difference time domain (FDTD) approach overcomes all the drawbacks of the plane wave method. It was first described by Yee in 1966 [156] and so has been known to the electrical engineering community for 40 years. The methodology and computational schemes for a variety of photonic problems can be found in the excellent book by Taflove [157].

The FDTD method is a general method for numerically solving the time-dependent Maxwell's equations in real space, approximating the space and time derivatives with finite differences. With the appropriate choice of the points at which the various field components are to be evaluated, the set of finite difference equations can be solved and the solution will satisfy the boundary [156].

It is a widely used technique for solving electromagnetic problems and has many advantages: the method is a direct solution of Maxwell's time-domain equations, consequently, it is a complete full-wave solution that contains no approximations; it is extremely general in the materials and geometries that it can analyze; and, finally, the memory requirements of FDTD are significantly less than other methods, like PWM [158].

The principal disadvantage of the classical implementation of FDTD is that all structures must conform to a Cartesian grid; consequently, all curved

UNIVERSITAT ROVIRA I VIRGILI
DESIGN, FABRICATION AND CHARACTERIZATION OF POROUS SILICON MULTILAYER OPTICAL DEVICES
Elisabet Xifré Pérez
ISBN: 978-84-691-0362-3/DL: T.2181-2007

surfaces must be modeled by a "stairstep" approximation, which can introduce errors in the results.

3.2. Development of the simulation programs

The simulation and study of the optical behavior of multilayer structures has been carried out with two programs especially developed. The optical behavior of multilayers is characterized by the reflectivity, transmission and absorption spectra, as well as by the band diagram. Omnidirectional mirrors are also characterized by the projected band structure (PBS), which determines the band diagram for all incident angles and for both polarizations.

The realized programs calculate all these characteristics using the transfer matrix method [151]. All the graphs that are presented in the next sections have been calculated using these simulation programs.

3.2.1. Program for the calculation of reflectivity, transmission, and absorption spectra.

The main objective of this program is to study the optical response of a multilayer before its fabrication. The simulated structures can be either all-dielectric or metallo-dielectric multilayers. The program is based on the transfer matrix method. In Fig. 3.2 we can observe the main program window, where the user can define all the parameters required for the simulation. These parameters are:

- **Incidence angle**: Angle between the propagation direction of the incident wave and the normal to the surface of the layers. This angle (θ) can go from 0 to 90 degrees.
- **Refractive index of the ambient medium**: the ambient medium is the medium from which the incident wave arrives to the surface of the multilayer.

ISBN: 978-84-691-0362-3/DL: T.2181-2007

- **Refractive index of the substrate**: the substrate can be either a material in case that the multilayer is stacked to the wafer or a medium if the multilayer is a membrane detached form the substrate.
- **Data plotted**: reflectivity, transmission, absorption or any combination of them.
- **Wavelength range**: the initial and the final values of the wavelength range to be studied and the step, all of them in nanometers.
- **Graphs**: the data calculated is plotted in two different graphs, one for TE polarization and the other for TM polarization. Each graph or both can be also plotted in a separate window selecting the check box "Plot in a separate window", where the user can change the properties of the plot in the same way that any Matlab plot.

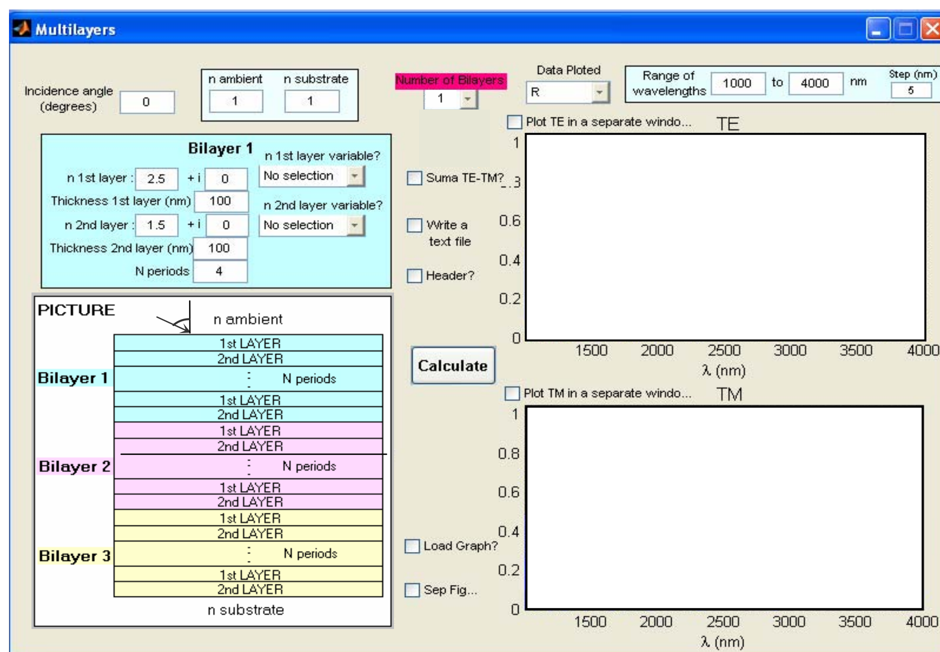

Fig. 3.2. Main program window. The schematic of a multilayer is presented to visually indicate the user the parameters that can be adjusted. The default values of the parameters can be observed.

UNIVERSITAT ROVIRA I VIRGILI
DESIGN, FABRICATION AND CHARACTERIZATION OF POROUS SILICON MULTILAYER OPTICAL DEVICES
Elisabet Xifré Pérez
ISBN: 978-84-691-0362-3/DL: T.2181-2007

- **Number of bilayers**: number of periodic multilayers stacked together that form the multilayer structure. This number can range from 1 to 6 bilayers. When the user chooses the number of bilayers of the structure, one frame for each bilayer appears in the program window with the parameters to be adjusted: refractive indices and thicknesses of the two layers and number of periods. An example with three bilayers is shown in Fig. 3.3.
- **Bilayer frame**: The parameters of each periodic bilayer are determined in this frame. These parameters are the **thicknesses** and **refractive indices** of the two materials that form the bilayer and the **number of periods**. The refractive index can be either constant (real or complex) or variable with the wavelength, in which case different materials can be selected from the popup menu **n layer variable?**: silver (Ag), aluminium (Al), gold (Au), copper (Cu), water (H_2O), magnesium fluoride (MgF_2), nickel (Ni), silicon nitride (Si_3N_4), and silicon dioxide (SiO_2). The variable refractive indices used for these materials have been obtained from [159]. The possibility to determine up to six different periodic bilayers stacked together makes it possible to simulate different multilaye
- **Sum TE-TM**: The spectrum of a wave containing both polarizations is plotted in a separate graph when this check box is selected.
- **Write a text file**: Enables the possibility to save the data plotted in one or both graphs to a text file.
- **Header**: The text file with the results of the simulation can be written with or without a header. Selecting this check box, the text file is written with a header.
- **Load Graph**: Selecting this checkbox, the data from a text file can be also plotted with the simulated results. With this option, it is possible to compare simulations with measurements and different plots in an easy way.
- **Calculate**: Once all the parameters for the simulation have been selected, the program is executed pushing this button.

UNIVERSITAT ROVIRA I VIRGILI
DESIGN, FABRICATION AND CHARACTERIZATION OF POROUS SILICON MULTILAYER OPTICAL DEVICES
Elisabet Xifré Pérez
ISBN: 978-84-691-0362-3/DL: T.2181-2007

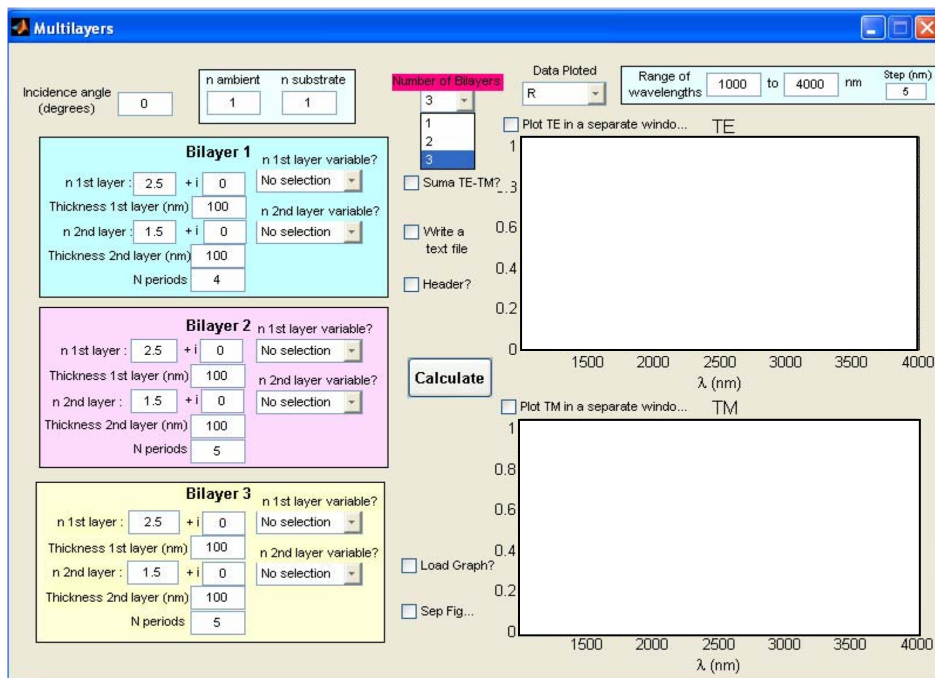

Fig. 3.3. Main program window. In this case the user has selected to simulate a structure formed by three bilayers.

Fig. 3.4 shows the simulation of a multilayer with two bilayers. The first bilayer consists of the repetition of two dielectric materials with constant refractive indices whereas the second bilayer is formed by a dielectric layer with constant refractive index and a silver layer. The refractive index of the silver layer is variable with the wavelength and the best way to simulate this material is to select its refractive index in the popup menu. The reflectivity spectrum of the multilayer is plotted in the graphs. We can also observe the difference between the TE and TM polarizations when the incidence angle is 50 degrees.

ISBN: 978-84-691-0362-3/DL: T.2181-2007

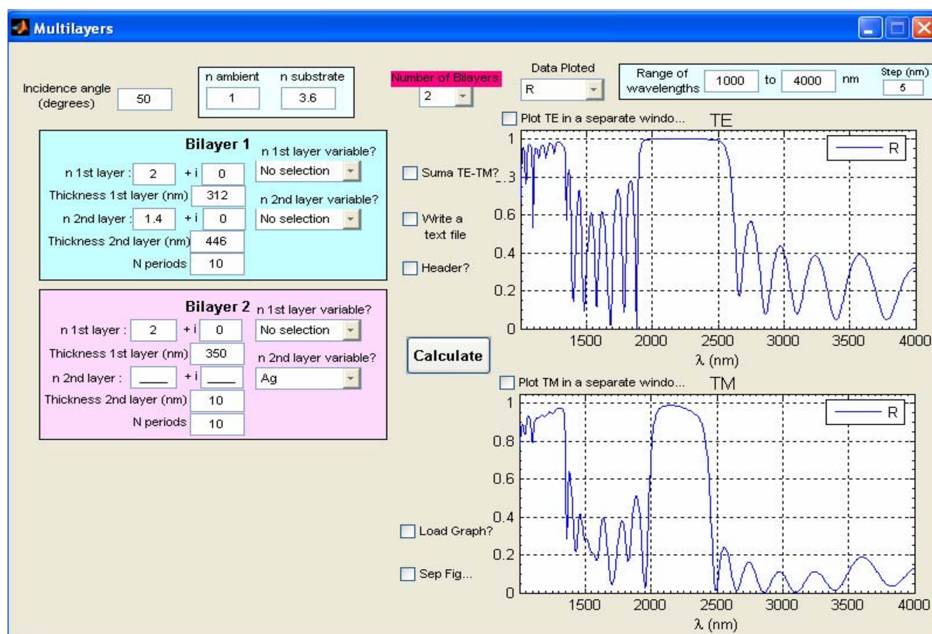

Fig. 3.4. Example of the simulation of a multilayer consisting of two periodic bilayers stacked together. In Bilayer 2 the second layer is silver, for this reason the corresponding refractive index variable with wavelength has been selected.

3.2.2. Program for the calculation of photonic band diagrams

The main objective of this program is to study the band diagram of a multilayer before its fabrication. It also compares the band diagram with the reflectivity or transmission spectra of the multilayer to confirm that there is an agreement between the calculated band diagram and the spectrum of the multilayer and to observe the influence of the finite number of periods on the bandgap edges. The program can also calculate the projected band structure (PBS) of the studied multilayer, which represents the band diagrams for all incidence angles from 0 to 90 degrees. This program is also based on the transfer matrix method.

UNIVERSITAT ROVIRA I VIRGILI
DESIGN, FABRICATION AND CHARACTERIZATION OF POROUS SILICON MULTILAYER OPTICAL DEVICES
Elisabet Xifré Pérez
ISBN: 978-84-691-0362-3/DL: T.2181-2007

In Fig. 3.5 we can observe the main window of this simulation program, where the user can define all the parameters for the simulation. The band diagram is a characteristic of infinite periodic multilayers therefore for the calculation of the band diagram and the PBS, the only required parameters are the ones presented in the frames named "Infinite periodic structure" and "Band diagram":

- **Refractive index of the layers**: denoted by **n 1st layer** and **n 2nd layer**.
- **h1/period**: Thickness of the first layer normalized to the period thickness. Thus, h_1/period can range from 0 to 1. The thickness of layer 2 is calculated from h_1 using: h_2=period-h_1.
- **Maximum value of the normalized frequency**: maximum value of ($\omega\Lambda/2\pi c$) for the calculation of the band diagram.
- **Plot PBS**: The projected band structure (PBS) of the multilayer is also plotted in a separated window when this check box is marked. In Fig. 3.6 the PBS calculated by the program is shown.

The band diagram calculated for this multilayer is plotted in the left side graph. This band diagram belongs to an infinite multilayer but the fabricated multilayers are finite, consequently it would be interesting to compare the high reflectivity (or low transmission) bands of the finite multilayer with the band diagram. For this reason, the right-side graphs show the reflection/transmission spectrum of the finite multilayer (upper graph) and the band diagram of the infinite multilayer (lower graph) for an easy comparison. For the calculation of the spectrum the next parameters are required:

- **Refractive index of the ambient medium**: the ambient medium is the medium from which the incident wave arrives to the surface of the multilayer.
- **Refractive index of the substrate**: the substrate can be either a material in case that the multilayer is stacked to the wafer or a medium if the multilayer is a membrane detached form the substrate.

UNIVERSITAT ROVIRA I VIRGILI
DESIGN, FABRICATION AND CHARACTERIZATION OF POROUS SILICON MULTILAYER OPTICAL DEVICES
Elisabet Xifré Pérez
ISBN: 978-84-691-0362-3/DL: T.2181-2007

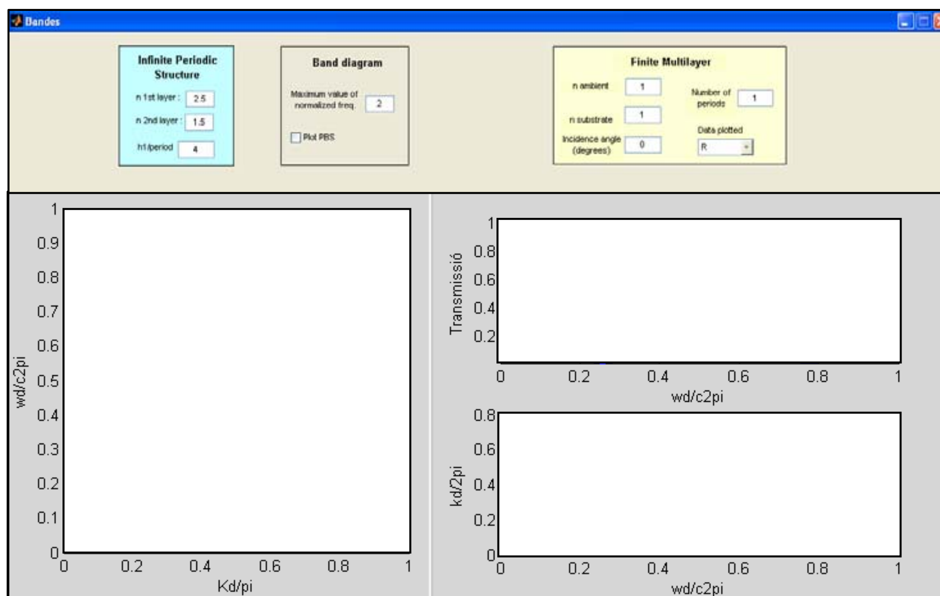

Fig. 3.5. Program for the calculations of the band diagram and projected band structure of a periodic multilayer. The reflectivity spectrum is also presented.

- **Incidence angle**: Angle between the propagation direction of the incident wave and the normal to the surface of the layers. From 0 to 90 degrees.
- **Number of periods** of the multilayer.
- **Data plotted**: reflectivity or transmission spectrum.

Fig. 3.6 shows the main program window with the results of the simulation for an example multilayer. The design parameters of the multilayer can be read in the window program. The comparison between the band diagram and the transmission spectrum indicates that, for this number of periods, the edges of the bandgaps are not sharp. For this reason, the ranges of frequencies with transmission zero are slightly narrower than the bandgaps of the infinite multilayer. In the next sections the relation between the sharpness of the band edges and the number of periods of the periodic multilayer is studied. The PBS

UNIVERSITAT ROVIRA I VIRGILI
DESIGN, FABRICATION AND CHARACTERIZATION OF POROUS SILICON MULTILAYER OPTICAL DEVICES
Elisabet Xifré Pérez
ISBN: 978-84-691-0362-3/DL: T.2181-2007

of the multilayer is plotted in a separate window and can be observed at the bottom of Fig. 3.6. The omnidirectional bandgap (black region) is also plotted.

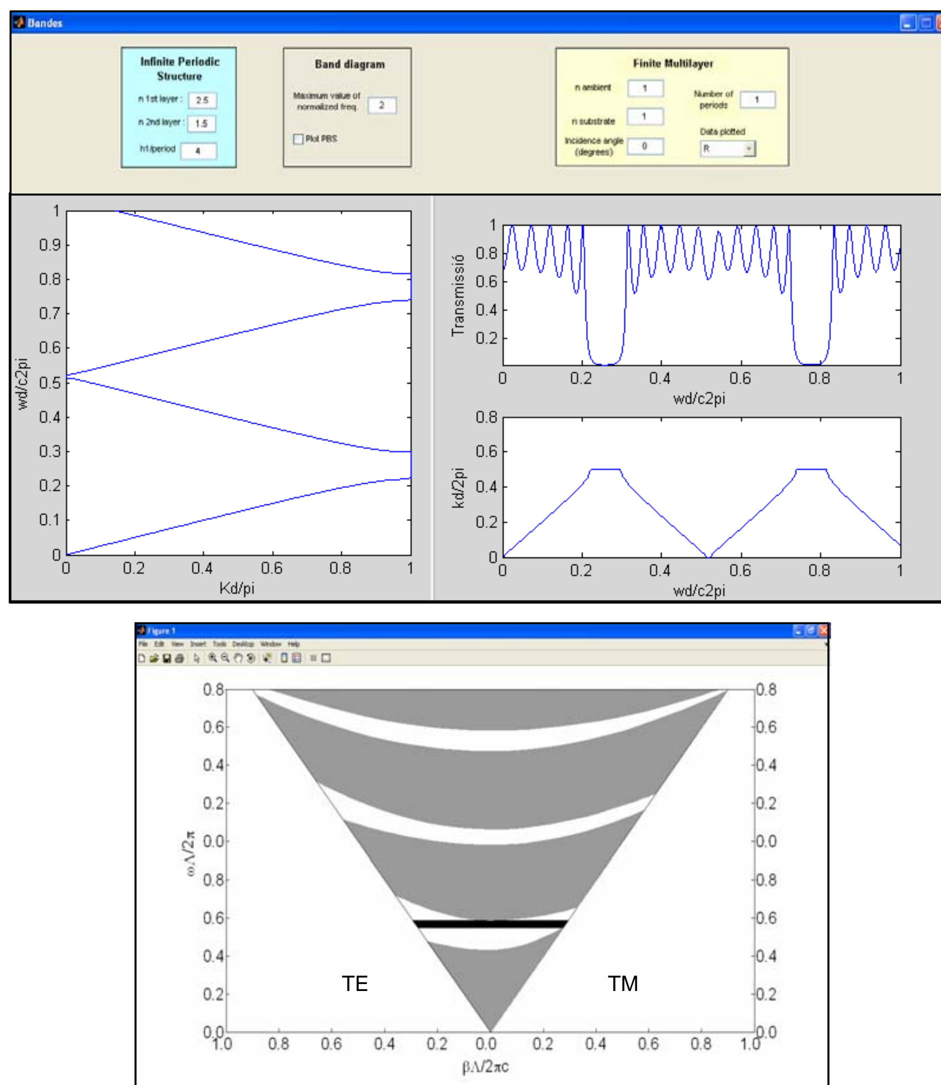

Fig. 3.6. Top: Example of the simulation of a multilayer using the explained program. Bottom: Window with the PBS of the infinite multilayer simulated.

UNIVERSITAT ROVIRA I VIRGILI
DESIGN, FABRICATION AND CHARACTERIZATION OF POROUS SILICON MULTILAYER OPTICAL DEVICES
Elisabet Xifré Pérez
ISBN: 978-84-691-0362-3/DL: T.2181-2007

All the different optical devices studied in this work have been analyzed using these two simulation programs.

3.3. Performance of the developed programs for the study of optical devices

In order to evaluate the performance of the developed programs explained in the previous section, different optical devices based on multilayers and widely reported in the literature have been simulated. The obtained spectra have been compared with the ones reported. These optical devices are Distributed Bragg Reflectors and microcavities. Besides, the developed programs have been used to study the influence of the different parameters of these devices on their optical behavior.

3.3.1. Distributed Bragg Reflectors (DBR)

These filters, as is explained in chapter 2, are characterized by a spectral region with a very high reflectivity, the so-called forbidden band or bandgap, centered at wavelength λ. This high reflectivity is due to the fact that all the beams that are reflected at the multiple interfaces of the multilayer have the same phase when they arrive to the top interface, interfering constructively. For wavelengths different to λ, the interference is not constructive and for this reason the reflectivity decreases.

3.3.1.1. Performance of the developed programs for the simulation of DBRs

The developed programs have been realized to theoretically study multilayers consisting of dielectric and/or metallic layers. To evaluate the performance of the programs, the spectra of two DBRs made of different materials have simulated. Firstly, a dielectric DBR, in concrete one of the porous silicon DBRs presented by Pavesi in [78], is simulated with the same

ISBN: 978-84-691-0362-3/DL: T.2181-2007

parameters used by the author. The reported DBR consists of two layers with n_H=1.86 and n_L=1.27 repeated 20 times. It is a λ/4-DBR, so the optical thickness of the layers are $\lambda/4= n_H\ d_H=n_L\ d_L$ with λ =600 nm. For the simulations, the author considered no absorption, n_{air}=1 and refractive index of the substrate n_{Subs}=4.1. This structure has been simulated with our program and the reflectivity spectrum obtained is shown in Fig. 3.7 together with the spectrum reported in the literature. It can be observed that our simulated spectrum completely agrees with the spectrum reported in [78].

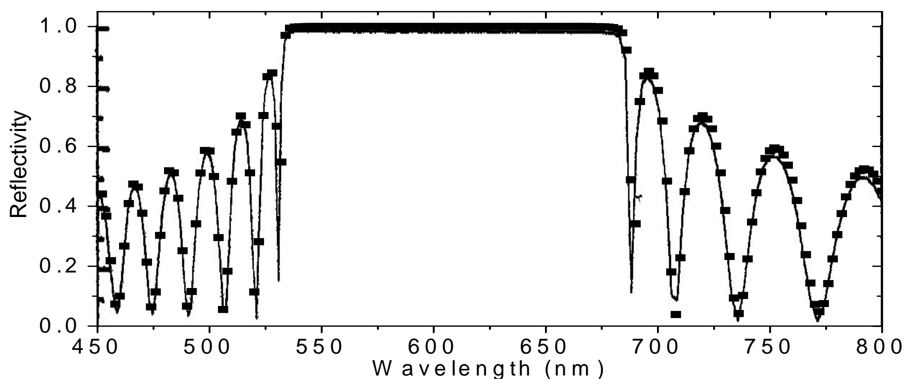

Fig. 3.7. Reflectivity spectrum of the porous silicon DBR simulated by Pavesi (After [78]) (solid line). It is compared with the simulated reflectivity spectrum obtained with our program for the same multilayer structure (symbols).

The developed programs can also simulate metallo-dielectric multilayers as the one presented by Scalora *et. al.* in [160]. In that work, the transmission spectrum of a multilayer consisting of a layer of silver and another of magnesium fluoride (MgF_2) repeated 4 times is studied. The thickness of the silver layer is 10 nm and the one of the MgF_2 layer is 110 nm. Fig. 3.8 shows the comparison between the transmission spectrum reported in the literature and

ISBN: 978-84-691-0362-3/DL: T.2181-2007

the one simulated with our program. It can be observed that the two spectra agree.

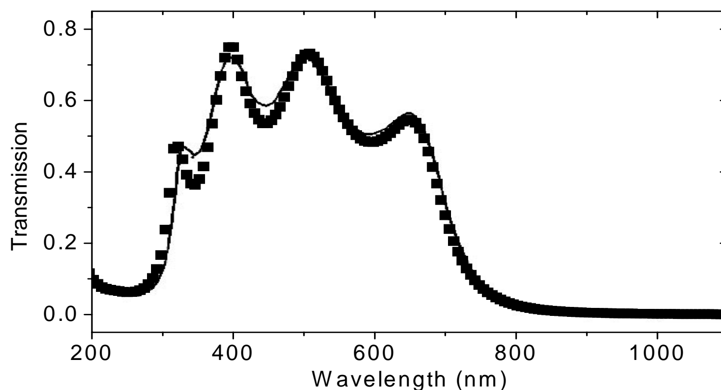

Fig. 3.8. Transmission spectrum of the metallo-dielectric multilayer simulated by Scalora (After [160]) (solid line). It can be compared with the transmission spectra simulated with our programs (symbols).

The agreement between the simulated spectra and the spectra reported in the literature confirms the properly performance of the developed programs and their suitability for the simulation of dielectric and metallo-dielectric multilayers.

3.3.1.2. Study of the DBR parameters

The simulation is a very helpful tool to study the influence of the different parameters of DBR on the reflectivity spectrum. These parameters are:

a) Refractive index ratio n_H/n_L

This ratio influences on the width and the sharpness of the DBR bandgap. The increase of the ratio n_H/n_L leads to the widening of the bandgap. This effect can be observed in Fig. 3.9, where the reflectivity spectra of three $\lambda/4$-DBRs with different n_H/n_L ratio show a bandgap with different width. We can also observe that the band edges become sharper when the ratio increases.

UNIVERSITAT ROVIRA I VIRGILI
DESIGN, FABRICATION AND CHARACTERIZATION OF POROUS SILICON MULTILAYER OPTICAL DEVICES
Elisabet Xifré Pérez
ISBN: 978-84-691-0362-3/DL: T.2181-2007

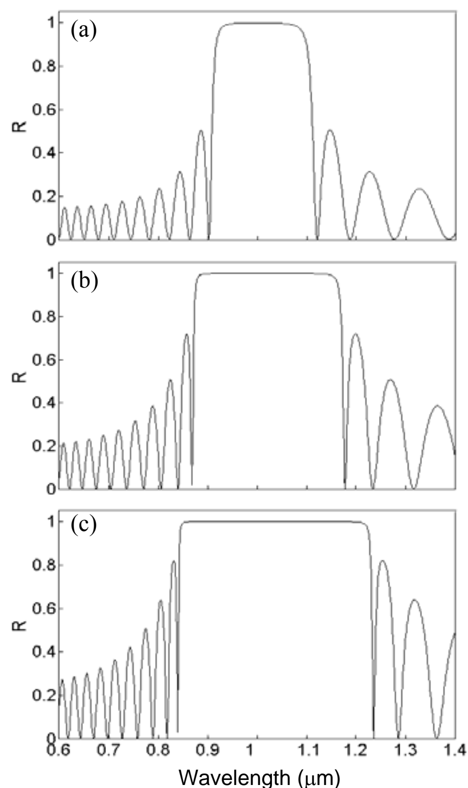

Fig. 3.9. Reflectivity spectrum for normal incidence of three different λ/4-DBR with 15 periods. The thickness of the layers have been calculated to obtain a bandgap centered at λ=1 μm. The n_H/n_L ratio is a) 1.7/1.3, b) 2/1.3, c) 2.3/1.3.

The bandgap of these spectra are not symmetric around the central wavelength, in this case 1 μm, because the symmetry can be observed when the magnitude of the x-axis is wavenumber instead of wavelength. To verify this symmetry, the three spectra of Fig. 3.9 are plotted in Fig. 3.10 using wavenumber for the x-axis.

ISBN: 978-84-691-0362-3/DL: T.2181-2007

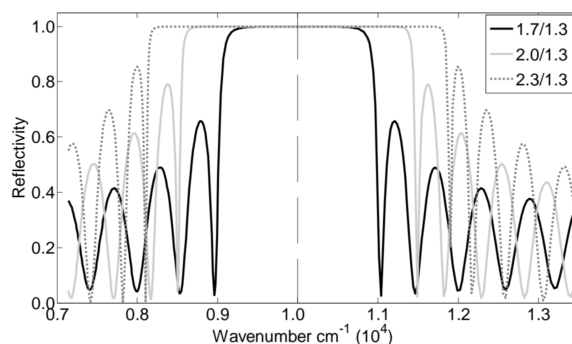

Fig. 3.10. Reflectivity spectrum for normal incidence of three different multilayers already presented in Fig. 3.9. In this case, the wavenumber is used for the x-axis. The symmetry of the bandgaps, centered at 1 cm^{-1} can be observed.

b) Number of periods of the multilayer

The number of periods (N) influences on different characteristics of the bandgap. The increase in the number of periods N leads to an increase of the reflectivity within the bandgap, and enlarges its width. The band edges also become sharper. Fig. 3.11 shows four λ/4-DBR with n_H=2.1, n_L=1.5 and different number of periods N. We can observe that when N increases, the band edges of the filter are sharper and the reflectivity tends to the unity exponentially with N [161].

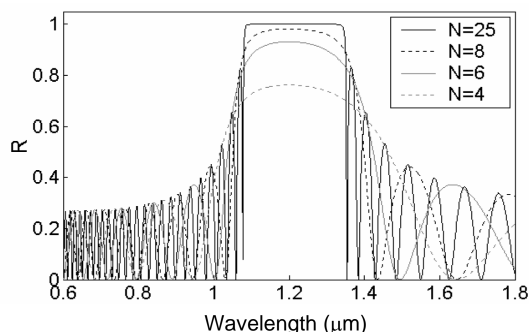

Fig. 3.11. Reflectivity spectrum of a λ/4-DBR with n_H=2.1, n_L=1.5 and number of periods 4, 6, 8 and 25.

UNIVERSITAT ROVIRA I VIRGILI
DESIGN, FABRICATION AND CHARACTERIZATION OF POROUS SILICON MULTILAYER OPTICAL DEVICES
Elisabet Xifré Pérez
ISBN: 978-84-691-0362-3/DL: T.2181-2007

3.3.1.3. Design of a porous silicon DBR for 1.55 μm applications

The use of porous silicon for the study and design of DBR does not imply more difficulties than any other dielectric material. The main consequence of the use of porous silicon is that the range of refractive indices that can be obtained is limited due to the characteristics of the material. For this reason, the bandgap width of porous silicon DBR is limited because of the n_H/n_L ratio limitation. In order to obtain a DBR with a wide bandgap, two typical values, one of the highest and one of the lowest values of this refractive index range, have been chosen [19]: n_H=2.5 and n_L=1.55. The number of periods is high enough to obtain reflectivity near 1 within almost all the bandgap (N=25).

This DBR is designed to work for 1.55 μm applications, like all the porous silicon optical devices studied in this work. This wavelength is usually used for telecommunications applications. Since the bandgap of the λ/4-DBR must be centered at 1.55 μm, the optical thickness of the layers must be 1.55 μm/4 = $n_H h_H = n_L h_L$. According to this, the layer thicknesses are h_H=155 nm and h_L=258.3 nm. The reflectivity spectrum of this DBR can be observed in Fig. 3.12. The bandgap width is around 500 nm for reflectivity higher than 99.9%. This would be one of the widest bandgaps obtainable with periodic porous silicon DBR centered at this wavelength.

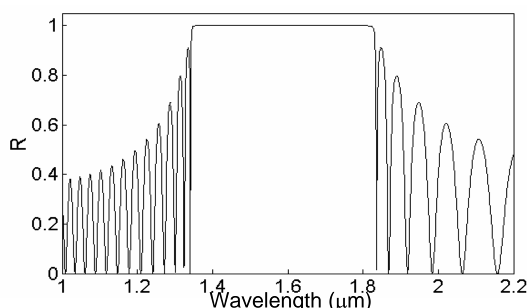

Fig. 3.12. Reflectivity spectrum of a porous silicon λ/4-DBR for 1.55 μm applications. It has 25 periods, n_H=2.5, n_L=1.55, h_H=155 nm and h_L=258.3 nm.

ISBN: 978-84-691-0362-3/DL: T.2181-2007

3.3.1.4. Reflectivity spectrum of stacked filters

Usually, the applications of DBR require wide bandgaps. As has been demonstrated in the previous section, the widening of the bandgap is obtained with the increase in the n_H/n_L ratio. Due to the limits of the n_H/n_L ratio for porous silicon, an easy way for obtaining enlarged bandgap reflectors is to stack together two or more reflectors. The reflectors used for the stack must have their bandgaps centered at different wavelengths but close enough to intersect one with the other.

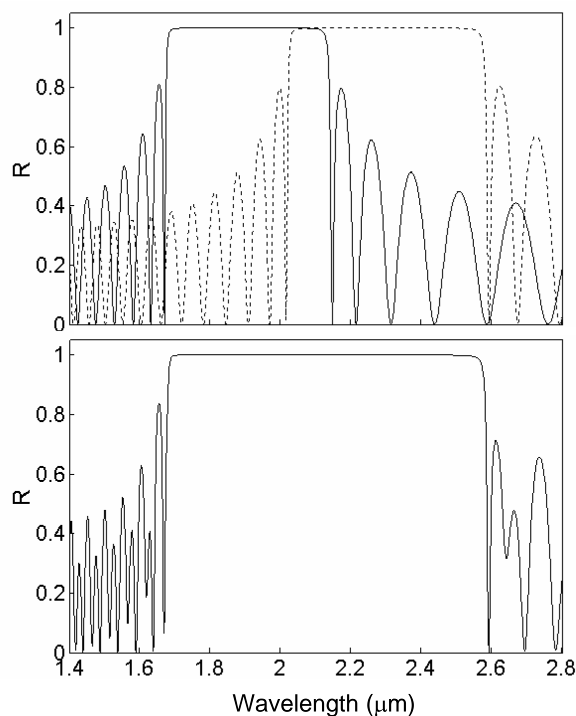

Fig. 3.13. Reflectivity spectrum of a) two DBR with n_H=2.3, n_L=1.6 and N=20. One of them is formed by layers with optical thickness λ/4=1.88 μm/4, and the other is formed by layers with optical thickness λ/4=2.27 μm/4. b) DBR with 40 periods and n_H=2.3, n_L=1.6 consisting of the two DBRs stacked together.

UNIVERSITAT ROVIRA I VIRGILI
DESIGN, FABRICATION AND CHARACTERIZATION OF POROUS SILICON MULTILAYER OPTICAL DEVICES
Elisabet Xifré Pérez
ISBN: 978-84-691-0362-3/DL: T.2181-2007

Fig. 3.13a shows the reflectivity spectrum, for normal incidence, of two DBR with the same refractive indices and the same number of periods. On the contrary, the thicknesses of the layers are different for each DBR, and therefore their bandgaps are centered at different wavelengths. We can observe that the bandgaps intersect. Fig. 3.913b shows the reflectivity spectrum of a multilayer formed by the two DBR stacked together. We can see that its bandgap is the union of the bandgaps of the DBRs presented in Fig. 3.913a .

Although, in this example, the filters have the same refractive indices and different thicknessese, it could be possible to use different refractive indices and/or thicknesses. One of the aims of the stack of filters is the widening of the DBR bandgap but it could be also used for obtaining a DBR with high reflectivity at separated wavelength ranges. In this case, the stacked filters should have bandgaps situated at the desired wavelength ranges.

3.3.2. Microcavities

It is possible to fabricate a particular class of interferometers, named microcavities or Fabry-Pérot filters, by using two parallel reflectors separated by a spacer layer. Usually the reflectors used are λ/4 DBR. The reflectivity spectrum of microcavities consists of a wide high-reflectivity bandgap with a narrow pass-band in its center. The wavelength at which this pass-band (also called transmission peak) is situated, its width and its reflectivity level depend on different parameters.

3.3.2.1. Performance of the developed programs for the simulation of microcavities

Microcavities are multilayer structures widely studied for many different applications. We use here a porous silicon microcavity reported in [78] to evaluate the performance of the simulation programs. The microcavity consists of two λ/4-DBR with 4 periods where n_H=2.24 and n_L=1.27. The optical thickness of the layers are $\lambda/4= n_H\, d_H = n_L\, d_L$ with λ =600 nm. The spacer layer

UNIVERSITAT ROVIRA I VIRGILI
DESIGN, FABRICATION AND CHARACTERIZATION OF POROUS SILICON MULTILAYER OPTICAL DEVICES
Elisabet Xifré Pérez
ISBN: 978-84-691-0362-3/DL: T.2181-2007

thickness is λ/2 and its refractive index is n_s=1.27. Fig. 3.14 shows the simulated reflectivity spectrum of this multilayer where we can observe that it completely agrees with the reflectivity spectrum reported in [78].

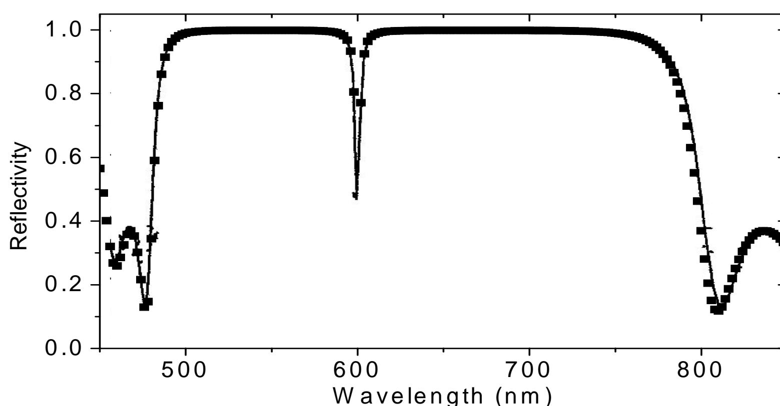

Fig. 3.14. Reflectivity spectrum simulated with our program (symbols) and simulated reflectivity spectrum of the same microcavity structure reported in [78].

3.3.2.2. Study of the microcavity parameters

The influence of the different parameters of microcavities on the reflectivity spectrum has been also studied.

a) Thickness of the spacer layer (h_s)

Whereas the optical thickness of the DBRs are usually λ/4, the optical thickness of the spacer layer can be either λ or λ/2. In both cases, the transmission peak is centered at wavelength λ. The reflectivity spectra of microcavities with a λ or a λ/2 spacer layer are compared in Fig. 3.15. This figure shows the reflectivity spectra for normal incidence of microcavities consisting of two parallel DBR with 6 periods and optical thickness λ/4, where λ=1.55 μm. In Fig. 3.15a, the optical thickness of the spacer is λ, whereas in

UNIVERSITAT ROVIRA I VIRGILI
DESIGN, FABRICATION AND CHARACTERIZATION OF POROUS SILICON MULTILAYER OPTICAL DEVICES
Elisabet Xifré Pérez
ISBN: 978-84-691-0362-3/DL: T.2181-2007

Fig. 3.15b this thickness is λ/2. Both spectra are very similar. The transmission peak is centered at 1.55 μm in both cases and the reflectivity for both is almost zero at this wavelength. However, the bandgap of the microcavity with the λ/2 spacer is slightly wider than the one with thickness λ and the side-lobes closer to the bandgap show a lower reflectivity.

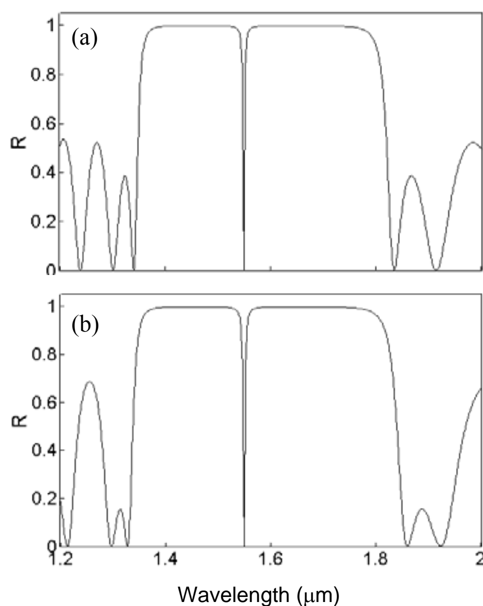

Fig. 3.15. Reflectivity spectrum of a microcavity consisting of two DBR with optical thickness λ/4 and a spacer layer of thickness a) λ, b) λ/2.

b) Refractive index of the spacer layer

The refractive index o the spacer layer can be one of the indices used in the DBRs (n_H,n_L) of the microcavity or a different value. The influence of this value on the reflectivity spectrum of the microcavity has been studied for all the possible cases: for a refractive index lower than n_L, equal to n_L, between n_L and n_H, and equal to n_H. The results can be observed in Fig. 3.16. The four plots belong to porous silicon microcavities for 1.55 μm applications. The λ/4-DBRs

ISBN: 978-84-691-0362-3/DL: T.2181-2007

that form them have n_L=1.6, n_H=2.3 and N=6. The spacer thickness is λ/2 and its index n_s is 1.4 (n_s<n_L), 1.6 (n_s=n_L), 1.8 (n_L< n_s<n_H), and 2.3 (n_s=n_H). The transmission peak is positioned for all of them at 1.55 μm and its reflectivity is almost zero for all, therefore we can deduce that the refractive index of the spacer does not noticeable affect the bandgap or the transmission peak. The difference between these spectra is observed at the side-lobes.

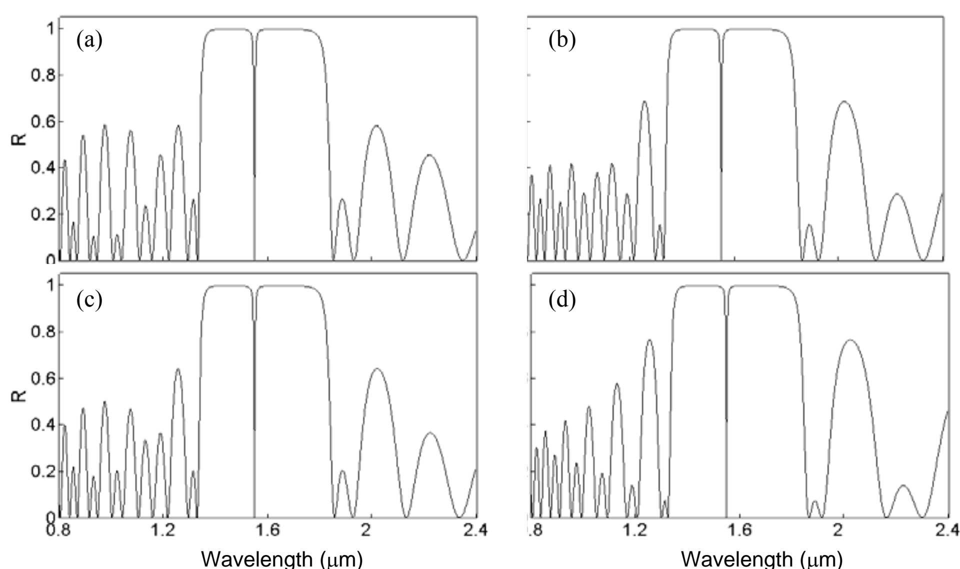

Fig. 3.16. Reflectivity spectrum of a microcavity consisting of two DBR with n_L=1.6 and n_H=2.3. The thickness of the spacer layer is λ/2 and its refractive index is a) 1.4, b) 1.8, c) 1.6 d) 2.3.

c) *Number of periods of the DBR*

The width of the transmission peak depends on the number of periods N of the DBRs of the microcavity. When N increases, the transmission peak becomes narrower, the reflectivity of the bandgap increases and its edges are sharper. These effects can be observed in Fig. 3.17.

UNIVERSITAT ROVIRA I VIRGILI
DESIGN, FABRICATION AND CHARACTERIZATION OF POROUS SILICON MULTILAYER OPTICAL DEVICES
Elisabet Xifré Pérez
ISBN: 978-84-691-0362-3/DL: T.2181-2007

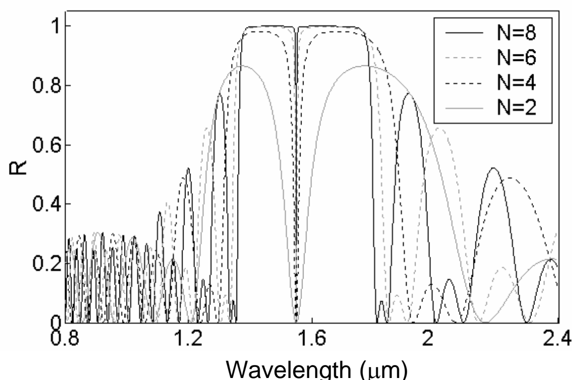

Fig. 3.17. Reflectivity spectrum of a porous silicon microcavity for 1.55 μm applications where the DBRs that form it have a different number of periods.

3.4. Summary and conclusions

We have demonstrated that the transfer matrix method is a very useful and simple mathematical method for the simulation of multilayers. Very user-friendly programs based on this method have been developed and all their variable parameters have been explained. They calculate the reflectivity, transmission and absorption spectra; and the photonic band diagrams of multilayers. The parameters that can be adjusted by the used are the refractive index and thickness of the layers, the number of periods, the incidence angle and the wavelength range. Besides, one of the programs can be used for the study of different periodic multilayers stacked together.

Although the simulations realized during this work have been focused on porous silicon layers, any other material could be simulated because the user can select the refractive indices. These refractive indices can be either constant (real or complex) or variable with wavelength, in which case different materials can be selected (Ag, Al, Au, Cu, MgF_2, Ni, Si_3N_4, and SiO_2). The number of selectable materials will be increased in a near future.

To evaluate the performance of the developed programs we have simulated different Distributed Bragg Reflectors (DBR) and microcavities. The

UNIVERSITAT ROVIRA I VIRGILI
DESIGN, FABRICATION AND CHARACTERIZATION OF POROUS SILICON MULTILAYER OPTICAL DEVICES
Elisabet Xifré Pérez
ISBN: 978-84-691-0362-3/DL: T.2181-2007

simulated spectra agree with the ones reported in the literature, which indicates the suitability of the developed programs. With the study of DBRs, we have observed that porous silicon is a suitable material for the fabrication of filters with a wide bandgap centered at λ=1.55 μm. This bandgap can be wider with the fabrication of porous silicon stacked filters. The introduction of defect layers in the DBR has lead to the study of microcavities and the understanding of the effect of these layers on the reflectivity spectrum of the multilayer structure.

ISBN: 978-84-691-0362-3/DL: T.2181-2007

Chapter 1

Introduction and objectives

Porous silicon was discovered in 1956 by Uhlir [1] while performing electropolishing experiments on silicon wafers using an electrolyte containing hydrofluoric acid. Its development was first justified for technological reasons, in particular, localized isolation in microelectronics. A renewed interest in porous silicon occurred in 1990 when its photoluminescence and electroluminescence properties were demonstrated [2,3]. The optical properties of porous silicon have been extensively investigated [3,4,5,6] and promising electroluminescent devices have been fabricated [7].

Porous silicon is usually designed in a complex shape, using suitably doped structures and then dissolved selectively to leave silicon membranes, beams or trenches [8-9]. Depending on the anodization conditions [10], this material presents a porous texture with pore diameters varying from 2 to 15 nm, density varying from 20 % to 80 % and specific surface area varying from 100 to 600 m^2 cm^{-3}.

It has been established that the most important parameters which fix the characteristics of porous silicon obtained by electrochemical anodization are the electrolyte composition, particularly the hydrofluorhydric concentration, the

UNIVERSITAT ROVIRA I VIRGILI
DESIGN, FABRICATION AND CHARACTERIZATION OF POROUS SILICON MULTILAYER OPTICAL DEVICES
Elisabet Xifré Pérez
ISBN: 978-84-691-0362-3/DL: T.2181-2007

current density across the wafer, and the time of current application. Whereas the time determines the thickness of the porous silicon layer, the current determines the refractive index. In a first approximation, as the silicon dissolution only occurs at the pore tips, at the interface between the silicon substrate and the electrolyte, the porous silicon layer already formed is not affected by the subsequent conditions of fabrication. Therefore, any kind of profile can be prepared, being the easiest way the current modulation during the porous silicon fabrication process. This makes of porous silicon a very suitable material for the fabrication of multilayers.

In this context, this thesis focuses on the study of multilayer optical devices made of porous silicon. In order to achieve this objective, different steps have been realized. Firstly, the theoretical study of multilayers has been developed because by choosing, in an appropriate way, the thicknesses and the refractive indices of the various layers, it is possible to fabricate different optical devices, such as filters, microcavities, waveguides, etc. With the simulation, we study the suitability of porous silicon for the fabrication of the optical devices. Once simulated and designed the porous silicon multilayer devices, we fabricate them. For this purpose, a fabrication system has been established and calibrated and several porous silicon monolayers and multilayers have been fabricated. Finally, these fabricated layers have been characterized to determine their physical and optical properties. All these steps are necessary to achieve our main and final objective: the fabrication and characterization of porous silicon multilayer optical devices.

The thesis is organized as follows:

In Chapter 2 an introduction to porous silicon basics and the underlying theory that governs their unusual optical properties are explained. The physics of the porous silicon formation and the different parameters of the process that influence on the final characteristics of the fabricated layers are discussed. Different applications of porous silicon are presented, especially the optical applications that have been studied during this work.

Chapter 3 is focused on the development of different programs for the simulation of multilayers. An overview of the mathematical methods used for

UNIVERSITAT ROVIRA I VIRGILI
DESIGN, FABRICATION AND CHARACTERIZATION OF POROUS SILICON MULTILAYER OPTICAL DEVICES
Elisabet Xifré Pérez
ISBN: 978-84-691-0362-3/DL: T.2181-2007

the simulation of multilayers is explained, specially the transfer matrix method, that is explained in detail because it is the method implemented for our theoretical study. Several programs that use the transfer matrix method have been realized and are explained in this chapter. The performance of the programs is studied by comparing the simulated optical responses of well-known multilayer structures with the ones obtained in the literature.

Chapter 4 presents the theoretical study of two different optical devices: omnidirectional mirrors and waveguides. For each device, the different physical parameters that influence on its optical characteristics are analyzed and the suitability of porous silicon for their fabrication is discussed. For the case of omnidirectional mirrors, three different new multilayer structures have been proposed for the widening of the omnidirectional bandgap. For the case of waveguides, the modal study of porous silicon waveguides based on total internal reflection has been developed whereas waveguides based on the properties of photonic crystals have been widely studied, proposing the use of omnidirectional mirrors and DBR for the cladding. All these devices have been designed for 1.55 μm applications, a wavelength widely used in telecommunications

Chapter 5 gives a complete description of the porous silicon fabrication system that we have established in the Department of Electronic, Electric and Automatic Engineering at the University Rovira i Virgili. The influence of the elements of the system on the properties of the fabricated porous silicon layers is discussed. The most important element of the system is the electrochemical cell, for this reason a study of this element is realized and the differences between two types of electrochemical cells are presented. The calibration of the fabrication system, that is the study of the relations between the anodization parameters and the two most important physical characteristics of porous layers (refractive index and thickness) is presented. To conclude this chapter, the different methods used for the characterization of porous silicon layers are explained.

Chapter 6 is dedicated to the characterization of porous silicon monolayers and multilayers using spectroscopic ellipsometry. This work has

UNIVERSITAT ROVIRA I VIRGILI
DESIGN, FABRICATION AND CHARACTERIZATION OF POROUS SILICON MULTILAYER OPTICAL DEVICES
Elisabet Xifré Pérez
ISBN: 978-84-691-0362-3/DL: T.2181-2007

been realized during one stage at the Ecole Polytechnique (Palaiseau, France) under the supervision of Dr. Enric Garcia-Caurel. This technique has been used to determine the main physical characteristics of the porous layers: porosity (and therefore refractive index) and thickness. In addition, spectroscopic ellipsometry allows the analysis of the anisotropy of the porous layers. Whereas the thickness and porosity of the layers have been also obtained with the characterization methods explained in chapter 5, the anisotropy can only been analyzed with ellipsometry, providing additional information about the fabricated porous layers.

Chapter 7 describes some of the optical devices fabricated with porous silicon multilayers. DBRs, microcavities and omnidirectional mirrors are designed, fabricated and characterized. The comparison between the optical properties of the fabricated device and the simulations are presented for each device.

Finally, chapter 8 presents the conclusions of our work.

UNIVERSITAT ROVIRA I VIRGILI
DESIGN, FABRICATION AND CHARACTERIZATION OF POROUS SILICON MULTILAYER OPTICAL DEVICES
Elisabet Xifré Pérez
ISBN: 978-84-691-0362-3/DL: T.2181-2007

Chapter 2

Fundamentals of porous silicon and applications

In this chapter, the porous silicon formation process in explained. This process consists of the electrochemical etching of silicon wafers in solutions based on hydrofluoric acid. Firstly, the electrochemical etching process is described and the different stages of the porous silicon formation are explained. The anodization parameters that influence on the final characteristics of the fabricated layers are also discussed and the porous silicon photoluminescence is briefly explained, as the discovery in the 90s of this property generated the scientific interest on this material. Finally different applications of porous silicon are presented. Although porous silicon has many potential applications in many areas we especially focus on the optical applications, that are the ones studied during this work.

UNIVERSITAT ROVIRA I VIRGILI
DESIGN, FABRICATION AND CHARACTERIZATION OF POROUS SILICON MULTILAYER OPTICAL DEVICES
Elisabet Xifré Pérez
ISBN: 978-84-691-0362-3/DL: T.2181-2007

2.1. History of Porous silicon

Porous silicon was discovered in 1956 by Uhlir [1] while performing electropolishing experiments on silicon wafers using an electrolyte containing hydrofluoric acid (HF). He found that under the appropriate conditions of applied current and solution composition, the silicon did not dissolve uniformly but instead fine holes were produced, which propagated primarily in the <100> direction in the wafer. Therefore, porous silicon formation was obtained by electrochemical dissolution of silicon wafers in aqueous or ethanoic HF solutions.

In the 1970s and 1980s the interest on porous silicon increased because the high surface area of porous silicon was found to be useful as a model of the crystalline silicon surface in spectroscopic studies [11,12], as a precursor to generate thick oxide layers on silicon, and as a dielectric layer in capacitance-based chemical sensors [13].

In the 1990s Leigh Canham published his results on red-luminescence [14,15] from porous silicon, that was explained in terms of quantum confinement of carriers in nano-crystals of silicon which are present in the pore walls. Since that time, the interest of researchers and technologists to this material (and other porous semiconductors as well) is constantly growing and the number of publications dedicated to this class of materials increases every year. With the discovery of efficient visible light emission from porous silicon came an explosion of work focused on creating silicon-based optoelectronic switches, displays, and lasers. During the last twenty years, the optical properties of porous silicon have become a very intense area of research [16].

Porous silicon is a very promising material due to its excellent mechanical and thermal properties, its obvious compatibility with silicon-based microelectronics [17] and its low cost. Its large surface area within a small volume, its controllable pore sizes, its convenient surface chemistry, and the ability to modulate its refractive index as a function of depth [18] makes porous silicon a suitable dielectric material for the formation of multilayers [19].

All these features also leads, on one hand, to interesting optical properties by mixing silicon with air in the effective medium approximation. On the other

UNIVERSITAT ROVIRA I VIRGILI
DESIGN, FABRICATION AND CHARACTERIZATION OF POROUS SILICON MULTILAYER OPTICAL DEVICES
Elisabet Xifré Pérez
ISBN: 978-84-691-0362-3/DL: T.2181-2007

hand the pores allow the penetration of chemical and biological substances, liquids, cells, molecules to change i.e. the optical behavior of the original system. These effects inspired research into different applications like optical sensing applications [20,21] and biomedical applications [22,23].

2.2. Basics of the porous silicon formation process

2.2.1. Electrochemical etching of porous silicon

One of the most important advantages of porous silicon is its simple and easy preparation [24]. Since the first studies of Uhlir [1] and Turner [25], and lately Cahnam [2], porous silicon has been mainly obtained by electrochemical dissolution of silicon wafers in solutions based on hydrofluoric acid (HF) [26].

A schematic of the porous silicon formation process can be seen in Fig. 2.1. The surface of a silicon wafer, contacted on the back, is in contact with a solution containing hydrofluoric acid (HF). After applying a voltage (in the right direction) between the wafer backside contact and an electrode in the HF solution, a pore growth by silicon dissolution starts, provided certain key parameters are set correctly.

In the past, many studies of porous silicon formation have been limited exclusively to an electrochemical characterization of its current-voltage *(i-V)* relationships with the Schottky diode model of the semiconductor/electrolyte interface playing a predominant role. Although additional analysis techniques have been recently used to study porous silicon, the understanding of porous silicon formation still comes from the *i-V* relationships, and a basic knowledge of silicon electrochemistry is essential to understand the fundamentals of pore formation [27-32]. An overview of semiconductor electrochemistry can be found in Fig. 2.2.

ISBN: 978-84-691-0362-3/DL: T.2181-2007

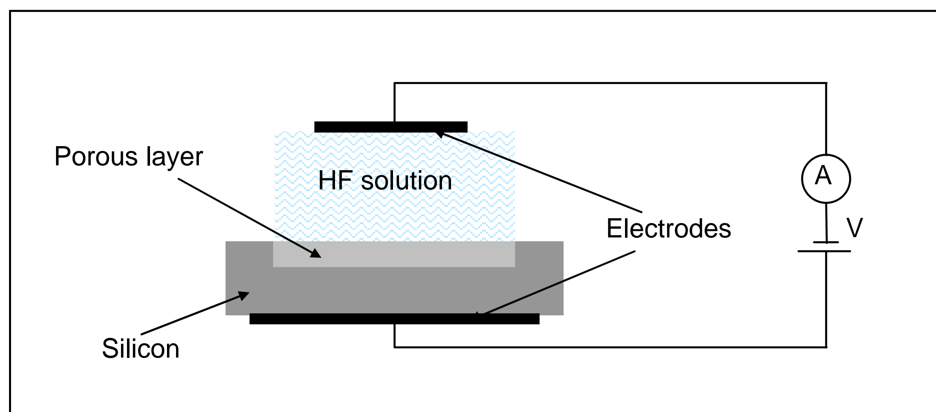

Fig. 2.1. Schematic diagram of the porous silicon anodization circuit.

In this section we outline only the more basic electrochemical features of the *i-V* relationships. Fig. 2.2 shows the typical *i-V* curves for n- and p-type silicon in aqueous HF. The *i-V* curves show some basic similarities to the normal Schottky diode behavior expected from a semiconductor/electrolyte interface, including photogenerated currents at reverse bias. But there also exist some differences [27-30,33]. The first of all is that even though the type of majority carriers changes between n- and p-type, the chemical reactions at the interface remain the same. Second the reverse-bias dark currents have been reported at least three orders of magnitude higher than those normally expected for Schottky diodes.

Both n- and p-type silicon are stable under cathodic polarization. The only important cathodic reaction is the reduction of water at the silicon/HF interface, with the simultaneous formation of gaseous hydrogen. This reaction occurs only at high cathodic overpotentials or, using Schottky-diode terminology, at reverse biased breakdown.

Dissolution of silicon occurs only under anodic polarization. At high anodic overpotentials the silicon surface goes under electropolishing. On the contrary, at low anodic overpotentials the surface morphology is dominated by a dense array of channels penetrating deeply into the bulk of the silicon [34].

ISBN: 978-84-691-0362-3/DL: T.2181-2007

The pore formation occurs only during the initial rising part of the *i-V* curve, for a potential value below the potential of the first sharp peak. The current at this peak is named as the electropolishing current (J_{PS}). The zone of the *i-V* curve at which the pore formation occurs is gray colored in Fig. 2.2.

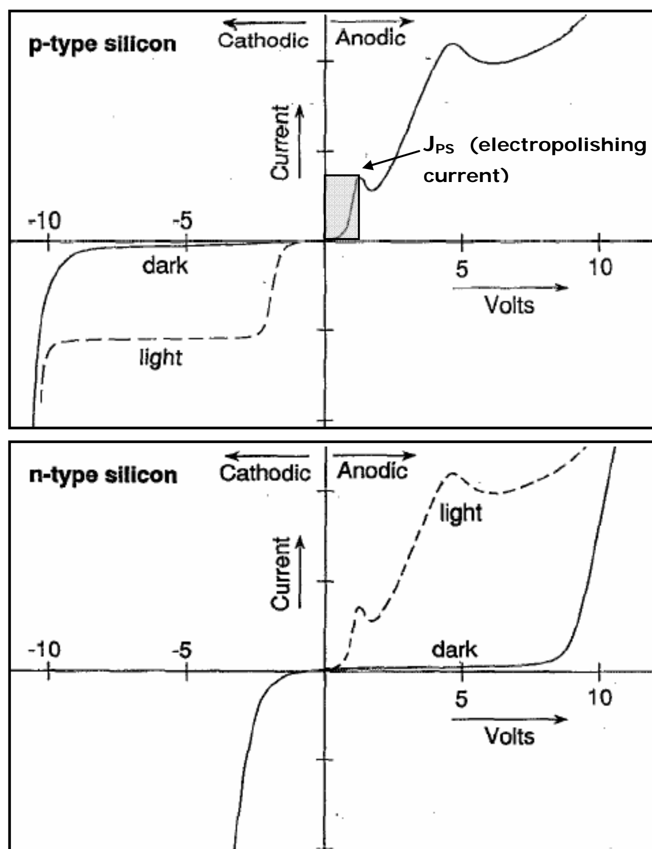

Fig. 2.2. Characteristic *i-V* curves for n- and p-type doped silicon in aqueous HF. The solid line indicates the dark response and the dashed line shows a response under illumination. The first (lower) current peak J_{PS} corresponds to the formation of a surface anodic oxide formed during, and required for, electropolishing. The second (higher) current peak marks the beginning of stable current (potential) oscillations with the possible formation of a second type of anodic oxide. The gray area indicates the useful regime for the formation of porous silicon [Adapted from 26].

UNIVERSITAT ROVIRA I VIRGILI
DESIGN, FABRICATION AND CHARACTERIZATION OF POROUS SILICON MULTILAYER OPTICAL DEVICES
Elisabet Xifré Pérez
ISBN: 978-84-691-0362-3/DL: T.2181-2007

The quantitative values of the *i-V* curves, as well as the values corresponding to the electropolishing peak, depend on the etching parameters and wafer doping. For n-type substrates, this typical *i-V* behavior is observed only under illumination because hole supply is needed. More details about the characteristics of the curves *i-V* are extensively explained in [26,33,35].

It is worth to underline that the parameter that has physical meaning in the anodization process is the current density *J* (at the silicon/electrolyte interface), rather than the absolute current *i*. *J* and *i* scale with a fixed constant for a given cell, provided that the area of the silicon sample exposed to the electrolyte is well defined and fixed.

2.2.2. Porous silicon formation chemistry

To form porous silicon the current at the silicon side of the silicon/electrolyte interface must be carried by holes, injected from the bulk towards the interface. The current must be kept between zero and the electropolishing threshold, as has already been shown in Fig. 2.2. In order to achieve significant hole current in n-type silicon, external illumination of the sample is required, depending on the doping level. If the current exceeds the electropolishing threshold, the anodization results in a progressive, complete removal of silicon. The wafer has then a mirror-like appearance.

Up to now, several different mechanisms regarding the dissolution chemistry of silicon have been proposed but it is generally accepted that holes are required for both electropolishing and pores formation.

The global anodic semi-reaction can be written during pore formation as

$$Si + 6HF \rightarrow H_2SiF_6 + H_2 + 2H^+ + 2e^- \quad (2.1)$$

The final and stable product for silicon in HF is H_2SiF_6, or some of its ionized forms; it follows that during the pore formation only two of the four available silicon electrons participate in an interface charge transfer while the remaining two undergo a corrosive hydrogen formation.

UNIVERSITAT ROVIRA I VIRGILI
DESIGN, FABRICATION AND CHARACTERIZATION OF POROUS SILICON MULTILAYER OPTICAL DEVICES
Elisabet Xifré Pérez
ISBN: 978-84-691-0362-3/DL: T.2181-2007

Amongst the various models proposed for the silicon dissolution reaction, the mechanism presented by Lehmann and Gösele [4] is the most accepted in the porous silicon community.

Similarly to most semiconductor junctions, at the silicon/electrolyte interface a depletion zone is formed (see Fig. 2.3). The width of this depletion zone depends on the doping and may explain the different pore sizes found in p- and p+ type doped silicon. In addition, the depletion layer width depends on the surface curvature: the anodization preferentially occurs at the pore tips where the curvature is largest. Moreover, when the depletion zones of adjacent pores meet each other, the current flow is suddenly pinched off. Further silicon etching is blocked, and pore collapsing is prevented. For this reason the reaction is self limited in the colored anodization regimes of and leads to a porous structure rather than to electropolishing. As further practical consequence, in stationary conditions, the porosity remains approximately constant, whereas the overall thickness of the porous silicon layer grows essentially linearly in time.

Further dissolution occurs only at the pore tips, where enough holes are available, as is schematically represented in Fig. 2.3. In this way the etching of porous silicon proceeds in depth with an overall directionality which follows the anodic current paths inside silicon. Once a porous silicon layer is formed no more electrochemical etching occurs but a slow chemical one starts, due to the permanence in HF.

For the case of n-type silicon, the application of back-side illumination in potentiostatic regime allows further control on the hole injection, both in terms of carrier flux (which is proportional to illumination intensity) and of localization of the injection, which is concentrated in the region of the pore tips, acting as hole collectors. The etching process leads to a very regular pore growth, which is most effectively exploited to fabricate macroporous photonic crystal devices, as the one presented in Fig. 2.4.

UNIVERSITAT ROVIRA I VIRGILI
DESIGN, FABRICATION AND CHARACTERIZATION OF POROUS SILICON MULTILAYER OPTICAL DEVICES
Elisabet Xifré Pérez
ISBN: 978-84-691-0362-3/DL: T.2181-2007

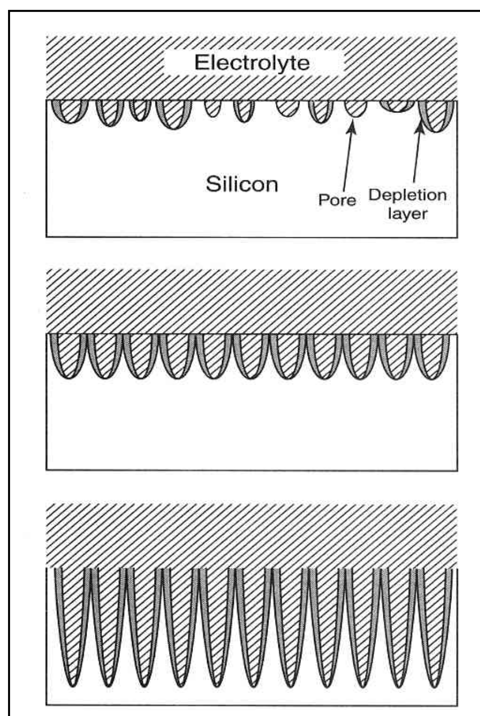

Fig. 2.3. Pore formation in porous silicon. The upper figure shows the initial stage, where the pores develop randomly on the silicon surface. In the middle, the self-regulating process is shown. When the depletion zones around each pore overlap, the pore growth changes from an isotropic growth to a highly directional growth. The bottom figure shows how the dissolution advances only at the pore tips. [After 36].

Up to this point, we can say that the main requirements for porous silicon formation are:

1. The silicon wafer must be anodically biased. This corresponds to forward biasing for p-type doped silicon, and reverse biasing for n-type doped silicon.
2. For n-type doped and semi-insulating p-type doped silicon, light must be supplied.
3. Current densities below the critical value, J_{PS}, must be used.

UNIVERSITAT ROVIRA I VIRGILI
DESIGN, FABRICATION AND CHARACTERIZATION OF POROUS SILICON MULTILAYER OPTICAL DEVICES
Elisabet Xifré Pérez
ISBN: 978-84-691-0362-3/DL: T.2181-2007

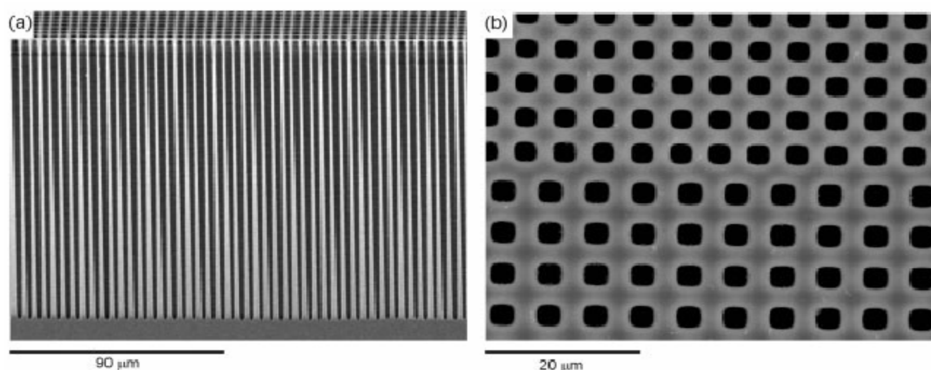

Fig. 2.4. Example of a two-dimensional photonic crystal. a) Cross section and b) top-view images of the same sample. It was realized with ordered macroporous porous silicon in a n-type doped silicon substrate [After 37].

The first two conditions are due to the fact that holes are consumed during the silicon etching. When the third condition is not fulfilled, the reaction is limited by mass transfer to the solution: holes pile up at the silicon-HF interface and electropolishing occurs.

For all the three conditions mentioned above the holes play an important role: in fact, porous silicon formation is a self-regulated mechanism, with hole depletion as the limiting agent. The dissolution reaction begins at defects on the silicon wafer surface, the pores are formed and their walls are eroded until they are emptied of the holes. This formation process passivates them from further attack, and the reaction proceeds at the pore end, as is represented in Fig. 2.3.

The overall etching process is self-adjusting and the average pore size is given by the electrochemical parameters only.

2.2.3. Pore size and morphology

The existing nomenclature, adopted by the International Union of Pure and Applied Chemistry (IUPAC), distinguishes three categories with regard to the pore dimensions [38]: micropores, mesopores and macropores with average pore diameters of < 2 nm, 2-50 nm and > 50 nm, respectively.

UNIVERSITAT ROVIRA I VIRGILI
DESIGN, FABRICATION AND CHARACTERIZATION OF POROUS SILICON MULTILAYER OPTICAL DEVICES
Elisabet Xifré Pérez
ISBN: 978-84-691-0362-3/DL: T.2181-2007

This categorization is related only to the pore diameter, but does not contain much information about the pore morphology. The term pore morphology is used for properties like shape (smooth, branched, facetted, etc.), orientation, interconnection of pores, etc. The morphology is the least quantifiable aspect of porous silicon. It is very difficult to systematically characterize the morphology of porous silicon, which has extremely rich details with respect to variations in pore size, shape and spatial distribution. In terms of the pore morphology, it can be summarized that microporous and mesoporous silicon exhibit typically a sponge-like structure with densely and randomly branched pores, which do not show a clear orientation. The tendency to branch increases with decreasing pore diameter. In contrast, macroporous silicon can have discrete pores with smooth walls, with short branches or with dendritic branches.

The pores grow preferentially along <100> directions and towards the source of positive carriers (holes), which are involved in the electrochemical dissolution reaction. Pores with smooth walls tend to be aligned to the source of holes, while dendritic pores are aligned in the <100> direction. In this thesis we study microporous silicon and the pore size and shape are not considered but for the reason that their variation and presence determine the refractive index of the porous silicon layer.

The formation of porous silicon is selective with respect to the doping of the substrate. Some general trends on the layer morphology can be derived for different types of starting silicon substrates. Fig. 2.5 shows four cross-sectional TEM images of porous silicon samples with different starting substrates [24]. The difference in morphology is evident. For p-type doped silicon both size and interpore spacing are very small (Fig. 2.5a), typically between 1 and 5 nm, and the pore network looks very homogeneous and interconnected. As the dopant concentration increases, pore sizes and interpore spacing increases, while the specific surface area decreases. The structure becomes anisotropic, with long voids running perpendicular to the surface, very evident in highly p-type doped silicon (p^+), as shown in Fig. 2.5c.

UNIVERSITAT ROVIRA I VIRGILI
DESIGN, FABRICATION AND CHARACTERIZATION OF POROUS SILICON MULTILAYER OPTICAL DEVICES
Elisabet Xifré Pérez
ISBN: 978-84-691-0362-3/DL: T.2181-2007

For n-type doped silicon the situation is more complicated. Generally, pores in n-type doped silicon are much larger than in p-type doped silicon, and pore size and interpore spacing decreases with increasing dopant concentrations. Lightly doped n-type substrates anodized in the dark have low porosity (1-10 %), with pores in the micrometer range. Under illumination higher values of porosity can be achieved, and mesopores are formed together with macropores. The final structure depends strongly on anodization conditions, especially on light intensity and current density. While highly n- and p-type doped silicon show similar structures (compare Fig. 2.5c and d), in n-type doped silicon the pores tend to form a randomly directed filamentary structure and tend to pipe forming large straight channels approaching the electropolishing regime (see Fig. 2.5b).

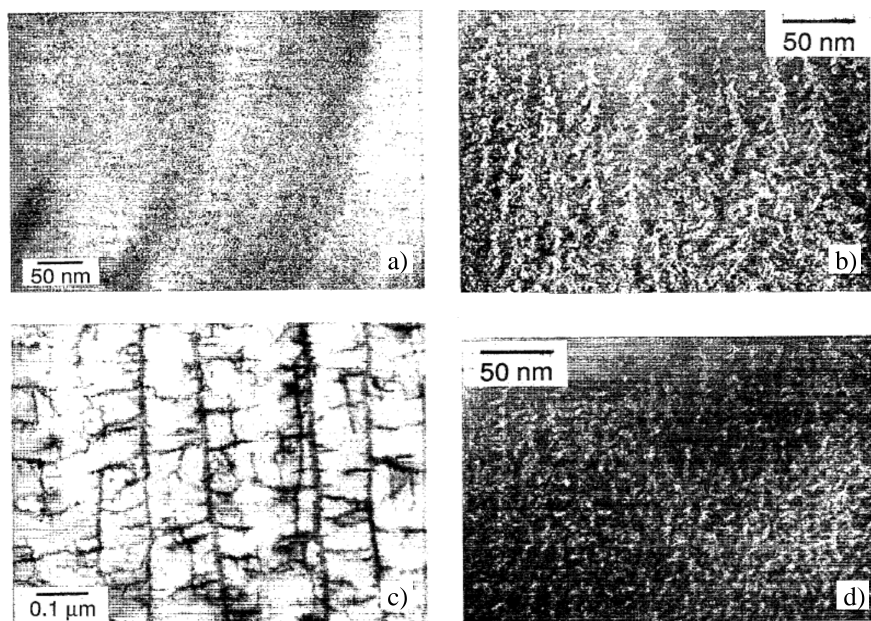

Fig. 2.5. Cross-sectional TEM images showing the basic differences in morphology among different types of samples. (a) p-type silicon; (b) n-type silicon; (c) p^+-type silicon; (d) n^+-type silicon. [After 26].

ISBN: 978-84-691-0362-3/DL: T.2181-2007

2.2.4. Anodization parameters

The porous silicon formation process with electrochemical anodization has been widely developed by many authors. [39-44]. The parameters that influence on this formation process are:

- The substrate doping.
- The current density.
- The HF concentration: the higher the concentration, the lower the pore size and the porosity. HF concentration determines J_{PS}, that is the upper limit to current density values. With a fixed and low HF concentration the range over which the current density can be varied is short, and it becomes wider by increasing the HF concentration.
- The solvent where the HF is diluted: since porous silicon is organophilic and hydrophobic, the use of ethanol guarantees a higher homogeneity, due to a better wettability of the surface than deionized water.
- The etching time: longer etching times lead to thicker layers, but for long times an anisotropy in depth in the layer due to the chemical action of the electrolyte is introduced.
- The illumination during the etch, essential for n-type substrates [40].

The porosity, thickness, pore diameter and microstructure of porous silicon depend on the anodization conditions, as is briefly explained in Table 2.I. These conditions include HF concentration, current density, wafer type and resistivity, anodization time, illumination (required for n-type silicon and semi-insulating p-type silicon), temperature, ambient humidity and drying conditions.

For a fixed current density, the porosity decreases when HF concentration increases [45,46]). Fixing the HF concentration and the current density, the porosity increases with the thickness. This happens because of the extra chemical dissolution of the porous silicon layer in HF.

UNIVERSITAT ROVIRA I VIRGILI
DESIGN, FABRICATION AND CHARACTERIZATION OF POROUS SILICON MULTILAYER OPTICAL DEVICES
Elisabet Xifré Pérez
ISBN: 978-84-691-0362-3/DL: T.2181-2007

	Porosity	Etch rate	Critical current
HF concentration	*decreases*	*decreases*	*increases*
Current density	*increases*	*increases*	-
Anodization time	*increases*	*almost constant*	-
Temperature	-	-	*increases*
Wafer doping (p-type)	*decreases*	*increases*	*increases*
Wafer doping (n-type)	*increases*	*increases*	-

Table 2.I. Effect of anodization parameters on porous silicon formation. An increase of the parameters of the first column leads to a variation of the elements in the rest of columns. Adapted from [47].

The thickness of a porous silicon layer is determined by the time that the current density is applied, that is the anodization time. To have a thicker layer, a longer anodization time is required. For this reason, the periodic variation of the current density during the etching process allows the production of multilayers formed by layers with different optical thicknesses.

Another advantage of the formation process of porous silicon is that once a porous layer has been formed, no more electrochemical etching occurs for it during the following current density variations. Hence, the porosity can be modulated in depth [48]. This fact allows the fabrication of any refractive index profile.

A longer permanence time of silicon in HF solution results in a higher mass of chemically dissolved silicon. This effect is more important for lightly doped silicon, while it is almost negligible for heavily doped silicon. This is due to the lower specific surface area.

All these characteristics contribute to the easy formation of porous silicon one-dimensional photonic structures, with no need to use excessively expensive equipment [49].

ISBN: 978-84-691-0362-3/DL: T.2181-2007

2.2.5. Photoluminescence of porous silicon

The discovery by Canham [2] in 1990 of strong visible luminescence from anodically etched p-doped silicon generated much interest within the scientific community because porous silicon became an attractive material in the field of electronics and optoelectronics [50-53].

Porous silicon offers a considerable technological interest because it may allow the convenient incorporation of optical elements into silicon integrated circuits. The incorporation of a stable and efficient luminescent porous silicon element into a microelectronic circuit encourages the possibility of commercial applications significantly.

Porous silicon based structures have been reported to luminescence efficiently across the whole range from the near infrared (~1.5 μm), through the visible region, and into the near UV. Emission over such a broad spectral range arises from a small number of clearly distinct luminescence bands of different origin, which are listed in Table 2.II.

Spectral range	Peak wavelength (nm)	Luminescence band label	PL	EL
UV	*~350*	*UV band*	*Yes*	*No*
Blue-green	*~470*	*F band*	*Yes*	*No*
Blue-red	*400-800*	*S band*	*Yes*	*Yes*
Near IR	*1100-1500*	*IR band*	*Yes*	*No*

Table 2.II. Porous silicon luminescence bands [After 54]

The general properties of each luminescence band and the conditions under which they are observed have been briefly reviewed quite recently [55]. The so-called ‘‘S-band’’ luminescence has received by far the most attention to date [56-59], and has the most technological significance, since it can be efficiently electrically excited. This band has been tuned across the entire visible range from deep red to blue [60]. However, it is worth briefly mentioning the most likely origin of the other luminescence bands. The blue-

UNIVERSITAT ROVIRA I VIRGILI
DESIGN, FABRICATION AND CHARACTERIZATION OF POROUS SILICON MULTILAYER OPTICAL DEVICES
Elisabet Xifré Pérez
ISBN: 978-84-691-0362-3/DL: T.2181-2007

green photoluminescence (PL) emission (the so-called ''F-band'' due to its fast nanosecond decay time) was first reported by Harvey *et al.* [61] in 1992. Following the demonstration by Kovalev *et al.* [62] of quite strong PL output of this type from oxidized porous silicon produced by RTO treatment, the F-band has been the subject of several recent studies [55,63-66]. It is, however, only observed in oxidized structures and is very likely to originate from contaminated [67] or defective silicon oxide [63].

Infrared emission at room temperature was first achieved by Fauchet *et al.* [68] for material annealed under ultrahigh vacuum (UHV). As discussed in [69] the origin of this radiation could be dangling bond related [70], although no direct correlation has yet been demonstrated.

Ultraviolet emission was first reported by Jiang *et al.* [171] in 1993 from oxidized material under soft x-ray excitation. Stronger room temperature output has been subsequently reported [72-76]. As with the blue-green F-band, the UV bands are only observed from oxidized layers and are likely also to arise from the defective oxide phase [73].

2.3. Applications of porous silicon

Porous silicon is a dielectric material with many different applications. The potential application areas of porous silicon are summarized in Table 2.III, where the property of porous silicon used for each application is shown.

In this work, porous silicon has been used for the fabrication of multilayers for optical applications, using the photonic bandgap characteristic of these multilayers for the formation of filters, microcavities, omnidirectional mirrors and waveguides. These applications are explained in detail in the next subsections together with some other porous silicon applications widely reported.

UNIVERSITAT ROVIRA I VIRGILI
DESIGN, FABRICATION AND CHARACTERIZATION OF POROUS SILICON MULTILAYER OPTICAL DEVICES
Elisabet Xifré Pérez
ISBN: 978-84-691-0362-3/DL: T.2181-2007

Application area	**Role of porous silicon**	**Key property**
Optoelectronics	LED Waveguide Field emitter Optical memory	Efficient electroluminescence Tunability of refractive index Hot carrier emission Non-linear properties
Micro-optics	Fabry-Pérot Filters Photonic bandgap structures All optical switching	Refractive index modulation Regular macropore array Highly non-linear properties
Energy conversion	Antireflection coatings Photo-electrochemical cells	Low refractive index Photocorrosion cells
Environmental monitoring	Gas sensing	Ambient sensitive properties
Microelectronics	Micro-capacitor Insulator layer Low-k material	High specific surface area High resistance Electrical properties
Wafer technology	Buffer layer in heteroepitaxy SOI wafers	Variable lattice parameter High etching selectivity
Micromachining	Thick sacrificial layer	Highly controllable etching
Biotechnology	Tissue bonding Biosensor	Tunable chemical reactivity Enzyme immobilization

Table 2.III. Potential application areas of porous silicon [Adapted from 77].

2.3.1. Distributed Bragg Reflectors

Distributed Bragg reflectors are dielectric multilayers based on the effect of multiple interferences that occurs when a light beam is reflected by various dielectric interfaces. A simple scheme of multiple interferences is shown in Fig. 2.6 [78], where a single film is compared with a stack of thin films (multilayer). At each interface between the two materials with different refractive index, a reflection occurs. In the case of a single layer film the reflected beam is the result of the interference of the two beams reflected at the air-film and film-

ISBN: 978-84-691-0362-3/DL: T.2181-2007

substrate interfaces. Instead in the case of the multilayer film, the reflected beam is the result of the interference of the multiple beams reflected at each of the different interfaces. By choosing, in an appropriate way, the thicknesses and the values of the refractive indices of the various layers, it is possible to generate different reflectivity spectra. The final result is the possibility to realize constructive and destructive interferences at different wavelengths.

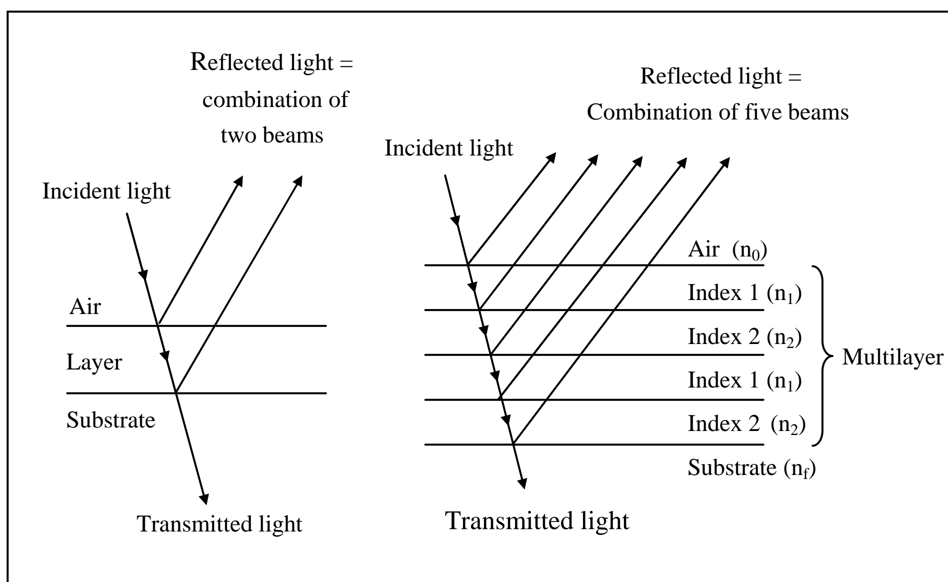

Fig. 2.6. On the left part of the figure it is shown the reflection and transmission of light by a single thin film. On the right the case of a multilayer is shown. After [78].

Distributed Bragg Reflectors (DBR) are multilayer structures formed by the periodic repetition of two layers with different refractive index (n_H and n_L) and thicknesses (h_H and h_L, respectively). The reflectivity spectrum of a DBR presents a high reflectivity for a given spectral region, centered at wavelength λ. The reason of this is due to the fact that for the wavelengths close to this λ all the beams, which are reflected by the multiple interfaces, have the same phase when they reach the top interface. Thus they interfere constructively. For other

UNIVERSITAT ROVIRA I VIRGILI
DESIGN, FABRICATION AND CHARACTERIZATION OF POROUS SILICON MULTILAYER OPTICAL DEVICES
Elisabet Xifré Pérez
ISBN: 978-84-691-0362-3/DL: T.2181-2007

wavelengths the interference is no longer constructive and the reflectivity consequently drops. The range of wavelengths that are reflected is called the photonic stopband. Within this range of wavelengths, light is "forbidden" to propagate in the structure.

The most commonly used structure of DBR is the so called quarter wave DBR, where the optical thickness of the layers is $n_H h_H = n_L h_L = \lambda/4$ and the period of the structure is $\Lambda = h_H + h_L$ [40]. The schematic structure of a DBR can be observed in Fig. 2.7.

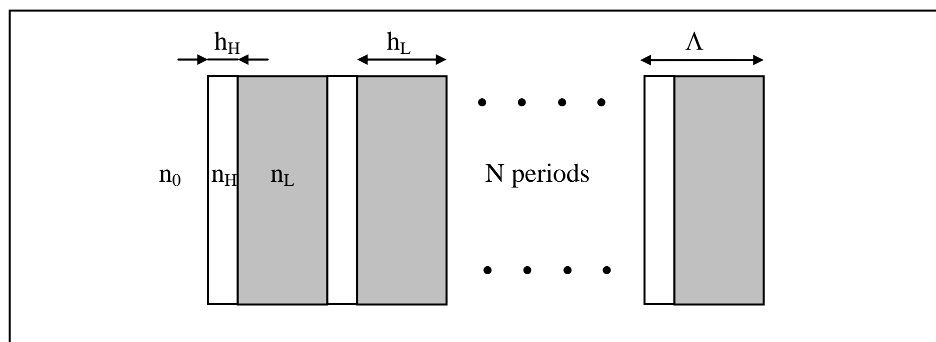

Fig. 2.7. Schematic cross-section of a periodic DBR. n_i and h_i are the refractive index and thickness of layer *i*, respectively. N is the number of periods.

In the explanation of the porous silicon formation process, we have observed that it is a very suitable material for the fabrication of multilayers because the refractive index and thickness of the layers can be selected by changing the formation parameters during the fabrication process [19].

Porous silicon DBRs have been fabricated by many different groups [79-84,]. The reflectivity of these structures has been widely studied [19,80,85], but also their photo-emission [85] and the roughness between their layers [86]. The most common application of these DBRs is filtering [81,87], but they have

UNIVERSITAT ROVIRA I VIRGILI
DESIGN, FABRICATION AND CHARACTERIZATION OF POROUS SILICON MULTILAYER OPTICAL DEVICES
Elisabet Xifré Pérez
ISBN: 978-84-691-0362-3/DL: T.2181-2007

also been used as sensors of the light polarization [88] and part of lasers [89] and waveguides [90].

2.3.2. Microcavities

The structure of microcavities, also called Fabry-Pérot filters, consists of two parallel DBR separated by a spacer layer, whose refractive index can be the same or different to the ones used for the DBRs. The optical thickness of the spacer layer can be λ or λ/2 [91]. Fig. 2.8 shows the schematic structure of a microcavity. The reflectivity spectrum of this structure is characterized by a very narrow pass-band centered in a high reflectivity wavelength range.

Microcavities can be used as band-pass filters with a tuned position of the peak [19,92], tunable mirrors [93] and detectors of substances like ethanol, methanol, acetone, chlorobenzene and nitrogen dioxide, among others [94-97]. They also improve the light emitting capacity of porous silicon. Microcavity structures can also be advantageous for photoluminescence and electroluminescence in order to reduce the full width at half maximum (FWHM) [91,98-101].

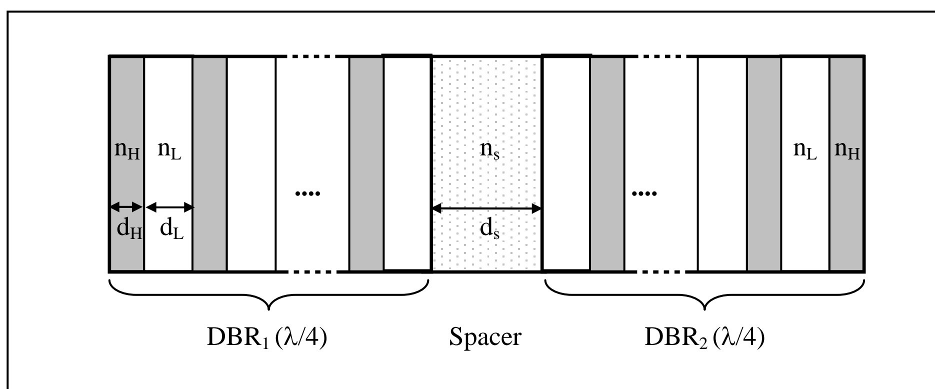

Fig. 2.8. Schematic cross-section of a microcavity. The spacer layer refractive index is n_S and its thickness is d_S. It is inserted in between two symmetric DBR with refractive indices n_H and n_L and thicknesses h_H and h_L.

ISBN: 978-84-691-0362-3/DL: T.2181-2007

2.3.3. Rugate filters

These filters are characterized by a continuous, mostly sinusoidal change of the refractive index with depth [102]. These structures have been investigated for 20 years, because a smooth index profile can improve many features of optical devices with respect to dielectric multilayers [103]. The main difficulty is the experimental realization, which requires gradual mixing of different materials; this is the reason for the low number of works in this area. Rugate filters have been reported in the past by evaporation [104-105], reactive sputtering [106], plasma-enhanced chemical vapor deposition [107] and glancing angle deposition [108].

Porous silicon is an excellent material for the fabrications of rugate filters because the anodization current can be gradually modulated obtaining soft index profiles [48]. In the last years, some groups have reported the first porous silicon-based rugate filters [102,109]. Some of the main advantages of these structures are that they do not show higher harmonics and that the typical DBR sidelobes of the reflection bands are reduced or even suppressed [103].

2.3.4. Omnidirectional mirrors

Omnidirectional mirrors are multilayers that reflect light for any incidence angle and for any polarization in a wavelength range [110]. This characteristic is due to the existence of a bandgap that exists for any incidence angle and for both polarizations TE and TM.

The most widely used structure of one-dimensional mirrors is the one consisting of the periodic repetition of two dielectric layers with different refractive index [111,112], although other structures have been reported. [39,113,114]. Dielectric mirrors have many advantages over metallic mirrors, like low optical loss, no light absorption, high mechanical strength, and high reflectivity within a wide range of wavelengths [115,116].

Although different groups have reported dielectric omnidirectional mirrors, porous silicon omnidirectional mirrors have been only analyzed and fabricated by the group of G. Lérondel [39].

UNIVERSITAT ROVIRA I VIRGILI
DESIGN, FABRICATION AND CHARACTERIZATION OF POROUS SILICON MULTILAYER OPTICAL DEVICES
Elisabet Xifré Pérez
ISBN: 978-84-691-0362-3/DL: T.2181-2007

2.3.5. Waveguides

Since the first report on the use of porous silicon as an optical waveguide medium in the 90s, significant development has been made towards the understanding and applicability of such material. Different groups have studied the fabrication of porous silicon waveguides and their basic properties (modes, losses) [117-121].

The infiltration of liquids in the pores resulting in an induced phase shift and/or variation in the guided light intensity allows the use of porous silicon waveguide as sensors. For example, the introduction of solvents (acetone, methanol, and propan-2-ol) into the pores is shown to dramatically reduce the loss of the waveguides in a reversible manner [122,123].

Waveguides based on porous silicon multilayers allow the micromachining of photonic integrated circuits as it can be used to confine, manipulate, and guide the photons [124-127].

Waveguides based on multilayers have attracted a great interest because their guiding mechanism is completely different to the conventional waveguides based on total internal reflection [125,128] but these waveguides made of porous silicon have not been widely reported [129].

2.3.6. Sensors

Porous silicon multilayers have been used for sensing different substances. In particular microcavity structures have been used for hydrocarbon sensors [42,130] or biosensors [131,132], where changes of the optical properties of the porous silicon microcavity are analyzed. On the other hand, porous silicon monolayers have been used in humidity sensors, designed to detect humidity through changes of its electrical properties [133-134]. Despite optical measurements may be more robust for some applications, only a few authors proposed the analysis of the optical properties of porous silicon microcavities for the detection of humidity changes [135].

UNIVERSITAT ROVIRA I VIRGILI
DESIGN, FABRICATION AND CHARACTERIZATION OF POROUS SILICON MULTILAYER OPTICAL DEVICES
Elisabet Xifré Pérez
ISBN: 978-84-691-0362-3/DL: T.2181-2007

2.3.7. Other applications

The possibility of electroluminescent devices fabricated with porous silicon was realised soon after the demonstration of photoluminescence from porous silicon. Electroluminescent devices like light emitting diodes (LEDs) or injection lasers [136-140] made of porous silicon have been reported. To complement light emission from the material a variety of photodetectors made of porous silicon have also been reported [141,142]. Porous silicon multilayers have also been used for the realization of integrated optoelectronic devices, consisting of a LED connected to a photodetector with a waveguide [124,143]. This material has also been investigated as a possible anti-reflecting coating in solar cells [144]. Porous silicon dissolves quickly in alkaline solutions, which has led to numerous applications for porous silicon as sacrificial layer in micromachining [145-148].

ISBN: 978-84-691-0362-3/DL: T.2181-2007

Chapter 4

Analysis and design of optical devices based on porous silicon multilayers

In this chapter, the study and design of multilayer optical devices are presented. These optical devices are omnidirectional mirrors and waveguides. For the case of omnidirectional mirrors, in addition to the known periodic multilayer structure, three different new multilayer structures are proposed for the widening of the omnidirectional bandgap. For the case of waveguides, the modal study of porous silicon waveguides based on total internal reflection is developed. Waveguides based on the properties of photonic crystals are also widely studied, proposing the use of omnidirectional mirrors and DBR for their cladding. All these multilayer optical devices have been designed for 1.55 μm applications and the use of porous silicon for their fabrication is discussed. For this study, the simulation programs explained in the previous chapter have been used.

UNIVERSITAT ROVIRA I VIRGILI
DESIGN, FABRICATION AND CHARACTERIZATION OF POROUS SILICON MULTILAYER OPTICAL DEVICES
Elisabet Xifré Pérez
ISBN: 978-84-691-0362-3/DL: T.2181-2007

4.1. Omnidirectional mirrors (OM)

Omnidirectional mirrors are characterized by their omnidirectional bandgap, that is the wavelength range where the reflectivity is the unity for any incidence angle and any polarization. The width of the omnidirectional bandgap depends on the structure of the mirror.

In the next sections, multilayer omnidirectional mirrors with different structures based on porous silicon are studied for 1.55 μm applications. They are explained and mathematically analyzed using the transfer matrix method [151]. The aim of this study is the design of a porous silicon mirror with an enlarged omnidirectional bandgap. Firstly, the widely used periodic mirror is presented and studied. Next, the fairly used chirped structure is described and its advantages are evaluated. Finally, the analysis and study of the random structure lead us to two new OM structures with an enlarged omnidirectional bandgap: the balanced and the unbalanced mirrors.

4.1.1. Periodic OM

The multilayer structure most commonly used for the formation of omnidirectional mirrors is the periodic structure [110-112,116]. Ideally, it is an infinitely extended multilayer consisting of the periodic repetition of two different refractive index layers n_H and n_L and thicknesses h_H and h_L, respectively. The period thickness or bilayer thickness of the structure is $\Lambda=h_H+h_L$, and the refractive index profile is given by $n(x)=n(x+\Lambda)$.

Porous silicon periodic OMs have been simulated and analyzed. From the study of these structures, the presence and width of the omnidirectional bandgap has been observed to depend mainly on three different factors.

4.1.1.1. Refractive indices n_H and n_L

The existence of one or more omnidirectional bandgaps depends on the refractive indices n_H and n_L of the mirror [161]. This dependence can be observed in the examples presented in Fig. 4.1. This figure shows the projected

UNIVERSITAT ROVIRA I VIRGILI
DESIGN, FABRICATION AND CHARACTERIZATION OF POROUS SILICON MULTILAYER OPTICAL DEVICES
Elisabet Xifré Pérez
ISBN: 978-84-691-0362-3/DL: T.2181-2007

band structure (PBS) of a periodic infinite multilayer for three different n_H/n_L ratios. The omnidirectional bandgaps are black colored. We can observe that the structure with ratio n_H/n_L=2.1/1.55 does not have any omnidirectional bandgap. On the contrary, the other two structures have an omnidirectional bandgap.

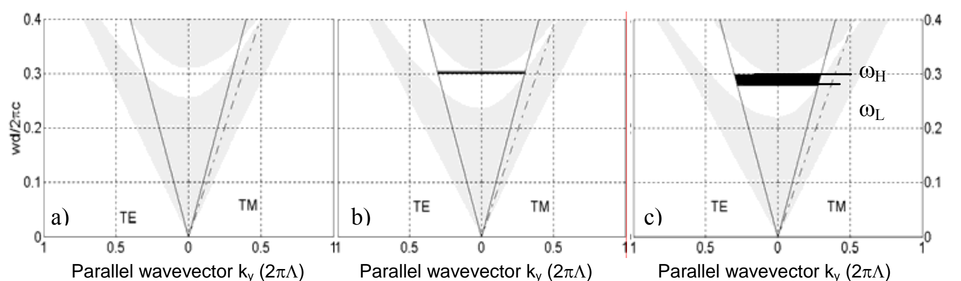

Fig. 4.1. Projected band structure of a multilayer with n_H/n_L=2.1/1.5 (left), n_H/n_L=2.3/1.5 (center) and n_H/n_L=2.5/1.5 (right).

In this figure we can also observe that the refractive indices not only determine the existence of the bandgap but also its width. The omnidirectional bandgap of the structure represented in Fig. 4.1c is wider than the one in Fig. 4.1b. Is the width of the omnidirectional bandgap related to the n_H/n_L ratio? Or there is an optimum n_L for each n_H? Can we calculate the optimum n_H and n_L for obtaining the widest omnidirectional bandgap? The answers to all these questions are given in the two next subsections.

a) Influence of n_H on the width of the omnidirectional bandgap

In this section we study the omnidirectional bandgap width for a given high refractive index layer, n_H. In fact, we study the relative gap width, which is expressed as $(\Delta\omega/\omega_0)$

$$\frac{\Delta\omega}{\omega_0} = \frac{\omega_H - \omega_L}{(1/2)(\omega_H + \omega_L)} \tag{4.1}$$

UNIVERSITAT ROVIRA I VIRGILI
DESIGN, FABRICATION AND CHARACTERIZATION OF POROUS SILICON MULTILAYER OPTICAL DEVICES
Elisabet Xifré Pérez
ISBN: 978-84-691-0362-3/DL: T.2181-2007

where ω_H and ω_L are the upper and lower limits of the omnidirectional bandgap (see Fig. 4.1) and ω_0 is the center frequency of the omnidirectional bandgap.

The influence of n_H on the omnidirectional bandgap width can be observed in Fig. 4.2 that shows the maximum relative band width, $(\Delta\omega/\omega_0)_{max}$ as a function of the high-index value n_H. It is clear from the graph that the maximum value of $(\Delta\omega/\omega_0)$ increases when increasing n_H. It can be observed that the minimum value for n_H to obtain an omnidirectional reflection is 2.25 and that the maximum $(\Delta\omega/\omega_0)$ is around 0.12, which is approximately the maximum attainable $(\Delta\omega/\omega_0)$ using porous silicon.

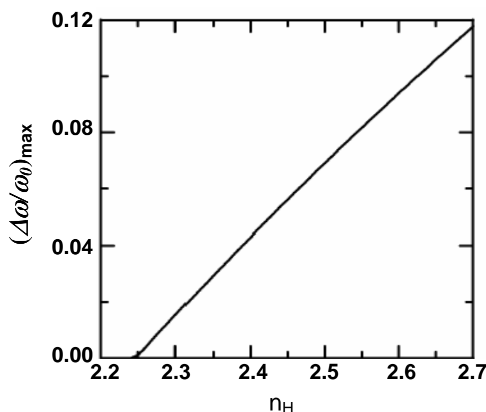

Fig. 4.2. Maximum $(\Delta\omega/\omega_0)$ ratio as a function of the high refractive index (n_H).

b) Influence of n_L on the width of the omnidirectional bandgap

We now analyse the influence of the low refractive index value on the width of the omnidirectional bandgap. From the field of photonic crystals, it is known that the bigger the contrast between the high- and low-refractive indices the wider the photonic bandgap. We have observed in the previous section that the relative gap width increases with increasing n_H until the upper bound for n_H

UNIVERSITAT ROVIRA I VIRGILI
DESIGN, FABRICATION AND CHARACTERIZATION OF POROUS SILICON MULTILAYER OPTICAL DEVICES
Elisabet Xifré Pérez
ISBN: 978-84-691-0362-3/DL: T.2181-2007

(limited by the porous silicon technology) is reached. In this section we evaluate if the complementary hypothesis is right, that is, if the decrease of n_L leads to a increase of the relative gap width.

To this end, we have calculated the relative bandgap width ($\Delta\omega/\omega_0$) that can be attained for every pair (n_H,n_L). The results are plotted in Fig. 4.3a, where ($\Delta\omega/\omega_0$) is represented for every point (n_H,n_L). The points with the same ($\Delta\omega/\omega_0$) are connected obtaining the contours of constant ($\Delta\omega/\omega_0$). The straight line connects the maximum ($\Delta\omega/\omega_0$) for every value of n_H. From this plot we can conclude that there exists an optimal n_L for every n_H, and that for the whole range of n_H this optimal n_L is around 1.5. Fig. 4.3b shows the straight line in Fig. 4.3a with a closer scale so that the variation can be observed in detail.

This fact leads to an important conclusion for porous silicon omnidirectional mirrors: there is no advantage in lowering the low refractive index below this optimal n_L, and therefore the decrease of n_L does not necessary lead to an increase of the relative gap width. Another important conclusion obtained from these results is the difference between the optimal refractive indices for a DBR and for an omnidirectional mirror. For DBR, where the structure is optimised for only one angle of incidence, the widening of the bandgap depends on the ratio n_H/n_L and the higher the ratio the widest the bandgap; whereas for omnidirectional mirrors, the width of the omnidirectional bandgap cannot be studied in terms of n_H/n_L ratio. For the design of an omnidirectional mirror, the most appropriate is to consider both refractive indices separately, as has been done in this section, because an increment of the n_H/n_L ratio, does not necessarily lead to a widening of the omnidirectional bandgap.

ISBN: 978-84-691-0362-3/DL: T.2181-2007

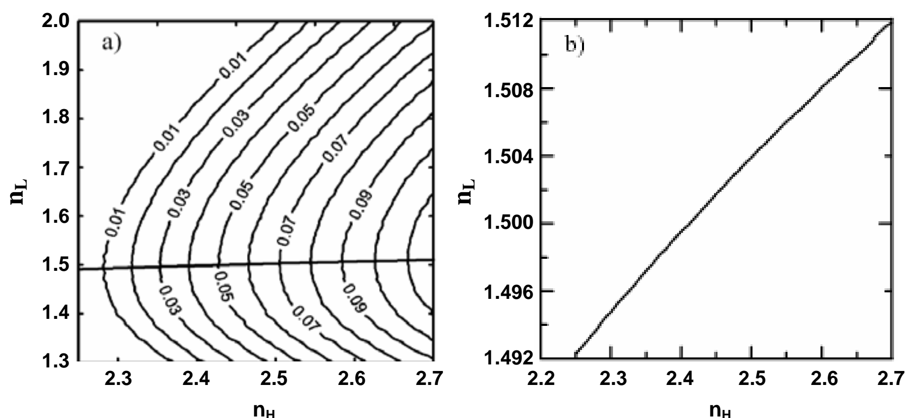

Fig. 4.3. a) Contours of constant ($\Delta\omega/\omega_0$) as a function of the high refractive index n_H and the low refractive index n_L. The straight line connects the points (n_H,n_L) with the $(\Delta\omega/\omega_0)_{\max}$ for every value of n_H. b) Zoom of the straight line plotted in a) to show the variation of the optimal n_L.

4.1.1.2. Thickness of one layer (h_H) and period thickness (Λ) ratio: (h_H/Λ)

The first question that arise when designing an omnidirectional mirror, and after the determination of (n_H,n_L), is the optimal value of thickness for the high-index and the low-index layers. It is well accepted that for mirrors for a fixed angle of incidence (with applications in laser resonators, laser optics, imaging systems), the optimal design is the quarter wave stack: a stack where the optical thickness of the layers is a quarter of the design wavelength, taking into account the angle of incidence in the case of non-normal incidence. However, the case here is quite different as there is not a fixed angle of incidence, but the mirror must be high-reflecting for all possible angles and all polarizations for a wavelength range as large as possible.

The bandgap width depends on three variables n_H, n_L and h_H, because h_L depends on h_H with the expression $h_L=\Lambda-h_H$. Therefore we could the relativegap

width as a function for these variables. But here we study the bandgap as a function of two different variables: the total optical thickness of one period of the photonic crystal, $o_T = n_H \cdot h_H + n_L \cdot h_L$, and the ratio between optical thicknesses $o_R = n_L \cdot h_L / n_H \cdot h_H$. The choice of o_R and o_T for the representation is motivated by the fact that in this way it is easier to recognize the maximum width and its position. Besides, with these two variables it is easier to interpret the results in terms of usual magnitudes in thin-film coating design. In order to be general enough, the optical thicknesses are expressed in terms of the design wavelength.

Fig. 4.4 shows the contours of constant $(\Delta\omega/\omega_0)$ as a function of o_T and o_R for three different values of n_H: $n_H=2.30$, $n_H=2.50$, $n_H=2.70$. It is worth reminding that the refractive index of porous silicon may range from 1.2 to 2.7, approximately. The maximum $(\Delta\omega/\omega_0)$, its position and its value are indicated in each plot.

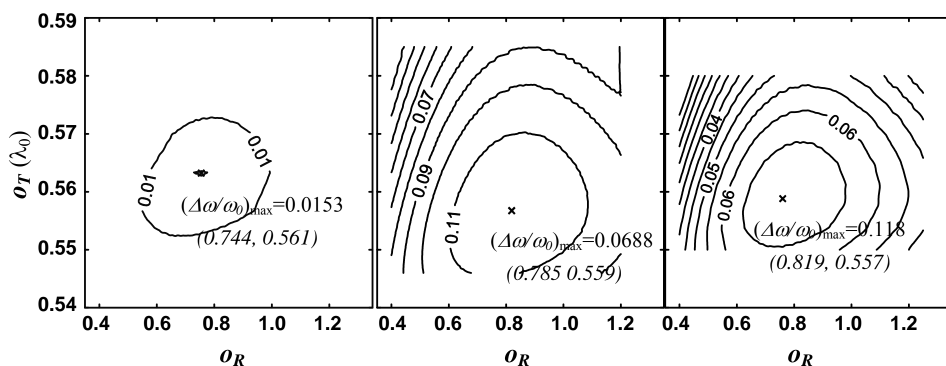

Fig. 4.4. Contours of constant $(\Delta\omega/\omega_0)$ for a) n_H =2.3, b) n_H=2.5, c) n_H=2.7. The maximum $(\Delta\omega/\omega_0)$ is marked by a cross symbol and its value and the pair (o_R, o_T) for this maximum is written.

In the graphs we can observe that the maximum $(\Delta\omega/\omega_0)$ appears approximately at the same position for all the values of n_H. If we observe the results for $n_H=2.50$, this maximum is at $o_R=0.785$ and $o_T= 0.559\lambda_0$, that correspond to optical thicknesses $o_H=n_H \cdot d_H=0.313\lambda_0$ and $o_L=n_L \cdot d_L=0.246\lambda_0$.

ISBN: 978-84-691-0362-3/DL: T.2181-2007

Notice that the total optical thickness o_T is slightly bigger than half of the design wavelength and that the ratio of the optical thicknesses o_R is not 1. Consequently, the quarter-wave design, which gives the maximum width at a given angle of incidence, is not the optimal if all incidence angles are considered.

Now that the quarter-wave structure is known not to be the optimal design, we study the optimal h_H/Λ that leads to the maximum ($\Delta\omega/\omega_0$). In Fig. 4.5, an example case with n_H=2.5 and n_L=1.5 is shown. The PBS of the periodic infinite multilayer for three different values of h_H/Λ are plotted. We can observe that the width of the omnidirectional bandgap depends on the h_H/Λ ratio, and that there is an optimal h_H/Λ ratio for which the omnidirectional bandgap is maximum. Although Fig. 4.5 only shows the simulations for three h_H/Λ values, the simulations have been realized for all the values of h_H/Λ between 0.2 and 0.8, with step 0.01, and it has been observed that the ratio resulting in the widest omnidirectional bandgap is h_H/Λ=0.4. Although the optimal ratio is 0.4 for these n_H and n_L values, each pair (n_H,n_L) that presents an omnidirectional bandgap has its own optimal h_H/Λ, that has to be calculated for every single case.

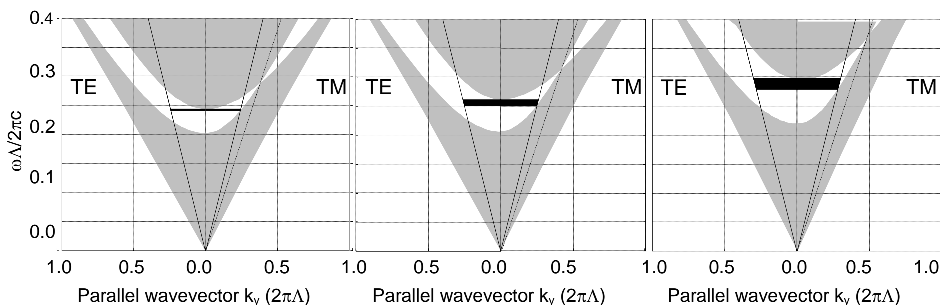

Fig. 4.5. Projected band structure of a multilayer with n_H=2.5, n_L=1.5 for h_H/Λ=0.7 (left), h_H/Λ=0.6 (center) and h_H/Λ=0.4 (right).

UNIVERSITAT ROVIRA I VIRGILI
DESIGN, FABRICATION AND CHARACTERIZATION OF POROUS SILICON MULTILAYER OPTICAL DEVICES
Elisabet Xifré Pérez
ISBN: 978-84-691-0362-3/DL: T.2181-2007

4.1.1.3. Number of periods

The mirrors studied in the previous subsections are infinite periodic structures. These structures are ideal since real multilayers have a finite number of periods N. Although real multilayers have few periods, the reflectivity spectrum of finite multilayers tends to the reflectivity spectrum of infinite multilayers exponentially with N [161] Thus, not many periods of the finite multilayer are needed to obtain bandgap widths similar to the ones calculated from the PBS. When the number of periods N increases, the reflectivity of the bandgap increases and its edges are sharper.

This can be observed in Fig. 4.6 that shows the reflectivity spectrum of a multilayer with n_H=2.5, n_L=1.55 and h_H/Λ=0.4 for different number of periods. The omnidirectional bandgap is defined between the lower band-edge of the normal incidence spectrum and the higher band-edge of the perpendicular incidence spectrum for TM polarization, because this polarization is more restrictive than TE polarization. For N=5, it can be clearly seen that the normal incidence spectrum has a low reflectivity and that, for perpendicular incidence the reflectivity neither reaches the unity for any wavelength within the bandgap. It can be considered that the omnidirectional bandgap does not exist. For N=20, the omnidirectional bandgap exists and is centered at 1.55 μm. It can be also observed that the limits of the omnidirectional bandgap are sharper when N increases.

Up to this point, the influence of the different parameters on the omnidirectional bandgap is known. Now, the optimal parameters to obtain the widest omnidirectional bandgap at λ=1.55 μm with porous silicon are estimated.

UNIVERSITAT ROVIRA I VIRGILI
DESIGN, FABRICATION AND CHARACTERIZATION OF POROUS SILICON MULTILAYER OPTICAL DEVICES
Elisabet Xifré Pérez
ISBN: 978-84-691-0362-3/DL: T.2181-2007

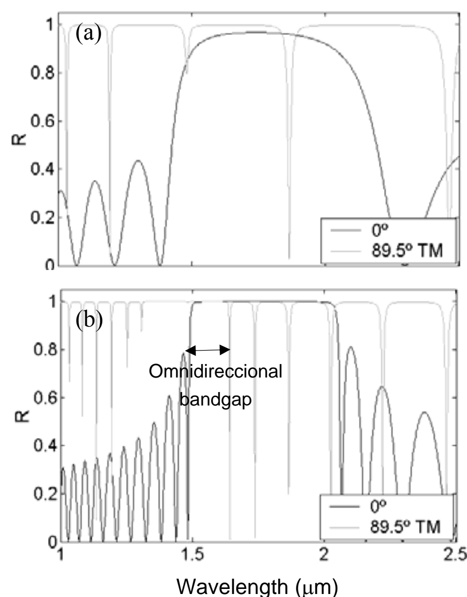

Fig. 4.6. Reflectivity spectrum of a multilayer with n_H=2.5, n_L=1.55 and h_H/Λ=0.4 and number of periods a) N= 5 b) N=20.

4.1.1.4. Omnidireccional mirror with a periodic structure for 1.55 μm applications.

As we have demonstrated in previous sections, the refractive indices (n_H, n_L) and the thickness ratio h_H/Λ determine the existence and the width of the omnidirectional bandgap in a periodic multilayer. It has also been observed that the projected band structure of the multilayer shows graphically the width of the omnidirectional bandgap and the normalized frequencies at which it exists.

For the design of the periodic porous silicon mirror for 1.55 μm applications, two typical and obtainable porous silicon refractive indices [19] have been chosen. In the previous sections it has been demonstrated that the higher n_H, the wider the omnidirectional bandgap. For this reason, the high refractive index chosen is 2.5, that is a typical high refractive index for porous silicon. A higher n_H value would imply a high complexity during the fabrication

UNIVERSITAT ROVIRA I VIRGILI
DESIGN, FABRICATION AND CHARACTERIZATION OF POROUS SILICON MULTILAYER OPTICAL DEVICES
Elisabet Xifré Pérez
ISBN: 978-84-691-0362-3/DL: T.2181-2007

process of porous silicon. In the previous section it has been demonstrated that for this n_H, the optimal low refractive index for the widest omnidirectional bandgap is n_L=1.5, when the incidence medium is air. These two refractive indices have been obtained by other authors using the porous silicon technology [39].

The periodic mirror structure obtained with these two refractive indices has an omnidirectional bandgap, whose width depends on the ratio h_H/Λ. The largest omnidirectional bandgap of this structure is obtained when ratio h_H/Λ is 0.4. Fig. 4.7a shows the projected band structure of this infinite periodic multilayer calculated with the transfer matrix method. The central normalized frequency of the omnidirectional bandgap is ω_c=0.2954, and the width is ω_H-ω_L =0.3053-0.2855=0.0198. The central wavelength of the bandgap (λ_c) depends on the period thickness Λ, according to $\omega_c=\Lambda/\lambda_c$. Therefore, the periodic structure with the omnidirectional bandgap centered at 1.55 μm has a $\Lambda=\omega_c{\cdot}\lambda_c$ = 458 nm. The thickness of the two layers of the period will be $h_H=0.4\Lambda$=183 nm and h_L=275 nm.

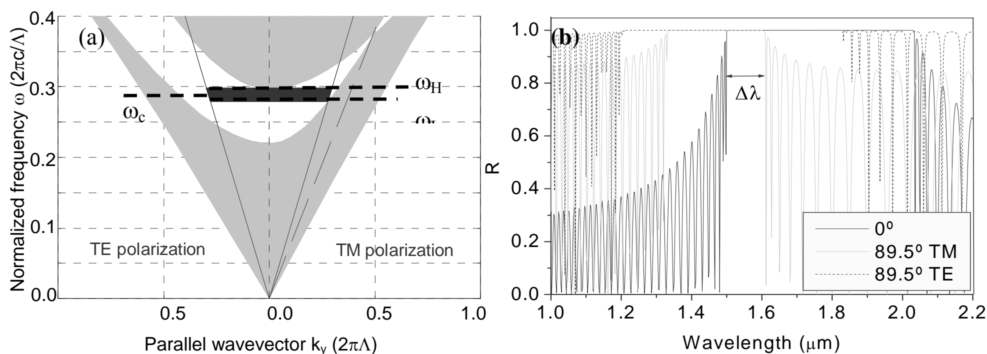

Fig. 4.7. (a) Projected band structure of an infinite periodic multilayer with n_H=2.5, n_L=1.5, h_H/Λ=0.4. The solid lines indicate the light lines and the dashed line indicates the Brewster line. The black area indicates the omnidirectional bandgap. (b) Reflectivity spectrum of a periodic multilayer with 42 periods for TE and TM polarizations and for incidence angles 0º and 89.5º. The width of the omnidirectional bandgap is $\Delta\lambda$=110 nm, centered at 1.55 μm.

UNIVERSITAT ROVIRA I VIRGILI
DESIGN, FABRICATION AND CHARACTERIZATION OF POROUS SILICON MULTILAYER OPTICAL DEVICES
Elisabet Xifré Pérez
ISBN: 978-84-691-0362-3/DL: T.2181-2007

The reflectivity spectrum of this mirror with a finite number of periods (N=42) is shown in Fig. 4.7b. The width of the omnidirectional bandgap is 110 nm for a reflectivity higher that 99%. As can be seen in this figure, the omnidirectional bandgap is centered at 1.55 μm.

Some omnidirectional mirror applications (waveguides [128], antennas substrates [162], etc.) require wide bandgaps. A wide omnidirectional bandgap can be obtained appropriately choosing (n_H,n_L) and its corresponding optimal h_H/Λ, as has been demonstrated in this section. But, as explained before, the maximum refractive index of porous silicon is limited due to the characteristics of the material. Another way for obtaining mirrors with a wider omnidirectional bandgap, keeping constant the refractive indices (n_H,n_L), is modifying the structure of the multilayer. The aim of the multilayer structures that are explained in the next sections is the widening of the omnidirectional bandgap. The omnidirectional bandgap width of all of them will be compared with the one of the periodic mirror structure studied in this section.

4.1.2. Chirped OM

In order to obtain enlarged omnidirectional bandgap mirrors, Yablonovitch [113] proposed the chirped structure. It is a multilayer consisting of N bilayers with refractive index n_H and n_L, where the thickness of the bilayer Λ is continuously increased. In the case of porous silicon, this increment is obtained by increasing the etching time for each layer. Although this structure was firstly proposed by E. Yablonovitch [113] it has been fabricated in porous silicon only by the group of G. Lérondel for 1.3 μm applications [39], demonstrating that chirped structures exhibit an enlarged omnidirectional bandgap.

ISBN: 978-84-691-0362-3/DL: T.2181-2007

4.1.2.1. Omnidirectional mirror with chirped structure for 1.55 μm applications.

For the design and simulation of the chirped structure, the parameters chosen are the ones determined in the periodic OM study. These parameters are n_H=2.5, n_L=1.5 and h_H/Λ=0.4. The use of these same parameters for all the mirror structures studied in this section will enable the comparison between them.

The group of values of Λ in the chirped structure is named bilayers thickness range [Λ], and it determines the wavelength at which the omnidirectional bandgap is centered. By studying the behavior of the chirped structure, a relation between the range [Λ] and the central wavelength of the omnidirectional bandgap (λ_C) has been determined: it can be considered that a chirped structure is a periodic structure with Λ equal to an averaged value of [Λ]. In section 4.1.1.4 the thickness Λ of the periodic structure with these characteristics has been calculated for λ_c=1.55 μm, resulting in Λ= 458 nm. Therefore, the average value of the thickness range [Λ] has to be approximately 458 nm.

Fig. 4.8 shows the reflectivity spectrum of this chirped structure consisting of 42 bilayers where the thickness Λ increases continuously from 381 to 516 nm. The number of bilayers is the same used for the periodic mirror in order to better compare the results with both structures. The omnidirectional bandgap is centered at 1.55 μm and its width for reflectivity higher than 99% is 362 nm.

Notice that the omnidirectional bandgap of the chirped structure is wider than the one of the structure with the same characteristics. This can be observed by comparing the bandgap of the periodic structure in Fig. 4.7b and the one of the chirped structure in Fig. 4.8. Both structures have the same refractive indices, the same h_H/Λ ratio and the same number of periods but the bandgap of the chirped structure is 2.7 times wider than the one of the periodic structure.

UNIVERSITAT ROVIRA I VIRGILI
DESIGN, FABRICATION AND CHARACTERIZATION OF POROUS SILICON MULTILAYER OPTICAL DEVICES
Elisabet Xifré Pérez
ISBN: 978-84-691-0362-3/DL: T.2181-2007

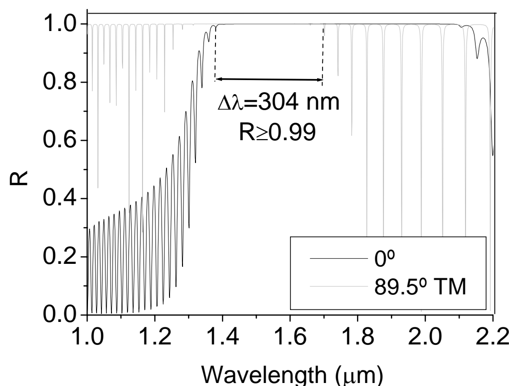

Fig. 4.8. Reflectivity spectrum of the chirped multilayer. The width of the omnidirectional bandgap is 304 nm, centered at 1.55 μm.

4.1.3. Random OM

The multilayers with a random structure were studied for normal incidence by Pavesi [163]. This structure consists of the repetition of two layers with refractive indices n_H (high refractive index layer) and n_L (low refractive index layer). The randomness is obtained as a variation in the thickness of the high refractive index layer (h_H). The set of thicknesses h_H^I is randomly generated, with a histogram that tends to a gaussian distribution centered at the average value $\langle h_H \rangle$ and with standard deviation σ.

Here we study the omnidirectional reflectivity of the random structure. Different parameters of the random multilayer have been studied. All of them have a great influence on the width of the omnidirectional bandgap. Next, these characteristics are explained and discussed:

a) Refractive index of the first layer of the structure.

This layer is in contact with the ambient medium, characterized as n_0 that is usually air. When this first layer is the one with the high refractive index (n_H), the mirror has a wider omnidirectional bandgap than the mirror with the same characteristics where this first layer is the low refractive index layer (n_L).

UNIVERSITAT ROVIRA I VIRGILI
DESIGN, FABRICATION AND CHARACTERIZATION OF POROUS SILICON MULTILAYER OPTICAL DEVICES
Elisabet Xifré Pérez
ISBN: 978-84-691-0362-3/DL: T.2181-2007

Fig. 4.9 shows the reflectivity spectrum of two random mirrors with the same parameters and where the only difference between them lies on this different layer order. It is clearly observable that the bandgap of the first mirror is wider than the one of the second mirror. This effect could be due to the fact that the difference between the refractive indices of air and n_H is higher than the difference between air and n_L [40].

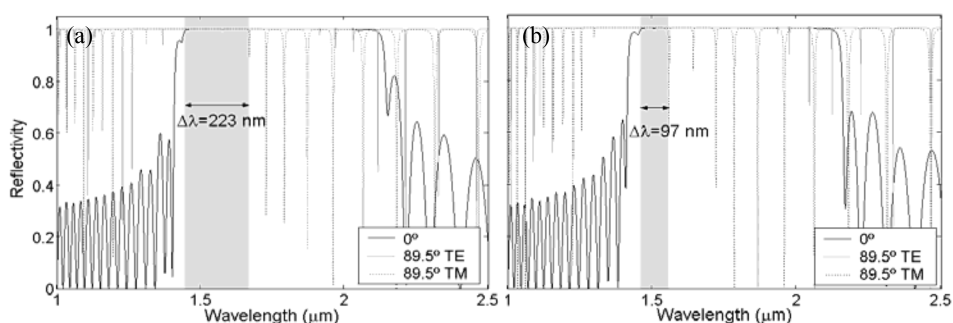

Fig. 4.9. Reflectivity spectrum of two mirrors with n_H=2.5, n_L=1.55, h_L=268 nm and the same h_H^I. The first layer of the mirror is a) n_H and b) n_L. The omnidirectional bandgap of the mirrors is gray colored.

b) Standard deviation

The standard deviation σ of the set of thicknesses h_H^I influences on the width of the bandgap. Fig. 4.10 shows three random structures where the only difference among them is the deviation σ. We can observe that the increase of the deviation σ leads to the widening of the omnidirectional bandgap of the mirror.

UNIVERSITAT ROVIRA I VIRGILI
DESIGN, FABRICATION AND CHARACTERIZATION OF POROUS SILICON MULTILAYER OPTICAL DEVICES
Elisabet Xifré Pérez
ISBN: 978-84-691-0362-3/DL: T.2181-2007

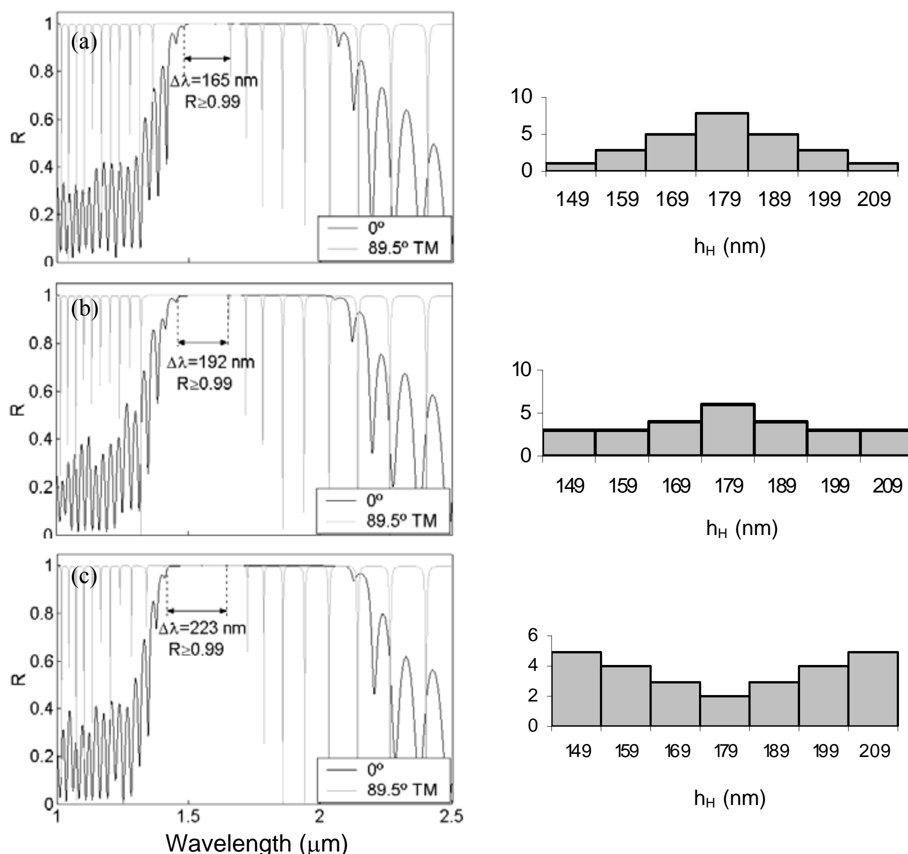

Fig. 4.10. Reflectivity spectrum of random structure mirrors with n_H=2.5, n_L=1.5, h_L=268 nm and 26 periods. The deviation σ of the set of values h_H^I is a) σ=14.14e-9 b) σ=18.19e-9 c) σ=22.19e-9. At the right side of the spectral representation, the histogram with the number of times that each thickness h_H has been used is shown.

c) Average of the set of values h_H^I (<h_H>)

The central wavelength (λ_c) of the omnidirectional bandgap is determined by the average value <h_H>. In fact, the random structure can be considered a periodic structure regarding to the refractive index, and its period Λ can be expressed as Λ=<h_H>+h_L. Using this nomenclature, the projected band

ISBN: 978-84-691-0362-3/DL: T.2181-2007

structure (PBS) is the one of the multilayer with n_H, n_L and ratio $\langle h_H\rangle/(\langle h_H\rangle+h_L)$. From the PBS, the normalized central frequency of the omnidirectional bandgap $\langle\omega_c\rangle$ is obtained. As has been explained before, this frequency is related with λ_c according to $\lambda_c=\Lambda/\omega_c$. By this way, the estimated central wavelength of the random structure can be calculated as $\lambda_c=(\langle h_H\rangle+h_L)/\langle\omega_c\rangle$. The value of the calculated λ_c is orientative, it can not be considered an exact value as the average value $\langle h_H\rangle$ is used.

d) *Difference between two consecutive elements h_H^I*

The difference between two consecutive thicknesses h_H^I, that can be expressed as $\Delta=h_H^{i+1}-h_H^i$ for i=1..(N-1), also influences on the width of the omnidirectional bandgap. Fig. 4.11 shows the reflectivity spectrum of two random mirrors with the same characteristics and with the same set of thicknesses h_H^I, but in a different order. Whereas for the first mirror Δ is constant or zero, the second has a variable Δ. It can be observed that the omnidirectional bandgap of the second mirror is considerably narrower than the one of the first mirror. We can conclude that the mirrors with the set of thicknesses h_H^I where Δ is constant or zero have a wider omnidirectional bandgap than those where Δ is variable.

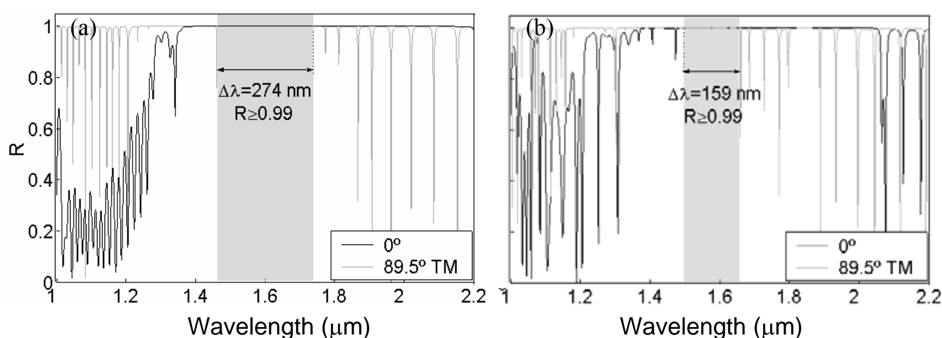

Fig. 4.11. Reflectivity spectrum of two mirrors with n_H=2.5, n_L=1.55, h_L=268 nm and 42 periods. The difference Δ is a) constant or zero, b) variable.

UNIVERSITAT ROVIRA I VIRGILI
DESIGN, FABRICATION AND CHARACTERIZATION OF POROUS SILICON MULTILAYER OPTICAL DEVICES
Elisabet Xifré Pérez
ISBN: 978-84-691-0362-3/DL: T.2181-2007

e) Distribution of the elements h_H^I

The order of the elements in the set h_H^I influences on the width of the omnidirectional bandgap. The elements h_H^I can be increasingly ordered, that is, from low to high thickness, being the lower the one in contact with the air. They could also be decreasingly ordered, or in a random order. Fig. 4.12 shows the reflectivity spectrum of a mirror where the order of the elements h_H^I is different for each case. The multilayer that shows a narrower bandgap is the one with the decreasing order. In the case of the multilayers with random order, it can be clearly seen that the width of the bandgap has a great dependence on the set of elements h_H^I. From these results, we can consider that the mirror with the h_H^I elements decreasingly ordered is the structure that leads to a wide bandgap without the dependence, and therefore, the design complexity of the structure with random series.

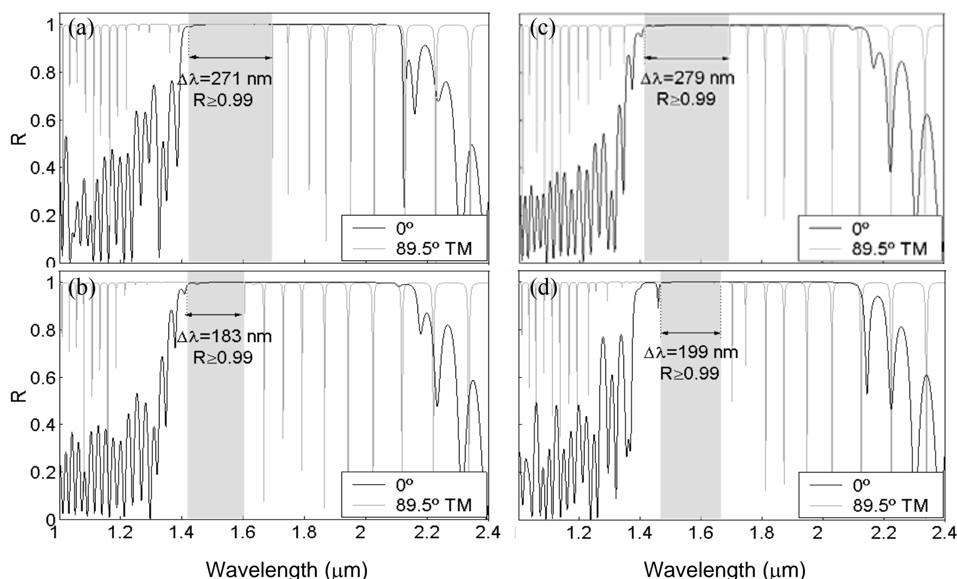

Fig. 4.12. Reflectivity spectrum of the random mirror with n_H=2.5, n_L=1.5, h_L=268 nm, 26 periods and σ=21.56e-9. The order of the elements in h_H^I is a) increasingly ordered, b) decreasingly ordered, c and d) the same set h_H^I but with two different random series. For the four cases Δ is constant or zero.

ISBN: 978-84-691-0362-3/DL: T.2181-2007

4.5.3.1. Random omnidirectional mirror for 1.55 μm applications.

For the design and simulation of the random mirror structure, we have used the same parameters than the ones used for the periodic and chirped structures studied in the previous sections: n_H=2.5, n_L=1.5, h_L=275 nm and N=42 periods. According to the results of the study, the first layer of the structure is the one with n_H.

Considering the similarity between the random and the periodic structure, from the value of ω_c in the projected band structure of the periodic mirror we can calculate the approximate value $<h_H>$ to obtain an omnidirectional bandgap centered at λ_c=1.55 μm. As ω_c=0.2954 (Fig. 4.7a), $<h_H>$ is calculated with $\lambda_c=(<h_H>+h_L)/<\omega_c>$, where λ_c=1.55 μm. For this case, the calculated $<h_H>$ is 183 nm. Therefore, the set h_H^I will consist of 42 elements, where $<h_H>$ will be 183 nm.

The reflectivity spectrum of two random mirrors with these characteristics can be observed in Fig. 4.13a. The distribution of thicknesses h_H^I is random and the difference between two consecutive thicknesses is constant or zero. The average value $<h_H>$ is 183 nm.

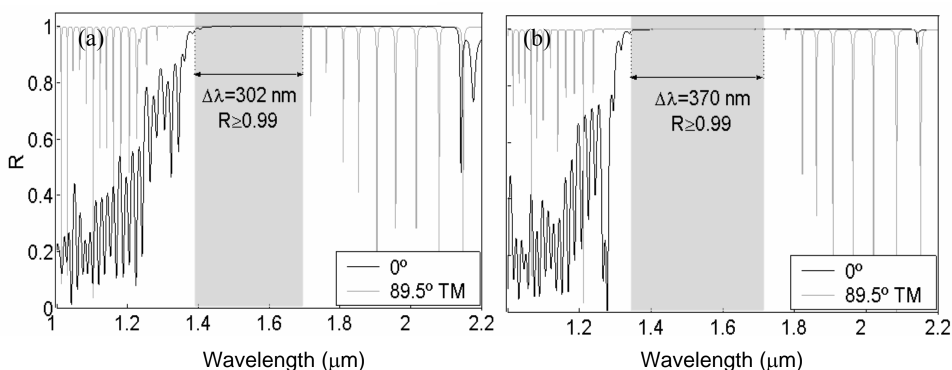

Fig. 4.13. Reflectivity spectrum of two random mirrors with n_H=2.5, n_L=1.5, h_L=275 nm and N=42 periods. The difference Δ is constant. The deviation is a) 23.66e-9 b) 32.38e-9.

UNIVERSITAT ROVIRA I VIRGILI
DESIGN, FABRICATION AND CHARACTERIZATION OF POROUS SILICON MULTILAYER OPTICAL DEVICES
Elisabet Xifré Pérez
ISBN: 978-84-691-0362-3/DL: T.2181-2007

The widest bandgap is obtained for the mirror with highest deviation. Its omnidirectional bandgap is centered at 1.57 μm and its width is 370 nm, 3.4 times the one of the periodic structure. These results agree with the conclusions obtained with the study of the random structure.

4.1.4. New enlarged omnidirectional bandgap mirrors

From the conclusions obtained with the study of the random structure, we have proposed two new omnidirectional mirror structures with enlarged omnidirectional bandgaps. Both mirror structures consist of a few periodic multilayers stacked together, which will be referred to as substructures from now on. Fig. 4.14 shows schematically the substructures that form this type of mirrors. All these substructures have the same refractive indices and the same h_H/Λ ratio. The only difference between them is the thickness period Λ, which is different for every substructure.

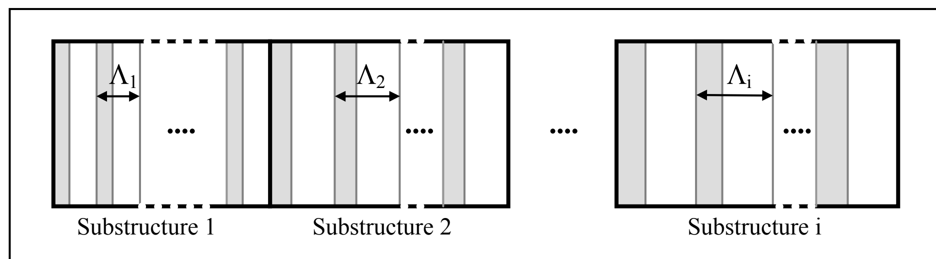

Fig. 4.14. Schematic of the balanced and the unbalanced mirror structures. Both are formed by i substructures with Λ_i and with the same number of periods for the balanced structure and with different number of periods for the unbalanced structure.

The substructures are stacked in order of increasing Λ from the incident medium. The omnidirectional bandgap of the mirror structure is the union of the omnidirectional bandgaps of the substructures that make it up. As has been explained before, the central wavelength of the omnidirectional bandgap is

ISBN: 978-84-691-0362-3/DL: T.2181-2007

determined by Λ. If an appropriate Λ is chosen for every substructure, the bandgaps of adjacent substructures intersect and the resulting mirror will present an enlarged omnidirectional bandgap.

We propose two mirror structures with these characteristics: a balanced mirror structure, where all the substructures that make up the mirror have the same number of periods N, and an unbalanced mirror structure, where the first and the last substructures have more periods than the others.

In order to achieve structures with a wide omnidirectional bandgap, it is important to understand the influence of the parameters characterizing these two new mirror structures. To this end, we consider the bandgap of each substructure separately and their combination. The characterizing parameters of the balanced and the unbalanced mirrors that we propose are:

i) The number of substructures. The width of the omnidirectional bandgap of the mirror is the union of all substructures bandgaps. Consequently, the larger the number of substructures, the wider the omnidirectional bandgap.

ii) The number of periods for each substructure. Since a substructure is not an infinite multilayer, its bandgap is not as wide as the ideal one but slightly narrower. The increment in the number of periods of a substructure leads to the enlargement of its omnidirectional bandgap. We will consider the omnidirectional bandgap of a substructure as the range of wavelengths where the reflectivity spectra is higher than a certain limit R_L for all incidence angles between 0º and 89.5º and for TE and TM polarizations.

iii) The overlap between the omnidirectional bandgaps of adjacent substructures. The smaller the overlap the wider the resulting bandgap. However, this overlap cannot be reduced arbitrarily because the intersection of adjacent bandgaps must result in a reflectivity higher than R_L within the overlapping region.

Taking into account all these parameters, it is clear that to achieve a wide bandgap it is necessary to increase the number of substructures and the

UNIVERSITAT ROVIRA I VIRGILI
DESIGN, FABRICATION AND CHARACTERIZATION OF POROUS SILICON MULTILAYER OPTICAL DEVICES
Elisabet Xifré Pérez
ISBN: 978-84-691-0362-3/DL: T.2181-2007

number of periods per substructure. However, when the total number of periods of the mirror increases, the fabrication complexity increases. If the total number of periods is limited, the first two parameters mentioned above (number of substructures and number of periods of each one) cannot be increased simultaneously and a compromise between them should be found. From this point of view, the periodic and the chirped structures can be considered as extreme configurations: the periodic mirror consisting of a single substructure and the chirped mirror consisting of many single-period substructures. It is expected that, for a fixed total number of periods, a compromise between the number of substructures and the number of periods per substructure could lead to an optimal bandgap width. The two new mirror structures proposed here attempt to meet this compromise.

4.1.4.1. Porous silicon balanced and unbalanced mirrors

In this section, the balanced and the unbalanced mirrors are proposed for applications based on porous silicon technology. To compare the results with the rest of mirror structures, the refractive indices used for the design are n_H=2.5 and n_L=1.5.

Both mirrors, designed here for 1.55 μm applications, are made up of a few periodic multilayer substructures. The number of substructures and their period thicknesses have been chosen as an example to illustrate the concepts introduced previously. The balanced and unbalanced mirrors that we propose are made up of six substructures with period thicknesses chosen as 381, 405, 431, 458, 486 and 516 nm. The first substructure is the one with Λ=381 nm, the second the one with Λ=405 nm and so on, the last one being the substructure with Λ=516 nm. The period thicknesses have been chosen so that the omnidirectional bandgaps overlap and that the omnidirectional bandgap of the resulting mirror is centered at approximately 1.55 μm. The omnidirectional bandgap of each of the six substructures is shown in Fig. 4.15. This figure shows that the omnidirectional bandgaps are adjacent and intersect. The central

UNIVERSITAT ROVIRA I VIRGILI
DESIGN, FABRICATION AND CHARACTERIZATION OF POROUS SILICON MULTILAYER OPTICAL DEVICES
Elisabet Xifré Pérez
ISBN: 978-84-691-0362-3/DL: T.2181-2007

wavelength λ_c and the width of the omnidirectional bandgap increase when Λ increases.

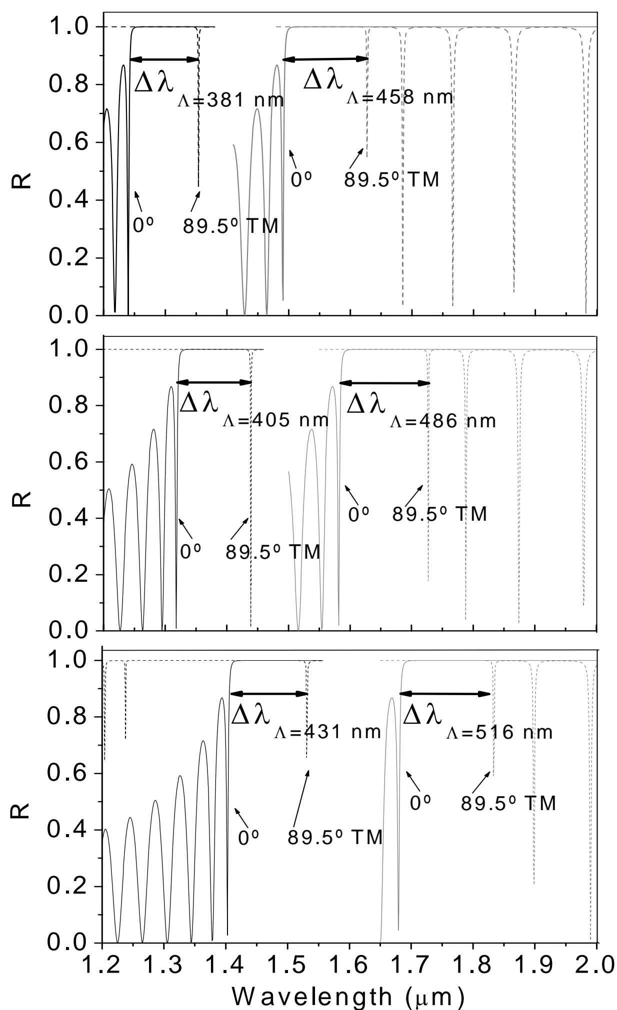

Fig. 4.15. Omnidirectional bandgap of six periodic substructures whose photonic band structure is shown in Fig. 4.7a and with different period thicknesses Λ.

ISBN: 978-84-691-0362-3/DL: T.2181-2007

4.1.4.2. Porous silicon balanced mirror for 1.55 μm applications

The balanced mirror is the one in which all the substructures that make it up have the same number of periods N (N_1=N_2=...= N_6= N). We show Table 4.I in order to study the influence of N on the width of the omnidirectional bandgap. The first row indicates the number of periods N of the substructures that make up the balanced mirror. The second row indicates the width of the omnidirectional bandgap for a reflectivity higher than R_L=99%. The third row indicates the total number of periods (N_t) of the balanced mirror. For N<3 the mirror has no omnidirectional bandgap at 1.55 μm. For N≥3, the width of the omnidirectional bandgap increases with N, but the higher N, the smaller the enlargement of the bandgap. As can be seen from the table, a 42-period mirror has a 411 nm omnidirectional bandgap. However, when we double the total number of periods of the balanced mirror (from 42 to 84), the omnidirectional bandgap is only 1.3 times wider. Therefore, the enlargement of the omnidirectional bandgap is not proportional to the N_t increment.

N	3	4	5	6	7	8	9	10	11	12	13	14	15	16
$\Delta\lambda$ (nm)	105	330	386	406	411	428	488	495	497	500	534	535	535	556
N_t	18	24	30	36	42	48	54	60	66	72	78	84	90	96

Table 4.I. Omnidirectional bandgap of the balanced mirror proposed for different number of periods N.

4.1.4.3. Porous silicon unbalanced mirror for 1.55 μm applications

The unbalanced mirror is the one in which the first and the last substructures have more periods than the other substructures. The enlargement of its omnidirectional bandgap can be explained by studying the bandgap of the substructures that make it up. The increase in the number of periods of the

UNIVERSITAT ROVIRA I VIRGILI
DESIGN, FABRICATION AND CHARACTERIZATION OF POROUS SILICON MULTILAYER OPTICAL DEVICES
Elisabet Xifré Pérez
ISBN: 978-84-691-0362-3/DL: T.2181-2007

substructure leads to a wider substructure bandgap and a higher reflectivity. If the bandgap of the first and the last substructures is wider, the bandgap of the resulting mirror will be wider as well. However, the other substructures do not need a high number of periods because their bandgaps overlap.

We have studied many different N_i distributions for the unbalanced mirror. One of these distributions is described in Table 4.II as an example of the unbalanced mirror. The table also shows the parameters of the balanced mirror with the same total number of periods (N_t=42), that are compared with the unbalanced mirror. The reflectivity spectra of the mirrors described in Table 4.II are shown in Fig. 4.16. The omnidirectional bandgap of the balanced mirror, corresponding to a reflectivity higher than 99%, is 411 nm, 3.7 times the periodic mirror bandgap. The one of the unbalanced mirror is 514 nm, 4.7 times the periodic multilayer bandgap. Both are centered at approximately 1.55 μm.

	1st	2nd	3rd	4th	5th	6th
Number of periods N (balanced mirror)	7	7	7	7	7	7
Number of periods N_t (unbalanced mirror)	12	5	4	4	5	12
Period thickness Λ (nm)	381	405	431	458	486	516

Table 4.II. Characteristics of the six substructures that make up the balanced and the unbalanced mirrors for 1.55 μm applications.

UNIVERSITAT ROVIRA I VIRGILI
DESIGN, FABRICATION AND CHARACTERIZATION OF POROUS SILICON MULTILAYER OPTICAL DEVICES
Elisabet Xifré Pérez
ISBN: 978-84-691-0362-3/DL: T.2181-2007

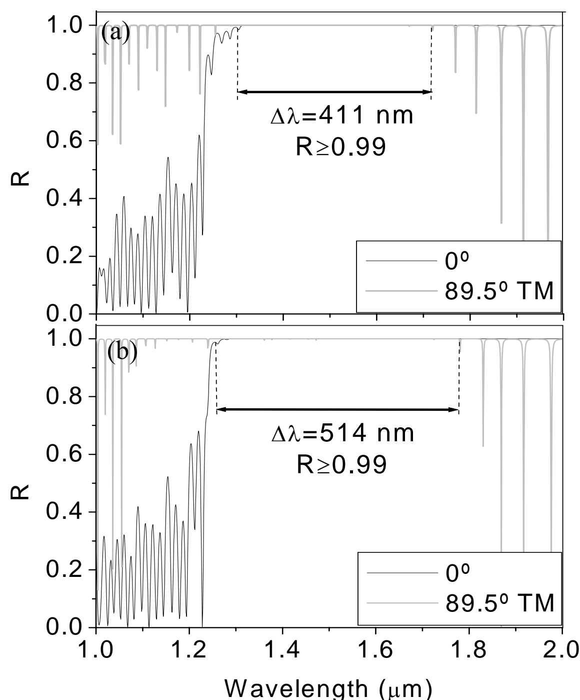

Fig. 4.16. Reflectivity spectra of a) the balanced mirror structure b) the unbalanced mirror structure. Both are centered at 1.55 μm.

4.1.5. Comparison of the studied mirror structures

The results obtained with the balanced and the unbalanced mirrors are compared with the ones obtained with equivalent periodic, chirped and random mirrors. We consider equivalent mirrors those with the same total number of periods, the same refractive indices and centered at 1.55 μm. Furthermore, for the case of the chirped and random mirror, the lower and the higher period thicknesses are the same as those for the proposed balanced and unbalanced mirrors. The bandgaps of these mirrors are summed up in Table 4.III. The omnidirectional bandgap of the periodic mirror with these characteristics is 110 nm, for a reflectivity higher than 99 %. The one of the chirped mirror is 304 nm and 370 nm for the random mirror.

ISBN: 978-84-691-0362-3/DL: T.2181-2007

	Periods	Initial Λ (nm)	Final Λ (nm)	Δλ (R≥0.99) (nm)
Periodic structure	42	458	458	110
Chirped	42	381	516	304
Random	42	391[1]	489[2]	370 (σ=32.38e-9)
Balanced mirror structure, N=(7,7,7,7,7,7)	42	381	516	411
Unbalanced mirror structure, N=(12,5,4,4,5,12)	42	381	516	514

[1]Λ minimum ; [2]Λ maximum

Table 4.III. Comparison of the omnidirectional bandgap of the five mirror structures studied.

We can observe that the unbalanced is the mirror with the widest omnidirectional bandgap, 4.7 times that of the periodic mirror, the optimal for the fabrication of omnidirectional mirrors. The balanced structure also has an enlarged omnidirectional bandgap, concretely 3.7 times the periodic mirror bandgap. The next widest bandgap is the one of the random mirror but this width strongly depends on the order of the thicknesses h_H^I. Finally, the chirped structure is the one with the lower widening, althought its bandgap is 2.7 times greater than the one of the periodic mirror.

The balanced and the unbalanced mirrors have the same number of periods, the same refractive indices and the same range or period thicknesses as the periodic, chirped and random structures. Therefore, the balanced and the unbalanced mirrors have the same technology requirements as the rest of the mirror structures having a widest omnidirectional bandgap.

UNIVERSITAT ROVIRA I VIRGILI
DESIGN, FABRICATION AND CHARACTERIZATION OF POROUS SILICON MULTILAYER OPTICAL DEVICES
Elisabet Xifré Pérez
ISBN: 978-84-691-0362-3/DL: T.2181-2007

4.2. Waveguides

Waveguide structures are important components in optoelectronics and telecommunication systems. Traditionally, light has been confined in waveguides by total internal reflection [125], due to the contrast of the refractive indices of the cladding and the core layers, or by metal cladding, due to the high reflection of a near-perfect metal [164]. A novel class of waveguides has been introduced recently, in which the confinement of the light is based on the properties of photonic crystals. The photonic bandgap, in which light cannot propagate in a certain frequency range, is used to confine light.

In the next sections we present the design of waveguide structures based on porous silicon multilayers, both based on total internal reflection and on photonic crystals. We investigate the necessary conditions for the existence of modes and the influence of the dimensions and refractive indices of the layers on the properties of the waveguide.

4.2.1. Total internal reflection waveguides

The most commonly used waveguide structures are the ones based on the total internal reflection effect (TIR). These dielectric slab waveguides consist of a core layer inserted in between two layers, named cladding. The refractive index of the core is higher than the refractive index of the cladding layers. We propose a symmetric planar dielectric waveguide made of a core with thickness *d* and refractive index n_1 surrounded by a cladding of smaller refractive index n_2, as illustrated in Fig. 4.17.

ISBN: 978-84-691-0362-3/DL: T.2181-2007

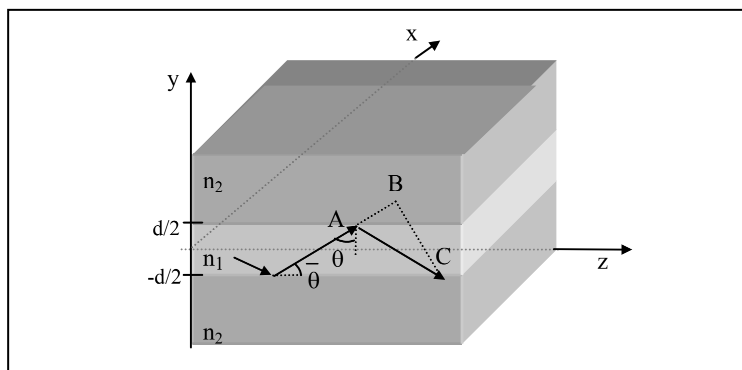

Fig. 4.17. Schematic of the multilayer waveguide consisting of three layers. The inner layer, with refractive index n_1, is the core of the waveguide. The outer layers are the cladding and their refractive index is n_2, that is lower than n_1. Rays making an angle $\theta>\theta_c$ are guided by total internal reflection.

4.2.1.1. Total internal reflection principles

Light rays making angles θ, measured from the normal to the interface, travel along the guiding layer if θ is greater than the critical angle θ_c. The critical angle is expressed as $\theta_c=\sin^{-1}(n_2/n_1)$. These light rays are totally internally reflected at the core/cladding boundary. When θ is smaller than θ_c, the light rays are refracted into the cladding and attenuated.

The waveguide modes can be determined by developing solutions to the Maxwell's equations in the inner and outer media with the appropriate boundary conditions imposed. In order to easily determine these modes, we will write the solution in terms of TEM plane waves bouncing between the surfaces of the slab.

We assume that the field in the slab is in the form of a monochromatic TEM plane wave. The wave travels with a phase velocity $c_1=c_0/n_1$, at a wavelength $\lambda=\lambda_0/n_1$. Its wave number is n_1k_0, and the wavevector components are $k_x=0$, $k_y=n_1k_0\sin\bar{\theta}$, and $k_z=n_1k_0\cos\bar{\theta}$, where $\bar{\theta}$ is the complement of the angle θ. In order to determine the modes of the waveguide, the self-consistency

UNIVERSITAT ROVIRA I VIRGILI
DESIGN, FABRICATION AND CHARACTERIZATION OF POROUS SILICON MULTILAYER OPTICAL DEVICES
Elisabet Xifré Pérez
ISBN: 978-84-691-0362-3/DL: T.2181-2007

condition is imposed. According to that condition, a wave reproduces itself after each round trip [165].

In one round trip, the twice-reflected wave lags behind the original wave by a distance $\overline{AC} - \overline{AB} = 2d \sin\overline{\theta}$, as in Fig. 4.17. Each internal reflection at the dielectric boundary introduces a phase φ_r. For self-consistency, the phase shift between the two waves must be zero or multiple of 2π,

$$\frac{2\pi}{\lambda} 2d \sin\overline{\theta} - 2\varphi_r = 2\pi m \qquad \text{m=0,1,2,..} \tag{4.2}$$

Equation (4.2) can be expressed as

$$2k_y d - 2\varphi_r = 2\pi m \tag{4.3}$$

The reflection phase shift φ_r is a function of the angle θ. It also depends on the polarization of the incident wave, TE or TM. In the TE case (the electric field is perpendicular to the plane y-z), the phase shift can be expressed as

$$\tan\frac{\varphi_r}{2} = \left(\frac{\sin^2\theta - \sin^2\theta_c}{\cos^2\theta}\right)^{1/2} \tag{4.4}$$

The dependence of the propagation constant β on the frequency ω can be examined by writing the self-consistency Eq. (4.3) in terms of β and ω. Since $\beta = k_z$ and $k_y^2 = (\omega / c_1)^2 - \beta^2$, Eq (4.3) gives,

$$2d\left[\left(\frac{\omega}{c_1}\right)^2 - \beta^2\right]^{1/2} = 2\varphi_r + 2\pi m \tag{4.5}$$

Since $\sin\theta = \beta/(\omega/c_1)$ and $\sin\theta_c = n_2/n_1 = c_1/c_2$, Eq. (4.4) becomes

$$\tan^2\frac{\varphi_r}{2} = \frac{\beta^2 - \omega^2/c_2^2}{\omega^2/c_1^2 - \beta^2} \tag{4.6}$$

Substituting (4.6) into (4.5) we obtain the self-consistency condition

ISBN: 978-84-691-0362-3/DL: T.2181-2007

$$\tan^2\left\{\frac{d}{2}\left[\left(\frac{\omega}{c_1}\right)^2-\beta^2\right]^{1/2}-\frac{m\pi}{2}\right\}=\frac{\beta^2-\omega^2/c_2^2}{\omega^2/c_1^2-\beta^2} \tag{4.7}$$

The self-consistency condition establishes a relation between β and ω, the dispersion relation for the different modes m=0,1,... .

The number of TE modes supported by this multilayer dielectric waveguide is the smallest integer greater than

$$M \doteq 2\frac{d}{\lambda_0}NA \tag{4.8}$$

The symbol $\doteq$ denotes that $2d\,NA/\lambda_0$ is increased to the nearest integer. For example, if $2d\,NA/\lambda_0$ =0.9, 1 or 1.1, the number of modes M is 1, 2, and 2, respectively. *NA* is the numerical aperture, expressed as

$$NA=\left(n_1^2-n_2^2\right)^{1/2} \tag{4.9}$$

For a fixed wavelength, the number of modes depends on the core thickness *d* and the difference between the refractive indices n_1 and n_2. The higher the thickness or the higher the difference between the refractive indices, the higher the number of TE modes of the waveguide.

In a dielectric waveguide, there is at least one TE mode, since the fundamental mode (m=0) is allowed for any wavelength [166]. However, the higher modes (m=1,2,...) have their own cutoff wavelength (λ_{cm}). It corresponds to the cutoff frequency $(\omega/c)_{cm}$, where $(\omega/c)_{cm}=2\pi/\lambda_{cm}$, that is the lowest frequency that can be guided by the structure for the m mode.

The waveguide with one allowed mode is called single-mode waveguide. This occurs when the slab is sufficiently thin for a fixed frequency.

UNIVERSITAT ROVIRA I VIRGILI
DESIGN, FABRICATION AND CHARACTERIZATION OF POROUS SILICON MULTILAYER OPTICAL DEVICES
Elisabet Xifré Pérez
ISBN: 978-84-691-0362-3/DL: T.2181-2007

4.2.1.2. Porous silicon slab waveguides for 1.55 μm applications

Two typical porous silicon refractive indices have been chosen for the theoretical study of this symmetric waveguide. The core consists of a porous silicon layer with refractive index n_1=2.5. The refractive index of the two cladding layers is n_2=1.5. These are two typical and obtainable porous silicon refractive indices [39].

The numerical aperture is determined by the refractive indices n_1 and n_2. For the refractive indices chosen, the numerical aperture is 2, calculated using Eq. (4.9). According to Eq. (4.8), for a fixed λ_0=1.55 μm, the number of TE modes *M* only depends on the core thickness *d.* From this equation, we obtain that for *d*<387.5 nm only one confined mode is allowed, and the waveguide is called single-mode. When thickness *d* increases, the number of TE modes increases. This effect can be observed in Fig. 4.18, that shows the dispersion relation of this waveguide for different thickness *d*. If we focus our attention for λ_0=1.55 μm ($\omega/c=4.05\cdot10^6$ rad/m), we can see that there is only one mode allowed for *d*=300 nm, there are two modes allowed for *d*=600 nm, three modes for *d*=900 nm, and four modes allowed for *d*=1300 nm, as was expected from the mathematical calculations of *M*.

For a fixed thickness *d*, the number of modes allowed depends on the wavelength. We can observe that all the waveguides presented in Fig. 4.18 have at least one mode of propagation (m=0) for any wavelength. The rest of the modes have a cutoff wavelength λ_{cm} (or cutoff frequency $(\omega/c)_{cm}$) that is the largest wavelength at which a mode is allowed. Fig. 4.18b shows the dispersion relation for *d*=600 nm. We can observe that the fundamental mode is allowed for any wavelength. The first mode (m=1) is allowed for wavelengths lower than approximately 2.6 μm (ω/c higher than $2.4\cdot10^6$ rad/m) and the second mode (m=2) is allowed for wavelengths lower than 1.2 μm (ω/c higher than $5.23\cdot10^6$ rad/m).

UNIVERSITAT ROVIRA I VIRGILI
DESIGN, FABRICATION AND CHARACTERIZATION OF POROUS SILICON MULTILAYER OPTICAL DEVICES
Elisabet Xifré Pérez
ISBN: 978-84-691-0362-3/DL: T.2181-2007

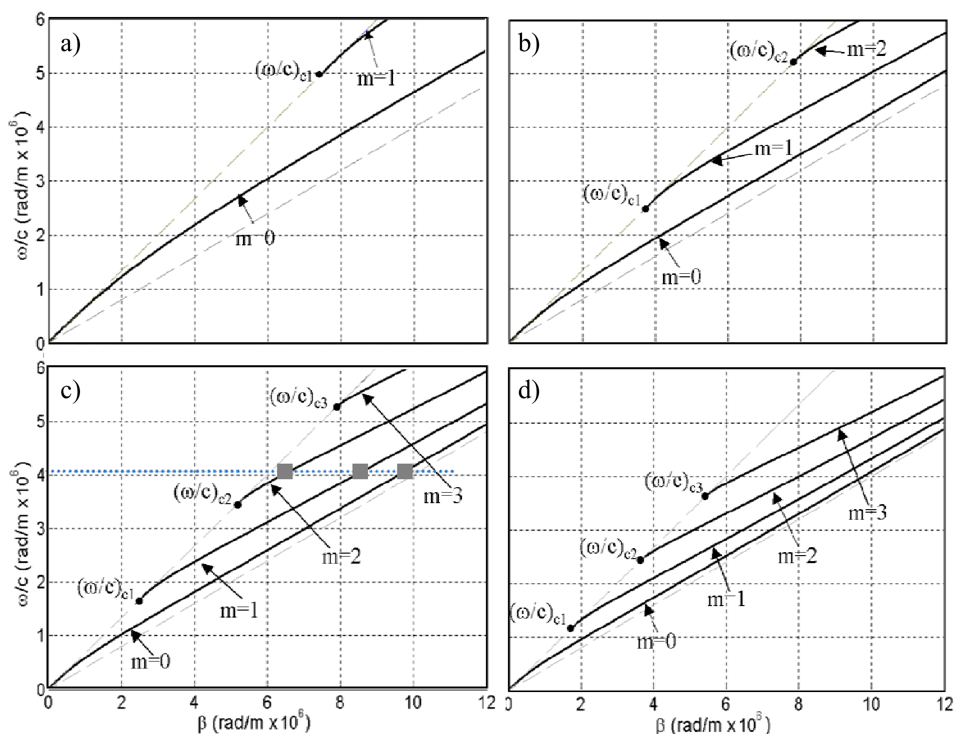

Fig. 4.18. Dispersion relation of the slab waveguide with n_1=2.5, n_2=1.5 and core thickness a) *d*=300 nm b) *d*=600 nm c) *d*=900 nm d) *d*=1300 nm. The modes of the waveguide take place for $n_2<\beta/(\omega/c)<n_1$. The dashed gray lines indicate these two limits. In c) the three modes for λ_0=1.55 μm ($\omega/c=4.05\cdot10^6$ rad/m) are denoted with squares.

We can also study the intensity distribution of all the modes that exist in the waveguide for a certain wavelength. If we focus our attention on the waveguide with *d*=900 nm, and we determine our working wavelength at λ_0=1.55 μm ($\omega/c=4.05\cdot10^6$ rad/m), we can observe in Fig. 4.18c that this waveguide has three different modes, each one for a different β value. The intensity distribution for these three modes is shown in Fig. 4.19. We can observe that all of them are well confined in the core layer, although mode 2 has a small part of the intensity within the cladding layer. All these modes could be

UNIVERSITAT ROVIRA I VIRGILI
DESIGN, FABRICATION AND CHARACTERIZATION OF POROUS SILICON MULTILAYER OPTICAL DEVICES
Elisabet Xifré Pérez
ISBN: 978-84-691-0362-3/DL: T.2181-2007

correctly transmitted through this porous silicon waveguide. The number of modes and the β at which they exist, for a certain wavelength, depends on the thickness of the core *d*, therefore, we could select these parameters adjusting the thickness *d*.

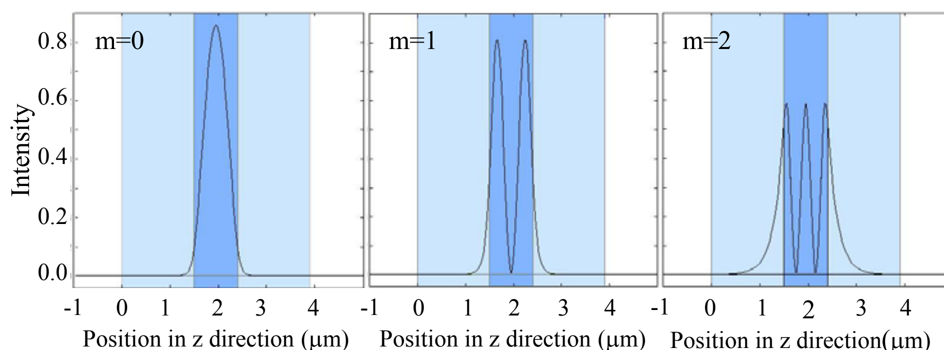

Fig. 4.19. Intensity distribution for the three modes of the waveguide with *d*=900 nm at λ_0=1.55 µm. The wavelength structure is also depicted being the dark gray region the core and the light gray regions the cladding.

Variation of the refractive indices of core and cladding

As explained before, the porous silicon formation technique permits the controlled variation of the refractive indices n_1 and n_2. We now study the influence of the refractive index variation on the cutoff wavelengths of the symmetric waveguides presented. Table 4.IV and Table 4.V show the cutoff wavelength of modes one, two and three for waveguides with core thickness *d* equal to 600 and 900 nm, respectively.

In both tables, we can observe that the variation of one or both refractive indices leads to a variation of the numerical aperture, and therefore a variation of the cutoff wavelengths. The decrease of n_1 and/or the increase of n_2 results in a lower numerical aperture, which leads to lower cutoff wavelengths for all modes.

ISBN: 978-84-691-0362-3/DL: T.2181-2007

n_1	n_2	NA	λ_{c1} (nm)	λ_{c2} (nm)	λ_{c3} (nm)
2.5	1.5	2	2400	1200	800
2.5	1.7	1.83	2196	1098	732
2.5	1.9	1.62	1944	972	648
2.3	1.5	1.74	2088	1044	696
2.1	1.5	1.47	1764	882	588
1.9	1.5	1.17	1404	702	462
2.35	1.7	1.62	1944	972	648

Table 4.IV. Cutoff wavelength of modes m=1...3 for core thickness *d*=600 nm and for different refractive indices n_1 and n_2.

n_1	n_2	NA	λ_{c1} (nm)	λ_{c2} (nm)	λ_{c3} (nm)
2.5	1.5	2	3600	1800	1200
2.5	1.7	1.83	3294	1647	1098
2.5	1.9	1.62	2916	1458	972
2.3	1.5	1.74	3132	1566	1044
2.1	1.5	1.47	2646	1323	882
1.9	1.5	1.17	2106	1053	702
2.35	1.7	1.62	2916	1458	972

Table 4.V. Cutoff wavelength of modes m=1..3 for core thickness *d*=900 nm and for different refractive indices n_1 and n_2.

In both tables, we can observe that, for a fixed *d*, the cutoff wavelength only depends on the resulting numerical aperture and that two waveguides with different refractive indices but with the same *NA* (e.g. *NA*=1.62) have the same cutoff wavelengths.

UNIVERSITAT ROVIRA I VIRGILI
DESIGN, FABRICATION AND CHARACTERIZATION OF POROUS SILICON MULTILAYER OPTICAL DEVICES
Elisabet Xifré Pérez
ISBN: 978-84-691-0362-3/DL: T.2181-2007

4.2.2. Photonic crystal waveguides

A novel class of waveguides has been introduced recently, in which the confinement of the light is based on the properties of photonic crystals (PC). The photonic bandgap, where light cannot propagate for a certain frequency range, is used to confine light.

One-dimensional photonic crystals are multilayer periodic structures that have already been used to confine light in the core layer. Some of them are Distributed Bragg Reflectors (DBR) either in cylindrical [167] or planar structures [125,128]. Others are omnidirectional mirrors (OM) [116,110-112,168,169] that reflect light for any incidence angle and any polarization over a range of frequencies, the so-called omnidirectional bandgap (OBG). We shall focus our attention on planar waveguide structures with OM [170] although cylindrical structures have also been studied [171,172].

4.2.2.1. Structure

The proposed waveguide structure is a porous silicon multilayer consisting of a core layer inserted between two symmetric OM. Fig. 4.20 represents the diagram of this waveguide structure. Each OM is a stack of alternating high and low refractive index layers (n_H and n_L) with thickness d_H and d_L respectively. The period of the OM is defined as $\Lambda=d_H+d_L$ and is repeated N times. The refractive index of the core layer is n_0 and its thickness is d_0.

The refractive indices chosen for the OM are n_H=2.5 and n_L=1.5 [152]. The number of periods N of the OM should be high enough for the intensity of the electric field (electromagnetic field) of the modes to decay in the OM cladding. The parameter d_H determines the width of the OBG whereas n_0 has an effect on the energy confinement of the modes within the core layer. The optimal values of these three parameters and the criteria for selecting their optimal values are discussed in the next section.

ISBN: 978-84-691-0362-3/DL: T.2181-2007

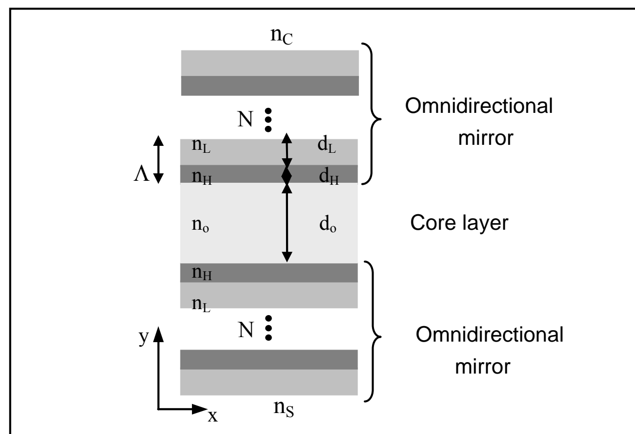

Fig. 4.20. Diagram of the porous silicon multilayer waveguide. n_0 and d_0 are the refractive index and thickness of the core layer, respectively. n_L and n_H are the low and high refractive indices of the omnidirectional mirror cladding layers, while d_L and d_H are their corresponding thicknesses. Each omnidirectional mirror has N periods with period thickness Λ and are surrounded by a cover and a substrate with refractive indices n_C and n_S, respectively. The propagation direction is along the x-axis.

4.2.2.2. Determination of the parameters n_0, d_H and N

In order to study how all the parameters of the structure affect the performance of the waveguide, we applied the transfer matrix method to planar multilayer optical waveguides [156], and restricted our discussion to TE modes. This method is especially suitable for analyzing one-dimensional photonic crystals such as the proposed structure.

Since photonic crystals are perfectly scalable structures, the units of all the magnitudes considered here (thickness, frequency and wavevector) are normalized to the period thickness of the OM (Λ). Thus, to apply the results of this study to a certain frequency, it is only necessary to adjust the period thickness Λ.

UNIVERSITAT ROVIRA I VIRGILI
DESIGN, FABRICATION AND CHARACTERIZATION OF POROUS SILICON MULTILAYER OPTICAL DEVICES
Elisabet Xifré Pérez
ISBN: 978-84-691-0362-3/DL: T.2181-2007

a) Determination of the refractive index of the core layer

The structure that we propose is completely made of porous silicon. Therefore the refractive index of the core layer n_0 could be any refractive index obtainable with the porous silicon fabrication techniques. The core is a porous silicon layer instead of the air layer proposed in previous studies [40,9,43,44]. A porous silicon core ensures the feasibility of the waveguide structure since it can be fabricated in a single etching process by appropriately modulating the etching current. Furthermore, although the core refractive index is higher than 1, it does not negatively affect the properties of the structure [173]; it only slightly reduces the width of the OBG.

The selection criterion used for n_0 is the energy confinement factor of the modes. The confinement (Γ) indicates the portion of the field energy that is confined within the core layer [40] and is defined as:

$$\Gamma = \frac{\int_{Core\ layer} |n_o E|^2 dy}{\int_{-\infty}^{\infty} |n_i E|^2 dy} \tag{4.10}$$

where n_i is the refractive index of the layer for that y and E is the electrical field amplitude.

Fig. 4.21 shows the confinement of the fundamental mode as a function of n_0 for the range of refractive indices obtainable with porous silicon. The simulated structure is the one presented in the section above and the calculation has been made for three different d_H/Λ so as to consider different possible structures. For the three cases, we can observe that when $n_0 > n_L$ the confinement of the mode decreases very quickly with n_0 until the mode disappears. On the other hand, for $n_0 \leq n_L$, the confinement is very similar for the different values of n_0 and the different core thicknesses. This, together with the experimental observation that the fabrication of porous silicon is increasingly more complex when the refractive indices are smaller lead us to choose $n_0 = n_L$.

ISBN: 978-84-691-0362-3/DL: T.2181-2007

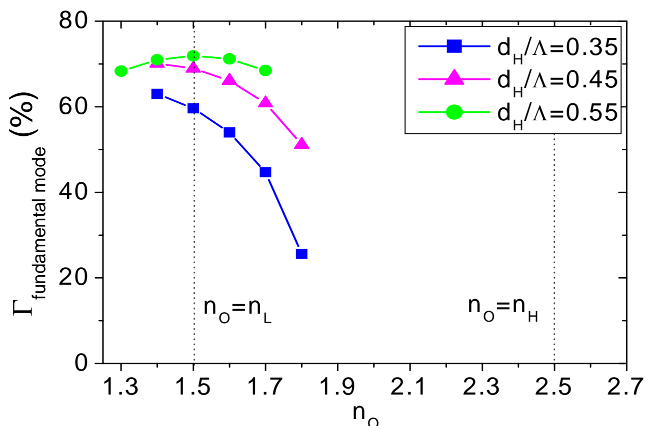

Fig. 4.21. Confinement of the fundamental mode as a function of n_0 in the range of refractive indices obtainable with the porous silicon formation technique. The confinement is calculated for different d_H/Λ and for $\omega(\Lambda/2\pi c)$=0.29 and d_0/Λ=2. We can observe that for $n_0 \geq 1.9$ the fundamental mode does not exist and for n_0=1.3 it does not exist for some d_H/Λ.

b) Determination of the layer thickness of the OM

Selecting the thickness of the OM layers can be reduced to selecting d_H/Λ because $1= d_H/\Lambda+ d_L/\Lambda$. The ratio d_H/Λ is an important parameter of the OM because it determines the width of its OBG. The projected band structure (PBS) of the multilayer can be used to easily observe the width of the OBG. Fig. 4.22 shows the PBS for TE polarization of the infinite multilayer with $n_0=n_L=1.5$ and n_H =2.5 for different d_H/Λ. An electromagnetic mode is defined by the frequency ω and the surface-parallel wavevector β, which are expressed in the figure in normalized units. The gray regions represent the allowed modes, the white region over the light line for n_0 represents the bandgap and the black region indicates the OBG. In Fig. 4.22 we can observe that the position and width of the bandgap varies with the thickness d_H/Λ and that the OBG only exists for $0.32 \leq d_H/\Lambda \leq 0.62$. For this study d_H/Λ was taken to satisfy the widest OBG condition, which corresponds to d_H/Λ=0.45.

UNIVERSITAT ROVIRA I VIRGILI
DESIGN, FABRICATION AND CHARACTERIZATION OF POROUS SILICON MULTILAYER OPTICAL DEVICES
Elisabet Xifré Pérez
ISBN: 978-84-691-0362-3/DL: T.2181-2007

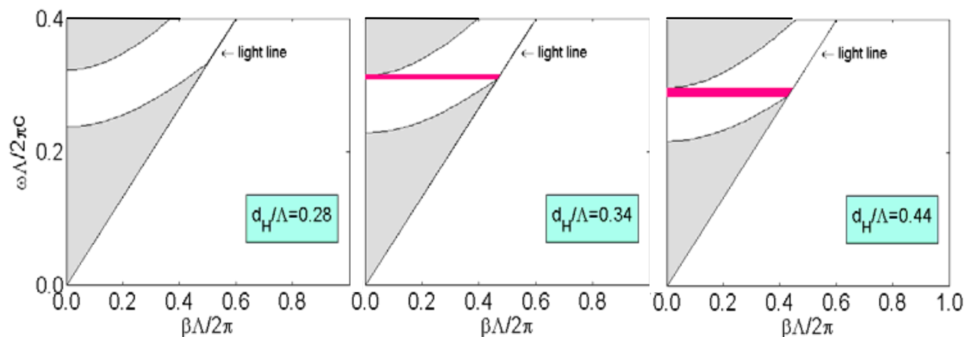

Fig. 4.22. Projected band structure of the mirror cladding with n_H=2.5 and n_L=1.5, for different d_H/Λ. The *x* axis corresponds to the normalized surface-parallel wavevector component β and the *y* axis is the normalized frequency ω. The thin black line is the light line for n_0=1.5. The black area is the OBG, which only exists for $0.32 \leq d_H/\Lambda \leq 0.62$.

c) Determination of the OM number of periods

The number of periods (N) affects the OM because the more there are, the more similar the behavior of the finite OM is to the ideal infinite photonic crystal. The field of a mode with (ω,β) in the bandgap of the OM is guided in the core layer and is attenuated as it penetrates the periods of the OM.

This effect can be observed in Fig. 4.23 where the field profiles of the three existing guided modes for d_0/Λ=6 and normalized frequency $\omega(\Lambda/2\pi c)$=0.29 are represented together with 15-period OM claddings. The field is highly confined within the core layer for all the guided modes while the field amplitude becomes attenuated as it penetrates the cladding. In this study, the criterion for determining N was the attenuation of the field amplitude in the cladding. In particular, the chosen N is the one that leads to an attenuation of 100 dB from the maximum in the core to the outermost period of the OM for the higher order mode. For the refractive indices and thicknesses determined above, the number of periods that fulfills this condition is N=15, for any core thickness.

ISBN: 978-84-691-0362-3/DL: T.2181-2007

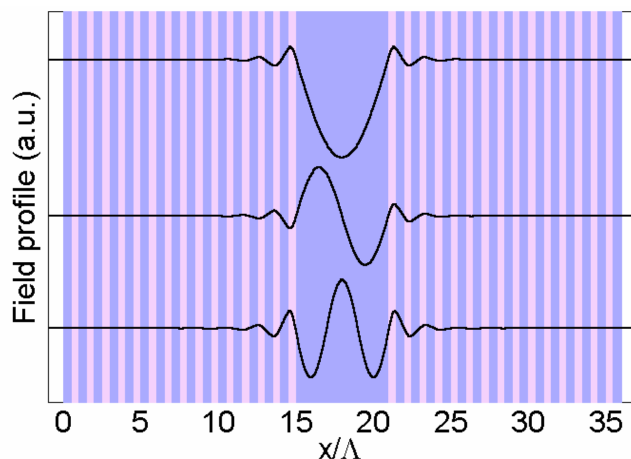

Fig. 4.23. Field profile of the guided modes in the proposed structure. The multilayer structure for 15 periods is depicted and the three modes for $d_0/\Lambda=6$ and $\omega(\Lambda/2\pi c)=0.29$ are superposed.

4.2.2.3. Omnidirectional Mirrors and Distributed Bragg Reflectors as cladding for porous silicon planar waveguides

Once the omnidirectional mirror parameters (n_H, n_L, d_H and N) and the refractive index of the core layer (n_0) have been determined, we can evaluate the use of the OM as cladding in planar waveguides. To this end, we will study how the core thickness influences on the number of guided modes and their confinement, and also the dependence of the confinement of the modes on frequency.

a) Influence of the core thickness

The number of guided modes and their confinement are determined by the core thickness d_0. Fig. 4.24 shows the dispersion relation for the modes for different core thicknesses d_0/Λ together with the PBS of the OM. Notice that the

ISBN: 978-84-691-0362-3/DL: T.2181-2007

PBS is the same for any d_0/Λ because the characteristics of the OM are independent of this parameter. When d_0/Λ is very low there is only one mode, the fundamental or first mode. When d_0/Λ increases, this mode shifts to the right and approaches the light line of n_0 whereas the second mode appears on the left when $d_0/\Lambda=1.80$.

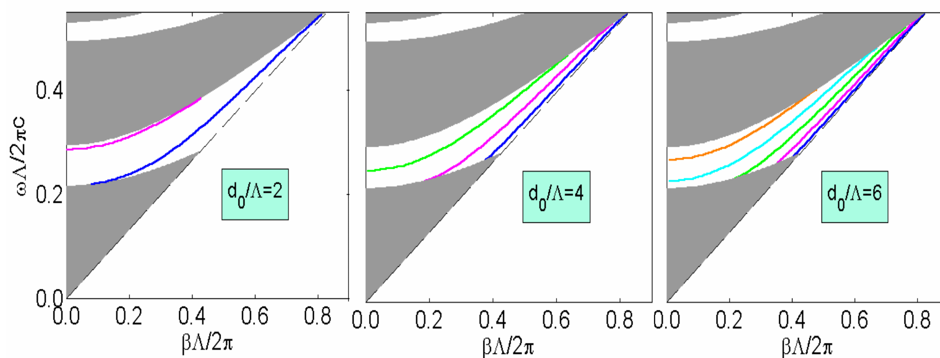

Fig. 4.24. Dispersion relation for the guided modes of the proposed waveguide (n_0=n_L=1.5, n_H=2.5, and d_H/Λ=0.45) for different core thickness d_0/Λ. Each line corresponds to one mode. The projected band structure of the OM is also depicted.

When the core thickness increases further, all the modes shift towards the light line and draw closer together as new modes appear on the left. This effect is better illustrated in Fig. 4.25a where β is represented for different d_0/Λ, for a constant normalized frequency $\omega(\Lambda/2\pi c)=0.29$. When d_0/Λ increases, β increases and asymptotically approaches a limit value corresponding to the light line for this frequency, which is $\beta(\Lambda/2\pi)= 0.435$.

The confinement gives important information about the modes as it indicates the fraction of the energy that is confined within the core layer. Fig. 4.25b shows the confinement of the modes represented in Fig. 4.25a. When d_0/Λ increases, the confinement of the modes increases and gets closer to

UNIVERSITAT ROVIRA I VIRGILI
DESIGN, FABRICATION AND CHARACTERIZATION OF POROUS SILICON MULTILAYER OPTICAL DEVICES
Elisabet Xifré Pérez
ISBN: 978-84-691-0362-3/DL: T.2181-2007

100 %. This indicates that the modes that are closer to the light line have a higher confinement.

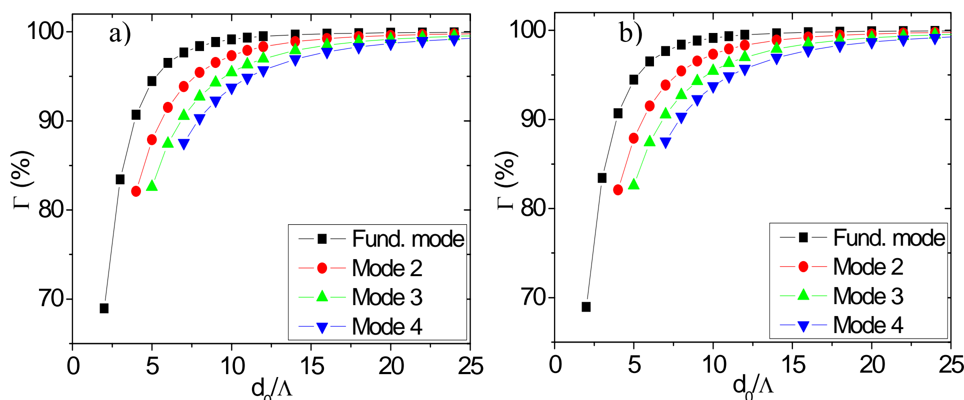

Fig. 4.25. Normalized surface-parallel wavevector $\beta(\Lambda/2\pi c)$ (a) and confinement Γ (b) for the first four guided modes as a function of the core thickness, for $\omega(\Lambda/2\pi c)$ =0.29. The dashed line in (a) indicates the value of $\beta\Lambda/2\pi c$ at the light line of n_0 for this frequency.

b) Analysis of the confinement for different DBR and OM cladding waveguides

In the framework of planar waveguides, a previous study [128] proposes a DBR cladding optimized for the propagation angle of the fundamental mode. However, the same study [128] also suggests that an OM might be more suitable for guiding more than one mode since it reflects the light regardless of the angle.The OM is indeed a particular case of DBR possessing an ORR. For this reason, in this section we analyze the performance of two different DBRs as cladding for waveguides and compare it with the performance of the OM waveguide. The three structures compared in this section (OM and DBRs) fulfill the condition that they have the same fabrication complexity: that is to say, they have the same refractive indices n_0=n_L=1.5 and n_H=2.5, the same number of periods (15) and the same period thickness (Λ).

UNIVERSITAT ROVIRA I VIRGILI
DESIGN, FABRICATION AND CHARACTERIZATION OF POROUS SILICON MULTILAYER OPTICAL DEVICES
Elisabet Xifré Pérez
ISBN: 978-84-691-0362-3/DL: T.2181-2007

The criterion to choose the first DBR cladding (DBR_1) is based on the fact that to have good light guiding and confining properties it is desirable that the region of forbidden frequencies would be as wide as possible. The DBR with the widest forbidden frequencies region is also the one with the widest frequency gap for normal incidence. This corresponds to the structure where the optical thicknesses of the two layers of the period are equal at normal incidence, that is $n_H d_H = n_L d_L$ and thus $d_H/\Lambda=0.375$.

For the second DBR cladding (DBR_2) we have applied the criterion that the fundamental mode confinement at the studied core thickness range is maximum. For the studied frequency of $\omega(\Lambda/2\pi c)=0.29$, the center frequency of the OBG, this condition is given for $d_H/\Lambda=0.60$.

The modal confinement of these three waveguide structures with different cladding is represented in Fig. 4.26. The first four guided modes for the central frequency of the OBG are analyzed in this figure. It can be observed that for all the modes, the OM and the DBR_2 cladding waveguides have a high confinement whereas the DBR_1 cladding waveguide has a lower confinement. Besides, for the DBR_1 cladding the modes only exist for a range of d_0/Λ. This happens because when d_0/Λ increases, β increases, making the mode lie within the allowed region (the gray region in the PBS). This means that the light is no longer confined by the cladding. This is a consequence that there are propagating angles for that frequency not supported by the DBR waveguide.

Fig. 4.26 also shows that, in general, the confinement of the OM is very similar to the confinement of DBR_2. For the four modes and most of the core thicknesses the confinement of DBR_2 is slightly higher except for some particular cases. The confinement of the OM is higher than the one of DBR_2 in the case of small core thickness. The higher the mode order, the wider the range of d_0/Λ where the confinement of the OM is higher. The confinement of DBR_1 is lower in all cases than the confinement of the OM and in some particular cases it is higher than the confinement of the DBR_2.

UNIVERSITAT ROVIRA I VIRGILI
DESIGN, FABRICATION AND CHARACTERIZATION OF POROUS SILICON MULTILAYER OPTICAL DEVICES
Elisabet Xifré Pérez
ISBN: 978-84-691-0362-3/DL: T.2181-2007

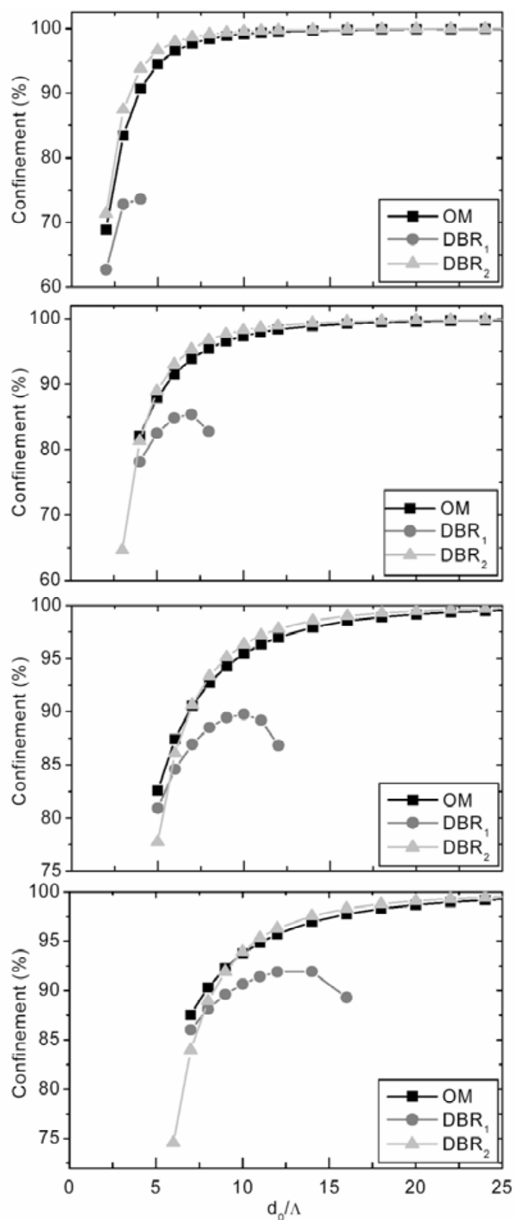

Fig. 4.26. Confinement of the four first modes of the OM cladding waveguide and the two DBR cladding waveguides as a function of the core thickness for d_0/Λ=15 and $\omega(\Lambda/2\pi c)$=0.29.

ISBN: 978-84-691-0362-3/DL: T.2181-2007

4.2.2.4. Modes of the multilayer waveguide

The modes of the multilayer waveguides have been studied using the PBS of the multilayer cladding. In this section, the modes that exist for the multilayer structure waveguide are discussed depending on their position in the PBS of the multilayer.

For this discussion, we study the modes of the waveguide whose refractive indices for the OM are the ones used in the previous section: n_H=2.5 and n_L=1.5 [174]. We concretely study the different types of modes that can exist in this waveguide for the central normalized frequency within the OBG: $\omega(\Lambda/2\pi c)$=0.29. The modal analysis of the waveguide structure has been carried out with the transfer matrix method applied to planar multilayer optical waveguides [175]. The values of β that satisfy the modal condition [eq. 26 in 175] have been calculated. For this discussion the core thickness d_H/Λ=5 has been chosen. Although this study has been done for d_o/Λ=5, the behavior of the modes is the same for any core thickness.

At this frequency and for this core thickness there are seven different β that satisfy the modal condition. The position of these modes within the PBS is given in Fig. 4.27.

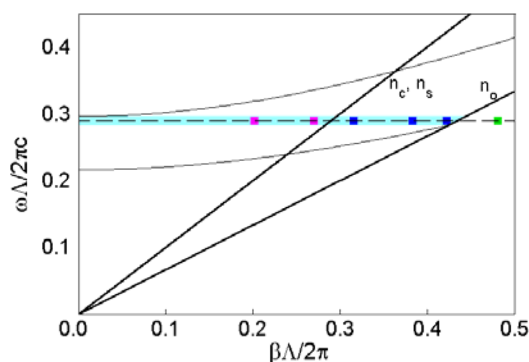

Fig. 4.27. PBS of the studied multilayer with the modes for d_0/Λ=5. The OBG is represented by a light gray area. The points indicate all the possible modes for ω=0.29·(Λ/2πc). The diagonal lines are the light lines of the core and the bounding media.

ISBN: 978-84-691-0362-3/DL: T.2181-2007

The two modes with the lowest β are the ones with β(Λ/2π)=0.2011 and 0.2698. They lie above the light line for n=1 (corresponding to either bounding medium n_s, n_c[175]) but inside the OBG These are radiation modes since, although they are confined within the core because of the photonic crystal effect of the OM, they can propagate in the cover or substrate, as it can be seen in Fig. 4.28.

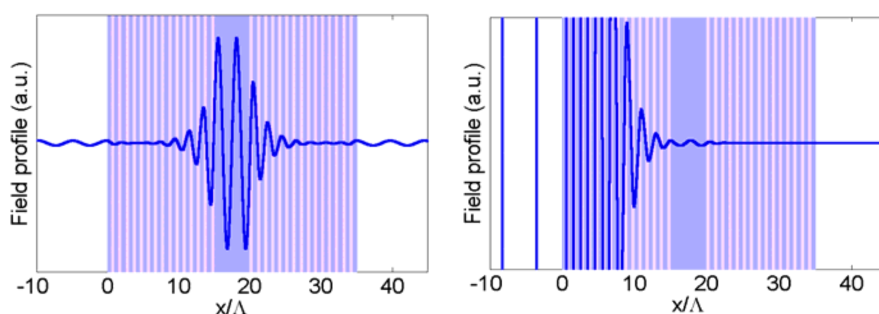

Fig. 4.28. Field profile of the two modes with β(Λ/2π)=0.2011 and 0.2698. Their corresponding β are lower than n_s,n_c. As can be observed, their are radiant modes.

The next three modes with β(Λ/2π)=0.3153, 0.3832, and 0.4219 lie below the light line of the bounding media and above that of the core. Fig. 4.29 shows that the field is confined within the core and is evanescent in the bounding media. Furthermore, a fundamental model and successive harmonics can be recognized.

ISBN: 978-84-691-0362-3/DL: T.2181-2007

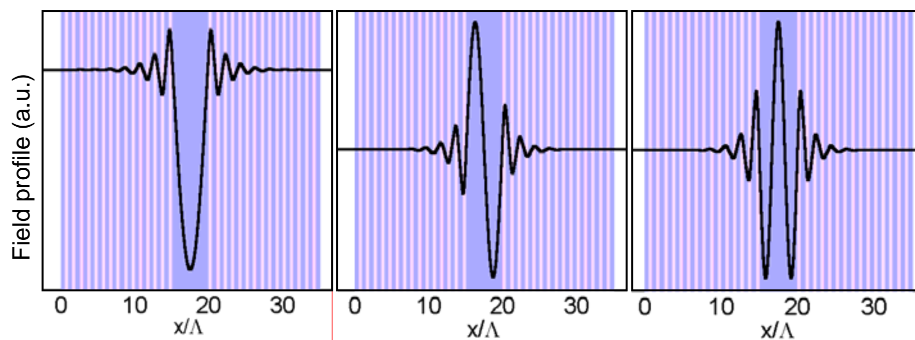

Fig. 4.29. Field profile of the three modes with β(Λ/2π)=0.3153, 0.3832, and 0.4219. Their corresponding β are between the light lines of the core and of the cover/substrate (n_s,n_c<β<n_o). They are guided modes.

Finally, the modes below the light line of the core, that is β(Λ/2π)=0.48081 and 0.48082, show an evanescent field in the bounding medium and in the low-index material (see Fig. 4.30). Even though these modes are confined in the multilayer structure cannot be considered as guided modes by the effect of the OM.

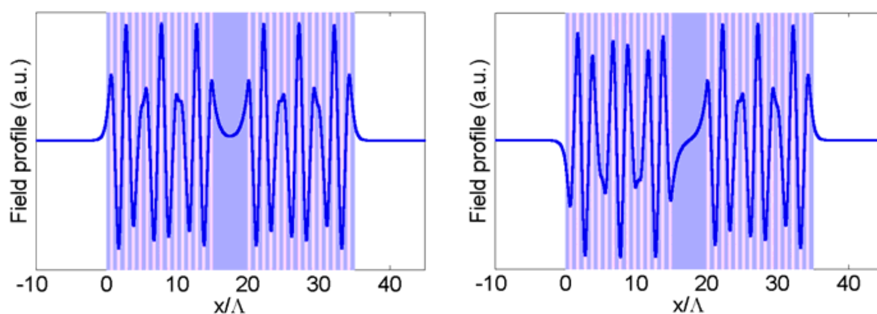

Fig. 4.30. Field profile of the two modes with β(Λ/2π)=0.48081, 0.48082. Their corresponding β are higher than n_o. As can be observed, they are not guided modes.

UNIVERSITAT ROVIRA I VIRGILI
DESIGN, FABRICATION AND CHARACTERIZATION OF POROUS SILICON MULTILAYER OPTICAL DEVICES
Elisabet Xifré Pérez
ISBN: 978-84-691-0362-3/DL: T.2181-2007

4.3. Conclusions

The simulation of different optical devices based on multilayers has been realized using the different programs presented in the previous chapter. These optical devices are omnidirectional mirrors and waveguides. All of them have been designed for 1.55 μm applications and the use of porous silicon for their fabrication has been discussed.

Omnidirectional mirrors are the optical devices most widely studied in this work. The periodic structure is the most commonly used for the formation of omnidirectional mirrors and the different parameters that influence on its omnidirectional bandgap have been studied. But the limited range of refractive indices obtainable with porous silicon restricts the omnidirectional bandgap width of this structure. One of the objectives of this work was to obtain porous silicon omnidirectional mirrors with a wide bandgap, as is required by different omnidirectional mirrors applications. For this reason different multilayer structures have been studied and proposed. The chirped structure, reported by a few groups, can be a suitable structure with a wider omnidirectional bandgap, just as has been demonstrated in this study. Besides, three different omnidirectional mirror structures have been proposed. It has been demonstrated that all of them have an omnidirectional bandgap wider than the one of the chirped structure.

The first structure proposed is the random structure where the thickness of the high refractive index layer varies randomly in the multilayer structure. The different parameters that influence on the omnidirectional bandgap width have been discussed and it has been demonstrated to have a wider omnidirectional bandgap than the periodic and the chirped structures. The main disadvantage of this structure is that the results strongly depend on many different parameters, which hinders its design. The study of this structure has lead us to propose two other mirror structures that have an enlarged omnidirectional bandgap and have very simple design rules: the balanced and the unbalanced structures. Both mirror structures consist of a few periodic multilayers (substuctures) stacked together where the period is different for each one, being their bangaps centered at different wavelengths. The bandgap of the

UNIVERSITAT ROVIRA I VIRGILI
DESIGN, FABRICATION AND CHARACTERIZATION OF POROUS SILICON MULTILAYER OPTICAL DEVICES
Elisabet Xifré Pérez
ISBN: 978-84-691-0362-3/DL: T.2181-2007

mirror structure is the union of the bandgaps of the substructures that make it up. The number of substructures stacked together is not limited, so wide omnidirectional bandgaps can be obtained without the limitation of the refractive index range. Whereas the substructures of the balanced mirror have the same number of periods, in the unbalanced mirror the first and the last substructures have more periods than the others. It has been demonstrated that the omnidirectional bandgap of both structures is wider than the ones obtained with the periodic and the chirped structures.

Porous silicon waveguides have been also theoretically studied. First, waveguides based on total refractive index have been analyzed for 1.55 μm applications, and the influence of the refractive indices and the core thickness on the number of modes has been studied. It has been theoretically demonstrated that a porous silicon multilayer may be used as a waveguide for 1.55 μm applications. The analysis of waveguides with different core thickness has demonstrated that when the thickness increases, the number of TE modes increases. Four waveguides with the same refractive indices but with different core thickness have been proposed. The dispersion relations of these waveguides have been presented and the cutoff wavelength of the modes allowed in the waveguide has also been studied for different refractive indices of core and cladding. It has been demonstrated that, for a fixed core thickness, different refractive indices resulting in the same numerical aperture have the same cutoff wavelengths.

However, the most widely analyzed waveguide structure has been the one where the confinement of the light is based on the properties of photonic crystals, as a multilayer is in fact a one-dimensional photonic crystal. In these waveguides, the multilayer is the cladding. In concrete, we have studied the use of omnidirectional mirrors and DBR to be used for the cladding. Three different types of modes have been observed depending on their position in the PBS of the multilayer cladding. It has been demonstrated that the guided modes are the ones with $n_s, n_c < \beta < n_o$. The influence of different parameters of the waveguide structure on the modes and the modal confinement has been studied. We have observed that the core refractive index that leads to the highest confinement is

ISBN: 978-84-691-0362-3/DL: T.2181-2007

$n \leq 1.5$. It has been observed that when the core thickness increases, the β of the modes gets closer to the light line and the confinement increases getting closer to 100 %. This indicates that the modes that are closer to the light line have a higher confinement. Besides, the increment of core thickness results in the increment of the number of modes, the same that happened with TIR waveguides. Finally, the confinement of the OM cladding waveguide was analyzed with respect to two other different DBR cladding waveguides with the same fabrication complexity. DBR_1 was chosen to present the widest forbidden frequencies region. The second DBR (DBR_2) is the one with the maximum fundamental mode confinement for the studied frequency. Analyzing the confinement for the four first modes of these three structures, we have concluded that in general, for all the modes, the OM and the DBR_2 cladding waveguides have a higher confinement than the DBR_1 cladding waveguide. Besides, for the DBR_1 cladding the modes only exist for a range of d_0/Λ. The confinement of the OM is very similar to the confinement of DBR_2, being for the DBR_2 slightly higher except for some particular cases. The confinement of the OM is higher for the smallest core thicknesses.

From these results, it can be said that the OM cladding might be a good trade off between the different types of DBR. The OM cladding offers the possibility of having a high confinement for a certain number of modes even with a small core thickness, what permits a simpler fabrication complexity, as the overall thickness of the waveguide can be smaller.

ISBN: 978-84-691-0362-3/DL: T.2181-2007

Chapter 5

Fabrication and characterization of porous silicon layers

In this chapter a complete description of the porous silicon fabrication system that we have established at the Department of Electronic, Electric and Automatic Engineering of the Universitat Rovira i Virgili is realized. In this description we also analyze the influence of the different elements used for the fabrication process on the characteristics of the fabricated porous silicon monolayers and multilayers, specially the differences between two types of electrochemical cells. Finally, the relations between the anodization parameters and the two most important physical characteristics of porous layers (refractive index and thickness) are presented. To conclude this chapter, the different methods used for the characterization of porous silicon layers are explained.

UNIVERSITAT ROVIRA I VIRGILI
DESIGN, FABRICATION AND CHARACTERIZATION OF POROUS SILICON MULTILAYER OPTICAL DEVICES
Elisabet Xifré Pérez
ISBN: 978-84-691-0362-3/DL: T.2181-2007

5.1. Fabrication System

In this section we describe in detail all the elements that are a part of the fabrication system. It is a self-controlled system created for the fabrication of porous silicon monolayers and multilayers that has been established at the Department of Electronic, Electric and Automatic Engineering at the University Rovira i Virgili. In this section, the importance of each element and its usefulness are explained, especially the electrochemical cell that is the most important part of all the process. The program realized for the control of the fabrication system is also explained.

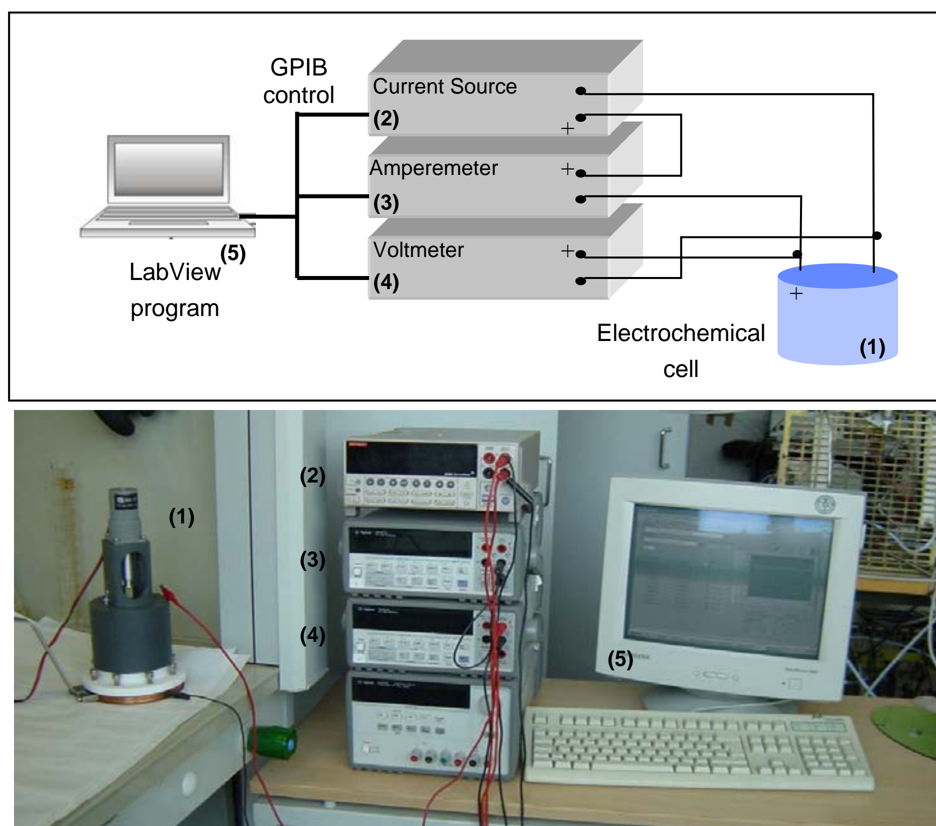

Fig. 5.1. a) Schematic of the designed porous silicon fabrication system b) Photograph of the system.

UNIVERSITAT ROVIRA I VIRGILI
DESIGN, FABRICATION AND CHARACTERIZATION OF POROUS SILICON MULTILAYER OPTICAL DEVICES
Elisabet Xifré Pérez
ISBN: 978-84-691-0362-3/DL: T.2181-2007

Fig. 5.1a shows the schematic of the fabrication system, wherea Fig. 5.1b shows its photograph. The main element of the system is the electrochemical cell (1), where the electrochemical etching of the silicon is realized. The current applied during the etch is provided by the current source (2). Two multimeters (3,4) are used for the measurement of the current and the voltage of the system during the etch process, respectively. They are used to supervise the etching process parameters. The whole system is controlled by a computer (5) where the developed LabView program controls continuously the two main parameters for the formation of the porous silicon structures: the current applied and the etching time.

In the next subsections, the elements of the system are described.

5.1.1. Electrochemical cell

The electrochemical cell is the most important part of the fabrication system because the homogeneity of the porous silicon samples depends on its structure. This conclusion has been obtained with the study of porous silicon monolayers and multilayers fabricated with two types of electrochemical cells.

5.1.1.1. Lateral-wafer electrochemical cell

The first type of cell that has been used for the fabrication process is the one that we have named lateral-wafer cell because its main characteristic is that the silicon wafer is located at the sidewall of the cell, as can be observed in the diagram of Fig. 5.2a. The **silicon wafer** acts as the anode and has a back-side contact that is a **metallic ring**. The front side of the wafer is sealed with an **O-ring**, so that only this part of the wafer surface is in contact with the electrolyte. The electrolyte is composed of high purity hydrofluoric acid (HF) in 40% aqueous solution diluted in ethanol (C_2H_5OH) at different concentrations. The **cathode** is made of platinum, a HF-resistant and conducting material. The **cell body** is a square-section teflon recipient. This material was selected because it

ISBN: 978-84-691-0362-3/DL: T.2181-2007

is a highly acid-resistant polymer. The stir of the electrolyte is realized with a **magnetic stirrer**. A photograph of this cell can be seen in Fig. 5.2b.

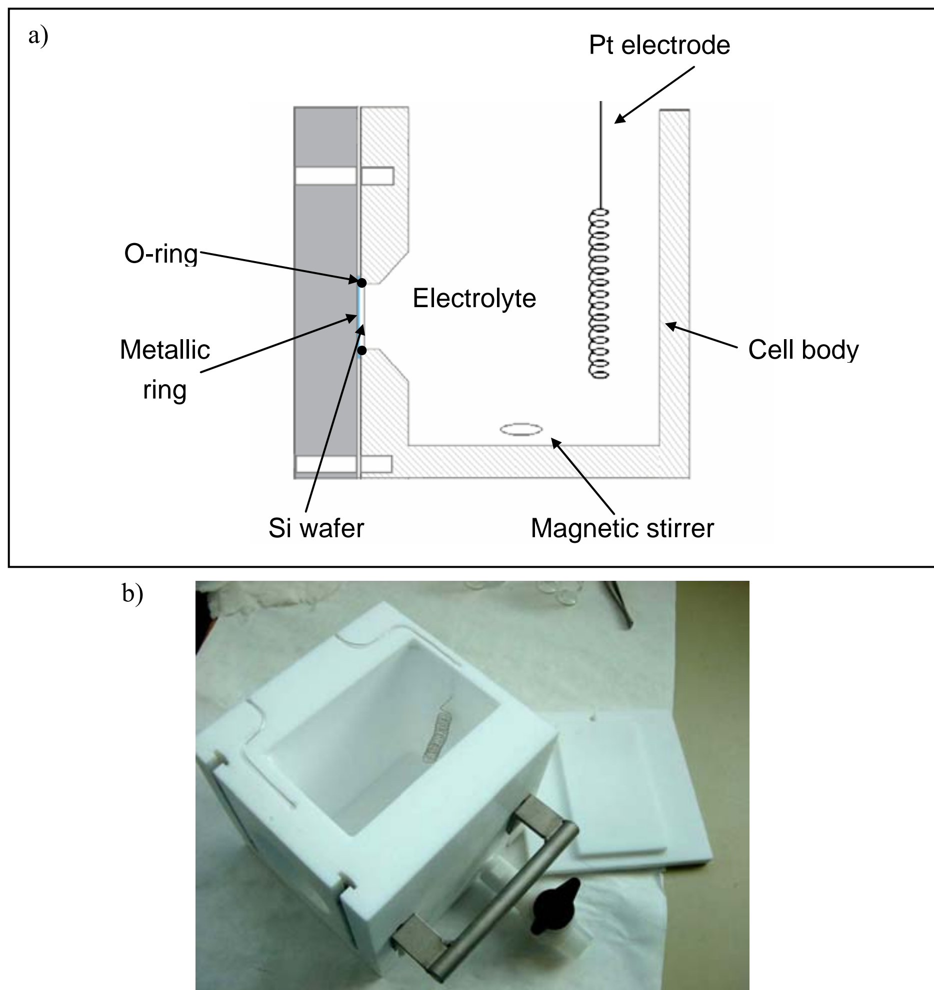

Fig. 5.2. The lateral-wafer cell used for the fabrication of porous silicon layers a) schematic of the cross sectional view. b) photograph of cell.

The main drawback of this cell is the inhomogeneity in porosity and thickness of the porous silicon layers. We have observed that the porous silicon

UNIVERSITAT ROVIRA I VIRGILI
DESIGN, FABRICATION AND CHARACTERIZATION OF POROUS SILICON MULTILAYER OPTICAL DEVICES
Elisabet Xifré Pérez
ISBN: 978-84-691-0362-3/DL: T.2181-2007

monolayers and multilayers fabricated with this lateral cell are highly inhomogeneous; in thickness, where the thickness from one point to another of the same sample can vary up to 30%, and in porosity where the refractive index may vary up to 0.5. This thickness variation can be observed in Fig. 5.3 where the cross section of a porous silicon monolayer fabricated with this cell has been observed with the Scanning Electron Microscope (SEM). The two different points of this section have different thickness and the difference between them is about 27 %. But it is not necessary to observe the samples with the SEM. At first sight it is possible to see the inhomogeneity of the fabricated monolayers in Fig. 5.4, where the color variation of the etched area indicates a variation of thickness and/or porosity.

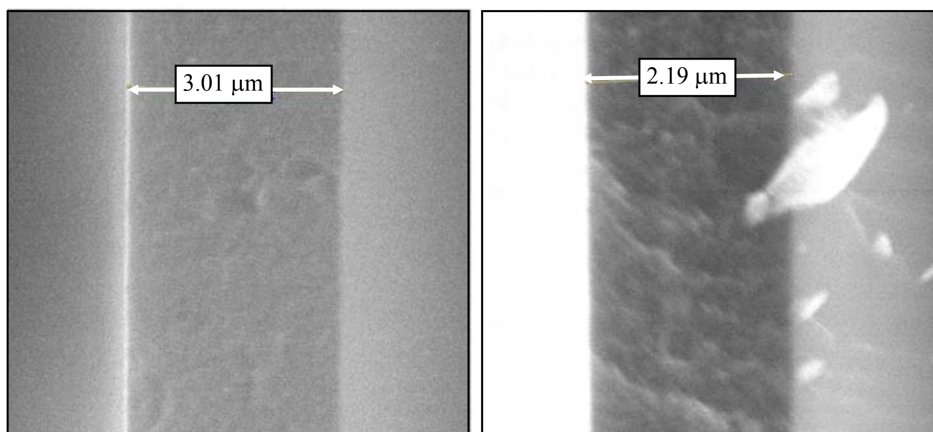

Fig. 5.3. SEM image of the cross section of a porous silicon monolayer fabricated with the lateral-wafer cell. The two images correspond to two different points of the same cross section. The thickness of the layer at each point is labeled.

The inhomogeneity of the porous silicon samples fabricated with this cell are most probably due to the bubbles that form and stick on the silicon surface. They must be removed and the concentration of HF has to be locally constant on the surface of the wafer. This type of cell does not facilitate the bubble

UNIVERSITAT ROVIRA I VIRGILI
DESIGN, FABRICATION AND CHARACTERIZATION OF POROUS SILICON MULTILAYER OPTICAL DEVICES
Elisabet Xifré Pérez
ISBN: 978-84-691-0362-3/DL: T.2181-2007

removal due in part to the lateral position of the sample, to the square section of the cell body, and to the limitations of the magnetic stirrer, that is low efficient for the large volume of the cell (around 800 ml).

To solve the inhomogeneity problems of the porous silicon samples due to the structure of the cell, a new electrochemical cell was designed and fabricated: the bottom-wafer cell.

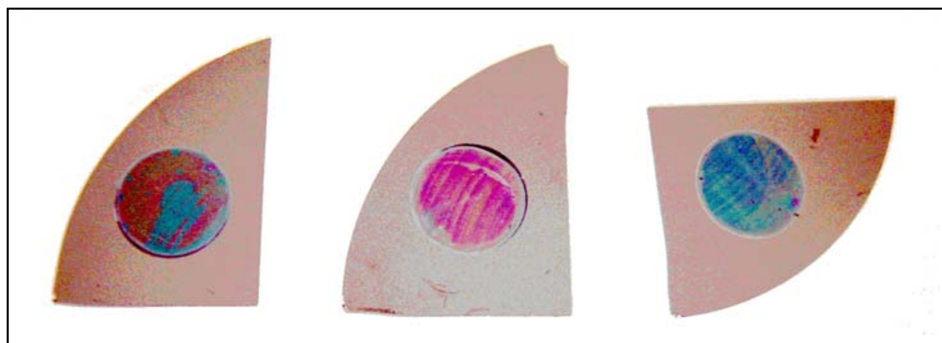

Fig. 5.4. Porous silicon layers fabricated with the lateral-wafer cell. The inhomogeneity of the etched area can be observed at first sight as the color varies indicating that either the porosity and/or the thickness of the layer changes.

5.1.1.2. Bottom-wafer electrochemical cell

The inhomogeneity problems of the former cell were mainly due to the lack of bubble removal on the surface of the wafer. This removal was hindered by the shape of the cell. To solve this problem, six structural variations have been introduced to the electrochemical cell design, as can be seen in Fig. 5.5a:

i) The cell body is a cylindrical-section recipient that facilitates the renovation of the electrolyte with the stirrer. Besides, the walls of the hole at the bottom of the recipient, realized for the contact of the electrolyte with the wafer, are not vertical but tilted to facilitate the renovation of the electrolyte and the removal of the bubbles on the surface of the wafer.

UNIVERSITAT ROVIRA I VIRGILI
DESIGN, FABRICATION AND CHARACTERIZATION OF POROUS SILICON MULTILAYER OPTICAL DEVICES
Elisabet Xifré Pérez
ISBN: 978-84-691-0362-3/DL: T.2181-2007

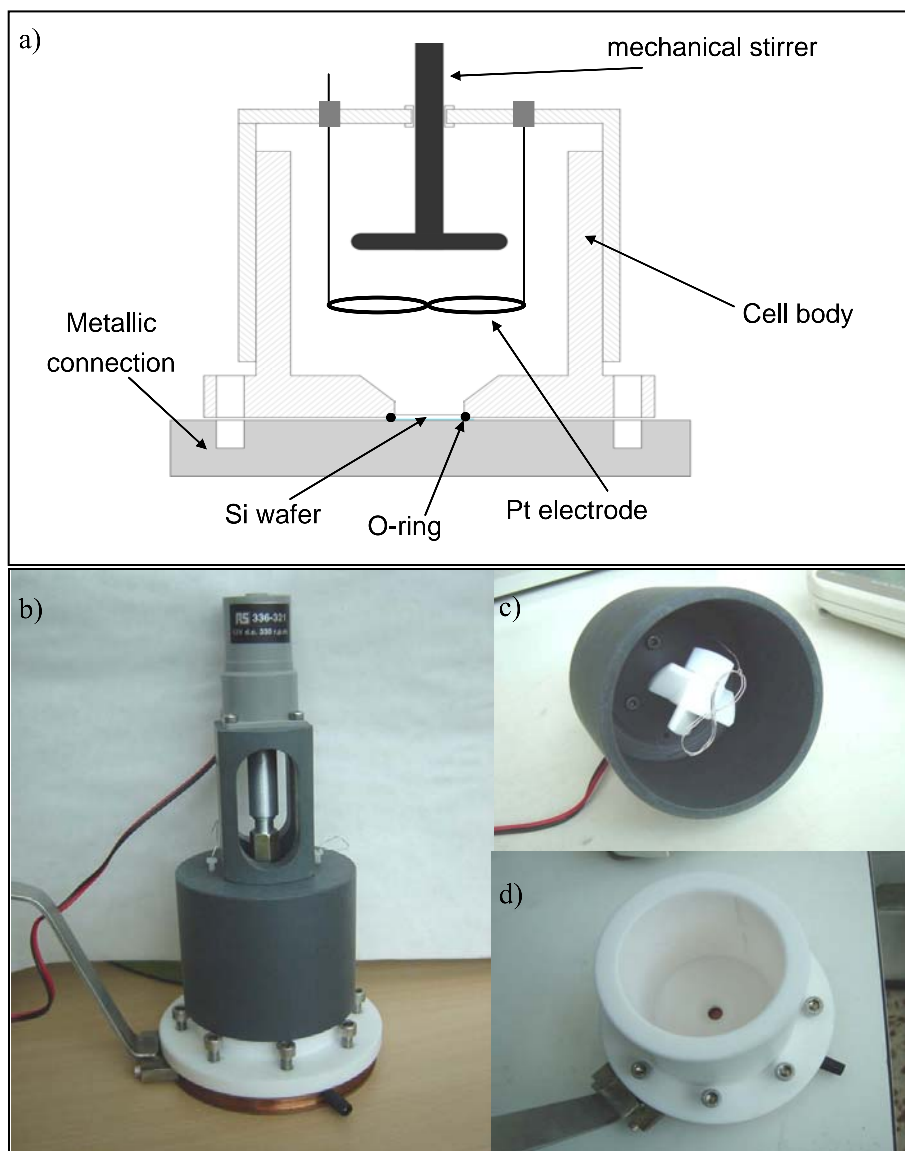

Fig. 5.5. Bottom-wafer cell designed and fabricated for the formation of porous silicon a) schematic of the cross sectional view b) photograph of the fabricated cell, c) view of the stirrer and the Pt electrode, d) view of the inside part of the cell body.

UNIVERSITAT ROVIRA I VIRGILI
DESIGN, FABRICATION AND CHARACTERIZATION OF POROUS SILICON MULTILAYER OPTICAL DEVICES
Elisabet Xifré Pérez
ISBN: 978-84-691-0362-3/DL: T.2181-2007

ii*)* The stirrer here is mechanic and larger. Its shape has been specially selected to stir the electrolyte from bottom to top. The stirrer rotates because of a continuous motor. The rotation velocity is selected by adjusting the DC voltage applied to the motor.

iii) The wafer is situated at the bottom of the cell. With this variation, the bubbles formed on the surface are removed due to the stirrer effects and with the help of the gravity.

iv) The volume of the cell has been reduced. The dimensions of the cell are the smallest ones for the dimensions of the stirrer and the cathode. By this way, the quantity of electrolyte to stir is the lowest possible (around 200 ml in our case).

v) The back-side contact of the wafer is a copper disk instead of a ring. The disk enables a uniform contact on the whole area of the wafer. The copper disk has to be cleaned in order to remove the oxide film that is formed on it after many etching processes.

vi) The shape of the platinum cathode does not influence on the homogeneity of the samples, on the contrary, the distance between the wafer and the cathode does. If the distance is too short, the porous layers are inhomogeneous. It is from a certain distance when the samples are homogenous. It is preferable not to choose an excessively great distance since this implies that the height of the cell will increase, increasing therefore the amount of electrolyte to stir. In the case of our cell, about 4 cm is enough.

This new cell design enables the fabrication of homogeneous porous silicon monolayers and multilayers, as will be demonstrated with the characterization process realized with spectroscopic ellipsometry (see chapter 6). A photograph of the bottom-wafer cell can be observed in Fig. 5.5b.

The homogeneity of the porous silicon layers obtained with this electrochemical cell can be observed at first sight in Fig. 5.6a where it can be observed that the etched area of the layers presents a homogeneous color. The cross-section SEM image of one of the layers presented in Fig. 5.6a can be observed in Fig. 5.6b and Fig. 5.6c, where two different points of the same

ISBN: 978-84-691-0362-3/DL: T.2181-2007

section have been measured and the thickness is labeled. It can be observed that the thickness of the layer at the two different and separated points is the same.

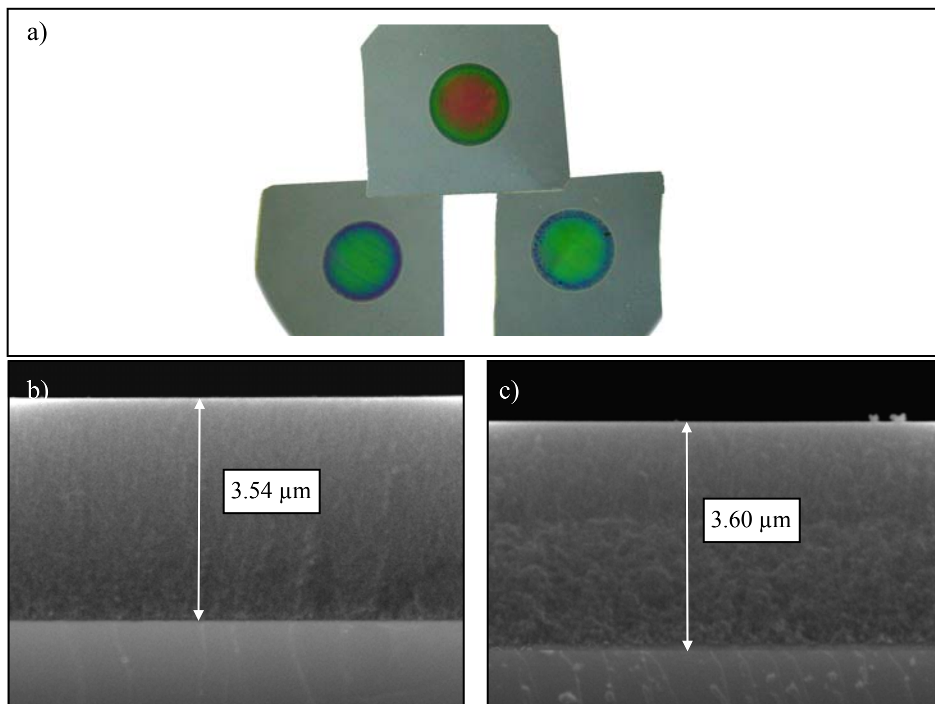

Fig. 5.6. a) Porous silicon layers fabricated with the bottom-wafer cell. The color of the etched area is very homogeneous at first sight indicating the homogeneity of the layer. b and c) SEM images of a porous silicon monolayer obtained with the bottom-wafer cell. Two different points of the same cross section are shown and their thickness is labeled.

5.1.2. Source for growth control

The process of pore growth can be realized either by controlling the anodic current or the potential. The most widely used method is the current control, because it allows a better control of the porosity, thickness and reproducibility of the porous silicon layer. For our fabrication system we have

UNIVERSITAT ROVIRA I VIRGILI
DESIGN, FABRICATION AND CHARACTERIZATION OF POROUS SILICON MULTILAYER OPTICAL DEVICES
Elisabet Xifré Pérez
ISBN: 978-84-691-0362-3/DL: T.2181-2007

realized current control using two different sources: a voltage source and a current source. The conclusions obtained with each of these two types of source are explained in the next subsections.

5.1.2.1. Voltage Source

The voltage source used for the system was an Agilent E3631A DC Power Supply. It was a part of the self-controlled system where two digital multimeters Agilent 34401A were used for the measurement and control of the voltage and current during the fabrication process. The measurements from the multimeters allowed the system to readjust the output of the voltage source continuously.

The only drawback of this system was the time that it needed to readjust the voltage source, the so-called response time of the system. This time was mainly due to the time needed by the multimeters to make a measurement and to communicate via GPIB with the computer. The response time of the system was about 400-500 ms and it affected the formation of the porous layers in two different ways:

- The transitions between two layers with different porosity were not rapid enough provoking an additional roughness between two porous layers with different porosity.
- The main problem appeared at the surface of the porous layer. The system required about 1 s during the beginning of the fabrication process to adjust the initial voltage. In microporous silicon growth, where the etching rate is very fast, this initialization time produced a residual porous layer, whose thickness and porosity depended on the initial conditions. In Fig. 5.7 the SEM image of a sample obtained with this system is shown, where the residual layer, created during the first seconds of the anodization process can be observed at the surface of the porous sample.

UNIVERSITAT ROVIRA I VIRGILI
DESIGN, FABRICATION AND CHARACTERIZATION OF POROUS SILICON MULTILAYER OPTICAL DEVICES
Elisabet Xifré Pérez
ISBN: 978-84-691-0362-3/DL: T.2181-2007

Although porosity was quite homogeneous within a layer and the response time was the only drawback of the voltage source system, this problem was important enough to lead us to use the current control.

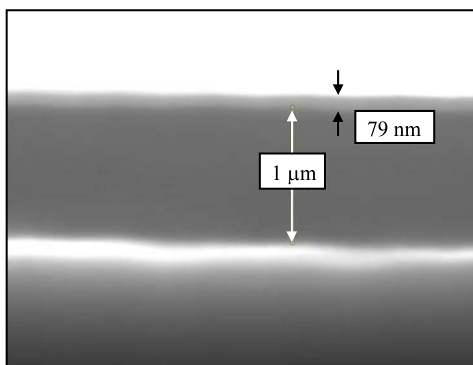

Fig. 5.7. SEM image of a monolayer obtained with the voltage source system. Its total thickness is 1 µm. We can also observe the residual layer created during the system adjust with a thickness 79 nm. The reflectivity spectrum of this sample measured with the FTIR also indicated that it is not a monolayer, but more that one layer was formed.

5.1.2.2. Current Source

The current source used for the fabrication system was a Keithley 2420 SourceMeter. This source enables a perfect control of the time and current applied during the growth and avoids the additional roughness between different porosity layers due to the response time of the system.

The homogeneity of a layer obtained with the current control can be observed in Fig. 5.8 where we can see that there is no residual layer at the upper part of the monolayer. For this reason, all the porous silicon layers presented in the next sections have been fabricated using this current source system.

ISBN: 978-84-691-0362-3/DL: T.2181-2007

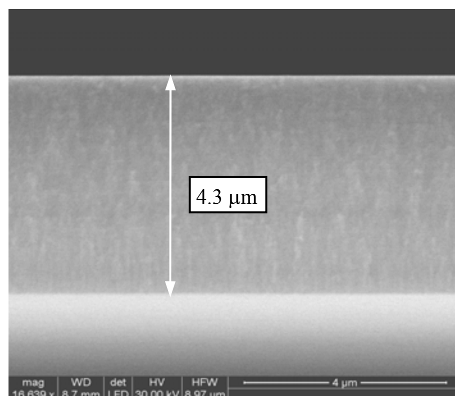

Fig. 5.8. SEM image of a porous silicon monolayer obtained using the current source. It is a homogeneous layer with thickness 4.3 μm.

5.1.3. Control Program

The fabrication process is completely controlled by a computer program. This program is a LabView virtual instrument realized to control the fabrication process of monolayers and multilayers of porous silicon with a very user-friendly interface. The program controls via GPIB the different elements of the system.

The main window of the program can be observed in Fig. 5.9. The user only has to introduce three data to the program:

- ***Input File***: the path of the text file where the steps of current are defined, that is where the current profile is determined.
- ***Output File***: the path of the text file where the program will write the measures realized during the fabrication process. This file is very useful for the user because it permits the comparison between the steps defined by the user and the steps applied by the system.
- ***Delay***: the time between two consecutive measures.

The input file is a text file defined by the user with all the current steps and the duration time of each step. It is a very simple file where the first column is the duration time of the step and the second column is the current that must

ISBN: 978-84-691-0362-3/DL: T.2181-2007

be applied. Each row corresponds to a layer of the multilayer (or monolayer if only one step is defined).

The rest of elements of the program window indicate the data obtained during the fabrication process:

- ***Graph***: Shows the current determined by the user and the current measured during the fabrication process in order to check if the process has been realized correctly.
- Arrays ***Time*** and ***I measured***: The values plotted in the graph can also be read here numerically.
- ***# Measured Points***: the number of measures that will be done during the formation process. It is calculated by the program from delay value introduced by the user.
- ***Error***: Indicates if there has been any problem with the Source or the measurements during the fabrication process.

Fig. 5.9. Main window of the program that controls the fabrication process of porous silicon.

UNIVERSITAT ROVIRA I VIRGILI
DESIGN, FABRICATION AND CHARACTERIZATION OF POROUS SILICON MULTILAYER OPTICAL DEVICES
Elisabet Xifré Pérez
ISBN: 978-84-691-0362-3/DL: T.2181-2007

5.1.4. Electrolyte

The electrolyte used for the fabrication of porous silicon is an aqueous dilution of hydrofluoric acid (HF). The dilution is necessary due to the hydrophobic character of the clean silicon surface. In fact, ethanoic solutions infiltrate the pores, on the contrary pure aqueous HF solutions do not. This is very important for the lateral homogeneity and the uniformity of the porous silicon layer in depth. Moreover, the lateral homogeneity and the surface roughness can be reduced increasing the electrolyte viscosity [86].

The electrolyte that we have used for the fabrication of our porous silicon samples is composed of high purity hydrofluoric acid (HF) in 40% aqueous solution diluted in ethanol. We have used the electrolyte with approximately 15% concentration of HF. This concentration was chosen because many works have used it [48,176,135] and in [19] is considered to give a large porosity variation.

The importance of the use of ethanol for the dissolution has also been observed during the tests made for the starting of the fabrication process. It is well known that during the reaction there is a hydrogen release and bubbles are formed on the surface of the silicon wafer. In the beginning of the work, the aqueous HF was diluted in water instead of ethanol. The number of bubbles formed with this dissolution was so high that they produced high variations of voltage between anode and cathode, and resulting in a very inhomogeneous sample. The formation of bubbles during the growth was drastically reduced when ethanol was used for the dissolution instead of water. We have checked that with ethanol, the potential between anode and cathode does not vary during the growth of the porous layers.

5.1.5. Silicon wafers and sample preparation

During realization of this work, the wafers used for the formation of microporous silicon are p-type silicon wafers doped with boron. The use of p-type wafers instead of n-type wafer permits us not to use back-side illumination for the generation of minority carriers (see chapter 2).

UNIVERSITAT ROVIRA I VIRGILI
DESIGN, FABRICATION AND CHARACTERIZATION OF POROUS SILICON MULTILAYER OPTICAL DEVICES
Elisabet Xifré Pérez
ISBN: 978-84-691-0362-3/DL: T.2181-2007

The resistivity of the wafer influences on the hardness/toughness of the microporous structure. At the beginning of this work, the growth of porous silicon was realized with three different resistivity wafers: 5-7 Ω, 1-10 Ω, and 10-20 mΩ. The two former ones are considered high resistivity wafers whereas the latter is a low resistivity wafer.

The porous silicon layers obtained with the high resistivity wafers (low doped) were very fragile, the surface of the wafer was very rough and some parts of the etched zone detached from the wafer either during the fabrication process or during the drying process. These results were obtained even for very low current densities (5 or 10 mA/cm^2). One of these porous wafers obtained with low doping substrates can be observed in Fig. 5.10a.

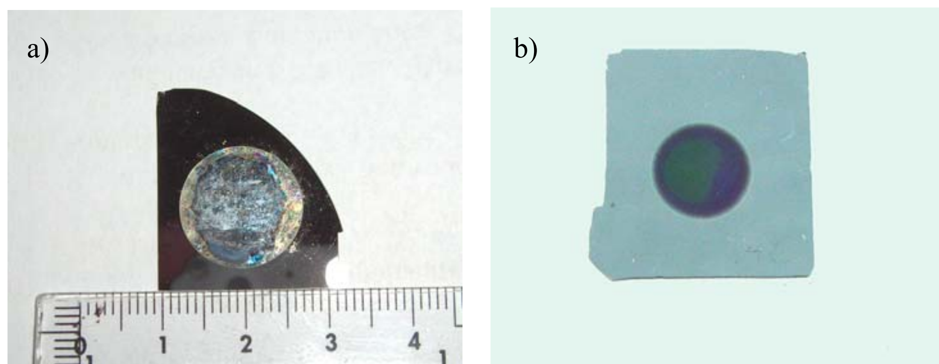

Fig. 5.10. Photograph of two porous silicon layers obtained with (a) a low doping silicon (b) a high doping silicon wafer.

On the contrary, the porous silicon layers obtained with low-resistivity wafers (high-doped) are strong and robust and their surface is flat, as can be seen in Fig. 5.10b. Furthermore, the very low resistivity of these wafers enables a good contact between the wafer and its back-side metallic connection (copper disk), without the need of a high dose implantation on the back surface of the

UNIVERSITAT ROVIRA I VIRGILI
DESIGN, FABRICATION AND CHARACTERIZATION OF POROUS SILICON MULTILAYER OPTICAL DEVICES
Elisabet Xifré Pérez
ISBN: 978-84-691-0362-3/DL: T.2181-2007

wafer. For these reasons, this type of wafers has been used for the fabrication of the porous silicon layers presented in this work.

The preparation of the silicon wafer for the porous silicon fabrication is very simple. Microporous silicon consists of the growth of disordered pores in the silicon wafer, therefore no lithography or preparation of the wafer is required. The preparation of the silicon wafer before the etching process is reduced to the removal of the oxidation of the wafer surface due to ambient conditions. This oxidation is easy to eliminate by immersing the wafer in low concentration (5 %) HF solution for a few minutes.

Drying of the porous silicon samples

Once the porous silicon has been formed, the etched wafer has to be dried. Due to large capillary stress, drying of samples is a critical step and can result in extended cracking if special procedures are not followed. Methods to reduce or eliminate the capillary stress include pentane drying, supercritical drying, freeze drying and slow evaporation rates.

Pentane drying is the easiest to implement. Pentane has a very low surface tension, and shows no chemical interaction with porous silicon (unlike ethanol). Using pentane as drying liquid enables to reduce strongly the capillary tension, but since water and pentane are non-miscible liquids, ethanol or methanol have to be used as intermediate liquids. Using this drying technique porous silicon layers with high porosity exhibit no cracking pattern after drying. All the porous silicon samples realized during this work have been dried with pentane.

ISBN: 978-84-691-0362-3/DL: T.2181-2007

5.1.6. Fabrication of porous silicon monolayers and multilayers

As all the elements of the fabrication system and their utility have been explained in the previous subsections, we can summarize the fabrication process of porous silicon monolayers talking about these elements. In the electrochemical cell, the surface of a silicon wafer, contacted on the back, is in contact with the electrolyte. After applying a current, controlled by the current source, between the wafer backside contact and the electrode in the electrolyte, a pore growth by silicon dissolution starts. The figure with the whole system has been presented in Fig. 5.1. The current density determines the porosity of the porous silicon layer and the time that it is applied determines the thickness of the layer.

The formation of multilayer structures of porous silicon opens a broad range of applications, some of them simulated and designed in chapters 3 and 4. The main advantage of porous silicon multilayers is the almost free combination of layers with different porosity and thickness because these two parameters can be easily determined during the formation process of porous silicon.

There are two main ways of producing porous silicon multilayers [177,92]: by periodically varying the etching parameters, such as for example the current density; or by using periodically doped substrates and maintaining constant the various etching parameters. All the multilayers fabricated during this work have been obtained with the first method, that is varying the etching parameters and using homogenously doped substrates. This method is used by almost all the other authors that fabricate porous silicon multilayers [39,81,178,179].

This method is based onto the following statements:

- the etching process is self-limited (once a porous layer is formed, the electrochemical etching of this layer stops).
- the etching occurs mainly in correspondence of the pore tips.
- the porosity depends only on the current density once the other etching parameters are kept fixed.

ISBN: 978-84-691-0362-3/DL: T.2181-2007

The application of a current density during a certain time results in the formation of one layer. A change of the current density yields the variation of porosity and as a result another layer with different refractive index is formed during the application of this second current density. In Fig. 5.11 we can observe the schematic of the growth of a porous silicon multilayer.

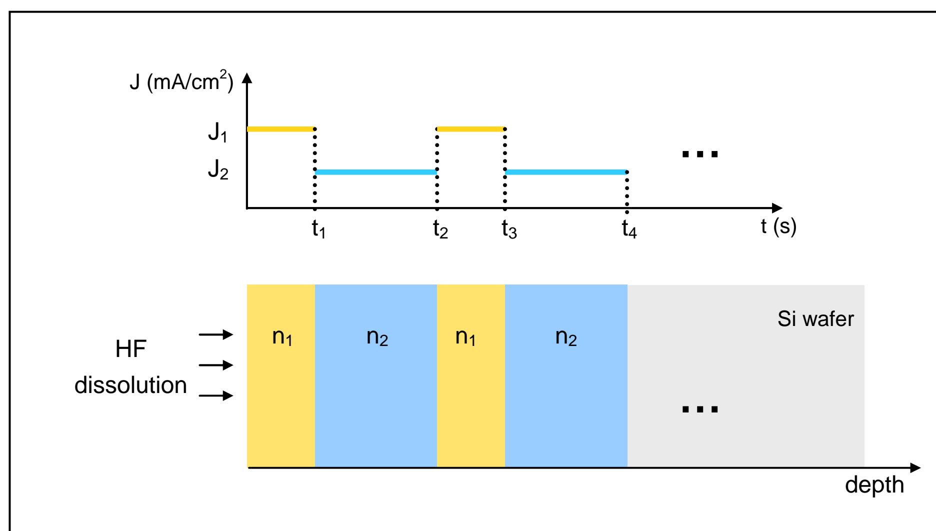

Fig. 5.11. Schematic of the formation process of a porous silicon multilayer (top) the time dependence of the current density (bottom) the formed porous silicon layer for each current density.

Hence, we can conclude that the variation of the current density during the etch process leads to the variation of the refractive index (porosity) in the etching direction only at the etch front. We can say that the current-versus-time profile is transferred to the porosity-versus-depth profile, that is refractive index-versus-depth profile.

This procedure has been used for the formation of all the multilayers fabricated during this thesis. Fig. 5.12 shows the SEM image of a multilayer formed by the periodic repetition of two layers with different refractive index.

UNIVERSITAT ROVIRA I VIRGILI
DESIGN, FABRICATION AND CHARACTERIZATION OF POROUS SILICON MULTILAYER OPTICAL DEVICES
Elisabet Xifré Pérez
ISBN: 978-84-691-0362-3/DL: T.2181-2007

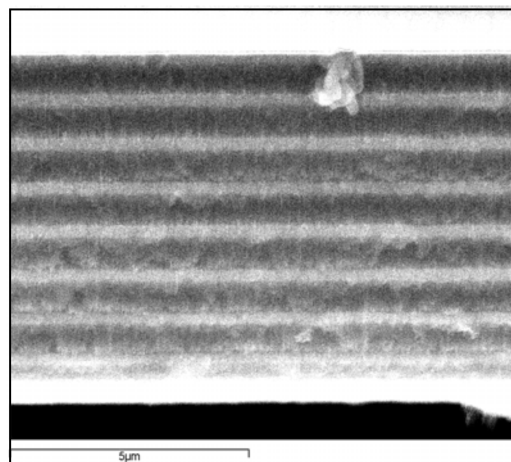

Fig. 5.12. SEM image of one of the fabricated porous silicon multilayers consisting of two layers with different refractive index repeated periodically.

5.2. Characterization of porous silicon layers

Once implemented the fabrication system, several porous silicon layers (monolayers and multilayers) have been fabricated. These layers have been measured with different techniques: Scanning electron microscopy, Fourier Transform Infrared Spectroscopy and Spectroscopic Ellipsometry. By processing these measurements, we can obtain different characteristics like the refractive index, thickness, anisotropy, etc.

This section is divided in two different parts. The first part is devoted to a brief explanation of the different techniques used for the measurement of the porous layers. The second part explains the two methods used for processing these measurements for determining the two main features of porous silicon layers: refractive index and thickness.

UNIVERSITAT ROVIRA I VIRGILI
DESIGN, FABRICATION AND CHARACTERIZATION OF POROUS SILICON MULTILAYER OPTICAL DEVICES
Elisabet Xifré Pérez
ISBN: 978-84-691-0362-3/DL: T.2181-2007

5.2.1. Measurement techniques

5.2.1.1. Scanning Electron Microscopy

The Scanning Electron Microscope (SEM) is a microscope that uses electrons rather than light to form an image. Some advantages of the SEM are the large depth of field, which allows a large amount of the sample to be in focus at a given time. The SEM also produces images of high resolution, which means that closely spaced features can be examined at a high magnification. Preparation of the samples is relatively easy since, most SEMs only require the sample to be conductive. The combination of higher magnification, larger depth of focus, greater resolution, and ease of sample observation makes the SEM one of the most widely used instruments in research areas today.

The SEM is an appropriate method to observe porous silicon layers. It is very useful for the determination of the structure, size and shape of the pores [41], especially for meso and macroporous silicon. For microporous silicon, the SEM image of the cross section of a porous silicon layer shows the porous zone clearly distinguished from the substrate [44,176]. For this reason it has been used for the thickness estimation of our monolayers.

SEM images present different gray levels depending on the porosity of the layers [39,180]. For this reason, the thickness of the different layers of a multilayer can be measured. It has also been used for evaluating the homogeneity of the porous silicon layers, for analyzing the interfaces, for observing the roughness between different porous layers and for the calculation of the etching rate [79,115,92,181]. Fig. 5.13 shows the SEM image of a porous silicon multilayer where the different layers can be clearly seen.

ISBN: 978-84-691-0362-3/DL: T.2181-2007

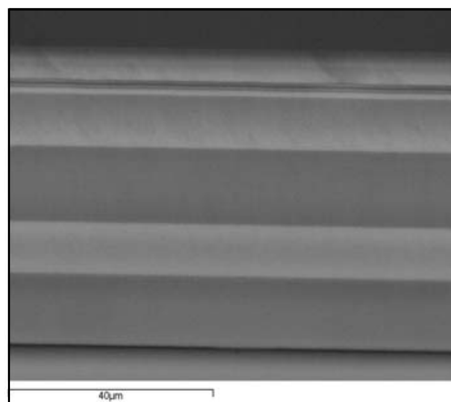

Fig. 5.13. SEM image of a porous silicon multilayer. It consists of two layers with different refractive index repeated two times.

5.2.1.2. Fourier Transform Infrared Spectroscopy

A Fourier Transform Infrared (FTIR) Spectrometer is a spectral instrument that collects and digitizes the interferogram, performs the FT function and displays the spectrum. Basically, the FTIR illuminates the sample and calculates the reflected, transmitted or absorbed light for a wavelength range [80]. It is used for the optical characterization of layers [39,80,98182-184].

The FTIR spectrometer used for the measurement of our porous silicon samples is a Bruker Vertex 70. The photograph of the spectrometer can be observed in Fig. 5.14. The spectra obtained with the FTIR, that have been used for the analysis of the porous layers, are the reflectivity and the transmission spectra for the wavelength range from 1 to 4 μm.

UNIVERSITAT ROVIRA I VIRGILI
DESIGN, FABRICATION AND CHARACTERIZATION OF POROUS SILICON MULTILAYER OPTICAL DEVICES
Elisabet Xifré Pérez
ISBN: 978-84-691-0362-3/DL: T.2181-2007

Fig. 5.14. Photograph of the FTIR spectrometer Bruker Vertex 70 used for the measurement of the porous silicon layers. The setup for the measurement of the reflectivity spectrum is placed.

5.2.1.3. Spectroscopic Ellipsometry

Spectroscopic Ellipsometry is a non-destructive optical technique widely used that measures the polarization of the light reflected on the surface of a sample in a wavelength range [185]. The ellipsometric measurements are evaluated to obtain the complex refractive index (n and extinction coefficient k), the interface roughness, the thickness and the composition of films [186]. One of the most widely used evaluation methods is the Bruggemann Effective Medium Approximation (EMA) [187-190].

For porous silicon layers, we have used ellipsometry to determine the optical properties of the layers and the substrate [79,187,191,192]. The thickness and refractive index of monolayers and multilayers have been calculated and the porosity of the layers, very difficult to determine with the other methods, has been estimated. Besides, the anisotropy of porous silicon layers with different porosity has been analyzed.

The complete analysis and characterization of the porous silicon layers realized with ellipsometry is extensively explained in chapter 6.

ISBN: 978-84-691-0362-3/DL: T.2181-2007

5.2.1.4. Atomic Force Microscopy

Another technique widely used for the analysis of porous silicon layers is the Atom Force Microscopy (AFM). AFM images are obtained by measurement of the force on a sharp tip (insulating or not) created by the proximity to the surface of the sample. This force is kept small and at constant level with a feedback mechanism. When the tip is moved sideways it will follow the surface contours [193]. By this way, three dimensional images of the surface of the samples are obtained.

The AFM studies are focused on the characterization, at nanometric scale, of the porous silicon layers, specially used for the study of layer inhomogeneities [194], surface roughness of the substrate [195], and morphology of porous silicon [196-199]. For many studies, AFM is applied together with another optical characterization or morphological technique. [200-203].

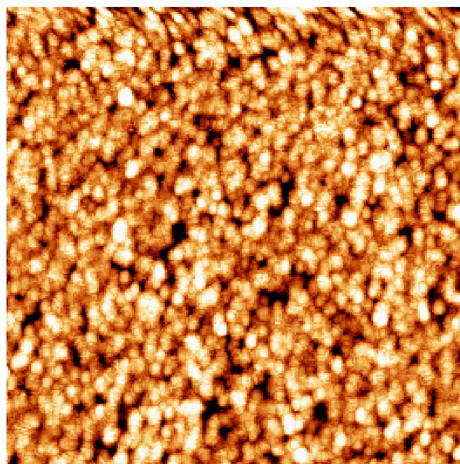

Fig. 5.15. AFM image of the surface of a porous silicon monolayer.

UNIVERSITAT ROVIRA I VIRGILI
DESIGN, FABRICATION AND CHARACTERIZATION OF POROUS SILICON MULTILAYER OPTICAL DEVICES
Elisabet Xifré Pérez
ISBN: 978-84-691-0362-3/DL: T.2181-2007

For our porous silicon layers, the AFM has been used for the study of the surface of the porous layers. Fig. 5.15 shows the AFM image of a porous silicon layer. These layers will be used in the near future as templates for the fabrication of liquid crystal photonic crystals where the knowledge of the surface contour of the layer is very important.

5.2.2. Mathematical methods for the determination of the refractive index and thickness

Each of the two mathematical methods explained here for the calculation of the refractive index and thickness use some of the measurements explained in the previous section. For the comparison of both methods, these characteristics are calculated for an example porous silicon monolayer and, at the end of this section, these results are evaluated.

5.2.2.1. Measurement of interference fringes

A very simple method for evaluating the refractive index of a film material is to measure the interference fringes, resulting from multiple reflections, to obtain the optical thickness. This method has been used by different authors only for normal incidence [19,103]. Here we develop the expressions for the refractive index calculation for any incidence angle.

Fig. 5.16 shows a typical arrangement for thin-film interference. Light traveling from one medium with refractive index n_0 encounters a thin film with refractive index n. Some of the light is transmitted through the film and some other is reflected. Thin film interference involves interference between light reflecting from the top surface of the film and light reflecting from the bottom surface of the film. For the case of porous silicon layers, the incident medium is air, being its refractive index n_0=1.

UNIVERSITAT ROVIRA I VIRGILI
DESIGN, FABRICATION AND CHARACTERIZATION OF POROUS SILICON MULTILAYER OPTICAL DEVICES
Elisabet Xifré Pérez
ISBN: 978-84-691-0362-3/DL: T.2181-2007

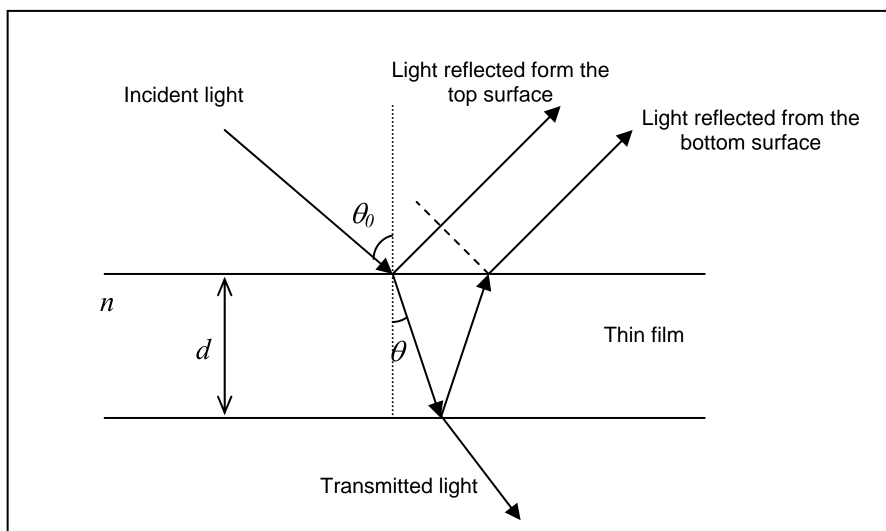

Fig. 5.16. Schematic of the light beam reflection when it arrives to a thin film with thickness *d* and refractive index *n* with an incident angle θ_0.

The reflectivity spectrum of the film is characterized by the multiple interference fringes caused by the air-porous silicon and porous silicon-silicon interfaces. By assuming that the porous silicon film has parallel surfaces and that the refractive index is a smooth function of the wavelength, it is possible to deduce from the wavelength position of adjacent reflectance maxima the value of the refractive index [204]. The condition for a constructive interference is:

$$2nd\cos\theta = m\,\lambda_m \qquad \text{for } m=0,1,2,\ldots \tag{5.1}$$

Therefore the expressions for two consecutive maxima are:

$$m = \frac{2nd\cos\theta}{\lambda_m} \quad \text{and} \quad m+1 = \frac{2nd\cos\theta}{\lambda_{m+1}} \tag{5.2}$$

ISBN: 978-84-691-0362-3/DL: T.2181-2007

From these two expressions we obtain:

$$2nd\cos\theta\left(\frac{1}{\lambda_{m+1}}-\frac{1}{\lambda_m}\right)=1 \tag{5.3}$$

Instead of θ we express Eq. (5.4) in terms of the incidence angle θ_0, applying Snell's law:

$$n\sqrt{1-\sin^2\theta}=n\sqrt{1-\frac{\sin^2\theta_0}{n^2}}=\left[2d\left(\frac{1}{\lambda_{m+1}}-\frac{1}{\lambda_m}\right)\right]^{-1} \tag{5.4}$$

The resulting expression of the refractive index n for any incidence angle θ_0 is:

$$n=\sqrt{\sin^2\theta_0+\left[2d\left(\frac{1}{\lambda_m}-\frac{1}{\lambda_{m+1}}\right)\right]^{-2}} \tag{5.5}$$

where θ_0 is the incidence angle, λ_m is the wavelength of the mth maximum of the reflectivity spectrum and d is the thickness of the monolayer.

Equation (5.5) has been used for the calculation of the refractive index of all the monolayers fabricated during this work. To apply this equation, two different measurements were realized to the monolayers. First, the reflectivity spectrum was measured for different angles of incidence with the Fourier Transform Infrared (FTIR) Spectrometer Bruker Vertex 70. By this way, the wavelengths corresponding to maximum reflectivity were determined. Fig. 5.17a shows the reflectivity spectrum of a monolayer fabricated by applying J=20 mA/cm^2 for 120 s. It was measured for incidence angle θ_0=12º and the different interference fringes can be observed.

The second value required for the application of Eq. (5.5) is the thickness of the monolayer, measured with SEM. In Fig. 5.17b the SEM image of the monolayer with the reflectivity spectrum shown in Fig. 5.17a can be observed.

UNIVERSITAT ROVIRA I VIRGILI
DESIGN, FABRICATION AND CHARACTERIZATION OF POROUS SILICON MULTILAYER OPTICAL DEVICES
Elisabet Xifré Pérez
ISBN: 978-84-691-0362-3/DL: T.2181-2007

The refractive index of this monolayer has been calculated using Eq. (5.5). It varies from 1.97 to 1.83 for the wavelength range between 1 μm and 4 μm, which demonstrates that the refractive index of porous silicon within this wavelength range is not constant (for more details see section 5.3.1).

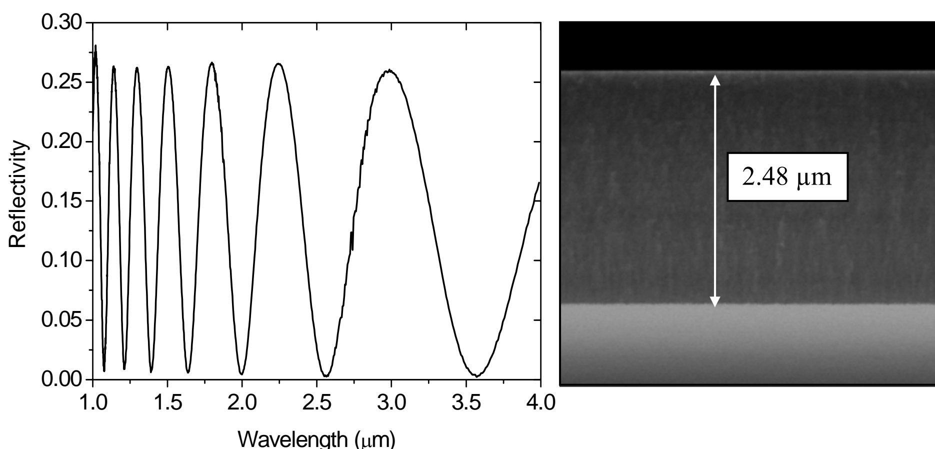

Fig. 5.17. (a) Reflectivity spectrum of a porous silicon monolayer obtained with J=20 mA/cm^2 and t=120 s, for θ_0=12º (b) SEM image of the cross section of the same porous silicon monolayer. Its thickness is 2.48 μm.

The main advantage of this method is that it is fast and easy. The main disadvantage is that the estimation of thickness with SEM is not very accurate, which can introduce an error of about 5% on the refractive index.

UNIVERSITAT ROVIRA I VIRGILI
DESIGN, FABRICATION AND CHARACTERIZATION OF POROUS SILICON MULTILAYER OPTICAL DEVICES
Elisabet Xifré Pérez
ISBN: 978-84-691-0362-3/DL: T.2181-2007

5.2.2.2. Spectrum analysis fitting

This is a procedure for the optical characterization of thin-film monolayers and stacks from spectrophotometric and/or ellipsometric data. It consists of a least-squares fitting of the simulated spectrum to a measured spectrum by assuming that the optical constants of the film follow a mathematical model [205]. With this method, the refractive index and the thickness of the monolayers are determined. The used program, inspired in this method, was developed by the Optical Characterization Group of the Universitat de Barcelona [206].

Two mathematical models can be used for the fitting of the measured data. One of them is the Cauchy model, useful for dielectric materials, far from the absorption band [204]. Cauchy's equation is an empirical relationship between the refractive index n and wavelength of light λ for a particular transparent material. The most general form of Cauchy's equation is:

$$\begin{aligned} n(\lambda) &= A + \frac{B}{\lambda^2} + \frac{C}{\lambda^4} \\ k(\lambda) &= De^{\frac{E}{\lambda}} \end{aligned} \tag{5.6}$$

where A, B, C, D, and E are coefficients (usually quoted for λ in micrometres) that can be determined for a material by fitting the equation to measured refractive indices at known wavelengths.

For porous silicon, the refractive index and the extinction coefficient can also be modelled with the Bruggemann Effective Medium Approximation (EMA), where it is assumed that the porous silicon layer is a mixture of the substrate silicon and air [207]. For this method, the dielectric constants of the components are named ε_i, f_i their volume fractions and y the screening parameter, the mathematical expression for the effective dielectric constant ε in terms of named ε_i, f_i and y is given (in implicit form) by

$$0 = \sum_i f_i \frac{\varepsilon_i - \varepsilon}{\varepsilon_i + y\varepsilon} \tag{5.7}$$

ISBN: 978-84-691-0362-3/DL: T.2181-2007

These methods enable the fitting of the reflectivity spectrum, obtained with the FTIR spectrometer; the fitting of the ellipsometric data, obtained with the ellipsometer, or the simultaneous fitting of both types of measured data.

The best fit can be obtained using simultaneously the reflectivity and the ellipsometric data. By this way, the optimal fit using measurements with two different techniques can be realized. In Fig. 5.18 and Fig. 5.19 the best fit obtained using both types of measured data can be observed for an example porous silicon layer. This monolayer was obtained by applying J=20 mA/cm^2 for 120 s. For this case the Cauchy model was applied. The values obtained with this simultaneous fitting are a refractive index varying from 1.92 at 0.9 μm wavelength to 1.85 at 4 μm and a thickness of 2.43 μm.

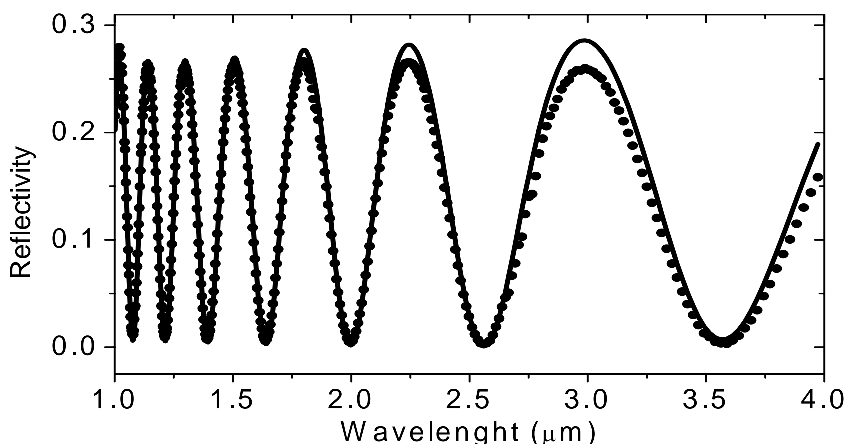

Fig. 5.18. Reflectivity spectrum of the porous silicon monolayer obtained with J=20 mA/cm^2 and t=120 s, measured with the FTIR spectrometer (symbols). The best least-squares fitted simulated spectrum is also shown (line).

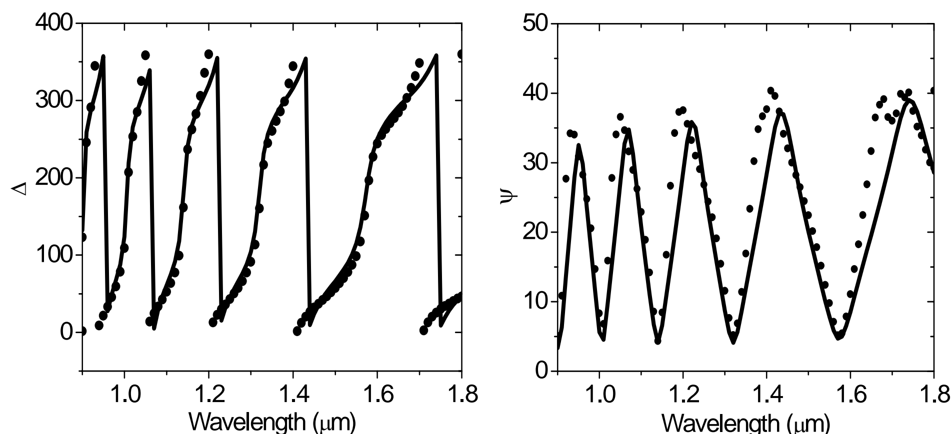

Fig. 5.19. Measured ellipsometric data Δ and Ψ (symbols) of the same porous silicon monolayer and the best least-squares fitted simulated ellipsometric data (line).

In Table 5.I we can compare the refractive indices obtained with the two explained methods, for this example porous silicon monolayer. The refractive index obtained with the Cauchy model agrees with the one calculated with the interference fringe method presented in the previous section. The thickness of the layer also agrees with the one determined with SEM. This agreement indicates that both methods are suitable for the calculation of the refractive index and thickness of porous silicon layers.

Method	Refractive index (for λ=0.9 - 4 μm)	Thickness (μm)
Interference fringes	1.97 - 1.83	2.48
Cauchy model	1.92 - 1.85	2.43

Table 5.I. Comparison of the refractive index and the thickness obtained with the method of the interference fringes and the Cauchy model. The porous silicon monolayer measured was obtained with J=20 mA/cm^2 for 120 s.

UNIVERSITAT ROVIRA I VIRGILI
DESIGN, FABRICATION AND CHARACTERIZATION OF POROUS SILICON MULTILAYER OPTICAL DEVICES
Elisabet Xifré Pérez
ISBN: 978-84-691-0362-3/DL: T.2181-2007

5.3. Calibration of the fabrication system (Anodization parameters)

We have seen that the two most important characteristics of a porous silicon layer are its refractive index and its thickness. These two physical characteristics of the layers depend on two different parameters of the anodization process: the current density and the anodization time respectively. Therefore, it is essential to determine the relation between the physical characteristics of the layers and the anodization parameters.

The calibration of the fabrication system establishes the current density-refractive index relation and the etching time-thickness relation for each current density. These relations are basic for the fabrication of the porous silicon multilayer devices studied and designed in chapters 3 and 4.

For the calibration of the fabrication process, several monolayers fabricated with different current densities and etch times have been characterized using the methods described in the previous section.

5.3.1. Current density - Refractive index relation

The current density applied during the formation process determines the porosity of the porous silicon layer, and consequently its refractive index. The higher the current applied the higher the porosity and, therefore the higher the quantity of air in the layer resulting in a lower refractive index.

For each current density applied, a porous silicon layer with different refractive index is obtained. In Fig. 5.20 we can see the relation current density-refractive index established from the measurements of the fabricated porous silicon monolayers. These refractive indices have been calculated using the measurement of interference fringes method. In Fig. 5.20 we can observe that the decrease of refractive index is exponential with the current density. These results agree with the ones presented in the literature [208].

UNIVERSITAT ROVIRA I VIRGILI
DESIGN, FABRICATION AND CHARACTERIZATION OF POROUS SILICON MULTILAYER OPTICAL DEVICES
Elisabet Xifré Pérez
ISBN: 978-84-691-0362-3/DL: T.2181-2007

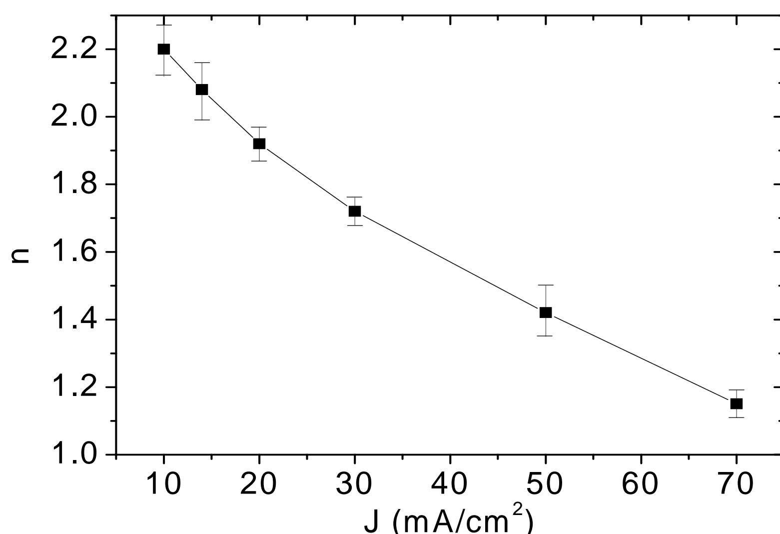

Fig. 5.20. Relation between current density and refractive index of porous silicon monolayers obtained with the bottom-wafer cell. The exponential dependence is also shown (black line). The bars indicate the variation of the refractive index for the wavelength range 1-4 μm.

The range of current densities studied goes from 10 to 70 mA/cm^2. Current densities higher than 70 mA/cm^2 yielded very fragile porous layers where frequently the etched area was slightly detached from the substrate. Current densities lower than 10 mA/cm^2 yielded porous layers with very slow etch rates, increasing the duration of the layer formation without a significant gain in the index. Besides, these layers can be hardly seen with SEM, which highly hinders their characterization. These considerations have been taken into account for the design of the fabricated multilayer devices presented in chapter 7.

The current density-refractive index relation in Fig. 5.20 permits us to calibrate the porous silicon formation system because it establishes the relation between the electric parameters (*J*) and the physical characteristics of the porous silicon layer (*n*). To complete the calibration of the fabrication system,

UNIVERSITAT ROVIRA I VIRGILI
DESIGN, FABRICATION AND CHARACTERIZATION OF POROUS SILICON MULTILAYER OPTICAL DEVICES
Elisabet Xifré Pérez
ISBN: 978-84-691-0362-3/DL: T.2181-2007

the knowledge of the relation anodization time-thickness is essential. This relation is analyzed in the next section.

The porous silicon multilayer structures fabricated during the realization of this thesis are designed to work in the wavelength range from 1 μm to 4 μm. Hence, the calibration of the fabrication system has been analyzed for this wavelength range. The refractive index of porous silicon is not constant within this wavelength range. This variation can be observed in Fig. 5.21 where the refractive index of a porous silicon monolayer is represented. It can be observed that the refractive index is higher for 1 μm and decreases until approximately 1.5 μm. From this wavelength on, the decrease of the refractive index is very slow, quite constant. This variation has been represented in Fig. 5.20 using the variation bars for each point.

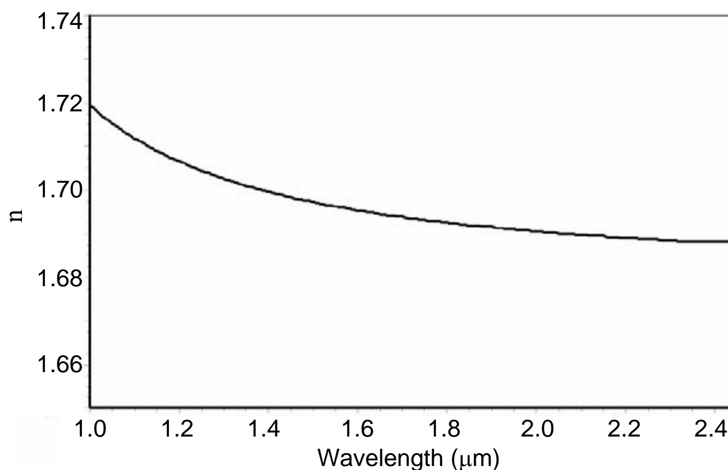

Fig. 5.21. Refractive index of a porous silicon layer simulated with a thin film EMA model for an example porosity of 35 %.

UNIVERSITAT ROVIRA I VIRGILI
DESIGN, FABRICATION AND CHARACTERIZATION OF POROUS SILICON MULTILAYER OPTICAL DEVICES
Elisabet Xifré Pérez
ISBN: 978-84-691-0362-3/DL: T.2181-2007

5.3.2. Current density - Porosity relation

One of the most important characteristics of a porous silicon layer is its porosity, defined as the fraction of air inside the porous layer. In fact, for the purpose of this thesis, the porosity of a layer is not an essential value but our essential parameter is the refractive index of the layer. As it has been explained before, for the simulation of any optical device the essential data of the layers that form the multilayer are the thickness and the refractive index, whereas the porosity is not used anywhere in the simulation and design process. Of course we know that the refractive index is determined by the porosity but for the simulation the concept porosity is completely invisible.

Similarly to simulation, for the fabrication the porosity is also "invisible" because the different methods used for the characterization of the porous silicon layers (interference fringes method and spectrum analysis fitting) calculate the refractive index and the thickness of the layers, not the porosity. However, here we present the relation between porosity and current density because it could be interesting for future applications of the porous silicon layers.

Fig. 5.22 the porosity-current density relation. These porosities have been calculated from the ellipsometric measurements (explained in chapter 7). In Fig. 5.22 we can observe that the porosity increases exponentially with the current density. The variation bars plotted for each current density are due to two different reasons. For $J<20$ mA/cm^2, we have concluded from the ellipsometric study that the porosity varies gradually in depth, being the porosity at the top of the monolayer higher than at the bottom of the monolayer. Therefore, the variation bars for these current densities indicate the top and the bottom porosity of the monolayer. For $J\geq20$ mA/cm^2, the pores of the porous silicon monolayers have not the same dimensions in all the directions, resulting in an anisotropic material. The variation bars for these current densities indicate these variations that are detailed explained in chapter 7.

UNIVERSITAT ROVIRA I VIRGILI
DESIGN, FABRICATION AND CHARACTERIZATION OF POROUS SILICON MULTILAYER OPTICAL DEVICES
Elisabet Xifré Pérez
ISBN: 978-84-691-0362-3/DL: T.2181-2007

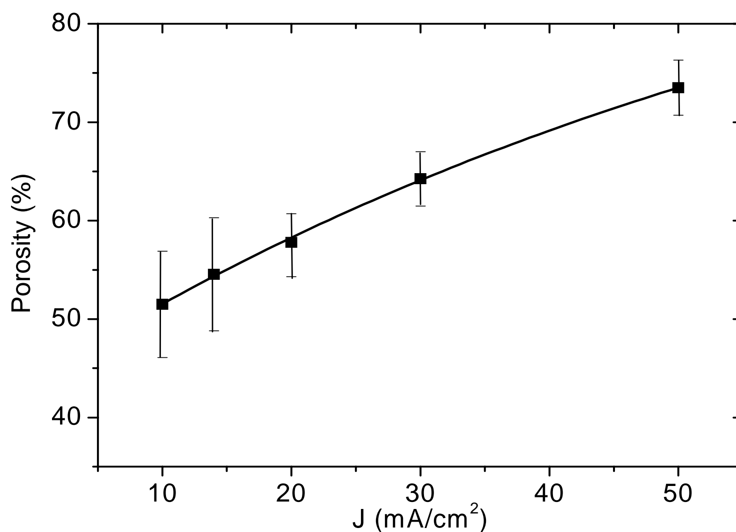

Fig. 5.22. Relation between porosity and current density. The exponential dependence is also shown (solid line).

5.3.3. Etching time - Thickness relation

The time during which a current density is applied is the etching time. It determines the thickness of the porous silicon layers. The anodization time-thickness relation for the fabricated porous silicon monolayers can be seen in Fig. 5.23, where the results for two different current densities are represented. It can be observed that it is a linear relation.

UNIVERSITAT ROVIRA I VIRGILI
DESIGN, FABRICATION AND CHARACTERIZATION OF POROUS SILICON MULTILAYER OPTICAL DEVICES
Elisabet Xifré Pérez
ISBN: 978-84-691-0362-3/DL: T.2181-2007

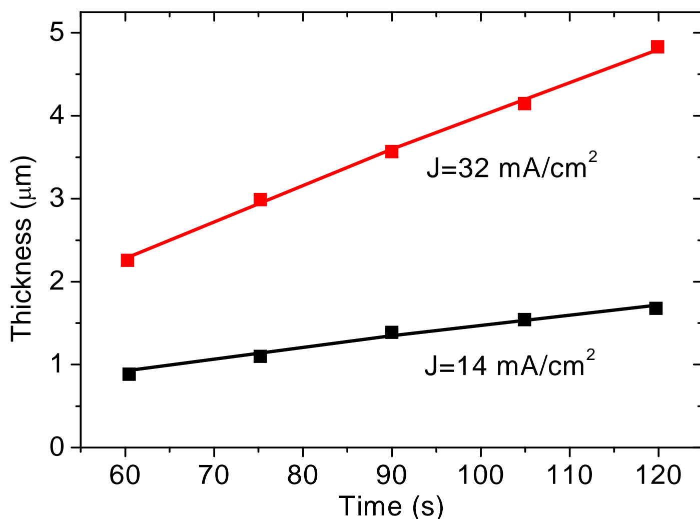

Fig. 5.23. Relation between the applied anodization time and the thickness of the monolayer, obtained for two different current densities (symbols). The lineal dependence is also shown (lines).

From this figure, we can also see that the slope is different for every current density and it increases when the current density increases. This slope let us define another formation parameter of porous silicon, the etch rate that is the velocity of formation of a layer with a certain porosity. In Fig. 5.24 the dependence of the etch rate with the current density is shown. From this figure we can conclude that the etch rate increases with the current density with exponential dependence. Another conclusion that we can obtain from Fig. 5.24 is that for high current densities, the fast etch rate hinders the fine control of the layer thickness. Also the precise control of the layer thickness is restricted by the "inertia" of the growth system.

UNIVERSITAT ROVIRA I VIRGILI
DESIGN, FABRICATION AND CHARACTERIZATION OF POROUS SILICON MULTILAYER OPTICAL DEVICES
Elisabet Xifré Pérez
ISBN: 978-84-691-0362-3/DL: T.2181-2007

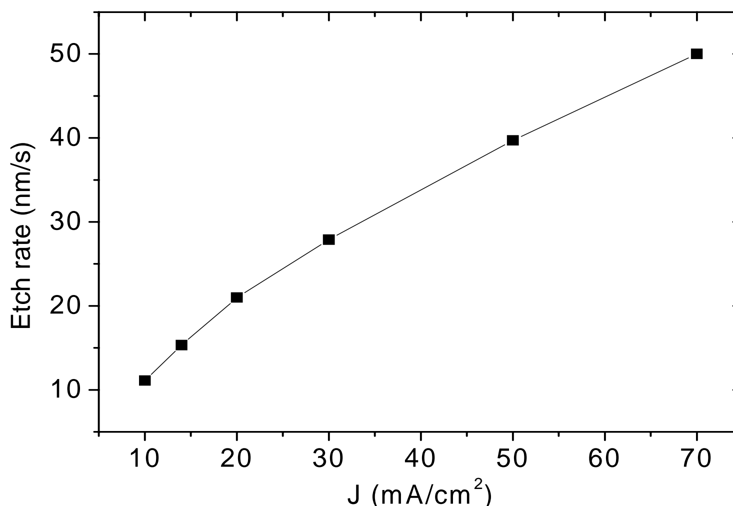

Fig. 5.24. Relation between de current density and the etch rate of porous silicon monolayers obtained with the bottom-wafer cell. The exponential dependence is also shown.

5.4. Conclusions

In this chapter we have explained two different processes: the fabrication and the characterization of the porous silicon layers.

The first part corresponds to the fabrication process and it explains in detail the porous silicon fabrication system established at the Department of Electronic, Electric and Automatic Engineering of the University Rovira i Virgili. The different elements that form this system have been presented and their influence on the porous silicon characteristics has been discussed. We have concluded that the structure of the electrochemical cell determines the homogeneity of the porous layers, being the most appropriate the cell where the silicon wafer is placed at the bottom and the electrolyte is stirred mechanically. The current source is another important element of the fabrication system because it determines the porosity and thickness of the porous silicon layers, and also the roughness of the interfaces. We have also concluded that the silicon wafers most suitable for the formation of microporous silicon are highly doped

UNIVERSITAT ROVIRA I VIRGILI
DESIGN, FABRICATION AND CHARACTERIZATION OF POROUS SILICON MULTILAYER OPTICAL DEVICES
Elisabet Xifré Pérez
ISBN: 978-84-691-0362-3/DL: T.2181-2007

p-type wafers (low resistivity). The rest of elements of the fabrication system are the electrolyte, being the one used an ethanol solution with 15 % HF concentration; and the control program realized for the control of the whole fabrication system, that has been also explained.

The characterization part is focused on the study of the fabricated porous silicon layers. The different measurement techniques used for the characterization of the fabricated porous silicon layers have been explained. These techniques are Scanning Electron Microscopy (SEM), Fourier Transform Infrared spectroscopy (FTIR) and Spectroscopic Ellipsometry (SE). From these measurements the two main characteristics of the porous silicon layers, refractive index and thickness, have been calculated using two different mathematical methods. The first is the interference fringes method that uses the SEM and the FTIR measurements to determine both refractive index and thickness. These two characteristics can also be calculated with the second method, the spectrum analysis fitting that uses the FTIR reflectivity spectrum and the ellipsometric measurements. The comparison of the results obtained with both methods indicates that both are equally suitable for the characterization of microporous silicon layers.

One of the applications of this characterization is the calibration of the fabrication system, that has permitted us to know well the system designed. This calibration has established the relations between the anodization parameters and the physical characteristics of the porous silicon layers, that are the current density-refractive index relation and the anodization time-thickness relation. The porosity has also been analyzed. We have concluded that the increase of the current density leads to an increase of the porosity and therefore a decrease of the refractive index. The relations of the current density with porosity and refractive index are both exponential. We have also concluded that the thickness increases linearly with the anodization time. From these values, we have also defined another parameter, the etch rate that is the velocity of formation of a porous silicon layer. The etch rate depends on the current density, basically it exponentially increases with current density.

UNIVERSITAT ROVIRA I VIRGILI
DESIGN, FABRICATION AND CHARACTERIZATION OF POROUS SILICON MULTILAYER OPTICAL DEVICES
Elisabet Xifré Pérez
ISBN: 978-84-691-0362-3/DL: T.2181-2007

Finally, the process for the fabrication of porous silicon multilayers has been explained. The values of the anodization parameters used for the formation of multilayers are based on the data given by the calibration process.

ISBN:978-84-691-0362-3 /DL: T.2181-2007

Chapter 6

Ellipsometric study of porous silicon layers

The ellipsometric study of porous silicon monolayers and multilayers is presented in this chapter. The objective of this study is to determine the main physical characteristics of these layers: porosity (and therefore refractive index) and thickness. These characteristics have been previously calculated with other methods and the comparison between those results and the results obtained with ellipsometry is also presented. In addition, spectroscopic ellipsometry allows the analysis of the anisotropy of the porous layers. This characteristic can not be analyzed by any of the previous characterization methods used, so ellipsometry provides this additional data for the knowledge of the fabricated porous silicon layers.

First, in this chapter, we briefly explain the theoretical concepts of spectroscopic ellipsometry. Next, we describe the equipment used for the ellipsometric measurements, the ellipsometer. The different steps followed for the characterization of the porous silicon layers are also explained. After that, we show the most relevant results obtained from ellipsometry, firstly the

UNIVERSITAT ROVIRA I VIRGILI
DESIGN, FABRICATION AND CHARACTERIZATION OF POROUS SILICON MULTILAYER OPTICAL DEVICES
Elisabet Xifré Pérez
ISBN:978-84-691-0362-3 /DL: T.2181-2007

ellipsometric study of fabricated porous silicon monolayers, and secondly the study of porous silicon multilayers consisting of a periodic repetition of two layers with different degrees of porosity. Finally, we present the conclusions obtained from our experiments.

6.1. Introduction to Spectroscopic Ellipsometry

Ellipsometry is an optical characterization technique based on the measurement of the polarization transformation that occurs after the reflection (or the transmission) of a polarized beam by a given sample [209]. Ellipsometry is a well known technique that has been currently practiced since the second half of nineteenth century and it is supported by a complete theoretical description [209].

When a beam of linearly polarized light of a known orientation is reflected at oblique incidence from a surface then the reflected light is elliptically polarized, for this reason the term ellipsometer was chosen. The shape and orientation of the ellipse depend on the angle of incidence, the direction of the polarization of the incident light, and the reflection properties of the surface.

Nowadays ellipsometry has many interesting applications. In particular, it is mainly used in semiconductor research and fabrication to measure the optical properties as well as the physical dimensions of complex systems such as multilayer stacks of thin films and the interfaces between those layers [210-214]. However, ellipsometry is also becoming more interesting to researchers in other disciplines such as biology and medicine [215,216]. These areas pose new challenges to the technique, such as measurements on unstable liquid surfaces and microscopic imaging [217-219].

Ellipsometry is sensitive to several material characteristics, such as layer thickness, optical constants (refractive index and extinction coefficient), surface roughness, composition, optical anisotropy; and is used to characterize both single layers and multilayer stacks [218,220,221].

UNIVERSITAT ROVIRA I VIRGILI
DESIGN, FABRICATION AND CHARACTERIZATION OF POROUS SILICON MULTILAYER OPTICAL DEVICES
Elisabet Xifré Pérez
ISBN:978-84-691-0362-3 /DL: T.2181-2007

6.1.1. Fundamentals of ellipsometry

All the expressions that will be mentioned from now on will be related to reflection ellipsometry. Anyway, broad information can be found in the literature [222,223] about the instrumentation and the mathematical formalism of transmission ellipsometry.

In both reflection and transmission ellipsometry, the direction of the incident and reflected beams determine the plane of incidence. To easily introduce the basic ellipsometric magnitudes and to generalize them, we will first consider the case of a plane wave whose electric field vector can be decomposed into two components, one parallel (subscript p) and another perpendicular (subscript s) to the incidence plane. Fig. 6.1 shows the schematic representation of the incident $\vec{E}^i$ and reflected $\vec{E}^r$ fields, and their corresponding components E^i_p, E^i_s, E^r_p, and E^r_s.

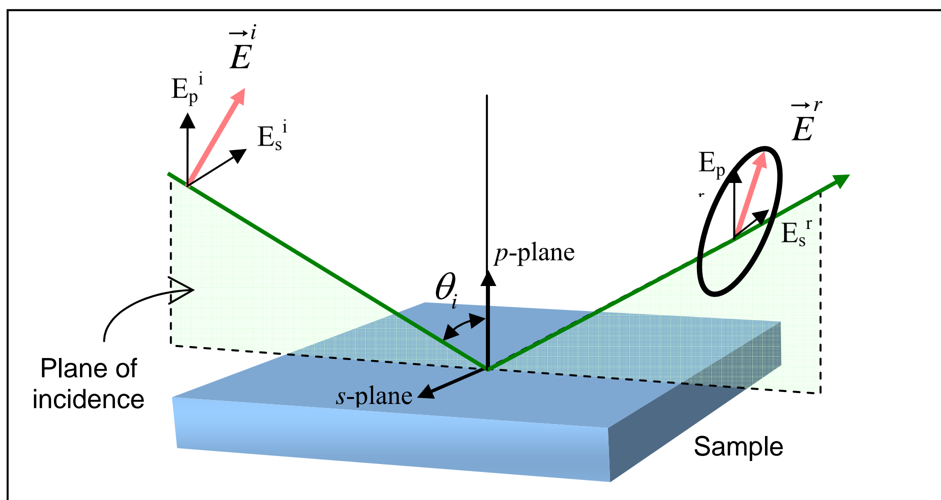

Fig. 6.1. Schematic of the incident electric field ($\vec{E}^i$) and the reflected electric field ($\vec{E}^r$).

ISBN:978-84-691-0362-3 /DL: T.2181-2007

These components are usually expressed in complex notation:

$$\vec{E}^{i,r} = \begin{pmatrix} E_p^{i,r} \\ E_s^{i,r} \end{pmatrix} = e^{j(\omega t - \vec{k}_0 \vec{z})} \begin{pmatrix} A_p^{i,r} \\ A_s^{i,r} \end{pmatrix} = e^{j(\omega t - \vec{k}_0 \vec{z})} \begin{pmatrix} \alpha_p^{i,r} e^{j\beta_p^{i,r}} \\ \alpha_s^{i,r} e^{j\beta_s^{i,r}} \end{pmatrix} \tag{6.1}$$

where ω is the angular frequency, $\vec{k}_0$ is the wavenumber vector in the vacuum, $A^{i,r}{}_p$ and $A^{i,r}{}_s$ are the complex amplitudes of the field components, $\alpha^{i,r}{}_p$ and $\alpha^{i,r}{}_s$ are their modulus and $\beta^{i,r}{}_p$ and $\beta^{i,r}{}_s$ are their relative phases for t=0 and z=0. As the physical magnitude actually detected by ellipsometers is the radiation intensity, the general phase, $e^{j(\omega t - \vec{k}_0 \vec{z})}$, is not considered because it does not affect the magnitude value. On the contrary, the relative phases are very important for the intensity value determination.

The p and s components of the incident and reflected electric fields are related to each other with the reflection coefficient in parallel polarization r_p and the reflection coefficient in perpendicular polarization r_s, respectively. The expressions of these two relations are:

$$\begin{aligned} A_p^r &= r_p A_p^i \\ A_s^r &= r_s A_s^i \end{aligned} \tag{6.2}$$

Ellipsometry measures the modulus and phase of the quotient between the reflection factor in parallel polarization and the reflection factor in perpendicular polarization. This quotient is named complex relation, ρ, and is expressed as:

$$\rho = \frac{r_p}{r_s} \tag{6.3}$$

From this relation the ellipsometric angles Ψ and Δ are defined as:

$$\rho = \tan\Psi \, e^{j\Delta} \tag{6.4}$$

where Ψ is the angle whose tangent is the quotient of the modulus of the reflection factors r_p and r_s and Δ is the phase change difference that the p and the s components undergo in the reflection.

UNIVERSITAT ROVIRA I VIRGILI
DESIGN, FABRICATION AND CHARACTERIZATION OF POROUS SILICON MULTILAYER OPTICAL DEVICES
Elisabet Xifré Pérez
ISBN:978-84-691-0362-3 /DL: T.2181-2007

Although the most used ellipsometric parameters are Ψ and Δ, for the study of the porous silicon layers we will study *Is* and *Ic*, because these are the magnitudes actually measured in the setup we have used [224] The relation of these values with Ψ and Δ are

$$I_S = \sin(2\Psi)\sin(\Delta)$$
$$I_C = \sin(2\Psi)\cos(\Delta) \qquad (6.5)$$

Because ellipsometry measures the ratio of two values, it can be highly accurate and very reproducible.

The most important application of ellipsometry is to study thin films. In the context of ellipsometry a thin film is one that ranges from essentially zero thickness to several thousand Angstroms, although this range can be extended in some cases. If a film is thin enough that it shows a colored interference pattern then it will probably be a good ellipsometric sample. The sensitivity of an ellipsometer is such that a change is film thickness of a few Angstroms is usually easy to detect.

The use of spectroscopic ellipsometry has many advantages. The most important one is that ellipsometry measures a ratio of two values which permits highly accurate and reproducible (even in low light levels) results. No reference sample is necessary and it is not as susceptible to scatter, lamp or purge fluctuations as other measurement techniques.

Ellipsometry provides two values at each wavelength so we obtain more information about sample and therefore more film properties. Some ellipsometers allow the variation of the incidence angle, being called Variable Angle Spectroscopic Ellipsometry (VASE) that report new information optimizing the sensitivity.

UNIVERSITAT ROVIRA I VIRGILI
DESIGN, FABRICATION AND CHARACTERIZATION OF POROUS SILICON MULTILAYER OPTICAL DEVICES
Elisabet Xifré Pérez
ISBN:978-84-691-0362-3 /DL: T.2181-2007

6.1.2. Equipments for ellipsometric measurements. Ellipsometers

There are many different ways of determining the polarisation of a beam of light. In the first ellipsometers, the operator observed the light beam that was reflected off the sample through an eyepiece. The polarisers and retarders were rotated by hand until the effect of the polarisation was inverted and no light would pass through the instrument. This is called the nulling technique. Many instruments are still based on the nulling technique although today's null ellipsometers are somewhat more sophisticated. The light sources used in these instruments were often fixed to a single wavelength.

Modern nulling ellipsometers use computers to rotate the elements and to automatically calculate the ellipsometry signal very quickly. However, the nulling technique is not ideal for automated instruments because it is based on measuring a zero signal. This was an advantage in the early ellipsometers because the human eye is very sensitive to small changes in the signal around the 'null'.

In recent years, the advent of computer control and multichannel detectors has made it possible to develop fast spectroscopic ellipsometers. A technique that is more suited to modern-day instrumentation is Phase Modulated Ellipsometry. The phase modulated ellipsometer (PME) is that in which the state of the radiation beam polarization in a certain point of its trajectory is modulated, obtaining information of the measured system with an analysis of the harmonics of the detected signal.

The most relevant advantages of the PME are the absence of mechanical vibrations of the optical elements and the high modulation frequency that allows the fast data acquisition, that makes possible the monitoring of processes of preparation and treatment of samples in real time.

UNIVERSITAT ROVIRA I VIRGILI
DESIGN, FABRICATION AND CHARACTERIZATION OF POROUS SILICON MULTILAYER OPTICAL DEVICES
Elisabet Xifré Pérez
ISBN:978-84-691-0362-3 /DL: T.2181-2007

6.2. Ellipsometric characterization process

The characterization of porous silicon layers using spectroscopic ellipsometry has been realized during my stage at the École polytechnique in Palaiseau (France), under the supervision of Dr. Enric García-Caurel. Part of the ellipsometric measurements were also realized at Horiba Jobin Yvon in Longjumeau (France). During this stage many porous silicon monolayers and multilayers where measured and characterized. In this section, the equipment and the process for the measurement and characterization of the layers are detailed.

6.2.1. UVISEL Ellipsometer

All the fabricated porous silicon layers have been measured using the UVISEL NIR Spectroscopic Phase Modulated Ellipsometer commercialized by HORIBA-Jobin Yvon. The ellipsometric data were acquired at an incident angle of 70° (some measurements for 55º) for the wavelength range 0.9-1.8 μm with a step of 10 nm.

Fig. 6.2a shows the photograph of the UVISEL ellipsometer used for the realization of the measurements. In Fig. 6.2b we can observe the different parts of this equipment [225].

Fig. 6.2b shows a schematic representation of the optical setup of the phase-modulated ellipsometer. The light source is a xenon lamp, which emits unpolarized light. The beam is focused on the entry of an optical fiber and then passes through a polarizer. After reflection on the sample, the beam is analyzed by a Photoelastic Modulator (PEM) with a 50 kHz modulation frequency, and a second polarizer called analyzer. The light intensity is then introduced to a spectrograph to process the data acquired.

ISBN:978-84-691-0362-3 /DL: T.2181-2007

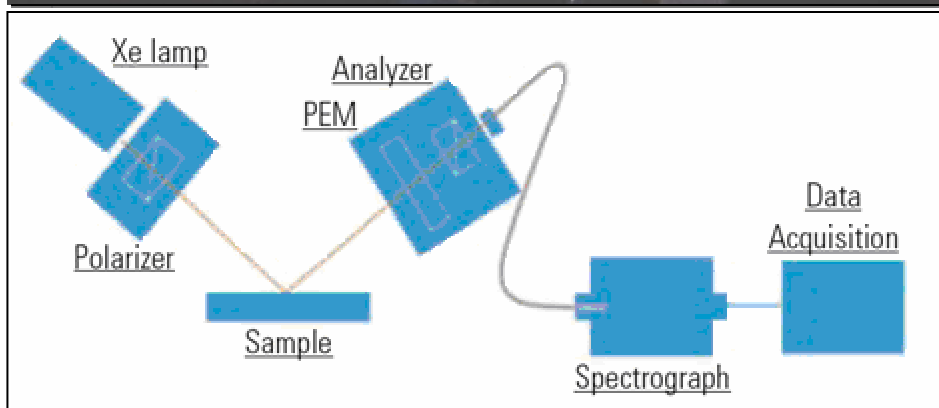

Fig. 6.2. a) UVISEL ellipsometer (École polytechnique) b) Schematic of the UVISEL ellipsometer elements [After 225].

6.2.2. Influence of the spot size on the ellipsometric measurements

Two different sets of samples have been characterized by ellipsometry. Each set has been fabricated using a different electrochemical cell: one set was fabricated with the lateral-wafer cell and the other with the bottom-wafer cell.

UNIVERSITAT ROVIRA I VIRGILI
DESIGN, FABRICATION AND CHARACTERIZATION OF POROUS SILICON MULTILAYER OPTICAL DEVICES
Elisabet Xifré Pérez
ISBN:978-84-691-0362-3 /DL: T.2181-2007

In section 5.1.1, we have concluded that the porous silicon layers obtained with the lateral wafer cell where very inhomogeneous, being the bottom-wafer cell the most appropriate for the fabrication of homogeneous porous silicon layers.

The inhomogeneity of the porous layers obtained with the lateral cell can be also observed from the ellipsometric measurements of the porous silicon layers. The spot size of the beam for the ellipsometric measurement can be adjusted in the UVISEL ellipsometer. Three different spot sizes can be selected: macrospot (1 x 2 mm), mesospot (0.1 mm x 0.2 mm) and microspot (0.01 mm x 0.02 mm). The ellipsometric measurement is an average of the measurement in the spot area. If the refractive index and/or the thickness across the spot area are different the resulting ellipsometric measurement will lead to an averaged result which cannot be fitted because averaging is not taken into account by our ellipsometry software. In consequence, it is very important to choose the appropriate spot size for each type of layer. For inhomogeneous layers the smallest spot size, the microspot is the most suitable whereas the homogeneous layers can be measured with a better signal-to-noise ratio with the meso or the macrospot.

Our porous silicon monolayers, obtained with both electrochemical cell types, have been measured with the three spot sizes. Fig. 6.3 shows the ellipsometric measurements realized to a porous silicon monolayer obtained with the lateral-wafer cell for two different spot sizes. We can observe that the results obtained are very different for the macrospot and for the mesospot. With the mesospot all the maxima and minima of I_S and I_C can be observed whereas with the macrospot these variations are attenuated and some of them are lost. This effect of aliasing is explained by the inhomogeneity of the samples, which corroborates the conclusions obtained in section 5.1.1 that the wafers obtained with the lateral-wafer cell are inhomogeneous.

Fig. 6.4 shows the ellipsometric measurements of a monolayer fabricated with the bottom-wafer cell. We can observe that I_S and I_C do not vary with the spot size, which indicates that the porous silicon monolayer is very homogeneous. The little variations of I_C at the maxima of the mesospot

ISBN:978-84-691-0362-3 /DL: T.2181-2007

measurements are not relevant, they are produced by the low signal-to-noise ratio of the instrument due to the small size of the spot.

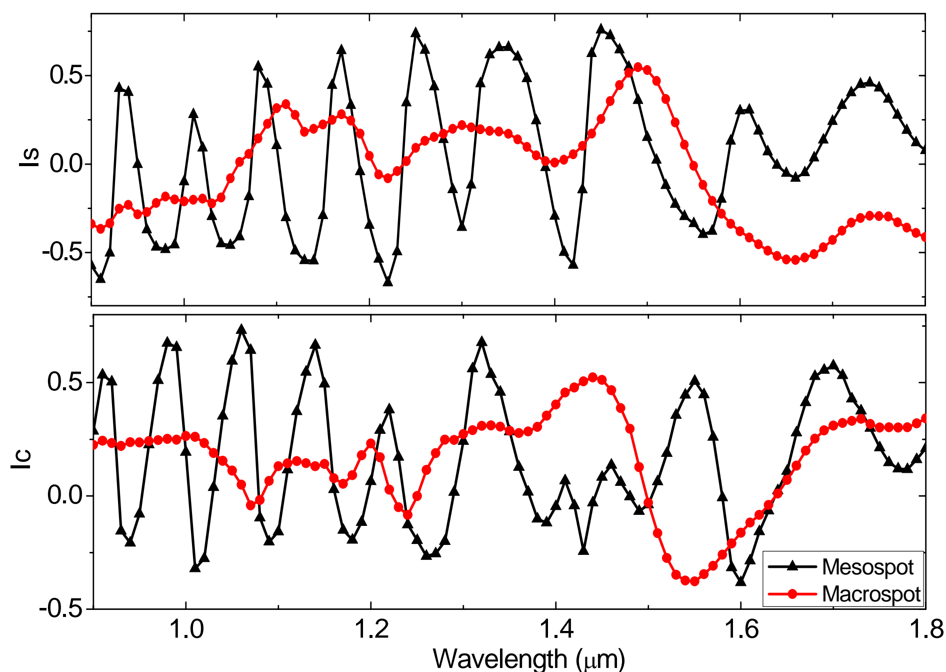

Fig. 6.3. Ellipsometric measurements of a porous silicon monolayer, fabricated with the lateral-wafer cell, for two different spot sizes.

The ellipsometric study has been realized for layers fabricated with both lateral and bottom-wafer cells. The results obtained with the latter cell are more accurate due to the homogeneity of the fabricated porous silicon layers. For this reason, in the next sections we only present the ellipsometric study realized for the bottom-wafer cell layers and the conclusions obtained from this study. The same conclusions have also been obtained for the lateral-wafer cell layers although the possible errors introduced in the characterization are slightly higher due to inhomogeneity.

ISBN:978-84-691-0362-3 /DL: T.2181-2007

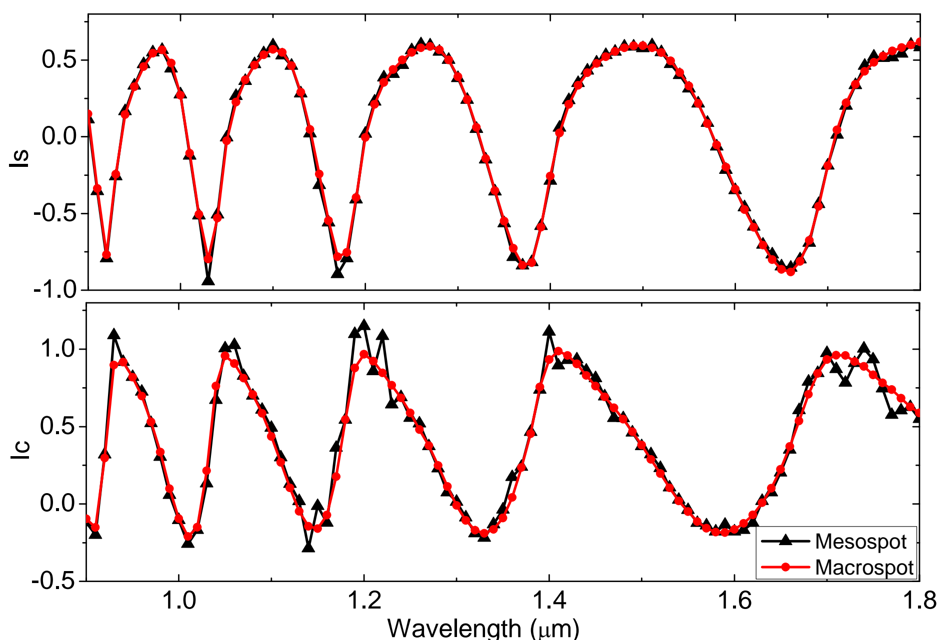

Fig. 6.4. Ellipsometric measurements of a porous silicon monolayer, fabricated with the bottom-wafer cell, for two different spot sizes.

6.2.3. Process for the determination of porous silicon characteristics using ellipsometric data

The characterization of porous silicon layers using spectroscopic ellipsometry is realized in two very different steps. Firstly, we measure the samples with the ellipsometer to obtain the experimental ellipsometric data, and second, we modelize the experimental data to interpret the measurement in terms of a physical model that connects the optical response with the physical structure of the given sample.

The optical model has been built using the DeltaPsi2 program, developed and commercialized by Jobin Yvon. A porous silicon layer has been modeled as a layer formed by two different materials, silicon and air (void), on a silicon crystalline substrate [226,227]. The law of mixture used to model the equivalent

UNIVERSITAT ROVIRA I VIRGILI
DESIGN, FABRICATION AND CHARACTERIZATION OF POROUS SILICON MULTILAYER OPTICAL DEVICES
Elisabet Xifré Pérez
ISBN:978-84-691-0362-3 /DL: T.2181-2007

dielectric function of the materials is the effective medium approximation of Bruggeman [228].

Although we have considered that a porous silicon layer is only formed by silicon and air, the existence of silicon dioxide could also be assumed. However, silicon dioxide has not been used for the model because its optical response is very similar to that of air and it is not possible to distinguish between their contributions.

Unknown parameters of this optical model can be thin film thickness, or optical constants or both. For our particular case, the unknown parameters are the thickness, and the volume fraction of void (porosity). The possible presence of uniaxial birefringence in the layers is also considered.

Using this optical model we have generated the simulated ellipsometric data. The unknown parameters are varied to try and produce the best fit between the simulated and the experimental ellipsometric data.

Numerical algorithms are used to vary the unknown parameters and minimize the difference between simulated and experimental data. In our particular case, we have used the Marquardt [229] minimization routine for the determination of porous silicon layers parameters. According to the article of Jellison [230] we have used a non biased mean-squared error (χ^2) function to measure the goodness of fit. The χ^2 is defined as follows

$$\chi = \frac{1}{2M-1}\sqrt{\sum_i \left[\frac{\left(Is_{Ti} - Is_{Xi}\right)^2}{\sigma_{is}^2} + \frac{\left(Ic_{Ti} - Ic_{Xi}\right)^2}{\sigma_{ic}^2} \right]} \tag{6.6}$$

where M is the number of points, Is_{Ti} is the simulated value Is for the i point, Is_{Xi} is the experimental value Is for the i point, Ic_{Ti} is the simulated value Ic for the i point, Ic_{Xi} is the experimental value Ic for the i point and σ_{is} and σ_{ic} are the error in the experimental determination, for this case $\sigma_{is}=\sigma_{ic}=0.01$.

UNIVERSITAT ROVIRA I VIRGILI
DESIGN, FABRICATION AND CHARACTERIZATION OF POROUS SILICON MULTILAYER OPTICAL DEVICES
Elisabet Xifré Pérez
ISBN:978-84-691-0362-3 /DL: T.2181-2007

6.3. Measurement and characterization of porous silicon monolayers

Several porous silicon monolayers have been fabricated with the fabrication method explained in detail in chapter 5. Each of them has been obtained applying a different current density, therefore each monolayer has a different porosity, and so a different refractive index. Although a set of monolayers has been fabricated with each of the two types of anodization cell, in this and the next sections we only present the ellipsometric study realized for the bottom-wafer cell layers for the reasons explained in the previous section.

Each monolayer is identified by the current density (J) applied during the fabrication process because it determines its porosity (refractive index). For each porous silicon monolayer we have measured the ellipsometric data, determined the optical model with the best fit parameters (thickness and porosity), and evaluated the difference between the measured and the simulated ellipsometric data. The isotropy/anisotropy of the porous layers has also been analyzed.

All the ellipsometric characterization procedure is presented in this section. For clarity reasons, the monolayers have been grouped according to the optical model used for their characterization. We have found that depending on the value of the current density, the porous silicon layers show either an isotropic or an anisotropic optical response.

Besides, the thicknesses and the refractive indices determined with the ellipsometric data have been compared with the ones obtained by SEM and by the measurement of the interference fringes method (MIF method), respectively.

6.3.1. Isotropic optical model

The lowest current density used for the fabrication of our porous silicon monolayers is J=10 mA/cm^2. For his reason, this is the monolayer with the lowest porosity, and therefore with the highest refractive index. The monolayer has been obtained applying J=10 mA/cm^2 for 120 s. Fig. 6.5 shows the cross

UNIVERSITAT ROVIRA I VIRGILI
DESIGN, FABRICATION AND CHARACTERIZATION OF POROUS SILICON MULTILAYER OPTICAL DEVICES
Elisabet Xifré Pérez
ISBN:978-84-691-0362-3 /DL: T.2181-2007

section SEM image of this monolayer. The thickness estimated from the SEM image is approximately 1.32 μm.

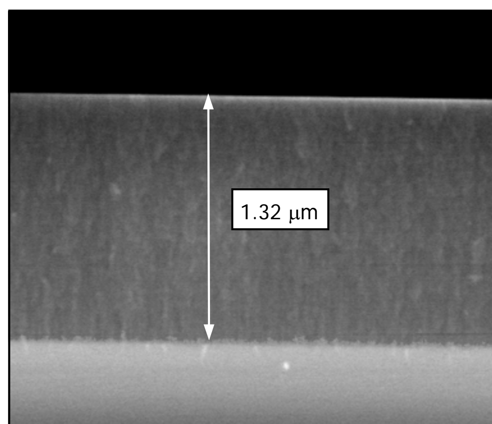

Fig. 6.5. Cross section SEM image of the porous silicon monolayer obtained with *J*=10 mA/cm^2 and anodization time 120 s. The thickness is 1.32 μm.

For the analysis of the measured ellipsometric data, the layer has been firstly assumed to be isotropic and composed of silicon and void (air). The optical model used for the characterization of this monolayer can be observed in Fig. 6.6a. It has been necessary to suppose that the monolayer is formed by two homogeneous and isotropic layers with different porosity because all the fits realized assuming only one isotropic layer had a too high χ^2. The parameters that have been varied for obtaining the best fit are the thickness and the porosity of both layers. The best fit parameters obtained for this two isotropic layer model can also be observed in Fig. 6.6a whereas Fig. 6.6b shows both the measured and the simulated ellipsometric data obtained with this model, with χ^2=36.4.

UNIVERSITAT ROVIRA I VIRGILI
DESIGN, FABRICATION AND CHARACTERIZATION OF POROUS SILICON MULTILAYER OPTICAL DEVICES
Elisabet Xifré Pérez
ISBN:978-84-691-0362-3 /DL: T.2181-2007

From Fig. 6.6a we can observe that the total thickness of the porous layers is 1.27 μm, very similar to the thickness estimated with SEM. The porosity of the top layer is higher than the one of the bottom layer, which is in line with the fabrication process, as the top layer is longer in contact with the electrolyte.

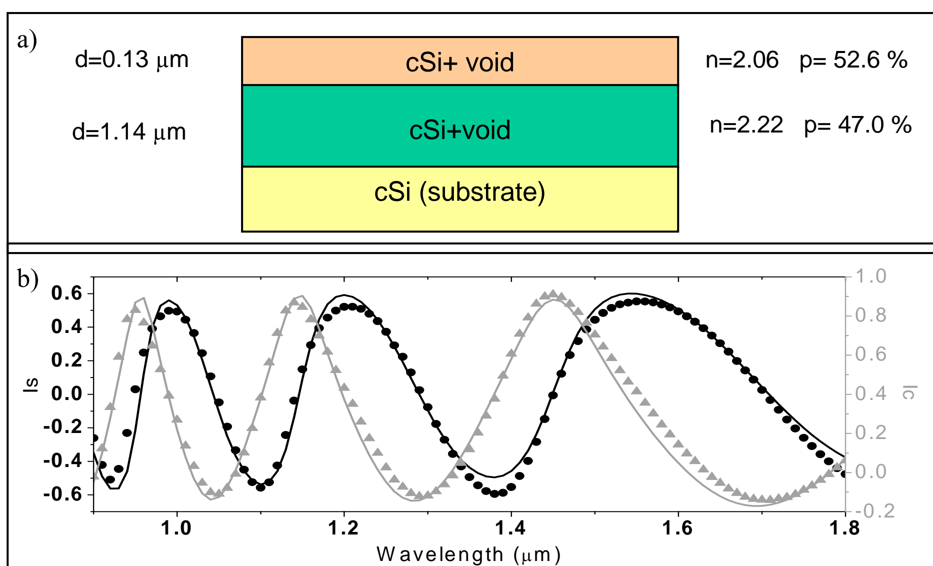

Fig. 6.6. a) Optical model consisting of two isotropic layers, the best fitted parameters (thickness, porosity) and refractive index for λ=1.8 μm b) Measured ellipsometric data (dots) and simulated ellipsometric data obtained with the optical model (line).

The porosity, that is the volume fraction of air in the silicon layer, determines the refractive index. This refractive index is not constant within the wavelength range measured by the ellipsometer (from 0.9 to 1.8 μm) it decreases as the wavelength increases. The variation of the refractive index within this wavelength range depends on the porosity level but it is lower than 3%.

UNIVERSITAT ROVIRA I VIRGILI
DESIGN, FABRICATION AND CHARACTERIZATION OF POROUS SILICON MULTILAYER OPTICAL DEVICES
Elisabet Xifré Pérez
ISBN:978-84-691-0362-3 /DL: T.2181-2007

We compare now the refractive index obtained with ellipsometry with the one obtained with the MIF method. According to the details given in section 5.2.2.1, we recall that the MIF method gives a refractive index within the wavelength range instead of a punctual value for each wavelength. To ease the comparison of the refractive indices obtained with both methods, we will compare the one obtained with ellipsometry for λ=1.8 μm with the highest refractive index obtained with the MIF method, because λ=1.8 μm is the closest wavelength to the wavelength range analyzed with the MIF method. For this reason, all the refractive indices calculated with the MIF method that will be presented in this and the next sections will be approximate values.

The refractive index obtained with the MIF method for this monolayer is n ≈ 2.05. The refractive indices obtained from ellipsometry are n_t=2.06 the top layer and n_b=2.22 for the bottom layer, at λ=1.8 μm. We can observe that although the refractive index of the top layer is very close to the one obtained with the MIF method, for the bottom layer the refractive index is more different.

Several studies concerning the fabrication process of porous silicon indicate that the porosity of a layer varies with depth [19,231], being the porosity at the top of the layer higher that the one at the bottom. It is known that once a porous silicon layer is formed no more electrochemical etching occurs but a slow chemical one starts, due to the permanence in HF [232,233]. This explains the fact that the top porosity is higher than the bottom porosity and it also leads to think that the variation of this porosity could be gradual in depth. From the analysis of ellipsometric measurements with the isotropic optical model we have already stated that this porosity variation exists in our layers. Now we are going to study whether a graded layer optical model can improve the description of the variation of porosity with thickness and consequently, the quality of fits of ellipsometric data.

Our optical simulation software represents a single graded layer as a multilayer stack made of a given number of homogeneous slices where the porosity changes slightly from slice to slice. Fig. 6.7a shows the graded optical

ISBN:978-84-691-0362-3 /DL: T.2181-2007

model, where the porosity decreases from top to bottom in a graded way. The parameters determined for the best fit are also shown.

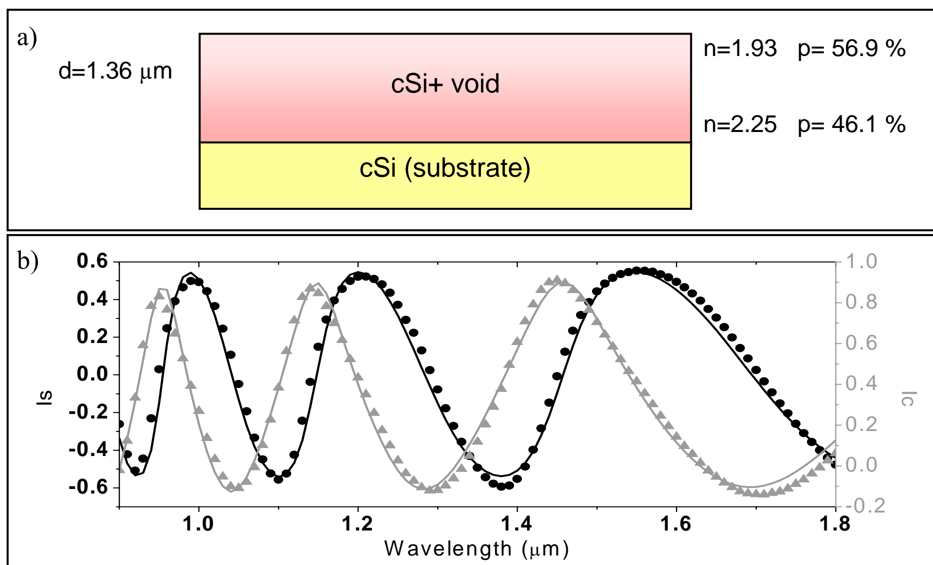

Fig. 6.7. a) Optical model with one gradient layer, the best fit parameters (thickness, and porosity) and refractive index for λ=1.8 μm at the top and bottom of the graded layer. b) Measured ellipsometric data (dots) and simulated ellipsometric data obtained with the optical model (line).

We can observe that the thickness of this monolayer is closer to the thickness estimated with SEM (1.32 μm). The difference between these two thicknesses is very low and we can consider it as negligible because it could be introduced by the low accuracy of the SEM image.

The refractive indices obtained with this model are n_t=1.93 at the top of the layer and it gradually increases towards the bottom until a value of n_b=2.25, both for λ=1.8 μm. To better compare these values with the one obtained with the MIF method we have calculated the average refractive index of the monolayer with $n_{average}=(n_t+n_b)/2$. The average refractive index is $n_{average}$=2.09

ISBN:978-84-691-0362-3 /DL: T.2181-2007

and n with the MIF method is 2.05. We can observe that they are almost equal. The small difference can be attributed to the dispersion of the refractive index with the wavelength.

The comparison between the measured and the simulated ellipsometric data can be observed in Fig. 6.7b. The value of χ^2 for the gradient model is lower (25.9) than the value of the same function corresponding to the homogeneous model (36.4).

From these results we conclude that the fit realized with the gradient optical model is better than the one realized with the homogeneous model for the following reasons: the thickness obtained is closer to the thickness estimated with SEM, the value of χ^2 is lower which means that variation of porosity with depth is better simulated, the average refractive index of the optical model is very close to the calculated with MIF method.

Therefore, we can conclude that this is an isotropic layer where the porosity decreases gradually from top to bottom.

The same graded isotropic optical model has been used for the characterization of a porous silicon monolayer obtained with J=14 mA/cm^2. This current density is higher than the one of the previous monolayer, so the porous silicon monolayer obtained is expected to have a higher porosity, and therefore a lower refractive index. The anodization time for the formation of this monolayer was t =90 s. The thickness of this layer is approximately 1.35 μm (SEM image) and the refractive index calculated with the MIF method is approximately $n \approx 1.97$.

The optical model for this monolayer can be observed in Fig. 6.8a. The best fit is obtained for thickness 1.3 μm and porosity varying gradually from 60.3 % at the top to 48.8 % at the bottom. For this porosity, the refractive indices are n_t=1.83 and n_b=2.17, being the averaged value $n_{average}$=1.99 (λ=1.8 μm). It can be observed that both the refractive index and the thickness obtained with the ellipsometric characterization agree with the values obtained with the MIF method and SEM, respectively. The ellipsometric data simulated with the

ISBN:978-84-691-0362-3 /DL: T.2181-2007

optical model can be compared with the measured data in Fig. 6.8b, where χ^2 is 81.4.

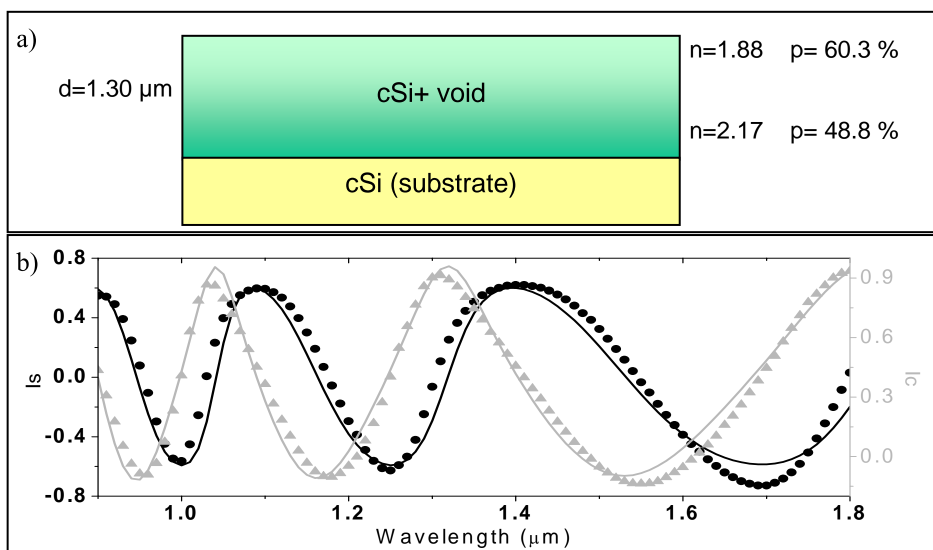

Fig. 6.8. a) Optical model with one gradient layer, the best fit parameters (thickness, and porosity) and refractive index for λ=1.8 µm at the top and bottom of the graded layer. b) Measured ellipsometric data (dots) and simulated ellipsometric data obtained with the optical model (line).

6.3.2. Anisotropic optical model

The porous silicon layers presented in this section have been obtained with current densities higher than 14 mA/cm^2, therefore their porosity is higher than the one of the previous monolayers.

The first monolayer to be characterized is the one obtained with J=20 mA/cm^2. The refractive index calculated with the MIF method is 1.92 and the thickness from the SEM image (see Fig. 6.9) is 2.48 µm.

ISBN:978-84-691-0362-3 /DL: T.2181-2007

The ellipsometric data from this porous silicon monolayer has been also modeled with a graded isotropic layer as the previous monolayers. This optical model can be observed in Fig. 6.10a together with the best-fitted values of the thickness and the porosity. The average refractive index for λ=1.8 μm is 1.98, that is similar to the MIF refractive index. However, the thickness obtained with ellipsometry is lower that the one estimated with SEM and the difference between the measured and the simulated ellipsometric data (Fig. 6.10b) is very high, χ^2=286.8.

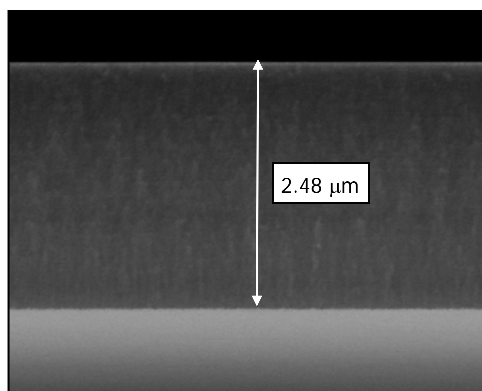

Fig. 6.9. SEM image of the porous silicon monolayer obtained with *J*=20 mA/cm^2 and anodization time 120 s. The thickness is 2.48 μm.

From these results, we can deduce that an isotropic graded layer is not the most appropriate optical model for the simulation of this porous silicon monolayer. The only difference between this monolayer and the previous ones is the higher current density used for its formation, that leads to higher porosity. Hence, we can deduce that the isotropic graded layer model is appropriate only for low porosity porous silicon layers (J≤14 mA/cm^2).

ISBN:978-84-691-0362-3 /DL: T.2181-2007

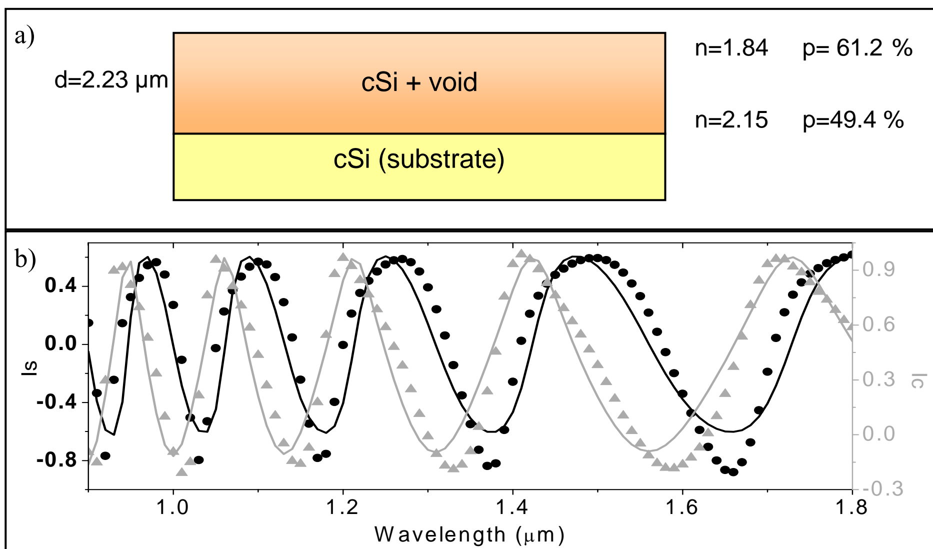

Fig. 6.10. a) Optical model with one gradient layer, the best fit parameters (thickness, and porosity) and refractive index for λ=1.8 µm at the top and bottom of the graded layer. b) Measured ellipsometric data (dots) and simulated ellipsometric data obtained with the optical model (line).

Another optical model has been studied consisting of an anisotropic layer [231,233,234]. The difference between an isotropic and an anisotropic material can be schematically observed in Fig. 6.11. An isotropic material is the one that has the same optical properties in all directions [204]. In the case of the refractive index, it means that the refractive index is the same in all directions. Anisotropy is the property of being directionally dependent, that is, the material has different physical properties (in this case refractive index) along different axes [204]. For the simulation of this porous silicon layer, we have supposed that the material is uniaxial and birefringence can be formalized by assigning two different refractive indices to the material for different polarizations. The birefringence magnitude is then defined by:

$$\Delta n = n_e - n_o \qquad (1)$$

ISBN:978-84-691-0362-3 /DL: T.2181-2007

where n_o and n_e are the refractive indices for polarizations perpendicular (ordinary) and parallel (extraordinary) to the axis of anisotropy respectively.

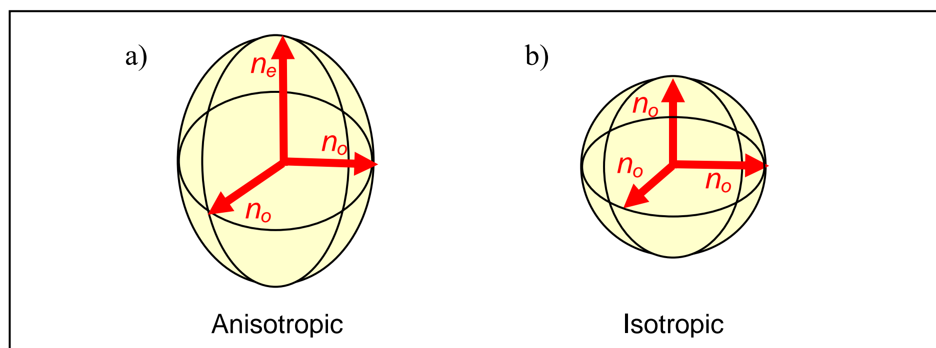

Fig. 6.11. Refractive index for every direction in an isotropic material (a) and anisotropic material (b).

The anisotropic optical model for the simulation of this porous silicon layer can be observed in Fig. 6.12a. The axis of anisotropy is perpendicular to the layer surface. The best fit with this model is obtained for thickness 2.44 μm and for refractive index n_e=2.01 and n_o=1.82 at λ=1.8 μm, being the averaged value $n_{average}$=1.91. Although the MIF method does not consider the anisotropy of the layer, we can compare the refractive index obtained with MIF (1.92) with the average value of the optical model. We can observe that the refractive indices and the thicknesses obtained with both methods agree. In Fig. 6.12b we can compare the simulated and the measured ellipsometric data, being χ^2=46.4, which is remarkably lower than the value obtained with the graded model.

This good agreement and the low value of χ^2 obtained with the anisotropic model, lead us to conclude that when the porosity of the porous silicon layer increases, the material is not isotropic but it has an anisotropic behavior.

ISBN:978-84-691-0362-3 /DL: T.2181-2007

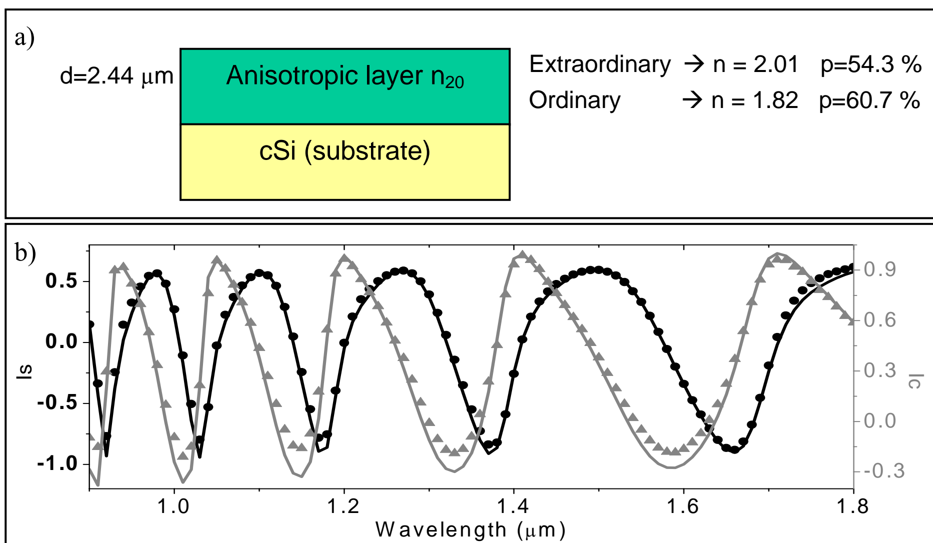

Fig. 6.12. a) Optical model consisting of an anisotropic layer, its best fit parameters (thickness, porosity) and the refractive index (λ=1.8 μm) for the extraordinary and the ordinary axes b) Measured ellipsometric data (dots) and simulated ellipsometric data obtained with the optical model (line).

Notice that the extraordinary refractive index is higher than the ordinary refractive index. This indicates that in one direction the quantity of air is higher than in the other direction. This agrees with the fabrication process because it is known that the anodization preferentially occurs at the pore tips and that the etching of the porous silicon proceeds in depth with an overall directionality which follows the anodic paths inside silicon.

From these results we could conclude that for $J \leq 14$ mA/cm^2, the difference between the extraordinary and the ordinary refractive indices is small enough to be masked by the in depth inhomogeneity, whereas for $J > 14$ mA/cm^2 the anisotropy is more important than the inhomogeneity.

UNIVERSITAT ROVIRA I VIRGILI
DESIGN, FABRICATION AND CHARACTERIZATION OF POROUS SILICON MULTILAYER OPTICAL DEVICES
Elisabet Xifré Pérez
ISBN:978-84-691-0362-3 /DL: T.2181-2007

The observed anisotropic behavior of the high porosity layers has also been studied with the ellipsometric characterization of two other high porosity layers: *J*=30 mA/cm^2 and *J*=50 mA/cm^2.

The monolayer obtained with the application of *J*=30 mA/cm^2 for 120 s has n ≈ 1.73 (MIF method) and thickness of approximately 3.28 μm (SEM). The best fit with the anisotropic optical model is obtained for thickness 3.28 μm (the same as the one estimated with SEM) and refractive indices n_e=1.8 and n_o=1.64 (Fig. 6.13), being $n_{average}$=1.72. The value of the merit figure χ^2 is 60.5, leading to the conclusion that this anisotropic optical model is appropriate for this porous silicon layer.

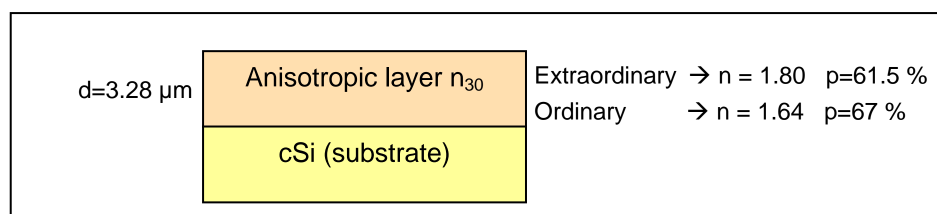

Fig. 6.13. Optical model consisting of an anisotropic layer, the best fit parameters (thickness, porosity) and the refractive index (λ=1.8 μm) for the extraordinary and the ordinary axes.

Finally, let's consider the last porous silicon monolayer characterized with ellipsometry, that is the one obtained with *J*=50 mA/cm^2 for 60 s. Its thickness is approximately 2.37 μm (SEM) and the refractive index calculated with the MIF method is n ≈ 1.45.

The anisotropic optical model used for this monolayer can be observed in Fig. 6.14a. The experimental and simulated ellipsometric data are shown in Fig. 6.14b, where we can observe that the agreement is good with a merit function χ^2=100.5. For this layer, the most porous of the monolayers set, the fit of the simulated to the measured ellipsometric data has been the most difficult

ISBN:978-84-691-0362-3 /DL: T.2181-2007

of all and the χ^2 obtained with this model is slightly higher than for the rest of monolayers. In spite of this difficulty, the parameters obtained with ellipsometry are very close to the parameters obtained with by SEM and MIF: the thickness difference is only 90 nm (about 4 %), that could be due to the inaccuracy of the SEM estimation; and the average refractive index is $n_{average}$=1.47 very close to the MIF refractive index (1.45).

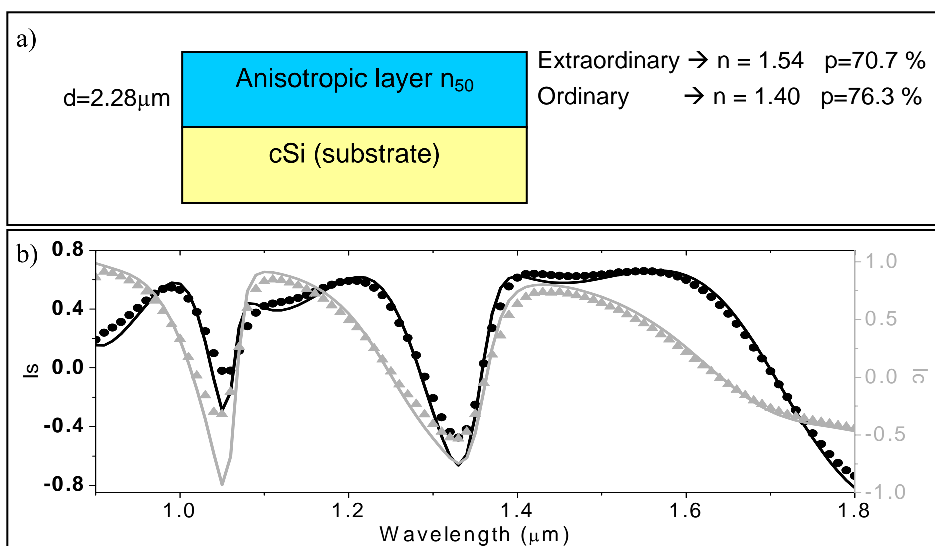

Fig. 6.14. a) Optical model consisting of an anisotropic layer and its best fit parameters: thickness, porosity and refractive index (λ=1.8 μm) for the extraordinary and the ordinary axes b) Measured ellipsometric data (dots) and simulated ellipsometric data obtained with the optical model (line).

Therefore, we can conclude that the anisotropic optical model is the most appropriate for high porosity layers.

UNIVERSITAT ROVIRA I VIRGILI
DESIGN, FABRICATION AND CHARACTERIZATION OF POROUS SILICON MULTILAYER OPTICAL DEVICES
Elisabet Xifré Pérez
ISBN:978-84-691-0362-3 /DL: T.2181-2007

6.3.3. Depolarization of porous silicon layers

From the ellipsometric study of these porous silicon monolayers we have observed that the difference between the measured and the simulated ellipsometric data, quantified with χ^2, was different for each layer. Specifically, χ^2 increased when the current density, and hence the porosity, increased. This can be due to the fact that the anisotropy of porous silicon produces the depolarization of light. If the sample depolarizes the light, the ellipsometric angles (Δ and Ψ) are not well defined, because they were measured under the supposition that there is no depolarization.

To explain the increment of χ^2 with the current density, we have measured the monolayers with a polarimeter, to study the depolarization of the light produce by each monolayer. The measurement of the depolarization of the different porous silicon monolayers has been realized with a polarimeter Jobin Yvon MM-16 at the Ecole polytechnique (Palaiseau).

In Fig. 6.15 we can observe the measured depolarization of three different porosity monolayers, where P is the degree of polarization. When P=1 indicates that the beam is completely polarized [235]. These layers have been obtained with J=10 mA/cm^2, J=20 mA/cm^2, and J=50 mA/cm^2 and the χ^2 of the corresponding models are $\chi^2_{10} < \chi^2_{20} < \chi^2_{50}$.

The layer obtained with J=10 mA/cm^2 is the one with the lower depolarization, that is the one with P closest to the unity for the whole wavelength range. The layer obtained with J=20 mA/cm^2 presents more depolarization than the previous one. The porosity of this layer is higher than the previous layer, which could be the reason for the increment of the depolarization. The increment of depolarization indicates that this layer is more difficult to characterize with ellipsometry than the previous one, explaining the reason for $\chi^2_{10}<\chi^2_{20}$.

UNIVERSITAT ROVIRA I VIRGILI
DESIGN, FABRICATION AND CHARACTERIZATION OF POROUS SILICON MULTILAYER OPTICAL DEVICES
Elisabet Xifré Pérez
ISBN:978-84-691-0362-3 /DL: T.2181-2007

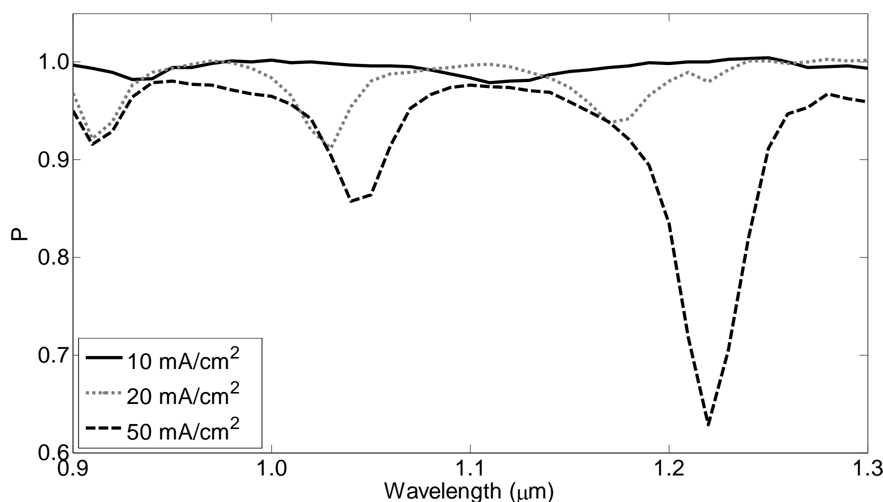

Fig. 6.15. Depolarization of three porous silicon layers with obtained with different current densities, therefore with different porosity.

The last layer analyzed is the one obtained with J=50 mA/cm^2. In Fig. 6.15 we can observe that this is the layer with the highest depolarization, which explains that the ellipsometric data simulated for this layer has a higher χ^2 than the others.

We can conclude that when the current density increases, that is when the porosity increases, the depolarization of the fabricated porous silicon layer increases making more difficult the characterization of the layer using ellipsometry.

6.3.4. Summary

The results obtained with the ellipsometric characterization of the porous silicon monolayers have been summed up in Table 6.II. In this table the thicknesses obtained for the different monolayers are indicated together with the values of porosity obtained for λ=1.8 μm and the refractive indices calculated for the different optical models.

ISBN:978-84-691-0362-3 /DL: T.2181-2007

J (mA/cm^2)	**Optical model**	**Thickness** (µm)	**Porosity** p (%)	**Refractive index** n
10	Gradient	1.36	p_{top}= 56.9 p_{bottom}= 46.1	n_{top}= 1.93 n_{bottom}= 2.25
14	Gradient	1.30	p_{top}= 60.3 p_{bottom}= 48.8	n_{top}= 1.88 n_{bottom}= 2.17
20	Anisotropic	2.44	p_{ext}= 54.3 p_{ord}= 60.7	n_{ext}= 2.01 n_{ord}= 1.82
30	Anisotropic	3.28	p_{ext}= 61.5 p_{ord}= 67.0	n_{ext}= 1.80 n_{ord}= 1.64
50	Anisotropic	2.28	p_{ext}= 70.7 p_{ord}= 76.3	n_{ext}= 1.54 n_{ord}= 1.40

Table 6.I. Summary of the ellipsometric characterization of the porous silicon layers obtained with different current densities. The porosities (and its corresponding refractive index) are the values at the top and at the bottom for the isotropic gradient model and the extraordinary and ordinary values for the anisotropic optical model. The porosity and refractive index values are the ones for λ=1.8 µm.

In Table 6.II the refractive index and the thickness obtained with this ellipsometric characterization are compared with the ones obtained with other methods (MIF method and SEM). To ease this comparison, the averaged value of the ellipsometric refractive index is used. We can observe that the results obtained with these different methods completely agree, therefore the spectroscopic ellipsometry can be considered an appropriate method for the characterization of porous silicon layers.

ISBN:978-84-691-0362-3 /DL: T.2181-2007

J (mA/cm^2)	**Optical model**	$\mathbf{n_{ellipsometry}}$ (averaged at λ=1.8 μm)	$\mathbf{n_{MIF}}$ (for λ near 1.8 μm)	$\mathbf{d_{ellipsometry}}$ (μm)	$\mathbf{d_{SEM}}$ (μm)	χ^2
10	Gradient	2.09	2.05	1.36	1.32	25.9
14	Gradient	1.99	1.97	1.30	1.35	81.4
20	Anisotropic	1.91	1.92	2.44	2.48	46.4
30	Anisotropic	1.72	1.73	3.28	3.28	60.5
50	Anisotropic	1.47	1.45	2.28	2.37	100.5

Table 6.II. Summary of the ellipsometric characterization of porous silicon monolayers obtained with different current densities. The results obtained with the MIF method and SEM are also presented for comparison.

In this table, it can be also observed that when the current density increases the porosity increases and therefore the refractive index decreases. The optical model used for the simulation of the ellipsometric data is different depending on the porosity of the layers: an isotropic gradient model is the appropriate for low porosity layers ($J \leq 14$ mA/cm^2) and an anisotropic one for the high porosity layers ($J > 14$ mA/cm^2).

6.4. Characterization of porous silicon multilayers

In this section, the ellipsometric study of porous silicon multilayers is presented. All these multilayers consist of the periodic repetition of two different porous layers: one layer was obtained with J=20 mA/cm^2 and the other with J= 50 mA/cm^2. The former is the lowest current density that produces an anisotropic layer whereas the latter is the highest current density used for the formation of porous silicon layers.

ISBN:978-84-691-0362-3 /DL: T.2181-2007

The anisotropic optical models obtained with the study of monolayers (section 6.3.2) are used now as a starting point for the characterization of the different layers of the multilayers.

6.4.1. One period multilayer

This multilayer consists of one period (two layers) where the top layer has been obtained with the application of J=20 mA/cm^2 for 30 s and the bottom layer with J=50 mA/cm^2 for 30 s as well. The SEM image of this multilayer is shown in Fig. 6.16, where we can observe that the bottom layer is thicker than the top layer.

The optical models obtained in the previous section for J=20 mA/cm^2 and J=50 mA/cm^2 were anisotropic. Hence, for the optical model of this multilayer we have used two anisotropic layers.

The parameters that have been determined in this model are the thickness and the porosity (ordinary and extraordinary indices) of the two layers of the stack. The resulting best fitted values of the parameters are presented in in Fig. 6.17a whereas Fig. 6.17b shows the agreement between the measured and the simulated ellipsometric data, with χ^2=23.6.

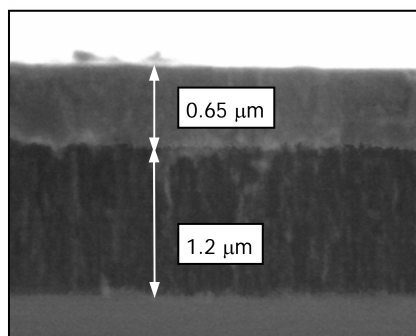

Fig. 6.16. SEM image of the one-period multilayer. Although the interface between the two porous layer is difficult to determine, the estimated thickness of the layers are approximately $d_1 \approx$ 0.65 µm and $d_2 \approx$ 1.2 µm.

ISBN:978-84-691-0362-3 /DL: T.2181-2007

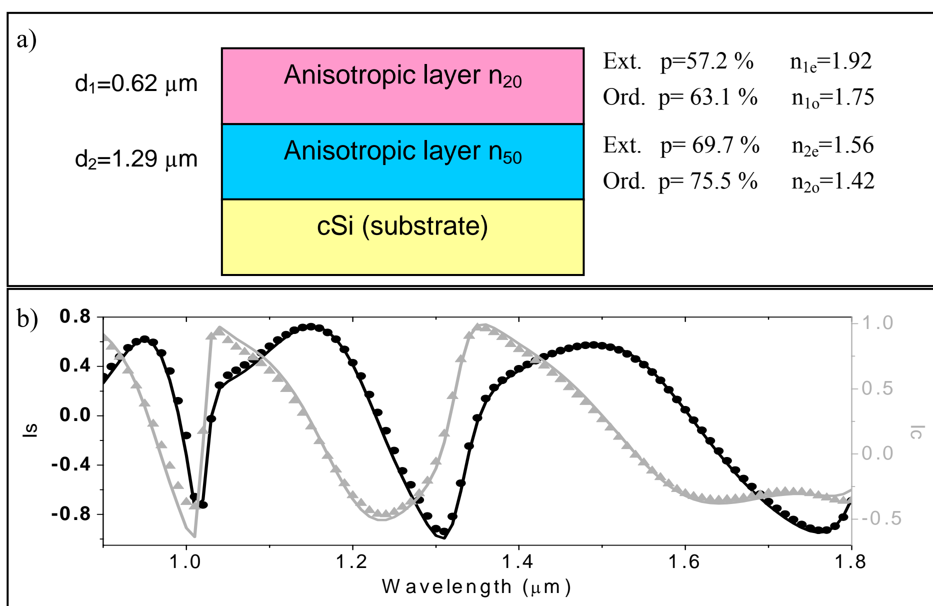

Fig. 6.17. a) Optical model consisting of two anisotropic layers and the resulting best fitted values for the corresponding parameters: thickness, porosity and refractive index (λ=1.8 μm) for the extraordinary and the ordinary axes b) Measured ellipsometric data (dots) and simulated ellipsometric data obtained with the optical model (line) of Fig. 6.17a.

In Fig. 6.17a, we can observe that the thicknesses d_1 and d_2 obtained with ellipsometry completely agree with the thicknesses estimated with the SEM image.

The best fitted refractive indices of these two layers are very close to the ones determined during the characterization of the corresponding monolayers, being in both cases the extraordinary refractive index higher than the ordinary. The small difference between the monolayer and the multilayer refractive indices was expected because bibliography about porous silicon suggests that the layers that form a multilayer may have a slightly different refractive index to the monolayers fabricated with the same current density [19].

ISBN:978-84-691-0362-3 /DL: T.2181-2007

6.4.2. Two period multilayer

This multilayer is formed by two periods. Each period consists of two layers. The top layer of the period has been obtained with the application of J=20 mA/cm^2 for 20 s and the bottom layer with J=50 mA/cm^2 for also 20 s. The SEM image of this multilayer can be observed in Fig. 6.18, where the thickness of each layer has been estimated.

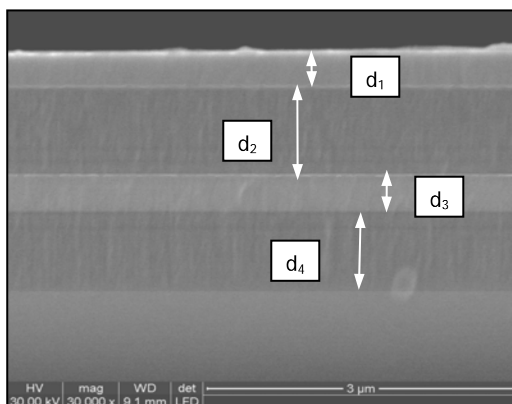

Fig. 6.18. SEM image of the two-period multilayer. Although the interface between the porous layers is difficult to determine, the estimated thickness of the layers are approximately $d_1 \approx 402$ nm, $d_2 \approx 806$ nm, $d_3 \approx 408$ nm, and $d_4 \approx 826$ nm.

The optical model used for this multilayer can be observed in Fig. 6.19a. The best fitted parameters obtained for the anisotropic monolayer model has been used as starting point for the characterization of each layer of the two period stack. In this case, the number of parameters to be fitted increased significantly: four different thicknesses and eight different porosities.

The best fitted thicknesses obtained with ellipsometry agree with the ones obtained with the SEM image, the difference between them is very small and it can be caused by the inaccuracy of the SEM image as the interface between the different layers cannot be defined clearly.

UNIVERSITAT ROVIRA I VIRGILI
DESIGN, FABRICATION AND CHARACTERIZATION OF POROUS SILICON MULTILAYER OPTICAL DEVICES
Elisabet Xifré Pérez
ISBN:978-84-691-0362-3 /DL: T.2181-2007

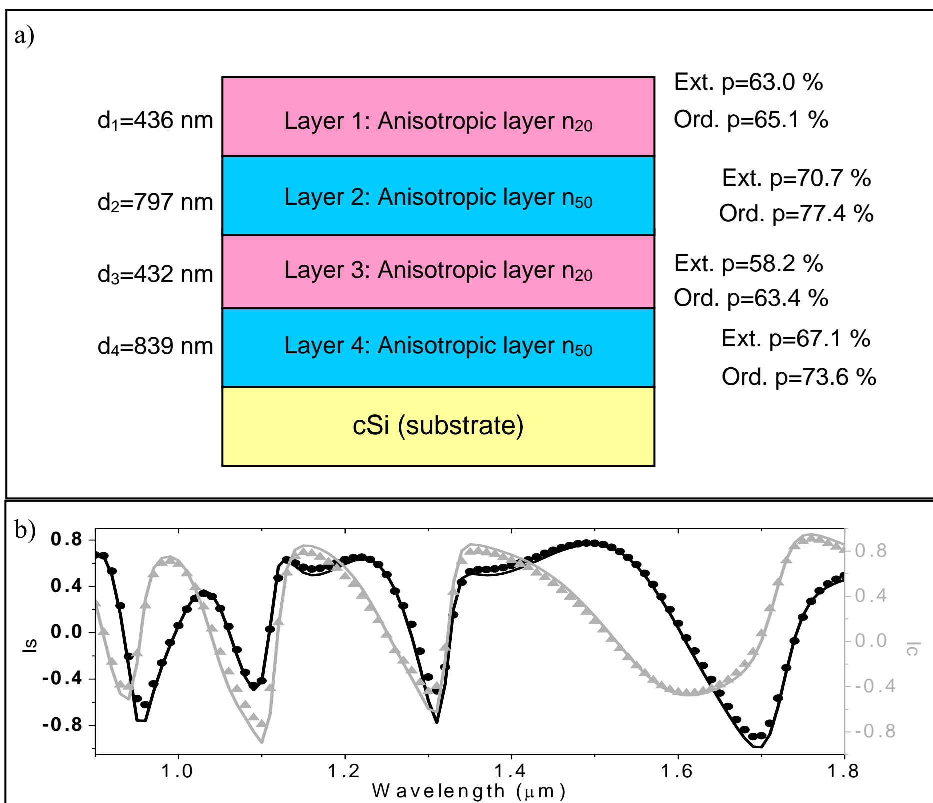

Fig. 6.19. a) Schematic representation of the ideal structure used to build the optical model consisting of four anisotropic layers (two periods) together with the best fitted values of the variable parameters: thickness and porosity for the extraordinary and the ordinary indices b) Measured (dots) and simulated (solid line) ellipsometric data obtained with the optical model shown in Fig. 6.19a. .

Concerning the porosities (refractive indices), we can observe that for both current densities the porosities are very close to the respective monolayers but they slightly decrease with depth. We can observe that the porosity of layer 1 is slightly higher than the porosity of layer 3 although they have been fabricated with the same current density. The same happens with layers 2 and 4. This variation in depth can be explained by the chemical etching that acts on the outer layers and that adds its contribution to that of the initial electrochemical

UNIVERSITAT ROVIRA I VIRGILI
DESIGN, FABRICATION AND CHARACTERIZATION OF POROUS SILICON MULTILAYER OPTICAL DEVICES
Elisabet Xifré Pérez
ISBN:978-84-691-0362-3 /DL: T.2181-2007

etching. Hence, it is usual for the outer layers to have a higher porosity than the inner layers obtained with the same current densities. The ellipsometric results corroborate this fact.

Fig. 6.19b compares the measured ellipsometric data with the ones obtained with the simulation of the optical model shown in Fig. 6.19b. The difference is very low, χ^2=48.9, considering the high number of parameters to be determined in the optical model.

6.4.3. Three period multilayer

This multilayer is formed by three periods (six layers). The top layer of the period has been obtained with the application of J=20 mA/cm^2 for 20 s and the bottom layer with J=50 mA/cm^2 for also 20 s. The SEM image of this multilayer can be observed in Fig. 6.20, where the thickness of each layer has been estimated. These thickness values are approximate because the SEM image does not allow an exact measurement due to the roughness of the interfaces, so we can consider that the error introduced in these estimations can be around 10-15 %.

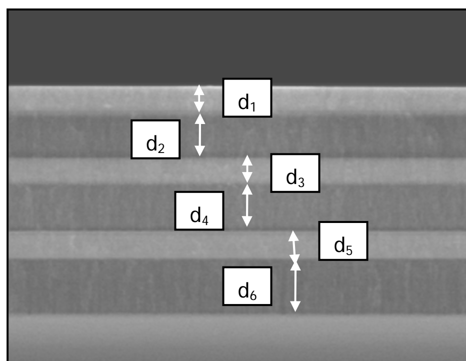

Fig. 6.20. SEM image of the three-period multilayer. The interfaces between the different porous layers can be seen. The thickness of the layers are approximately $d_1 \approx$ 440 nm, $d_2 \approx$ 790 nm, $d_3 \approx$ 370 nm, $d_4 \approx$ 775 nm, $d_5 \approx$ 411 nm, and $d_6 \approx$ 848 nm.

ISBN:978-84-691-0362-3 /DL: T.2181-2007

Fig. 6.21a shows the optical model realized for this multilayer where the variable parameters to be fitted are the thicknesses and the porosities (ordinary and extraordinary) of all the layers.

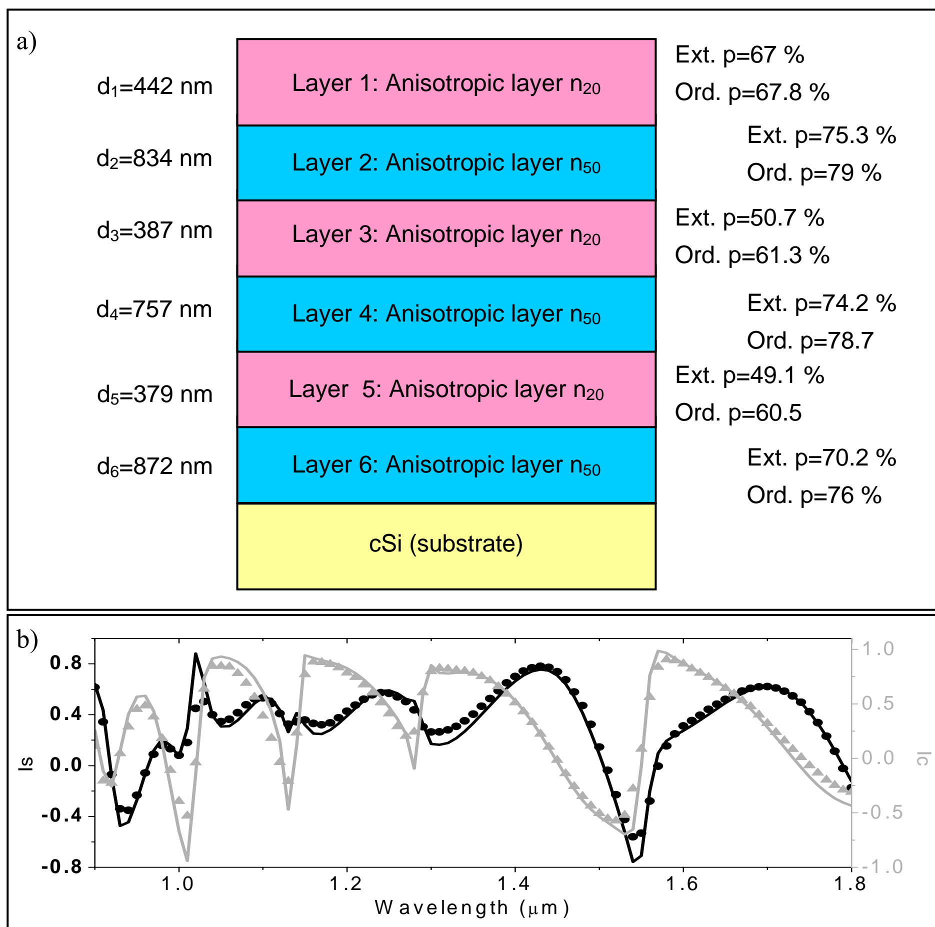

Fig. 6.21. a) Schematic representation of the ideal structure used to build the optical model consisting of six anisotropic layers (three periods) together with the best fitted values of the variable parameters: thickness and porosity for the extraordinary and the ordinary indices. b) Measured (dots) and simulated (solid line) ellipsometric data obtained with the optical model shown in Fig. 6.21a.

ISBN:978-84-691-0362-3 /DL: T.2181-2007

The number of parameters to be determined is very high, concretely 18, which increases the difficulty of finding an accurate fit. Many different values of these parameters give a good agreement between the simulated and the measured ellipsometric data. But not all of these fits are correct because their physical meaning can be contradictory with the characteristics of the multilayer that are *a priori* known, i.e. layer thicknesses or porosities very different to the expected. Here we present one of the best fits obtained that provided parameters that are in accordance with the expected values.

If we start considering the porosities of the layers we can observe that layers obtained with the same current density have different values of their respective porosity that depends on the depth. We have observed that the porosity decreases with depth. This effect has also been observed for stacks of two periods and a discussion is provided above in the text and in the bibliography. This porosity variation with depth happens for both types of layers, 20 mA/cm^2 and 50 mA/cm^2. We can also see that the porosities of these layers are similar to the ones obtained with the analysis of the respective monolayers but there is a difference between them that is higher when the thickness of the multilayer increases.

The differences between the measured and the simulated ellipsometric data can be observed in Fig. 6.21b, where χ^2=156.3. This error is higher than the ones of the previous multilayers. This is due to the higher number of layers of the multilayer to be characterized.

6.5. Conclusions

The ellipsometric characterization of porous silicon monolayers and multilayers has been realized. This characterization has determined the main physical characteristics of these layers, porosity (and therefore refractive index) and thickness; and has permitted the analysis of their anisotropy.

The refractive index of the porous material was modeled with the Bruggeman effective medium approximation (EMA) by assuming a mixture of crystalline silicon and void. For low porosities, the optical behavior of the

UNIVERSITAT ROVIRA I VIRGILI
DESIGN, FABRICATION AND CHARACTERIZATION OF POROUS SILICON MULTILAYER OPTICAL DEVICES
Elisabet Xifré Pérez
ISBN:978-84-691-0362-3 /DL: T.2181-2007

samples has been modeled with a graded index model. However, as porosity of the monolayers increases, the gradient index model is no longer valid, and it must be substituted by another one consisting of an anisotropic uniaxial layer with its optical axis oriented perpendicular to the surface of the sample. From the ellipsometric study, we demonstrate that the anisotropy increases with the porosity. The depolarization of light caused by sample thickness non-uniformity has been measured and used to estimate the quality of measurements as well as the adequacy and goodness of ellipsometric data fits. These monolayers have been also analyzed by spectroscopic reflectometry, using a FTIR spectrometer, and by scanning electron microscopy (SEM). A good agreement has been observed between the refractive indices and thicknesses obtained with these methods and the values estimated with the spectroscopic ellipsometry.

Apart from the monolayers, we have also studied multilayers consisting of a periodic repetition of two layers with different degrees of porosity. The thicknesses of the layers that form the multilayers have been determined by ellipsometry and they agree with the values obtained with the SEM analysis. The porosity of these layers have been also studied, a characteristic of the multilayers that could not be to analyze with any of the other characterization methods used. We have observed that the anisotropic models obtained from the study of the monolayers can be used as a starting point for the characterization of the different layers of the multilayers. However, the ellipsometric measurements revealed that there is a slight difference between the layers appertaining to the multilayer, and the corresponding monolayers obtained with identical fabrication parameters. In a multilayer, the layers fabricated with the same current density do not have the same porosity but it decreases with depth. This means that there is a gradient of porosity with depth.

UNIVERSITAT ROVIRA I VIRGILI
DESIGN, FABRICATION AND CHARACTERIZATION OF POROUS SILICON MULTILAYER OPTICAL DEVICES
Elisabet Xifré Pérez
ISBN: 978-84-691-0362-3 /DL: T.2181-2007

Chapter 7

Optical devices based on porous silicon multilayers

In this chapter we present multilayer optical devices fabricated with porous silicon. All these devices have been designed using the realized simulation programs and the mathematical study presented in chapters 3 and 4. They have been fabricated with the fabrication system explained and calibrated in chapter 5 and their optical response, specially the reflectivity spectrum, has been studied.

The optical devices presented here are DBRs, microcavities and omnidirectional mirrors. The optical response of a microcavity has been studied under different humidity conditions. The application of the periodic structure is evaluated for obtaining omnidirectional mirrors. Finally, the omnidirectional bandgap of a new structure consisting of periodic structures stacked together is studied.

UNIVERSITAT ROVIRA I VIRGILI
DESIGN, FABRICATION AND CHARACTERIZATION OF POROUS SILICON MULTILAYER OPTICAL DEVICES
Elisabet Xifré Pérez
ISBN: 978-84-691-0362-3 /DL: T.2181-2007

7.1. Distributed Bragg Reflector

7.1.1. Fabrication and characterization

The DBR consists of the periodic repetition of two layers obtained with different current densities, and therefore with different refractive indices. The two current densities chosen for the fabrication of this DBR are 30 and 70 mA/cm^2. For its formation we have used p+-type silicon wafers with a resistivity of 0.01 Ω·cm and ethanoic HF electrolyte with concentration of 15.4% (volumetric ratio).

The calibration of the fabrication system, realized with the measurement of interference fringes method (MIF) and SEM, indicated that for J=70 mA/cm^2, the refractive index varies from 1.33 to 1.28 for the wavelength range between 1 and 4 μm and the etch rate is 49.7 nm/s. For J=30 mA/cm^2, the etch rate is 26.7 nm/s and its refractive index varies between 1.72 and 1.65 for the same wavelength range. This multilayer has been obtained with the lateral-wafer cell, therefore the calibration of the system is different than the one presented in section 5.3, that was the calibration for the system with the bottom-wafer cell.

These refractive indices obtained with these current densities are very low, probably due to the low HF concentration used for the electrolyte, only 15.4 % (vol). These refractive indices agree with the ones obtained by other authors for similar HF concentrations [103]. For higher concentrations of HF, higher values of refractive index are possible for the same current densities [39,102].

The DBR was fabricated by applying the current densities J=30 mA/cm^2 (obtaining the n_H layer) and 70 mA/cm^2 (for the n_L layer) for 10 s. According to the etch rate calculated from the characterization of the monolayers, the thickness of the layers are supposed to be approximately h_H=267 nm and h_L=500 nm, respectively. The period thickness is expressed as $\Lambda = h_H + h_L$. Fig. 7.1 shows the cross section of the fabricated multilayer. The dark gray layers correspond to the layers with n_L and the light gray are the ones with refractive index n_H. The number of periods of the measured multilayer is 15.

ISBN: 978-84-691-0362-3 /DL: T.2181-2007

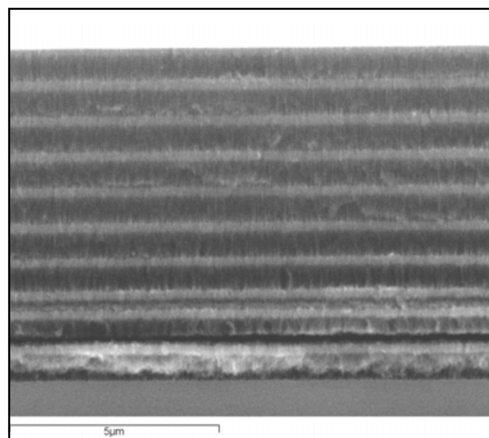

Fig. 7.1. SEM image of the fabricated multilayer. The light gray layers are the high refractive index ones that are thinner than and the low refractive index layers (dark gray layers).

The characterization of the DBR has been realized studying its reflectivity spectrum with the FTIR spectrometer Bruker Vertex 70 within the wavelength range from 1 to 4 µm. Fig. 7.2 shows the FTIR reflectivity spectrum measurements of the fabricated multilayer for different angles of incidence: 12, 30, 44, 50, 58 and 66 degrees. We can observe that the multilayer presents a high reflectivity band that is centered approximately at 2.2 µm for incidence angle 12º. When the angle of incidence increases, the high reflectivity band not only shifts to lower wavelengths, but also becomes narrower and its maximum decreases. For angles of incidence higher than 50º the maximum reflectivity is lower than 1.

ISBN: 978-84-691-0362-3 /DL: T.2181-2007

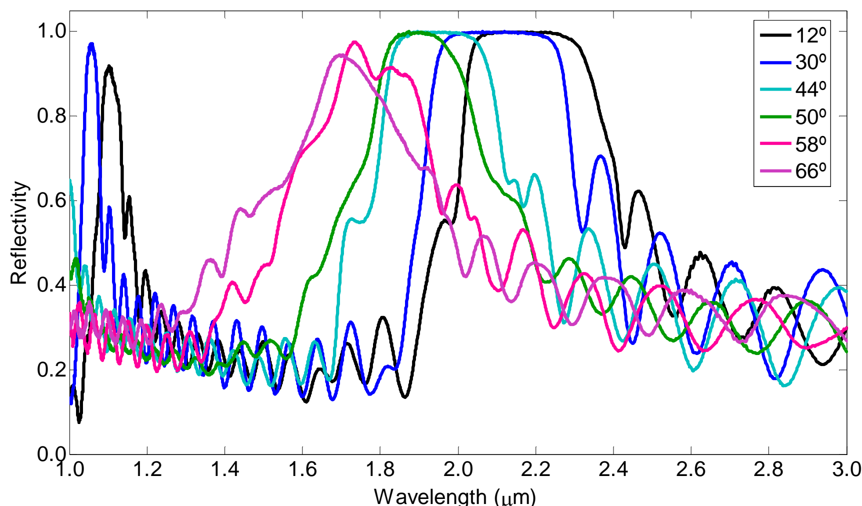

Fig. 7.2. Reflectivity spectra of the fabricated DBR, measured for six different angles of incidence. The bandgap can be clearly observed centered approximately at λ=2.2 μm for θ=12º and shifts to the left when the incidence angle increases.

7.1.2. Simulation

The fabricated multilayer structure has been simulated using the programs realized for this purpose. As has been explained in section 5.2.2, the variation of the refractive index in the studied wavelength range is small (less than 5%), for this reason, the refractive indices used for the simulation have been considered constant and with approximate values n_L=1.3 and n_H=1.7. The thicknesses of the layers have been adjusted by fitting the simulation to the experimental spectra and are h_L=500 nm and h_H=270 nm, which are in good agreement with the calculated etching rate. The simulated and the measured reflectivity spectra of the multilayer are presented for three different angles of incidence in Fig. 7.3. The agreement between the measured and the simulated spectra shows that the parameters of the fabricated DBR (refractive indices and thicknesses) are approximately the ones expected from the formation parameters (current density and etch time), which demonstrates the control of

UNIVERSITAT ROVIRA I VIRGILI
DESIGN, FABRICATION AND CHARACTERIZATION OF POROUS SILICON MULTILAYER OPTICAL DEVICES
Elisabet Xifré Pérez
ISBN: 978-84-691-0362-3 /DL: T.2181-2007

the etching process. Besides, this fact shows that the behavior of the DBR can be theoretically described.

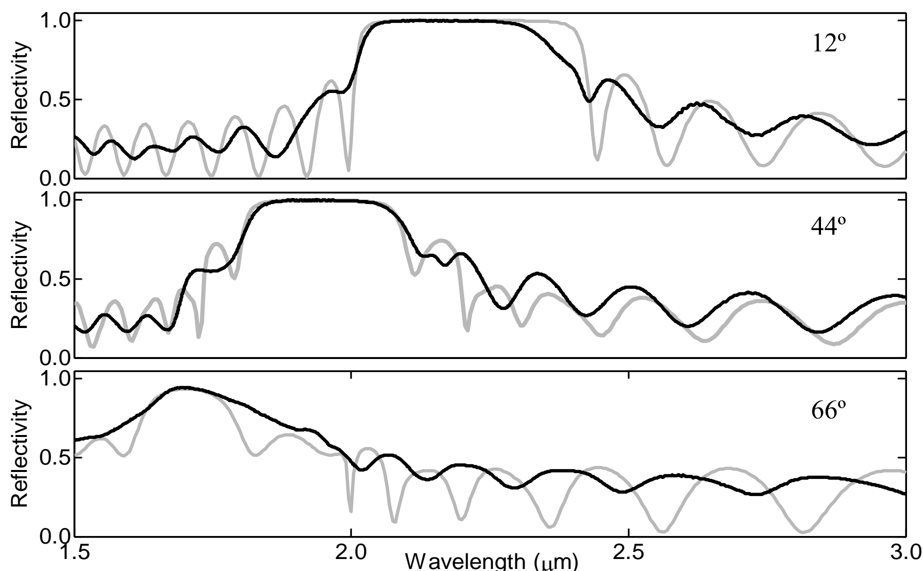

Fig. 7.3. Reflectivity spectra of the fabricated DBR for angles of incidence 12º, 44º and 66º. The thick solid lines represent measured spectra, whereas the gray solid lines are the simulated spectra.

For a particular wavelength λ, it is possible to calculate from the projected band structure (PBS) [116] the range of incidence angles for which the reflectivity is near 1. Fig. 7.4 shows the PBS of the fabricated multilayer. For a given wavelength λ (corresponding to $\omega\Lambda/2\pi c$), $\beta\Lambda/2\pi$ is related to the angle of incidence θ_i with $\beta=(\omega/c)n_i\sin(\theta_i)$. The light line indicates the relation between $\omega\Lambda/2\pi c$ and $\beta\Lambda/2\pi$ for incidence angle 90º in air. The shaded region represents the allowed states and the white region within the light lines represents the bandgap, that corresponds to the high reflectivity band. Although in the PBS both polarizations are represented, TM polarization is more restrictive than TE, therefore the TM polarization bandgap limits will be observed.

ISBN: 978-84-691-0362-3 /DL: T.2181-2007

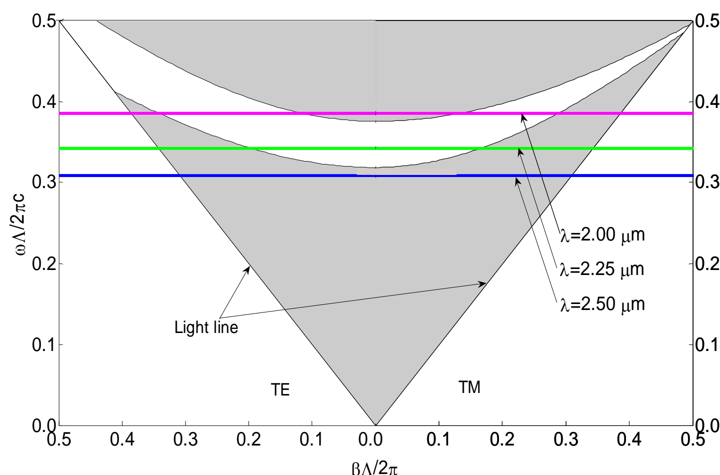

Fig. 7.4. Projected band structure (PBS) of the studied multilayer. The lines indicate the normalized frequencies corresponding to λ=2, 2.25 and 2.5 μm.

We now analyze the particular cases of three different λ: 2.50, 2.25 and 2.00 μm. For λ=2.5 μm ($\omega\Lambda/2\pi c$=0.308) there is no bandgap for any angle of incidence θ_i (Fig. 7.4). This can be also observed in Fig. 7.2, where the reflectivity for this wavelength is low for any θ_i. For λ=2.25 μm ($\omega\Lambda/2\pi c$=0.342), the bandgap exists for θ_i=0º to θ_i=30º. This fact is shown in Fig. 7.2, where we can see that for 12º and 30º the reflectivity at λ=2.25 μm is near 1 but for higher angles it is very low. Finally, for 2 μm ($\omega\Lambda/2\pi c$=0.385) the bandgap only exists for θ_i from 20º to 48º. In Fig. 7.3 this fact is clearly visible. We can observe that for 12º the reflectivity at λ=2 μm is low (this angle does not belong to the bandgap), when θ_i=44º the reflectivity is 1 (bandgap) and when θ_i increases (66º) the reflectivity is low again because this angle does not belong to the bandgap. Hence, it is demonstrated that for any wavelength, the range of incidence angles for which the bandgap exists can be studied with the projected band structure.

ISBN: 978-84-691-0362-3 /DL: T.2181-2007

7.2. Microcavity

7.2.1. Fabrication, characterization and simulation

The porous silicon microcavity has been obtained by the electrochemical etching of p+-type silicon wafers with a resistivity of 0.01Ω·cm in an ethanoic HF electrolyte with concentration of 15.4% (volumetric ratio). Fig. 7.5 shows the schematic of the microcavity and the SEM image of the fabricated microcavity, that consists of a spacer layer inserted in between two symmetric Distributed Bragg Reflectors (DBR). Each DBR has three periods. Each period consists of two layers with different refractive indices (n_1, n_2) and thicknesses (d_1, d_2).

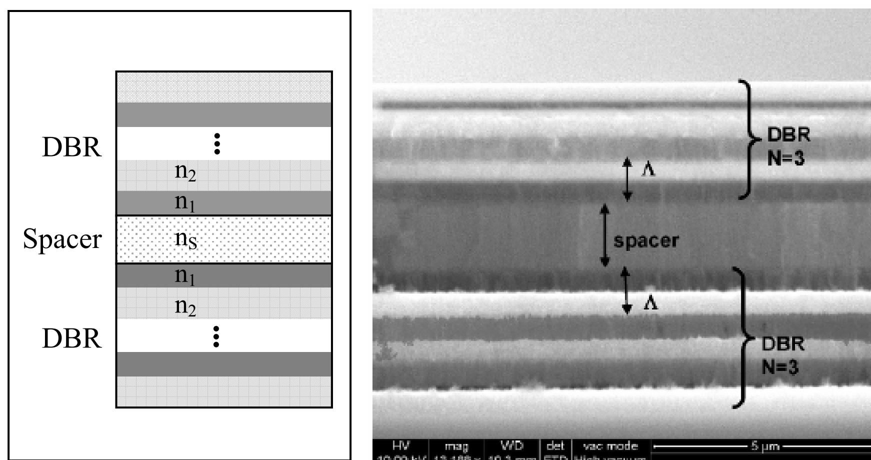

Fig. 7.5. Left: Schematic of the microcavity structure. Right: SEM image of the fabricated porous silicon microcavity. The spacer layer is located in between two DBR. Each DBR is formed by the periodic repetition (N=3) of two layers with low refractive index (gray layer) and high refractive index (light gray layer).

ISBN: 978-84-691-0362-3 /DL: T.2181-2007

These values of refractive indices and thicknesses have been used to simulate the optical properties of the porous silicon microcavity using the transfer matrix method. Fig. 7.6 shows the simulated reflectivity spectrum assuming an incidence angle of 20º, where we can observe the reflectivity resonance around 3 μm. Fig. 7.6 also shows the experimental reflectivity spectrum of the microcavity for an incidence angle 20º using a FTIR spectrometer Bruker Vertex 70. The spectrum is characterized by a reflectivity resonance at 2.97 μm in between two high reflectivity bands, in good agreement with the simulated results. Narrower resonance widths could be obtained either by increasing the number of periods of the DBR or by enhancing the fabrication conditions [98].

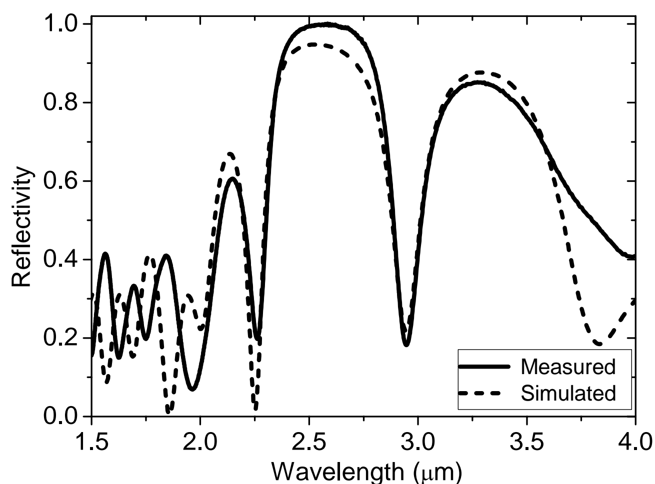

Fig. 7.6. Measured (solid line) and simulated (dashed line) reflectivity spectrum of the fabricated microcavity for incidence angle 20º. The reflectivity resonance is situated at λ=2.97 μm. The differences between the measured and the simulated spectra are due to the anisotropy of the low refractive index layers that is not considered in the simulation program.

UNIVERSITAT ROVIRA I VIRGILI
DESIGN, FABRICATION AND CHARACTERIZATION OF POROUS SILICON MULTILAYER OPTICAL DEVICES
Elisabet Xifré Pérez
ISBN: 978-84-691-0362-3 /DL: T.2181-2007

7.2.2. Influence of the relative humidity on the reflectivity spectrum of the microcavity

Fig. 7.7 shows the measured reflectivity spectrum of the fabricated microcavity for different humidity levels. The changes in the spectrum are small, in good agreement with previous results [135]. The inset in Fig. 7.7 shows the zoom of reflectivity resonance and its fitting by using a Gaussian function. We can observe that when humidity increases, the reflectivity resonance shifts to higher wavelengths and its reflectivity decreases. Fig. 7.8a shows this resonance shift. The reflectivity spectrum of the microcavity is recovered when the humidity returns to the initial laboratory conditions.

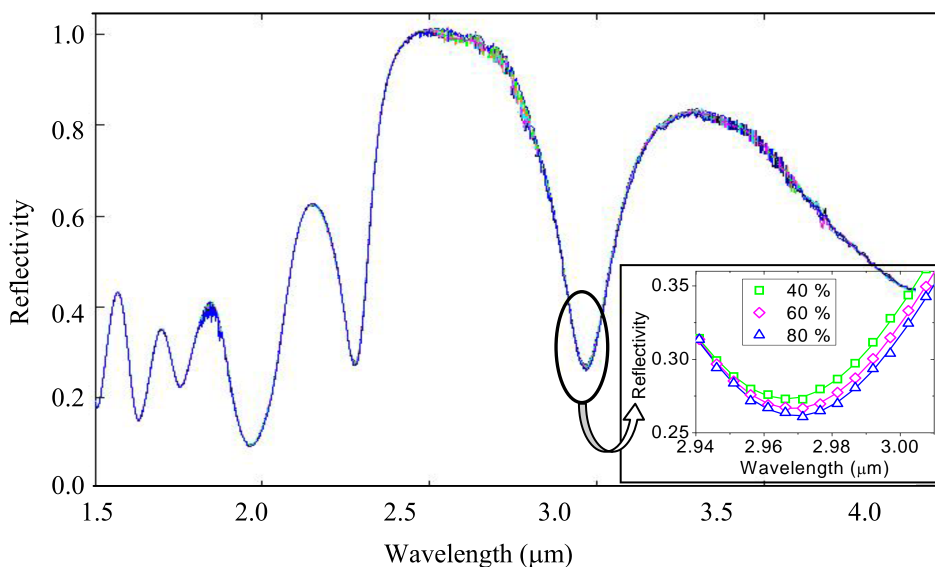

Fig. 7.7. Measured reflectivity spectrum for humidity levels of 40%, 50%, 60%, 70% and 80%. Inset: Zoom of the measured (symbol) reflectivity spectrum of the microcavity centered at the reflectivity resonance for humidity levels of 40%, 60% and 80%. The solid lines are the fitted values using a Gaussian function.

UNIVERSITAT ROVIRA I VIRGILI
DESIGN, FABRICATION AND CHARACTERIZATION OF POROUS SILICON MULTILAYER OPTICAL DEVICES
Elisabet Xifré Pérez
ISBN: 978-84-691-0362-3 /DL: T.2181-2007

These variations are probably due to water vapor infiltrated into the pores of the porous silicon layers. Water vapor slightly increases the effective refractive index of the layers as the air in the pores is substituted by water vapor. As the increase of the refractive index is very slight, we can explain the slight shift of the reflectivity resonance to higher wavelengths and the decrease of the reflectivity when the humidity rises.

To quantify the sensor sensitivity at a given λ, we define the merit function R as

$$R = \frac{R_H - R_{H\max}}{R_{H\max}} \times 100(\%) \tag{7.1}$$

where R_{Hmax} is the measured reflectivity for the maximum relative humidity and R_H is the measured reflectivity for a given relative humidity. Fig. 7.8b shows the linear dependence of this merit function for λ= 3 μm in the humidity range from 35% to 80%, where R_{Hmax} is 0.324 for 80%.

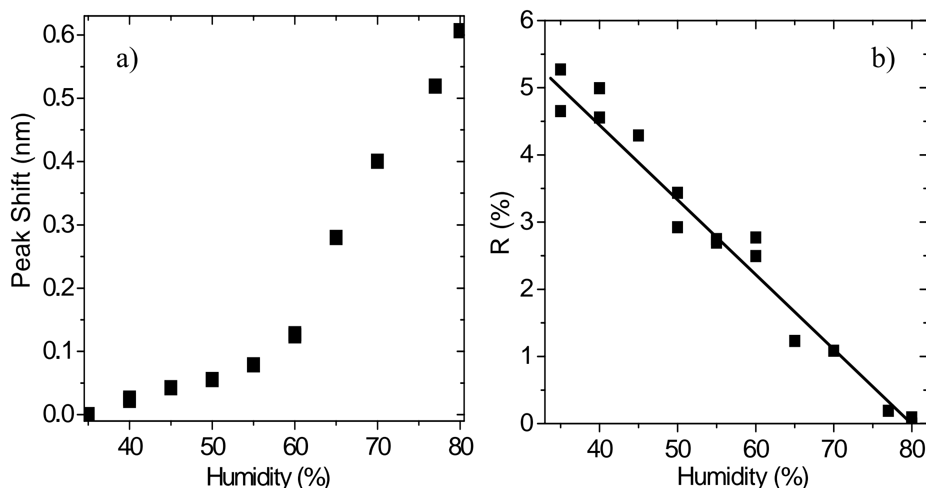

Fig. 7.8. a) Variation of the reflectivity resonance position for different humidity levels b) Variation of the merit function, defined by the Eq. (7.1), for different humidity levels at λ= 3 μm. The linear dependence is also shown.

ISBN: 978-84-691-0362-3 /DL: T.2181-2007

7.2.3. Water condensation on the surface of the microcavity

In this section, we study the changes in the reflectivity spectrum when water is not only present as vapor infiltrated into the pores but also as a thin film on the surface of the microcavity due to the water condensation.

Fig. 7.9 shows the measured reflectivity spectrum of the microcavity for different humidity levels with condensed water on the surface. The initial reflectivity measurement was realized when the microcavity was in a 60% relative humidity with a condensed water film on its surface. This measurement presents very low reflectivity values for the whole wavelength range. After this measurement, a desiccant has been inserted into the FTIR sample compartment to reduce the humidity of the ambient and the condensation on the microcavity, and the rest of measurements have been realized at different times during this drying process. We observe that when the humidity decreases, the reflectivity increases for the whole range of wavelengths and the position of the reflectivity resonance is also affected.

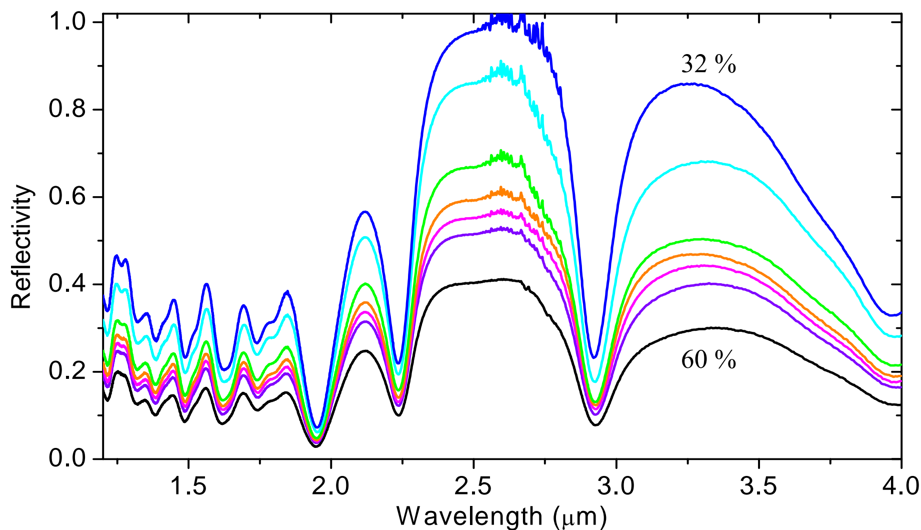

Fig. 7.9. Measured reflectivity spectrum for different humidity levels with the presence of condensed water on the surface of the microcavity. The lowest humidity level measured in 32 % and the highest is 60 %.

UNIVERSITAT ROVIRA I VIRGILI
DESIGN, FABRICATION AND CHARACTERIZATION OF POROUS SILICON MULTILAYER OPTICAL DEVICES
Elisabet Xifré Pérez
ISBN: 978-84-691-0362-3 /DL: T.2181-2007

To quantify the relative reflectivity variation, we used the merit function defined by the Eq. (7.1). Fig. 7.10a shows the merit function R for λ= 3 μm, where R_{Hmax} is 0.167 for 60%. The obtained values follow an exponential law instead of the linear law obtained in the previous section. According to these results, we could say that the condensation on the surface could mask the humidity measurements of this type of sensor. Fig. 7.10b shows the resonance shift. We can observe that the thin film of condensed water on the microcavity surface leads to larger shifts than when there is only water vapor infiltrated into the pores.

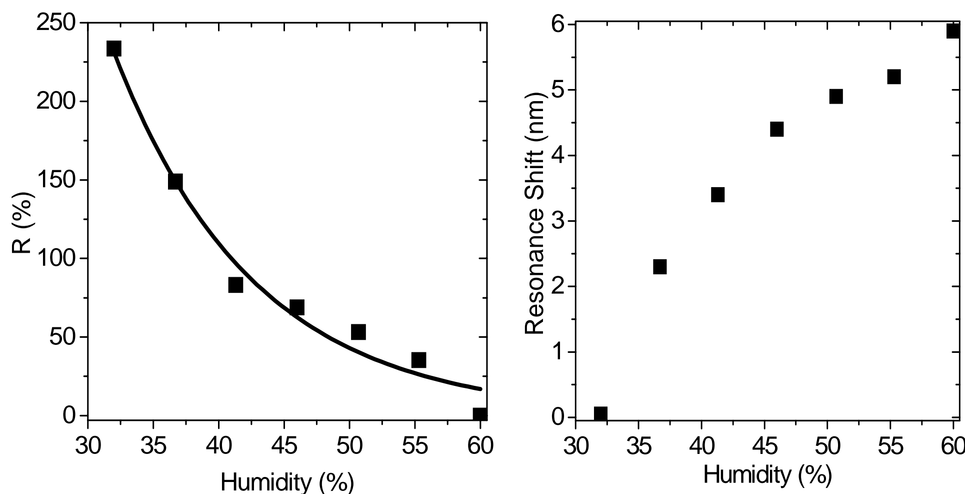

Fig. 7.10 a) Variation of the merit function for different humidity levels at λ=3 μm. The exponential dependence is also shown, b) Variation of the reflectivity resonance position for different humidity levels.

ISBN: 978-84-691-0362-3 /DL: T.2181-2007

7.3. Omnidirectional mirrors

Omnidirectional mirrors are characterized by their omnidirectional bandgap, that is the wavelength range where the reflectivity is the unity for any incidence angle and any polarization. All the parameters that determine the existence and the width of the omnidirectional bandgap have been already discussed in detail in chapter 4. In this section, we present some multilayer structures fabricated with porous silicon and we study the existence of an omnidirectional bandgap for all of them. Firstly, the widely used periodic structure is evaluated. Secondly, a new structure consisting of several periodic structures stacked together is fabricated and characterized and its suitability for obtaining omnidirectional mirrors is studied.

7.3.1. Design, fabrication and characterization of periodic structures

The periodic omnidirectional mirror structure consists of the periodic repetition of two layers obtained with different current densities. In chapter 4, a detailed study of the parameters that influence on the optical behavior of this structure has been presented.

For the fabrication of this periodic mirror we have chosen the current densities J_1=10 mA/cm^2 and J_2=50 mA/cm^2. Current densities lower than 10 mA/cm^2 yielded porous layers with very slow etch rates, increasing the duration of the layer formation without a significant gain in the index. Current densities higher than 50 mA/cm^2 yielded fragile porous layers that could not be characterized using spectroscopic ellipsometry.

For the fabrication of this structure, p^+-type silicon wafers with a resistivity of 0.01 Ω·cm and ethanoic HF electrolyte with concentration of 15.4% (volumetric ratio) have been used. For these formation parameters, the fabrication system of porous silicon layers has been calibrated (section 4.3). According to this calibration, for J_1=10 mA/cm^2, the refractive index varies from 2.21 to 2.12 for the wavelength range between 1 and 4 µm and the etch rate is approximately 10.7 nm/s. For J_2=50 mA/cm^2, the etch rate is estimated to

UNIVERSITAT ROVIRA I VIRGILI
DESIGN, FABRICATION AND CHARACTERIZATION OF POROUS SILICON MULTILAYER OPTICAL DEVICES
Elisabet Xifré Pérez
ISBN: 978-84-691-0362-3 /DL: T.2181-2007

be 36 nm/s and its refractive index varies between 1.5 and 1.45 for the same wavelength range.

From the theoretical study, we know that to obtain a mirror with the omnidirectional bandgap centered at λ=1.55 µm, the bandgap for normal incidence has to be centered at approximately λ=1.6 µm. The thickness of the layers for each refractive index determines this center wavelength. The layer thicknesses that lead to this center wavelength are approximately d_1=171.2 nm, and d_2=288 nm, being the period thickness $\Lambda= d_1+d_2$=459.2 nm.

The reflectivity spectrum of this periodic multilayer has been simulated using one of the developed programs. For the simulation, the refractive index of each layer has been supposed to be constant because its variation in the studied wavelength range is very small (less than 5%). The refractive indices used for the simulation are n_1=2.15 and n_2=1.45 and the thicknesses are the ones calculated: d_1=171.2 nm, and d_2=288 nm. The number of periods is 15. Fig. 7.11 shows the simulated reflectivity spectrum of this periodic structure for normal incidence. We can observe that the bandgap is centered at λ=1.6 µm.

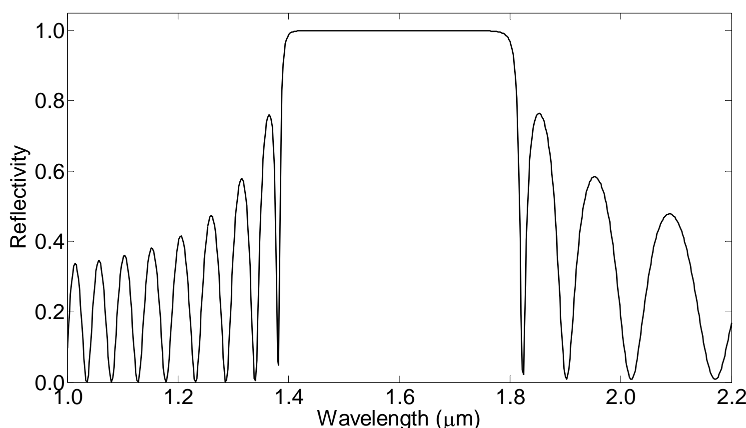

Fig. 7.11. Simulated reflectivity spectrum of the periodic structure for normal incidence. The bandgap is centered approximately at λ=1.6 µm.

UNIVERSITAT ROVIRA I VIRGILI
DESIGN, FABRICATION AND CHARACTERIZATION OF POROUS SILICON MULTILAYER OPTICAL DEVICES
Elisabet Xifré Pérez
ISBN: 978-84-691-0362-3 /DL: T.2181-2007

This designed structure has been fabricated. The refractive indices of the layers are determined by the current densities and the thicknesses are determined by the etching times. From the etch rate we calculate the etching times needed to obtain the desired thicknesses. For the current densities used, the etching times that lead to these thicknesses are t_1=16 s for J_1, and t_2= 8 s for J_2, The number of periods is 15. The reflectivity spectrum of the fabricated multilayer has been measured with the FTIR spectrometer Bruker Vertex 70 within the wavelength range from 1 to 3 µm. Fig. 7.12 shows the measured reflectivity spectra for different incidence angles. The lowest incidence angle that can be measured with this FTIR is 12º and we can observe that for this incidence angle the bandgap is centered approximately at λ=1.58 µm. When the incidence angle increases the bandgap width decreases and shifts to lower wavelengths. The highest incidence angle that can be measured with the FTIR is approximately 65º because reflectivity spectra measured for incidence angles between 65º and 80º are partially affected by the sample holder.

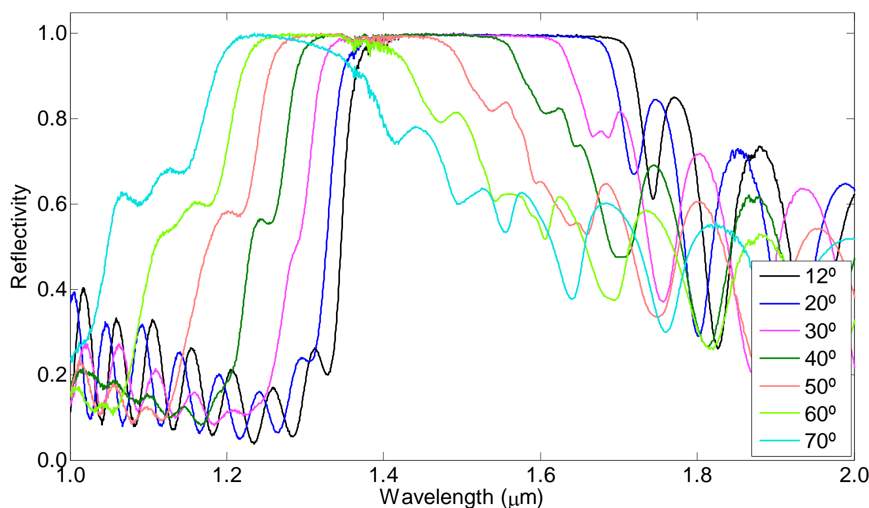

Fig. 7.12. Measured reflectivity spectrum of the periodic structure for seven different incidence angles. The bandgap is centered approximately at 1.58 µm for incidence angle 12º. When the incidence angle increases the bandgap shifts to lower wavelengths.

UNIVERSITAT ROVIRA I VIRGILI
DESIGN, FABRICATION AND CHARACTERIZATION OF POROUS SILICON MULTILAYER OPTICAL DEVICES
Elisabet Xifré Pérez
ISBN: 978-84-691-0362-3 /DL: T.2181-2007

From this figure, we can observe that the periodic multilayer structure has not an omnidirectional bandgap. It has a bandgap for an interval of incidence angles that goes from θ=12º to approximately θ=60º. It is not an omnidirectional mirror. This agrees with the theoretical study, where we deduced that to obtain an omnidirectional mirror, the high refractive index of the periodic multilayer must be higher than 2.25. The refractive index range obtainable with our fabrication conditions goes from 1.45 to 2.15 therefore to obtain an omnidirectional mirror one of the new structures proposed in chapter 4 consisting on different periodic structures stacked together has been designed and fabricated.

7.3.2. Design of a new omnidirectional mirror structure

We now study the reflectivity spectrum of a multilayer consisting of two different periodic structures (PS) stacked together. The schematic structure of this multilayer can be observed in Fig. 7.13.

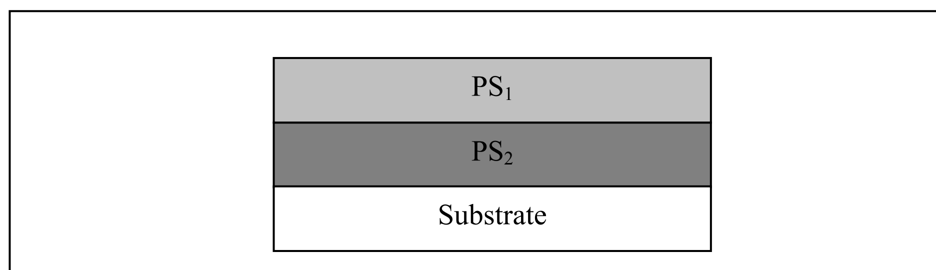

Fig. 7.13. Schematic of the multilayer formed by two periodic structures stacked together.

The theoretical study demonstrated that the bandgap of a multilayer formed by two structures stacked together is the union of the bandgaps of the two structures (section 3.3.1.4). This stacked structure presents a wider bandgap

ISBN: 978-84-691-0362-3 /DL: T.2181-2007

for all the incidence angles and therefore an omnidirectional bandgap could be obtained.

The two periodic structures that form this multilayer have to be appropriately chosen for the widening of the bandgap. The first periodic structure (PS_1) is the one described in the previous section. The second one (PS_2) is designed to have a bandgap centered at a slightly higher wavelength than the bandgap of PS_1. The refractive indices of PS_2 are the same used for PS_1: n_1=2.15 and n_2=1.45. Due to the small bandgap shift desired and to ease the fabrication process, we have chosen a larger thickness for the high refractive index layer whereas the thickness for the low refractive index layer remains the same. The chosen thicknesses for the layers of PS_2 are d_1=214 nm, and d_2=288 nm, being the period thickness $\Lambda=d_1+d_2$=502 μm.

Fig. 7.14 shows the simulated reflectivity spectrum of PS_2 for normal incidence and it is compared with the one of PS_1. The number of periods of both PS is 15. We can observe that both spectra intersect.

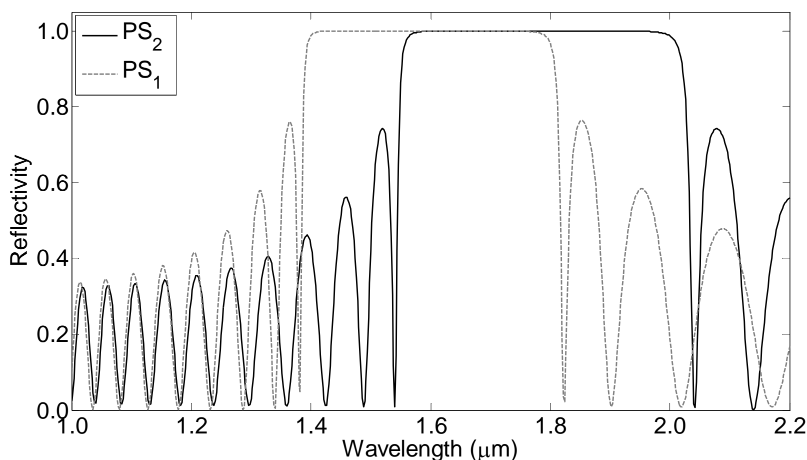

Fig. 7.14. Simulated reflectivity spectrum of PS_2 (black line). It can be compared with the reflectivity spectrum of PS_1 (dashed gray line). Both spectra have been simulated for normal incidence.

ISBN: 978-84-691-0362-3 /DL: T.2181-2007

The simulated reflectivity spectrum of the stacked structure is represented in Fig. 7.15. The refractive indices used for the simulation are n_1=2.15 and n_2=1.45. The thicknesses are the ones calculated before for each PS. The incidence angles simulated are the ones that determine the existence of the omndirectional bandgap. The simulated spectra show that this structure has an omnidirectional bangap, therefore it is an omnidirectional mirror. With this result it is demonstrated that the limitations of the refractive index range can be overcome by the use of this new stacked structure proposed.

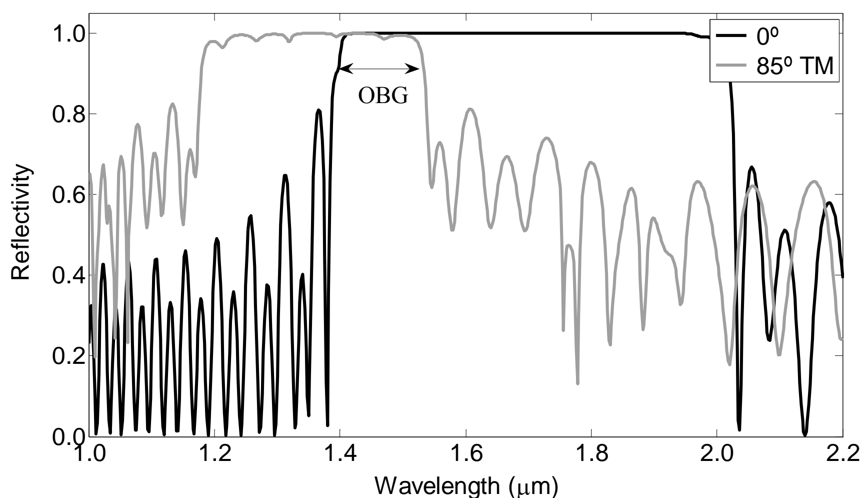

Fig. 7.15. Simulated reflectivity spectra of the stacked structure for incidence angles θ=0º and θ=85º. The omnidirectional bandgap (OBG) is indicated.

ISBN: 978-84-691-0362-3 /DL: T.2181-2007

7.3.3. Fabrication and characterization of the new omnidirectional mirror structure

The stacked multilayer consisting of the two PS stacked together has been fabricated using p^+-type silicon wafers with a resistivity of 0.01 Ω·cm and ethanoic HF electrolyte with concentration of 15.4% (volumetric ratio). The current densities applied are J_1=10 mA/cm^2 and J_2=50 mA/cm^2. For 15 periods the etching times are t_1=16 s for J_1, and t_2= 8 s for J_2 (corresponding to PS_1) and for the next 15 periods the etching times are t_1= 20 s for J_1, and t_2= 8 s for J_2. These last etching times correspond to PS_2 and have been calculated from the etch rate to obtain the thicknesses adjusted during the simulation process of this PS.

The PS_2 has been also fabricated to study its reflectivity spectrum and compare it with the one of the stacked structure. The parameters used for its fabrication are the same than for PS_1, therefore the refractive indices of the layers of this PS_2 are expected to be the same than the ones of PS_1. The etching times are t_1= 20 s for J_1, and t_2= 8 s for J_2, the same ones used for the stacked structure.

The reflectivity spectrum of the stacked multilayer is presented in Fig. 7.16 for incidence angle θ=12º. It is compared with the measured reflectivity spectra of PS_1 and PS_2 for the same incidence angle. They have been measured with the FTIR spectrometer Bruker Vertex 70 at the wavelength range from 1 to 3 µm. It can be observed that the bandgap of the stacked structure is wider than the bandgaps of PS_1 and PS_2 and is approximately the union of their bandgaps, as was expected. The bandgap of the stacked structure is slightly shifted to lower wavelengths than the bandgaps of PS_1 and PS_2. This is due to two effects: the small gradients of porosity and thickness with depth during the porous silicon fabrication process that are more visible in the stacked structure spectrum because this structure is thicker than the PS; and that the thicknesses of the layers in multilayers are systematically lower than the expected values calculated from the etch rate [19]. Apart from this small shift, we can clearly observe the widening of the bandgap.

UNIVERSITAT ROVIRA I VIRGILI
DESIGN, FABRICATION AND CHARACTERIZATION OF POROUS SILICON MULTILAYER OPTICAL DEVICES
Elisabet Xifré Pérez
ISBN: 978-84-691-0362-3 /DL: T.2181-2007

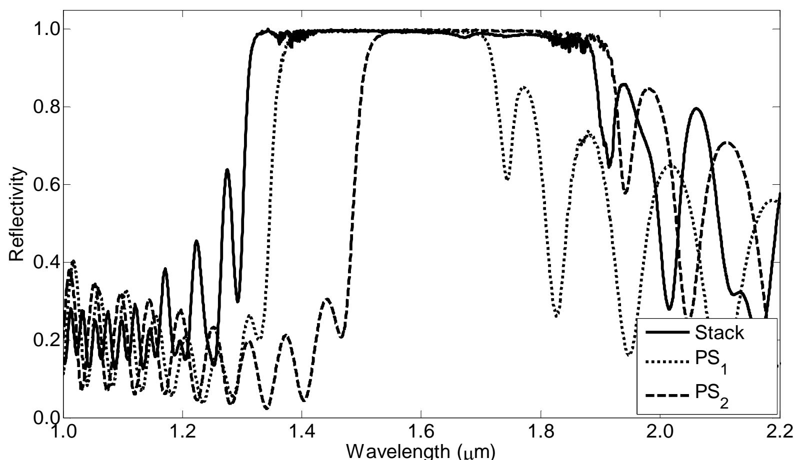

Fig. 7.16. Measured reflectivity spectrum of the stacked strcture for θ=12º (solid line). The measured reflectivity spectra of PS_1 and PS_2 for the same incidence angle can be also observed (dashed lines).

The widening of the bandgap can be observed for the rest of incidence angles in Fig. 7.17. It can be supposed that if the bandgap for each incidence angle is wider, the multilayer could present an omnidirectional bandgap or at least a bandgap for a wider interval of incidence angles. In this figure we can observe that there exists a bandgap for the incidence angle range from 12º to 60º. For incidence angles 70º and 80º the bandgap is suggested but the measurement is falsified due to the influence of the sample holder of the FTIR.

Although the limits of our FTIR do not permit us to obtain good reflectivity spectrum measurements for θ<12º and θ>65º, the measurements for incidence angle 70º and 80º seem to indicate that the stacked structure has an omnidirectional bandgap. In order to verify that this structure is an omnidirectional mirror we have simulated it to check the existence of the bandgap for θ<12º and θ>65º.

ISBN: 978-84-691-0362-3 /DL: T.2181-2007

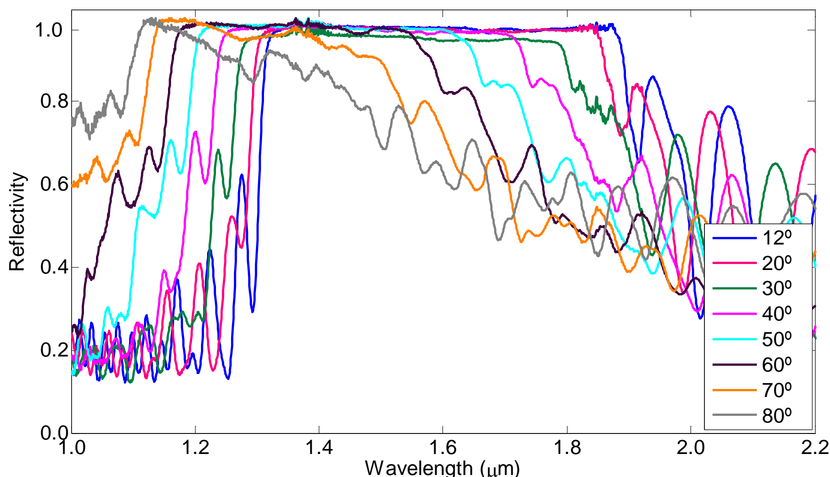

Fig. 7.17. Measured reflectivity spectrum of the stacked structure for different incidence angles.

A model of the stacked structure has been realized to simulate the bandgap for θ<12º and θ>65º. Fig. 7.18 shows the measured and the simulated reflectivity spectra of the stacked structure for incidence angle 12º. The parameters used for the model are for PS_1: n_1=2.1, n_2=1.45, d_1=168 nm and d_2=265 nm. And for PS_2: n_1=2.15, n_2=1.45, d_1=210 nm and d_2=261 nm. These refractive index values completely agree with the ones expected from the calibration of the system and the simulations of PS_1 and PS_2. A small gradient of refractive index and thickness has been included in the simulation values. The thicknesses are slightly lower than the ones calculated from the etch rate according to what has been observed in the comparison between the PS multilayers and the stacked structure (Fig. 7.16) and according with the literature [19].

In Fig. 7.18, we can observe that there is a good agreement between simulated and measured spectra. The bandgap for both exists for the same wavelength range. The sidelobes also exist for the same wavelengths although there is a small difference between the simulated and the measured amplitudes due to the anisotropy of the low refractive index layers (see chapter 6) that is

UNIVERSITAT ROVIRA I VIRGILI
DESIGN, FABRICATION AND CHARACTERIZATION OF POROUS SILICON MULTILAYER OPTICAL DEVICES
Elisabet Xifré Pérez
ISBN: 978-84-691-0362-3 /DL: T.2181-2007

not considered for the simulation program. The good agreement between simulation and measurement exists for all the incidence angles measured and in Fig. 7.18 we show the results for two of them. The simulation model is validated by the good agreement between the simulated and the measured reflectivity spectra.

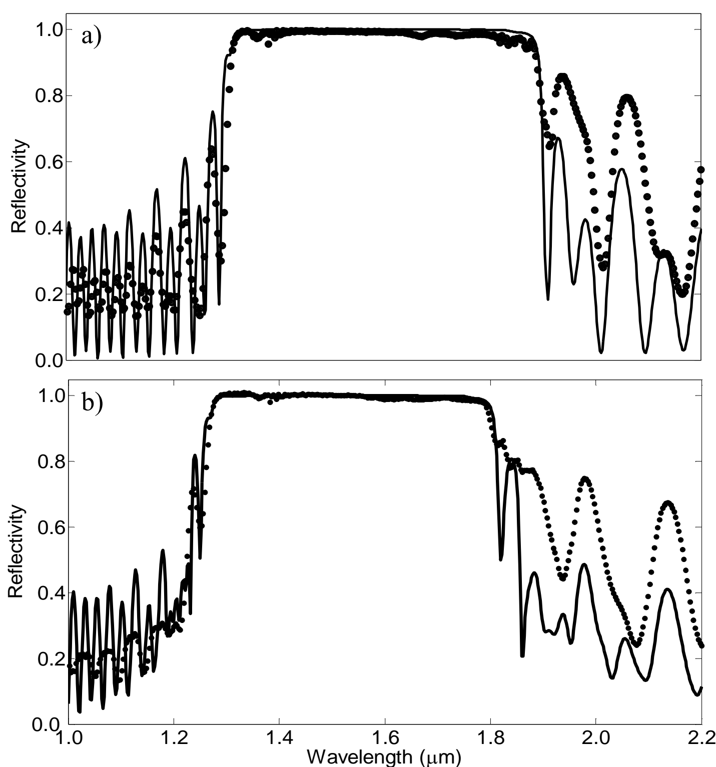

Fig. 7.18. Measured (symbols) and simulated (solid line) reflectivity spectra of the multilayer for incidence angle a) 12º and b) 30º.

With the simulation model we can study the existence of the omnidirectional bandgap suggested by the measurements. Fig. 7.19 shows the simulated reflectivity spectra for 0º and 85º obtained with this model. The

ISBN: 978-84-691-0362-3 /DL: T.2181-2007

omnidirectional bandgap with a reflectivity higher than 95 % can be observed for the wavelength range between 1.32 and 1.44 μm. This result supports the assumption that this stacked structure is an omnidirectional mirror.

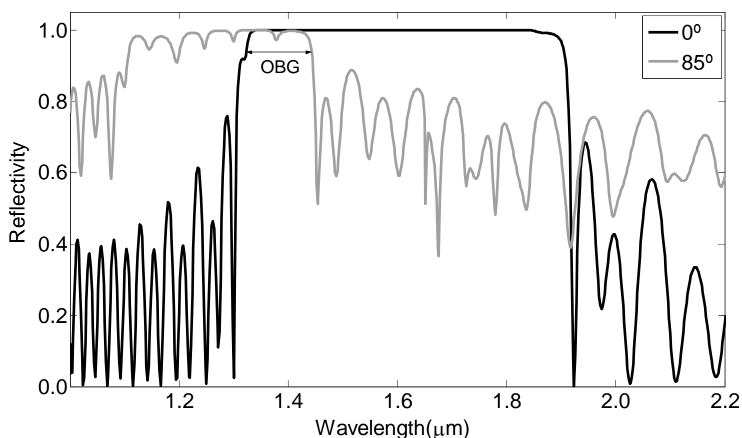

Fig. 7.19. Simulated reflectivity spectra of the stacked structure for incidence angles θ=0º and θ=85º. The omnidirectional bandgap (OBG) is indicated.

7.3.4. Enlargement of the omnidirectional mirror bandgap

We now study the reflectivity spectrum of a stacked structure consisting of three different PS stacked together. By increasing the number of PS of the stacked structure, the bandgap for each incidence angle will be wider and therefore the omnidirectional bandgap will enlarge.

The three PS that form this structure are the two ones presented before (PS_1 and PS_2) and a third one, PS_3. The schematic of this stacked structure can be observed in Fig. 7.20. The number of periods of the PS used for the formation of this stacked structure are 14 for the first, 13 for the second and 14 for the third, therefore it is a unbalanced structure, one of the mirror structures proposed in the theoretical study of omnidirectional mirrors (chapter 4).

ISBN: 978-84-691-0362-3 /DL: T.2181-2007

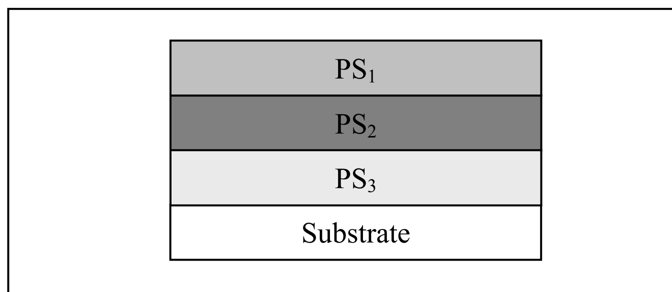

Fig. 7.20 Schematic of the stacked structure formed by three different periodic structures.

PS_3 consists of the periodic repetition of two layers obtained with current densities J_1=10 mA/cm^2 and J_2=50 mA/cm^2, the same ones used for PS_1 and PS_2. This PS_3 is designed to have a bandgap centered at a slightly higher wavelength than the one of PS_2. For this reason, the thickness d_1 (corresponding to J_1) is slightly higher than the one of PS_2 for this layer whereas the thickness d_2 remains the same. The period thickness is $\Lambda= d_1+d_2$ = 545 nm. The reflectivity spectrum of PS_3 has been simulated using n_1=2.15 and n_2=1.45. Fig. 7.21 shows the simulated reflectivity spectrum of PS_3 for normal incidence and it is compared with the ones of PS_1 and PS_2. The union of the three bandgaps is the expected bandgap of this stacked structure.

This stacked structure has been fabricated using p^+-type silicon wafers with a resistivity of 0.01 Ω·cm and ethanoic HF electrolyte with concentration of 15.4% (volumetric ratio). The current densities applied are J_1=10 mA/cm^2 and J_2=50 mA/cm^2. For 14 periods the etching times are t_1=16 s for J_1, and t_2= 8 s for J_2 (corresponding to PS_1), for the next 13 periods the etching times are t_1= 20 s for J_1, and t_2= 8 s for J_2 (corresponding to PS_2), and the for last 14 periods the etching times are t_1=24 s for J_1, and t_2= 8 s for J_2 (corresponding to PS_3). These last etching times correspond to PS_3 and have been calculated from the etch rate to obtain the thicknesses calculated during the simulation process of this PS. The SEM image of this fabricated stacked structure can be observed in Fig. 7.22.

UNIVERSITAT ROVIRA I VIRGILI
DESIGN, FABRICATION AND CHARACTERIZATION OF POROUS SILICON MULTILAYER OPTICAL DEVICES
Elisabet Xifré Pérez
ISBN: 978-84-691-0362-3 /DL: T.2181-2007

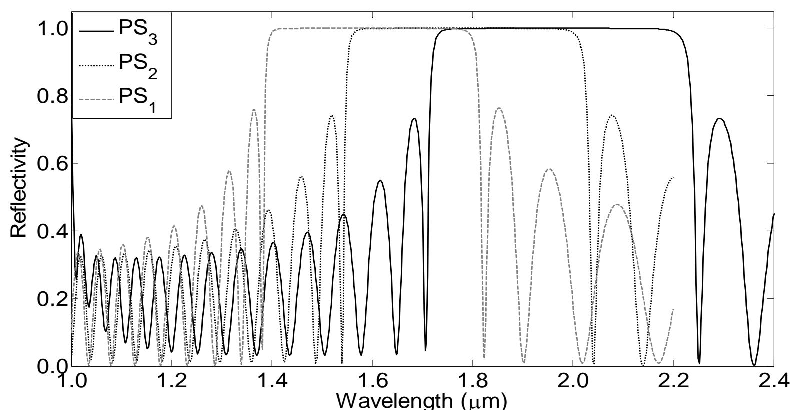

Fig. 7.21. Simulated reflectivity spectrum of PS_3 for normal incidence (solid line) and simulated reflectivity spectra of PS_1 and PS_2 for the same incidence angle (dotted lines).

The reflectivity spectrum of the fabricated stacked structure has been measured with the FTIR spectrometer Bruker Vertex 70 for different incidence angles. These spectra can be observed in Fig. 7.23. For incidence angles between 12º and 60º the bandgap is clearly visible whereas for incidence angles 70º and 76º it can be supposed. From these results we can consider that this stacked structure is an omnidirectional mirror with a wider bandgap than the stacked structure presented in the previous section as was expected.

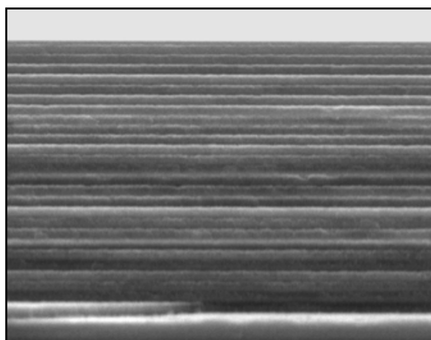

Fig. 7.22. SEM image of the fabricated stacked structure formed by three periodic structures.

UNIVERSITAT ROVIRA I VIRGILI
DESIGN, FABRICATION AND CHARACTERIZATION OF POROUS SILICON MULTILAYER OPTICAL DEVICES
Elisabet Xifré Pérez
ISBN: 978-84-691-0362-3 /DL: T.2181-2007

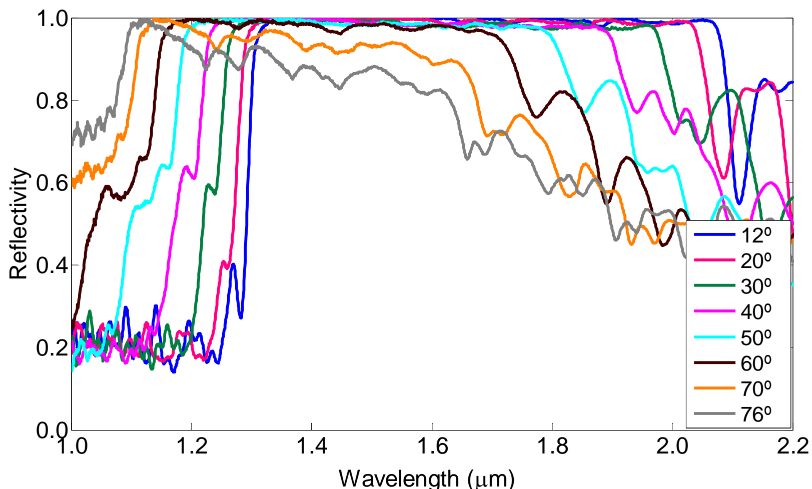

Fig. 7.23. Measured reflectivity spectra of the stacked structure for different incidence angles.

In order to study the reflectivity spectrum of the fabricated stacked structure for incidence angles θ<12º and θ>65º we have used a simulation model. The parameters used for the model are for PS_1: n_1=2.1, n_2=1.45, d_1=160 nm and d_2=270 nm; for PS_2: n_1=2.15, n_2=1.45, d_1=210 nm and d_2=265 nm and for PS_3: n_1=2.2, n_2=1.5, d_1=240 nm and d_2=265 nm. These refractive index values completely agree with the ones expected from the previous studies and the simulations of PS_1 and PS_2. We have simulated the refractive index gradient with depth by slightly increasing the refractive index of the PS. The thicknesses are slightly thinner than the ones expected from the etch rate calculation [19]. Fig. 7.24 shows the simulated reflectivity spectrum for two incidence angles. We can observe that the simulated reflectivity spectrum agrees with measured one, validating the model.

ISBN: 978-84-691-0362-3 /DL: T.2181-2007

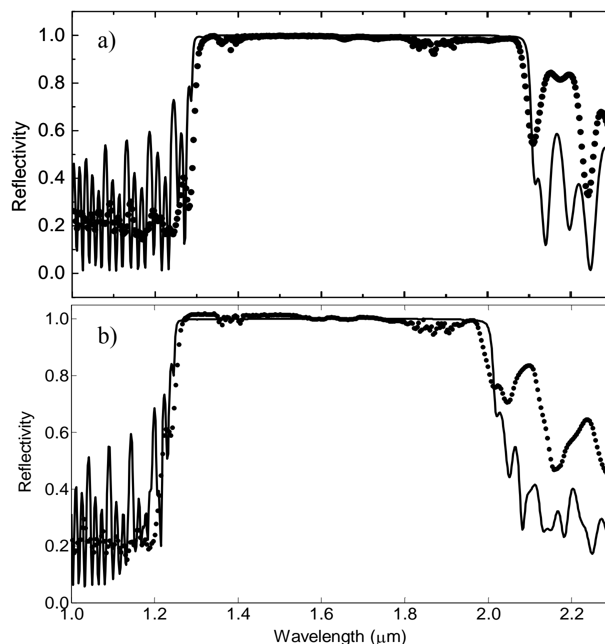

Fig. 7.24. Measured (symbols) and simulated (solid line) reflectivity spectra of the stacked structure for incidence angles a) 12º and b) 30º.

To study the omnidirectional bandgap (OBG) of this multilayer, we have used the model to simulate the reflectivity spectra for 0º and 85º (Fig. 7.25). In this figure, the OBG for reflectivity higher than 90 % exists for the wavelength range from 1.3 μm to 1.6 μm. Hence, we can conclude that this multilayer is an omnidirectional mirror. Besides, the omnidirectional bandgap of this multilayer is wider than the one of the multilayer studied in the previous section, consisting of two PS stacked together.

We can conclude that the stack of different PS is an appropriate structure to obtain porous silicon omnidirectional mirrors that cannot be obtained by increasing the refractive index contrast of the layers due to material limitations. The width of the omnidirectional bandgap can be selected by chosing the appropriate number of PS to be stacked and the wavelengths where they are centered.

ISBN: 978-84-691-0362-3 /DL: T.2181-2007

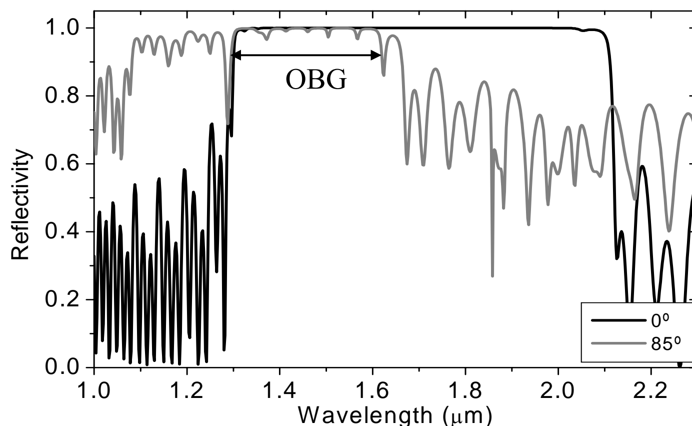

Fig. 7.25. Simulated reflectivity spectrum of the multilayer for incidence angles θ=0º and θ=85º. The omnidirectional bandgap (OBG) is indicated.

7.4. Conclusions

Many different porous silicon DBR, microcavities and omnidirectional mirrors have been designed, fabricated and characterized. In this chapter we have reported only the most representative.

The first optical device reported here is a porous silicon DBR. The reflectivity spectrum of this DBR has been measured for different angles of incidence. A high reflectivity band has been observed, that shifts to lower wavelengths, becomes narrower and its maximum decreases when the angle of incidence increases. The simulated spectra agree with the measured ones, which indicates that the behavior of the structure can be theoretically predicted. The refractive indices and thicknesses of the fabricated layers agree with the ones obtained with the simulations. It has also been demonstrated that for any wavelength, the range of incidence angles for which the bandgap exists can be studied with the projected band structure.

Porous silicon microcavities have also been fabricated, characterized and simulated. The reflectivity spectrum of the microcavity reported here has been measured for different humidity levels. We have observed that the reflectivity

UNIVERSITAT ROVIRA I VIRGILI
DESIGN, FABRICATION AND CHARACTERIZATION OF POROUS SILICON MULTILAYER OPTICAL DEVICES
Elisabet Xifré Pérez
ISBN: 978-84-691-0362-3 /DL: T.2181-2007

spectrum not only depends on the humidity level of the ambient medium but also on the presence of a water thin film on its surface due to the condensation of water. In both cases, the reflectivity resonance shifts to higher wavelengths and the reflectivity decreases when the humidity increases, but the relative changes in the reflectivity spectrum are much more significant with the presence of condensed water.

Omnidirectional mirrors have also been designed, fabricated and characterized. Firstly, a periodic structure has been fabricated. It was formed by the periodic repetition of two different refractive index layer. The two refractive indices used are the lowest one and the highest one obtainable with our fabrication parameters. The reflectivity spectrum of this structure was measured and it indicated that with these refractive indices an omnidirectional bandgap can not be obtained. Secondly, a new structure consisting of different periodic structures stacked together has been used to obtain omnidirectional mirrors. The refractive indices used for this new structure have been the same used for the periodic structure. A first stacked structure consisting of two PS stacked together has been designed, fabricated and characterized demonstrating that it is possible to obtain omnidirectional mirrors without changing the refractive indices. The enlargement of the omndirectional bandgap has been obtained with a second stacked structure consisting of three periodic structures stacked together. This is an unbalanced structure theoretically studied in chapter 4. With these results we have demonstrated that the refractive indices of the layers that form the multilayer are not a limitation for obtaining omnidirectional mirrors, as was for the periodic structure. We have also demonstrated that the new structure proposed in this work, formed by different periodic structures stacked together, is a suitable structure for obtaining wide band omnidirectional mirrors.

To conclude, it has been demonstrated that porous silicon is a suitable material for the fabrication of optical devices and that the material characteristics allows the application of these optical devices for the widely used in telecommunications wavelength of 1.55 μm.

ISBN: 978-84-691-0362-3/DL: T.2181-2007

Chapter 8

Summary and conclusions

The work presented in this thesis has dealt with the following subjects:

- Theoretical study and design of dielectric multilayers for different optical applications.
- Establishment and calibration of a porous silicon fabrication system for the formation of multilayers.
- Characterization of porous silicon layers using different methods.
- Design, fabrication and characterization of porous silicon optical components.

Porous silicon has many potential applications. In this work we have focused on the study and design of porous silicon multilayers for optical applications. Porous silicon is a suitable material for the fabrication of multilayers because the refractive index and thickness of the layers can be selected by changing the formation parameters during the fabrication process. Besides, once a porous layer has been formed, no more electrochemical etching occurs for it during the following current density variations. Hence, the

UNIVERSITAT ROVIRA I VIRGILI
DESIGN, FABRICATION AND CHARACTERIZATION OF POROUS SILICON MULTILAYER OPTICAL DEVICES
Elisabet Xifré Pérez
ISBN: 978-84-691-0362-3/DL: T.2181-2007

refractive index can be modulated in depth, making porous silicon a suitable dielectric material for the formation of multilayers

By choosing, in an appropriate way, the thicknesses and the refractive indices of the various layers, it is possible to generate different reflectivity spectra and therefore different optical components. In this work, the optical components studied are Distribute Bragg Reflectors (DBR), microcavities, omnidirectional mirrors and waveguides.

The theoretical methods for the study of multilayers have been developed in chapter 3 where different programs realized for the simulation of multilayers have been explained. All these programs are based on the transfer matrix method, a mathematical method that has been already developed in detail in this chapter. These programs have been used for the study of different optical devices, analyzing their design parameters and evaluating the influence of these parameters on the optical response. The performance of these programs has been verified simulating different Distributed Bragg Reflectors (DBR) and microcavities and comparing the results obtained with the ones reported in the literature. This comparison has demonstrated the suitability of the realized programs. From the study of the DBRs, we have observed that porous silicon is a suitable material for the fabrication of filters with a wide bandgap centered at λ=1.55 μm. Although the difference between the refractive indices of the layers determines the bandgap width, the possibility to easy fabricate porous silicon stacked filters centered at different wavelengths, widening the bandgap, compensates the limitations of the porous silicon refractive index range.

The simulation of different optical devices based on multilayers has been realized in chapter 4 using the different programs presented in the previous chapter. These optical devices are omnidirectional mirrors and waveguides. From the study of omnidirectional mirrors, we have observed that the omnidirectional bandgap of porous silicon mirrors is very narrow due to the limited refractive index range obtainable with porous silicon. In order to widen this bandgap we have proposed three different multilayer structures, the random, the balanced and the unbalanced mirrors, that overcome these material limitations and allow obtaining an enlarged omnidirectional bandgap with a

UNIVERSITAT ROVIRA I VIRGILI
DESIGN, FABRICATION AND CHARACTERIZATION OF POROUS SILICON MULTILAYER OPTICAL DEVICES
Elisabet Xifré Pérez
ISBN: 978-84-691-0362-3/DL: T.2181-2007

simple design. Therefore, we can conclude that porous silicon is a suitable material for the fabrication of omnidirectional mirrors although for obtaining wide omnidirectional bandgaps with this material, the structure of the multilayer is decisive. Besides, these omnidirectional mirrors have been designed to work at wavelength 1.55 μm, a wavelength widely used for telecommunication applications, demonstrating that porous silicon is appropriate for these applications.

Besides, in the same chapter two different types of porous silicon waveguides have been also designed. Firstly, the modal analysis of waveguides based on total internal reflection has been realized for 1.55 μm applications. The influence of the refractive indices and the core thickness on the number of modes has been studied. It has been demonstrated that when the thickness increases, the number of modes increases and that the cutoff wavelength of the modes allowed in the waveguide depends on the refractive indices of core and the cladding. It has been demonstrated that, for a fixed core thickness, different refractive indices resulting in the same numerical aperture have the same cutoff wavelength.

However, the most widely analyzed waveguide structure has been the one where the confinement of the light is based on the properties of photonic crystals. In these waveguides, the multilayer is the cladding. In concrete, we have studied the suitability of omnidirectional mirrors and DBR to be used for the cladding. We have obtained the optimal refractive index for the core, that is the refractive index that gives the highest confinement for all the modes. The different modes of this waveguide have been studied and we have demonstrated that the position of the mode in the projected band structure of the multilayer cladding determines the guiding condition of the modes. The influence of different parameters of the waveguide structure on the modes and the modal confinement has been studied. We concluded that when the core thickness increases, the confinement of the modes increases and gets closer to 100 % indicating that the modes closer to the light line have a higher confinement. Besides, the increment of core thickness results in the increment of the number of modes, the same that happened with TIR waveguides. The omnidirectional

UNIVERSITAT ROVIRA I VIRGILI
DESIGN, FABRICATION AND CHARACTERIZATION OF POROUS SILICON MULTILAYER OPTICAL DEVICES
Elisabet Xifré Pérez
ISBN: 978-84-691-0362-3/DL: T.2181-2007

mirror cladding has been also compared with a DBR cladding. From this study, we have observed that the DBR cladding can be also an appropriate structure for the cladding and the suitability of the DBR structure can be compared to the one of the omnidirectional mirror.

In chapter 5 we have explained in detail the fabrication and characterization processes of porous silicon layers. Firstly, the porous silicon fabrication system established at the Department of Electronic, Electric and Automatic Engineering of the University Rovira i Virgili has been presented and the influence of the different elements of the system on the porous silicon characteristics has been discussed. We have designed and fabricated an electrochemical cell that permits the fabrication of homogeneous porous silicon layers. The program realized for the control of the whole fabrication system has been also explained.

The characterization part has been focused on the study of the fabricated porous silicon layers. The different measurement techniques used for the characterization of the porous silicon layers have been explained. These techniques are Scanning Electron Microscopy (SEM), Fourier Transform Infrared spectroscopy (FTIR) and Spectroscopic Ellipsometry (SE). From these measurements the two main characteristics of the porous silicon layers, refractive index and thickness, have been calculated using two different mathematical methods: the interference fringes method and the spectrum analysis fitting. The comparison of the results obtained with both methods indicates that both are equally suitable for the characterization of microporous silicon layers.

These characterization methods have been also used to calibrate the porous silicon fabrication system. The calibration has established the relations between the anodization parameters and the physical characteristics of the porous silicon layers: the current density-refractive index relation and the anodization time-thickness relation. In addition, the porosity has been analyzed. We have concluded that the increase of the current density leads to an increase of the porosity and therefore a decrease of the refractive index. The relations of the current density with porosity and refractive index are both exponential. We

UNIVERSITAT ROVIRA I VIRGILI
DESIGN, FABRICATION AND CHARACTERIZATION OF POROUS SILICON MULTILAYER OPTICAL DEVICES
Elisabet Xifré Pérez
ISBN: 978-84-691-0362-3/DL: T.2181-2007

have also concluded that the thickness increases linearly with the anodization time. Moreover, the etch rate has been studied and we have observed that it depends on the current density; in particular it exponentially increases with current density.

The porous silicon layers have also been characterized using spectroscopic ellipsometry during a stage at the Ecole Polytechnique (Palaiseau, France). This characterization has determined the main physical features of these layers, porosity (and therefore refractive index) and thickness; and has allowed the analysis of their anisotropy. From the ellipsometric study of the porous silicon layers we have concluded that low porosity layers can be modelled with a graded index model. However, as porosity of the monolayers increases, the gradient index model is no longer valid, and it must be substituted by another one consisting of an anisotropic uniaxial layer with its optical axis oriented perpendicular to the surface of the sample. This indicates that the anisotropy increases with the porosity. In fact, we could conclude that depth inhomogeneity and anisotropy exist for all porosity layers but for low porosity layers the difference between the extraordinary and the ordinary refractive indices are small and the anisotropy of the layer is masked by the in depth inhomogeneity, and when the porosity increases the anisotropy becomes more important than the inhomogeneity.

The depolarization of light caused by sample thickness non-uniformity has also been measured and used to estimate the quality of measurements as well as the adequacy and goodness of ellipsometric data fits. We have concluded that when the current density increases, that is when the porosity increases, the depolarization of the fabricated porous silicon layer increases making more difficult the characterization of the layer using ellipsometry.

Chapter 7 presents multilayer optical components fabricated with porous silicon. In this chapter the different steps explained in the rest of chapters are used because each component is simulated, fabricated and characterized. Although many different components have been realized during the realization of this thesis, here we have only presented the most representatives.

UNIVERSITAT ROVIRA I VIRGILI
DESIGN, FABRICATION AND CHARACTERIZATION OF POROUS SILICON MULTILAYER OPTICAL DEVICES
Elisabet Xifré Pérez
ISBN: 978-84-691-0362-3/DL: T.2181-2007

The reflectivity spectrum of a DBR has been studied for different incidence angles. We have demonstrated that the behavior of the structure can be theoretically predicted and that for any wavelength, the range of incidence angles for which the bandgap exists can be studied with the projected band structure.

The reflectivity spectrum a microcavity has been measured for different humidity levels. We have observed that the reflectivity spectrum not only depends on the humidity level of the ambient medium but also on the presence of a water thin film on its surface due to the condensation of water. In both cases, the reflectivity resonance shifts to higher wavelengths and the reflectivity decreases when the humidity increases, but the relative changes in the reflectivity spectrum are much more significant with the presence of condensed water. This indicates that a porous silicon microcavity could be used for the sensing of humidity variations.

Finally, porous silicon omnidirectional mirrors have been fabricated and characterized. We have demonstrated that although the limited refractive index range of porous silicon does not permit the fabrication of omnidirectional mirrors with a wide omnidirectional bandgap using the typical periodic structure, the fabrication of multilayers consisting of different periodic structures stacked together solves these limitations. We have fabricated a mirror with the unbalanced structure propose in this work, which has demonstrated that a wide omnidirectional bandgap can be obtained using porous silicon and that this width can be enlarged by stacking periodic structures.

ISBN: 978-84-691-0362-3 /DL: T.2181-2007

CONTENTS

Acknowledgements vi

1. Introduction 1

2. Fundamentals of porous silicon and applications 5

2.1. History of porous silicon 6
2.2. Basics of the porous silicon formation process 7
2.2.1. Electrochemical etching of silicon 7
2.2.2. Porous silicon formation chemistry 10
2.2.3. Pore size and morphology 13
2.2.4. Anodization parameters 16
2.2.5. Photoluminescence of porous silicon 18
2.3. Applications of porous silicon 19
2.3.1. Distributed Bragg Reflectors 20
2.3.2. Microcavities 23
2.3.3. Rugate filters 24
2.3.4. Omnidirectional mirrors 24
2.3.5. Waveguides 25
2.3.6. Sensors 25
2.3.7. Other applications 26

3. Simulation programs for the analysis of multilayer media 27

3.1. Mathematical methods for the analysis and simulation of multilayers 28
3.1.1. Transfer matrix method (TMM) 28
3.1.1.1. Reflectance and transmittance 31
3.1.1.2. Bloch waves and band structures 32
3.1.1.3. Advantages and drawbacks of the TMM 34
3.1.2. Plane wave method 35
3.1.3. Finite Difference Time Domain 36

ISBN: 978-84-691-0362-3 /DL: T.2181-2007

3.2. Development of the simulation programs 37
3.2.1. Program for the calculation of reflectivity, transmission and absorption spectra. 37
3.2.2. Program for the calculation of photonic band diagrams 41
3.3. Performance of the developed programs for the study of optical devices 45
3.3.1. Distributed Bragg Reflectors 45
3.3.1.1. Performance of the developed programs for the simulation of DBRs 45
3.3.1.2. Study of the DBR parameters 47
3.3.1.3. Design of a porous silicon DBR for 1.55 µm applications 50
3.3.1.4. Reflectivity spectrum of stacked filters 51
3.3.2. Microcavities 52
3.3.2.1. Performance of the developed programs for the simulation of microcavities 52
3.3.2.2. Study of the microcavities parameters 53
3.4. Summary and conclusions 56

4. Analysis and design of optical devices based on porous silicon multilayers 59

4.1. Omnidirectional mirrors (OM) 60
4.1.1. Periodic OM 60
4.1.1.1. Refractive indices n_H and n_L 60
4.1.1.2. Thickness of one layer (h_H) and period thickness (Λ) ratio: (h_H/Λ) 64
4.1.1.3. Number of periods 67
4.1.1.4. Omnidirectional mirror with a periodic structure for 1.55 µm applications 68
4.1.2. Chirped OM 70
4.1.2.1. Omnidirectional mirror with chirped structure for 1.55 µm applications 71

ISBN: 978-84-691-0362-3 /DL: T.2181-2007

4.1.3. Random OM …… 72
4.1.3.1. Random omnidirectional mirror for 1.55 μm applications …… 77
4.1.4. New enlarged omnidirectional bandgap mirrors …… 78
4.1.4.1. Porous silicon balanced and unbalanced mirrors … 80
4.1.4.2. Porous silicon balanced mirror for 1.55 μm applications …… 82
4.1.4.3. Porous silicon unbalanced mirror for 1.55 μm applications …… 82
4.1.5. Comparison of the studied mirror structures …… 84

4.2. Waveguides …… 86
4.2.1. Total internal reflection waveguides …… 86
4.2.1.1. Total internal reflection principles …… 87
4.2.1.2. Porous silicon slab waveguides for 1.55 μm applications …… 90
4.2.2. Photonic crystal waveguides …… 94
4.2.2.1. Structure …… 94
4.2.2.2. Determination of the parameters n_0, d_H and N…. 95
4.2.2.3. Omnidirectional mirrors and DBR as cladding for porous silicon planar waveguides …… 99
4.2.2.4. Modes of the multilayer waveguide …… 104
4.3. Conclusions …… 107

5. Fabrication and characterization of porous silicon layers …… 111
5.1. Fabrication System …… 112
5.1.1. Electrochemical cell …… 113
5.1.1.1. Lateral-wafer electrochemical cell …… 113
5.1.1.2. Bottom-wafer electrochemical cell …… 116
5.1.2. Source for growth control …… 119
5.1.2.1. Voltage source …… 120
5.1.2.2. Current source …… 121
5.1.3. Control Program …… 122

UNIVERSITAT ROVIRA I VIRGILI
DESIGN, FABRICATION AND CHARACTERIZATION OF POROUS SILICON MULTILAYER OPTICAL DEVICES
Elisabet Xifré Pérez
ISBN: 978-84-691-0362-3 /DL: T.2181-2007

5.1.4. Electrolyte 124
5.1.5. Silicon wafers and sample preparation 124
5.1.6. Fabrication of porous silicon monolayers and multilayers ... 127
5.2. Characterization of the fabricated porous silicon layers.......... 129
5.2.1. Measurement techniques 130
5.2.1.1. Scanning Electron Microscopy 130
5.2.1.2. Fourier Transform Infrared Spectroscopy 131
5.2.1.3. Spectroscopic Ellipsometry 132
5.2.1.4. Atomic Force Microscopy 133
5.2.2. Mathematical methods for the determination of the refractive index and thickness 134
5.2.2.1. Measurement of interference fringes 134
5.2.2.2. Spectrum analysis fitting 138
5.3. Calibration of the fabrication system (Anodization parameters) 141
5.3.1. Current density-refractive index relation 141
5.3.2. Current density-porosity relation 144
5.3.3. Etching time-thickness relation 145
5.4. Conclusions 147

6. Ellipsometric study of porous silicon layers 151
6.1. Introduction to spectroscopic ellipsometry 152
6.1.1. Fundamentals of ellipsometry.......... 153
6.1.2. Equipments for ellipsometric measurements. Ellipsometers 156
6.2. Ellipsometric characterization process 157
6.2.1. UVISEL Ellipsometer 157
6.2.2. Influence of the spot size on the ellipsometric measurements 158
6.2.3. Process for the determination of porous silicon characteristics using ellipsometric data 161
6.3. Measurement and characterization of porous silicon monolayers ... 163
6.3.1. Isotropic optical model 163
6.3.2. Anisotropic optical model 169

ISBN: 978-84-691-0362-3 /DL: T.2181-2007

6.3.3. Depolarization of the porous silicon monolayers 176
6.3.4. Summary 177
6.4. Characterization of porous silicon multilayers 179
6.4.1. One period multilayer.. 180
6.4.2. Two period multilayer 182
6.4.3. Three period multilayer 184
6.5. Conclusions 186

7. Optical devices based on porous silicon multilayers 189
7.1. Distributed Bragg Reflector 190
7.1.1. Fabrication and characterization 190
7.1.2. Simulation 192
7.2. Microcavity 195
7.2.1. Fabrication, characterization and simulation 195
7.2.2. Influence of the relative humidity on the reflectivity spectrum 197
7.2.3. Water condensation on the surface of the microcavity 199
7.3. Omnidirectional mirrors 201
7.3.1. Design, fabrication and characterization of periodic structures 201
7.3.2. Design of a new omnidirectional mirror structure 204
7.3.3. Fabrication and characterization of the new omnidirectional mirror structure 207
7.3.4. Enlargement of the omnidirectional bandgap 211
7.4. Conclusions 216

8. Summary and Conclusions 219

References 225

Publications related to this thesis 241

UNIVERSITAT ROVIRA I VIRGILI
DESIGN, FABRICATION AND CHARACTERIZATION OF POROUS SILICON MULTILAYER OPTICAL DEVICES
Elisabet Xifré Pérez
ISBN: 978-84-691-0362-3 /DL: T.2181-2007

UNIVERSITAT ROVIRA I VIRGILI
DESIGN, FABRICATION AND CHARACTERIZATION OF POROUS SILICON MULTILAYER OPTICAL DEVICES
Elisabet Xifré Pérez
ISBN: 978-84-691-0362-3 /DL: T.2181-2007

Acknowledgments

I would like to express my deepest gratitude to my directors Dr. Josep Pallarès and Dr. Lluís Marsal for their guidance, support, encouragement and invaluable advices throughout these years in all aspects of the work. Without them this work was not possible. My more sincere thanks for both.

My special gratitude also to Dr. Josep Ferré for his suggestions, discussions, simulations and help with the FTIR measurements. And also for his very valuable hints and his guidance in mathematical and physics aspects that were essential for the development of all this work.

I am grateful to Dr. Enric Garcia-Caurel for his kindness that made possible my stage at the Ecole Polytechnique and all his help during the three months that I was there and until the defense of this thesis. His experience and knowledge of the ellipsometric techniques have permitted to realize a really interesting work.

I would also like to thank all the people of the Departament d'Enginyeria Electrònica, Elèctrica i Automàtica of the Universitat Rovira i Virgili, especially to Dr. Alfonso Romero for his guidance and his help with LabView control and also for his support, together with Dr. Xavier Correig at the beginning of my work at the University.

Many thanks are also given to the colleagues in the NePhoS group for their friendship and support, especially to Lukas for all his help with the samples and to Ivan and Mikhail. I wish to specially thank to Dr. Trifon Trifonov for teaching me how to make porous silicon layers and for all his help during the beginning of this work.

I would like to thank to all my doctoral companions for being such excellent colleagues. Especially to Raul for all his help and support, and to Edwin, Alexander, Mariona, Stella and Radu.

Many thanks to Mercè and Mariana for their help and guidance with the SEM equipment.

My deepest love to my parents for all their support, help and great patience.

UNIVERSITAT ROVIRA I VIRGILI
DESIGN, FABRICATION AND CHARACTERIZATION OF POROUS SILICON MULTILAYER OPTICAL DEVICES
Elisabet Xifré Pérez
ISBN: 978-84-691-0362-3 /DL: T.2181-2007

I would like to acknowledge the Universitat Rovira i Virgili for the doctoral fellowship that made it possible to conduct the doctoral work.

This work has been supported by the Ministerio de Educación y Ciencia under grant numbers TIC2002-04184-C05, TEC2005-02038 and TEC2006-06531.

UNIVERSITAT ROVIRA I VIRGILI
DESIGN, FABRICATION AND CHARACTERIZATION OF POROUS SILICON MULTILAYER OPTICAL DEVICES
Elisabet Xifré Pérez
ISBN:978-84-691-0362-3/DL:T.2181-2007

Publications related to this thesis

Journal articles

E. Xifré-Pérez, T. Trifonov, J. Pallarès, and L.F. Marsal "One-dimensional porous silicon photonic crystals for visible and NIR applications", *Physica Status Solidi c*, **2** (9), 3466-3470 (2005).

E. Xifré-Pérez, L.F. Marsal, J. Pallarès, and J. Ferré-Borrull, "Porous silicon mirrors with enlarged omnidirectional band gap", *Journal of Applied Physics*, **97** (6), 064503 (1-5) (2005).

E. Xifré-Pérez, L.F. Marsal, J. Ferré-Borrull, and J. Pallarès, "Confinement in a planar waveguide with porous silicon omnidirectional mirrors as confining walls", *Journal of Luminescence*, **121** (2), 301-303 (2006).

E. Xifré-Pérez, L.F. Marsal, J. Ferré-Borrull, and J. Pallarès, "Influence of the humidity conditions on the reflectivity spectrum of a porous silicon microcavity", *Physica E*, **38** (1-2), 172-175 (2007).

E. Xifré-Pérez, J. Pallarès, J. Ferré-Borrull, T. Trifonov, and L.F. Marsal, "Low refractive index porous silicon multilayer with a high reflection band", *Physica Status Solidi c*, **4** (6), 2034-2038 (2007).

UNIVERSITAT ROVIRA I VIRGILI
DESIGN, FABRICATION AND CHARACTERIZATION OF POROUS SILICON MULTILAYER OPTICAL DEVICES
Elisabet Xifré Pérez
ISBN:978-84-691-0362-3/DL:T.2181-2007

E. Xifré-Pérez, E. Garcia-Caurel, J. Pallarès, J. Ferré-Borrull, and L.F. Marsal, "Wide-band reflection porous silicon mirrors with ellipsometric investigation of the material monolayer components", *(submitted to Materials Science and Engineering B)*

E. Xifré-Pérez, E. Garcia-Caurel, J. Ferré-Borrull, L.F. Marsal, and J. Pallarès, "Spectroscopic ellipsometry of porous silicon monolayers and multilayers: study of the anisotropy and characterization", *(submitted to Physica Status Solidi c)*

E. Xifré-Pérez, L.F. Marsal, J. Ferré-Borrull, and J. Pallarès, "Suitability of porous silicon omnidirectional mirrors for planar waveguide applications", *(submitted to IEEE J. of Lightwave Technology)*

Communications to international conferences

E. Xifré-Pérez, J. Pallarès, T. Trifonov, and L.F. Marsal, "One-dimensional porous silicon photonic crystal for visible and NIR applications", *Porous semiconductors sciencie and technology, International Conference*, (14-19 March 2004, Cullera, Spain).

E. Xifré-Pérez, J. Ferré-Borrull, J. Pallarès, and L.F. Marsal, "Design elements of porous silicon omnidirectional mirrors", *International Symposium on Optical Systems Design 2005. Advances in Optical Thin Films II,* (12-16 September 2005, Jena , Germany).

E. Xifré-Pérez, J. Pallarès, J. Ferré-Borrull, T. Trifonov, and L.F. Marsal, "Fabrication and characterization of porous silicon multilayer structures", *Porous Semiconductors Sciencie and Technology, International Conference,* (12-17 March 2006, Sitges, Spain).

UNIVERSITAT ROVIRA I VIRGILI
DESIGN, FABRICATION AND CHARACTERIZATION OF POROUS SILICON MULTILAYER OPTICAL DEVICES
Elisabet Xifré Pérez
ISBN:978-84-691-0362-3/DL:T.2181-2007

E. Xifré-Pérez, L.F. Marsal, J. Ferré-Borrull, and J. Pallarès, "Porous silicon waveguides using photonic crystals as confining walls", *E-MRS IUMRS ICEM 2006 Spring Meeting (symposium D: Silicon-based Photonics),* (29 May-2 June 2006, Nice, France)

E. Xifré-Pérez, L.F. Marsal, J. Ferré-Borrull, T. Trifonov, J. Pallarès, "Reflectivity spectrum of a porous silicon Fabry-Pérot filter under different humidity conditions", *E-MRS IUMRS ICEM 2006 Spring Meeting (symposium D: Silicon-based Photonics* (29 May-2 June 2006, Nice, France).

E. Xifré-Pérez, E. Garcia-Caurel, J. Pallarès, J. Ferré-Borrull, and L.F. Marsal, "Wide-band reflection porous silicon mirrors with ellipsometric investigation of the material monolayer components", *EMRS 2007 Spring Meeting (Symposium B: Semiconductor Nanostructures towards Electronic and Optoelectronic Device Applications)* (28 May-1 June 2007, Strasbourg, France), *(Oral presentation).*

E. Xifré-Pérez, E. Garcia-Caurel, J. Ferré-Borrull, L.F. Marsal, and J. Pallarès, "Spectroscopic ellipsometry of porous silicon monolayers and multilayers: study of the anisotropy and characterization", *4th International Conference on Spectroscopic Ellipsometry ICSE* (11-15 June 2007, Stockholm, Sweden).

Communications to national conferences

E. Xifré Pérez, J. Pallarès, J. Ferré-Borrull, and L.F. Marsal, "Applications of One-Dimensional Porous Silicon Photonic Crystals", *Nanoelectronic and Photonic Systems Workshop*, (21-22 June 2004, Tarragona, Spain).

E. Xifré-Pérez, J. Pallarès, T. Trifonov, J. Ferré-Borrull, and L.F. Marsal, "Porous silicon slab waveguides", *V Conferencia de Dispositivos Electrónicos CDE'05* (2-4 February 2005, Tarragona, Spain).

UNIVERSITAT ROVIRA I VIRGILI
DESIGN, FABRICATION AND CHARACTERIZATION OF POROUS SILICON MULTILAYER OPTICAL DEVICES
Elisabet Xifré Pérez
ISBN:978-84-691-0362-3/DL:T.2181-2007

E. Xifré-Pérez, J. Pallarès, J. Ferré-Borrull, and L.F. Marsal, "One-dimensional porous silicon photonic crystals for 1.55 µm applications", *Nanoelectronic and Photonic Systems Workshop, (*June 2005, Tarragona, Spain)

E. Xifré-Pérez, J. Pallarès, J. Ferré-Borrull, and L.F. Marsal, "Design of one-dimensional porous silicon crystals for 1.55 µm applications", *4ª Reunión Española de Optoelectronica OPTOEL,* (13-15 July 2005, Elche, Spain).

E. Xifré-Pérez, J. Pallarès, J. Ferré-Borrull, and L.F. Marsal, "Guided modes in porous silicon multilayer waveguide structures", *Nanoelectronic and Photonic Systems Workshop* (26-27 June 2006, Tarragona, Spain).

J. Ferré-Borrull, E. Xifré-Pérez, L.F. Marsal, and J. Pallarès, "Real metals in metallo-dielectric photonic crystals in the visible", *6ª Conferencia de Dispositivos Electrónicos CDE'07* (31 January-2 February 2007, El Escorial, Madrid, Spain).

ISBN:978-84-691-0362-3/DL: T.2181-2007

REFERENCES

[1] A. Ulhir, *Bell System Technology Journal,* 35, p.333 (1956).

[2] L.T. Canham, *Appl. Phys. Lett.* 57, p.1046 (1990).

[3] D. E. Aspnes, J. 13. Theeten, and R Hottier, *Phys. Rev. B,* 20, 3292 (1979).

[4] V. Lehmann, and U. Gosele, *Appl. Phys. Lett.,* **58**, 856 (1991).

[5] C. Pickering, M I. J. Beale, D. J. Robbins, P. J. Pearson, and R. Greef, *Thin Solid Films*, **125**, 157 (1985).

[6] I. Sagnes, G. Vincent, and P. A. Badoz, *J. Appl. Phys.,* **62**, 1155 (1993).

[7] P. Steiner, F. Kozlowski, and W. Lang, *IEEE Electron. Devices Letters*., **62**, 317 (1993).

[8] J.M. Keen, W. Eccleston and P.J. Rosser, *Proc. 20th Eur. Solid State Device Research Conf.*, Nottingham (1990).

[9] P.C. Searson, *Appl. Phys. Letters*., **59**, 832 (1991).

[10] S.G. Johnson, and J.D. Joannopoulos, *Photonic crystals the road from theory to practice,* Kluwer, Boston, (2002).

[11] P. Gupta, A.C. Dillon, A.S. Bracker, S.M. George, *Surf. Sci.*, **245**, 360 (1991).

[12] A.C. Dillon, M.B. Robinson, M.Y. Han, and S.M. George, *J. Electrochem. Soc.*, **139**, 537 (1992).

[13] R.C. Anderson, R.S. Muller, and C.W. Tobias, *Sens. Actuators A*, **21**, 835 (1990).

[14] L.T. Canham, *Appl. Phys. Lett*., **57**, 1046 (1990).

[15] L.T. Canham, *Adv. Mater.*, **7**, 1033 (1995).

UNIVERSITAT ROVIRA I VIRGILI
DESIGN, FABRICATION AND CHARACTERIZATION OF POROUS SILICON MULTILAYER OPTICAL DEVICES
Elisabet Xifré Pérez
ISBN:978-84-691-0362-3/DL: T.2181-2007

[16] O. Bisi, S. Ossicini, and L. Pavesi, *Surf. Sci. Rep.*, **38**, 1 (2000).

[17] K. D. Hirschman, L. Tsybeskov, S. P. Duttagupta, and P. M. Fauchet, *Nature*, **384**, 338 (1996).

[18] C. C. Striemer and P. M. Fauchet, *Appl. Phys. Lett.*, **81**, 2980 (2002).

[19] C. Mazzoleni and L. Pavesi. *Appl. Phys. Lett.,* **67**, 2983 (1995).

[20] V.S.Y. Lin, K. Motesharei, K.P.S. Dancil, M.J. Sailor, M.R. Ghadiri, *Science*, **278**, 840 (1997).

[21] M.J. Sailor, *Sensor Applications of Porous Silicon* (in Properties of Porous Silicon), L. Canham, Ed., Short Run Press Ltd., London (1997).

[22] S. Chan, P.M. Fauchet, Y. Li, L.J. Rothberg, and B.L. Miller, *Phys. Stat. Solidi A*, **182**, 541 (2000).

[23] F. Cunin, T.A. Schmedake, J.R. Link, Y.Y. Li, J. Koh, S.N. Bhatia, M.J. Sailor, *Nature Mater.*, **1**, 39 (2002).

[24] W. Theiss, *Surf. Sci. Rep.,* **29**, 91 (1997).

[25] D.R. Turner, *J. Electrochem. Soc.,* **138**, 807 (1991).

[26] R.L. Smith, and S.D. Collins, *J. Appl. Phys.* **71**, R1 (1992).

[27] A. J. Bard, *Encyclopedia of Electrochemistry of the Elements*, Dekker, New York (1986).

[28] A.K. Vijh, *Electrochemistv of Metals and Semiconductors,* Dekker, New York (1973).

[29] B.E. Conway, J.O'M. Bockris, E. Yeager, S.U.M. Khan, and R.E. White, *Comprehensive Treatise of Electrochemistry (Vol. 7)*, Plenum, New York, (1983).

[30] P. J. Holmes, *The Electrochemistry of Semiconductors*, Academic, London, (1962).

[31] E. A. Efimov and I. G. Erusalimchik, *Electrochemistry of Germanium and Silicon,* Sigma, London (1963).

[32] J.B. Flynn, *J. Electrochem. Soc.*, **105**, 715 (1958).

[33] H. Foll, *Appl. Phys. A,* **53**, 8 (1991).

[34] L. Canham, New Scientist, **1868** (1993).

[35] M.I.J. Beale, J.D. Benjamin, M.J. Uren, N.G. Chew, and A.G. Cullis, *J. Cryst. Growth*, **73**, 622 (1985).

[36] L. Pavesi, *J. Appl. Phys*., **80**, 216 (1996).

[37] T. Trifonov, A. Rodriguez, F. Servera, L.F. Marsal, J. Pallarès, R. Alcubilla, *phys. stat. sol. (a),* **202**, 1634 (2005).

[38] P. Müller, IUPAC Manual of Symbols and Technology, *Pure Appl. Chem.,* **31**, 578 (1972).

[39] A. Bruyant, G. Lérondel, P.J. Reece, and M. Gal. *Appl. Phys. Lett*. **82**, 3227 (2003).

[40] H. S. Nalwa, *Silicon Based Materials and Devices, Vol. 2: Properties and Devices*, Academic Press, San Diego (2001).

[41] J. Charrier, M. Guendouz, L. Haji, and P. Joubert, *Phys. Stat. Sol. (a),* **182**, 431 (2000).

[42] L. De Stefano, L. Moretti, A.M. Rossi, and I. Rendina, *Sen. Actuators A,* **104**, 179 (2003).

[43] J. Volk, J. Balázs, A.L. Tóth, and I. Bársony, *Sen. Actuators B,* **100**, 163 (2004).

[44] E.K. Squire, P.A. Snow, P.St. Russell, L.T. Canham, A.J. Simons, and C.L. Reeves, *J. Luminescence,* **80**, 125 (1999).

[45] A. Halimaoui, *Porous Silicon formation by anodization* (in Properties of Porous Silicon), L. Canham, Ed., Short Run Press Ltd., London (1997).

[46] C. Mazzoleni, *Tesi di Laurea*, Universitá di Trento (1995).

[47] L. Pavesi, and V. Mulloni, *J. Luminescence*, **80**, 43 (1999).

[48] E. Lorenzo, C.J. Oton, N.E. Capuj, M. Ghulinyan, D. Navarro Urrios, Z. Gaburro, and L. Pavesi, *Applied Optics*, **44**, 5415 (2005).

[49] L. Pavesi. *Microelectronics Journal,* **27**, 437(1996).

ISBN:978-84-691-0362-3/DL: T.2181-2007

[50] J.C. Li, W.L. Chen, W.C. Tsai, *Optics Express*, **14**, 9764 (2006).

[51] L.G. Jacobsohn, B.L. Bennett, D.W. Cooke, *J. Appl. Phys.*, **97**, 33528 (2005).

[52] S. Chan, and P.M. Fauchet, *Appl. Phys. Lett.*, **75**, 274 (1999).

[53] Y. Zhou, P.A. Snow, and P.St.J. Russell, *Appl. Phys. Lett.,* **77**, 2440 (2000).

[54] A.G. Cullis, L.T. Canham, and P.D.J. Calcott. *J. Appl. Phys*., **82**, 909 (1997).

[55] L. T. Canham, *phys. stat. sol. (b)*, **190**, 9 (1995).

[56] A. Richter, P. Steiner, F. Kozlowski, and W. Lang, *IEEE Electron Device Lett.,* **12**, 691 (1991).

[57] N. Koshida, and H. Koyama, *Appl. Phys. Lett*., **60**, 347 (1992).

[58] W. Lang, P. Steiner, and F. Kozlowski, *J. Luminescence*, **57**, 341 (1993).

[59] H. Mimura, T. Matsumoto, T. Futagi, and Y. Kanemitsu, *J. Phys. Soc. Jpn*., **63**, 203 (1994).

[60] H. Mizuno, H. Koyama, and N. Koshida, *Appl. Phys. Lett.,* **69**, 3779 (1996).

[61] J.F. Harvey, M. Shen, R.A. Lux, M. Dutta, J. Pamulapti, and R. Tsu, *Mater. Res. Soc. Symp. Proc.*, **256**, 175 (1992).

[62] D.I. Kovalev, I.D. Yarostietzkii, T. Muschik, V. Petrova-Koch, and F. Koch, *Appl. Phys. Lett.*, **64**, 214 (1994).

[63] L. Tsybeskov, Y.V. Vandyshev, and P.M. Fauchet, *Phys. Rev. B*, **49**, 7821 (1994).

[64] C.I. Harris, M. Syvajarvi, J.P. Bergman, O. Kerdina, A. Henry, B. Monemar, and E. Janzen, *Appl. Phys. Lett.*, **65**, 2451 (1994).

[65] A. Kux, D. Kovalev, and F. Koch, *Appl. Phys. Lett.*, **66**, 49 (1995).

[66] A. Kux, D. Kovalev, and F. Koch, *Thin Solid Films,* **255**, 143 (1995).

UNIVERSITAT ROVIRA I VIRGILI
DESIGN, FABRICATION AND CHARACTERIZATION OF POROUS SILICON MULTILAYER OPTICAL DEVICES
Elisabet Xifré Pérez
ISBN:978-84-691-0362-3/DL: T.2181-2007

[67] L.T. Canham, A. Loni, P.D.J. Calcott, A.J. Simons, C. Reeves, M.R. Houlton, J.P. Newey, K.J. Nash, and T.I. Cox, *Thin Solid Films,* **276**, 112 (1996).

[68] P.M. Fauchet, E. Ettedgui, A. Raisanen, L.J. Brillson, F. Seiferth, S.K. Kurinec, Y. Gao, C. Peng, and L. Tsybeskov, *Mater. Res. Soc. Symp. Proc.*, **298**, 271 (1993).

[69] G. Mauckner, J. Hamann, W. Rebitzer, T. Baier, K. Thonke, and R. Sauer, *Mater. Res. Soc. Symp. Proc.*, **358**, 489 (1995).

[70] F. Koch, *Mater. Res. Soc. Symp. Proc.*, **298**, 319 (1993).

[71] D.T. Jiang, I. Coulthard, T.K. Sham, J.W. Lorimer, S.P. Frigo, X.H. Feng, and R.A. Rosenberg, *J. Appl. Phys.*, **74**, 6335 (1993).

[72] J. Zuk, R. Kuduk, M. Kulik, J. Liskiewicz, D. Maczka, P.V. Zhukovski, V.F. Stelmakh, V.I. Bondarenko, and A.M. Dorofeev, *J. Luminescence,* **57**, 57 (1993).

[73] J. Lin, G.Q. Yao, J.Q. Duan, and G.G. Qin, *Solid State Commun.,* **97**, 221 (1996).

[74] I. Coulthard, D.T. Jiang, and T.K. Sham, *J. Electron Spectrosc. Relat. Phenom.,* **79**, 233 (1996).

[75] G. Qin, J. Lin, J.Q. Duan, and G.Q. Yao, *Appl. Phys. Lett.*, **69**, 1689 (1996).

[76] Q. Chen, G. Zhou, J. Zhu, C. Fan, X.G. Li, and Y. Zhang, *Phys. Lett. A*, **224**, 133 (1996).

[77] L.T. Canham, A.G. Cullis, C. Pickering, O.D. Dosserm, T.I. Cox, T.P. Lynch, *Nature*, **368**, 133 (1994).

[78] L. Pavesi, *Riv. del Nuovo Cimento,* **10**, 1 (1997).

[79] V. Agarwal, and J.A. del Río, *Appl. Phys. Lett.*, **82**, 1512 (2003).

[80] S. Setzu, P. Ferrand, and R. Romestain, *Mat. Sci. and Eng. B*, **69**, 34 (2000).

[81] M.G. Berger, C. Dieker, M. Thönissen, L. Vescan, H. Lüth, H. Munder, W. Theiss, M. Wernke, and P. Grosse, *J. Phys. D*, **27**, 1333 (1994).

[82] L. Pavesi, *Riv. del Nuovo Cimento*, **20**, 18 (1997).

[83] S. Chan, P.M. Fauchet, *Appl. Phys Lett.*, **75**, 274, (1999).

[84] J.E. Lugo, H.A. Lópz, S. Cahn, P.M. Fauchet, *J. Appl. Phys.*, **91**, 4966 (2002).

[85] E.K. Squire, P.A. Snow, and P.St. Russell, *J. Porous Materials,* **7**, 209 (2000).

[86] S. Setzu, G. Lérondel, R. Romestain, *J. Appl. Phys.*, **84**, 3129 (1998).

[87] G. Vincent, *Appl. Phys. Lett.*, **64**, 2367 (1994).

[88] J. Diener, N. Künzner, D. Kovalev, E. Gross, V.Y. Timoshenko, G. Polisski, and F. Koch, *Appl. Phys. Lett.,* **78**, 3887 (2001).

[89] A. Szerling, D. Wawer, K. Hejduk, T. Piwonski, A. Wojcik, B. Mroziewicz, and M. Bugajski, *Optica Applicata,* **32**, 523 (2002).

[90] C.P. Hussell, and R.V. Ramaswamy, *IEEE Photonics Technology Letters,* **9**, 636 (1997).

[91] L. Pavesi, C. Mazzoleni, A. Tredicucci, and V. Pellegri, *Appl. Phys. Lett.,* **67**, 3280 (1995).

[92] A. Loni, L.T. Canham, M.G. Berger, R. Arens-Fischer, H. Munder, H. Luth, H.F. Arrand, and T.M. Benson, *Thin Solid Films,* **276**, 143 (1996).

[93] S.M. Weiss, and P.M. Fauchet, *Phys. Stat. Sol (a)*, **2**, 556 (2003).

[94] T. Gao, J. Gao, M.J. Sailor, *Langmuir,* **18**, 9953 (2002).

[95] L. De Stefano, I. Rendina, L. Moretti, and A.M. Rossi, *Mater. Sci. and Eng. B.,* **100**, 271 (2003).

[96] J. Volk, J. Balazs, A.L. Tóth, and I. Bársony, *Sens. Actuators B,* **100**, 163 (2004).

UNIVERSITAT ROVIRA I VIRGILI
DESIGN, FABRICATION AND CHARACTERIZATION OF POROUS SILICON MULTILAYER OPTICAL DEVICES
Elisabet Xifré Pérez
ISBN:978-84-691-0362-3/DL: T.2181-2007

[97] M.A. Anderson, A.Tinsley-Bown, P. Allcock, E.A. Perkins, P. Snow, M. Hollings, R.G. Smith, C. Reeves, D.J. Squirrell, S. Nicklin, and T.I. Cox, *Phys. Stat. Sol. (a),* **197**, 528 (2003).

[98] P.J. Reece, G. Lérondel, W.H. Zheng, and M. Gal, *Appl. Phys. Lett.*, **81**, 4895 (2002).

[99] Y.Y. Kim, K.W. Lee, C.W. Lee, S. Hong, J.W. Ryu and J.H. Jeon, *J. Korean Phys. Soc.,* **42**, 329 (2003).

[100] T.V. Dolgova, A.I. Maidykovski, M.G. Martemyanov, A.A. Fedyanin, O.A. Aktsipetrov, G. Marowsky, V.A. Yakovlev, and G. Mattei, *Appl. Phys. Lett.,* **81**, 2725 (2002).

[101] M.G. Martemyanov, E.M. Kim, T.V. Dolgova, A.A. Fedyanin, O.A. Aktsipetrov, and G. Marowsky, *Phys. Rev. B*, **70**, 073311 (2004).

[102] M.G. Berger, R. Arens-Fischer, M. Thönissen, M. Krüger, S. Billat, H. Lüth, S. Hilbrich, W. Theiss, and P. Grosse, *Thin Solid Films*, **297**, 237 (1997).

[103] E. Lorenzo, C.J. Oton, B.J. González Díaz, C. Hernández Rodríguez, R. Guerrero Lemus, and N.E. Capuj, *phys. stat. sol. (c)*, **2**, 3227 (2005).

[104] C.S. Bartholomew, M.D. Morrow, H.T. Betz, J.L. Grieser, R.A. Spence, and N.P. Murarka, *J. Vac. Sci. Technol. A*, **6**, 1703 (1988).

[105] W.J. Gunning, R.L. Hall, F.J. Woodberry, W.H. Southwell, and N.S. Gluck, *Appl. Opt.*, **28**, 2945 (1989).

[106] A.F. Jankowski, L.R. Schrawyer, and P.L. Perry, *J. Vac. Sci. Technol. A*, **9**, 1184 (1991).

[107] P.L. Swart, P.V. Bulkin, B.M. Lacquet, *Opt. Eng.*, **36**, 1214 (1997).

[108] K. Kaminska, T. Brown, G. Beydaghyan, and K. Robbie, *Proc. SPIE Int. Soc. Opt. Eng.*, **4833**, 633 (2003).

[109] F. Cunin, T.A. Schmedake, J.R. Link, Y. Li, J. Koh, S. Bhatioa, and M.J. Sailor, *Nature Materials*, **1**, 39 (2002).

UNIVERSITAT ROVIRA I VIRGILI
DESIGN, FABRICATION AND CHARACTERIZATION OF POROUS SILICON MULTILAYER OPTICAL DEVICES
Elisabet Xifré Pérez
ISBN:978-84-691-0362-3/DL: T.2181-2007

[110] J.N. Winn, Y. Fink, S. Fan, and J.D. Joannopoulos. *Opt. Lett.,* **23**, 1573 (1998).

[111] D.N. Chigrin, A.V. Lavrinenko, D.A. Yarotsky, and S.V. Gaponenko. *J. Lightwave Technol.*, **17**, 2018 (1999).

[112] D. Bria, B. Djafari-Rouhani, E. H. El Boudouti, A. Mir, A. Akjouj, and A. Nougaoui. *J. Appl. Phys.*, **91**, 2569 (2002).

[113] E. Yablonovitch, *Opt. Lett.*, **23**, 1648 (1998).

[114] D. Lusk, I. Abdulhalim, and F. Placido, *Opt. Commun.*, **198**, 273 (2001).

[115] S.M. Weiss, and P.M. Fauchet, *Phys. Stat. Sol (a)*, **197**, 556 (2003).

[116] Y. Fink, J.N. Winn, S. Fan, C. Chen, J. Michel, J.D. Joannopoulos, and E.L. Thomas. *Science*, **282**, 1679 (1998).

[117] P. Ferrand, and R. Romestain, *Appl. Phys. Lett.*, **77**, 3535 (2000).

[118] A.M. Rossi, G. Amato, V. Camarchia, L. Boarino, and S. Borini, *Appl. Phys. Lett.*, **78**, 3003 (2001).

[119] G. Amato, L. Boarino, S. Borini, and A.M. Rossi, *phys. stat. sol. (a)*, **182**, 425 (2000).

[120] M. Balucani, V. Bondarenko, N. Vorozov, and A. Ferraria, *Physica E*, **16**, 586 (2003).

[121] T.M. Benson, H.F. Arrand, P. Sewell, D. Niemeyer, A. Loni, R.J. Bozeat, M. Krüger, R. Arens-Fischer, M. Thönissen, and H. Lüth, *Mater. Sci. and Eng. B*, **69**, 92 (1999).

[122] H.F. Arrand, T.M. Benson, A. Loni, R. Arens-Fischer, M.G. Krueger, M. Thönissen, H. Lüth, S. Kershaw, N.N. Vorozov, *J. Luminescence*, **80**, 119 (1999).

[123] H.F. Arrand, T. M. Benson, A. Loni, R. Arens-Fischer, M. Krüger, M. Thönissen, H. Lüth, and S. Kershaw, *IEEE Photonics Technology Letters*, **10**, 1467 (1998).

ISBN:978-84-691-0362-3/DL: T.2181-2007

[124] S. Lazarouk, P. Jaguiro, and V. Borisenko, *Phys. Stat. Sol. (a),* **165**, 87 (1998).

[125] J.S. I, Y. Park, and H. Jeon, *J. Korean Phys. Soc,* **39**, 994 (2001).

[126] H. Taniyama, *J. Appl. Phys.*, **91**, 3511 (2002).

[127] A. Mekis, J.C. Chen, I. Kurland, S. Fan, P.R. Villeneuve, and J.D. Joannopoulos, *Phys. Rev. Lett.,* **77**, 3787 (1996).

[128] J.S. I, Y. Park, and H. Jeon, *J. Lightwave Technol.,* **22**, 509 (2004).

[129] P. Ferrand, D. Loi, R. Romestain, *Appl. Phys. Lett.*, **79**, 3017 (2001).

[130] J. Dorvee, and M.J. Sailor, *phys. stat. sol. (a),* **202**, 1619 (2005).

[131] C. Pacholski, M. Sartor, M.J. Sailor, F. Cunin, and G.M. Miskelly, *J. Am. Chem. Soc.*, **127**, 11636 (2005).

[132] H. Ouyang, C.C. Striemer, and P.M. Fauchet, *Appl. Phys. Lett*., **88**, 163108 (2006).

[133] Z.M. Rittersma, A. Splinter, A. Bodecker, and W. Benecke, *Sens. Actuators B*, **68**, 210 (2000).

[134] M. Björkqvist, J. Salonen, J. Paski, and E. Laine, *Sens. Actuators A*, **112**, 244 (2004).

[135] C.J. Oton, L. Pancheri, Z. Gaburro, L. Pavesi, C. Baratto, G. Faglia, and G. Sberveglieri, *Phys. Stat. Sol (a),* **197**, 523 (2003).

[136] R.T. Collins, P.M. Fauchet, and M.A. Tischler, *Physics Today*, **50**, 24 (1997).

[137] A. Richter, P. Steiner, F. Kozlowski, and W. Lang, *IEEE Electron Dev. Lett.*, **2**, 691 (1991).

[138] N. Koshida, and H. Koyama, *Appl. Phys. Lett*., **60**, 347 (1992).

[139] F. Namavar, H.P. Maruska, and N.M. Kalkhoran, *Appl. Phys. Lett*., **60**, 2514 (1992).

[140] T. Futagi, N. Ohtani, M. Karsuno, K. Kawamura, Y. Ohta, H. Mimura, and K. Kitamura, *J. Non- Crystalline Solids*, **137**, 1271 (1991).

UNIVERSITAT ROVIRA I VIRGILI
DESIGN, FABRICATION AND CHARACTERIZATION OF POROUS SILICON MULTILAYER OPTICAL DEVICES
Elisabet Xifré Pérez
ISBN:978-84-691-0362-3/DL: T.2181-2007

[141] L.Z. Yu and C.R. Wie, *Elec. Lett.*, **28**, 911 (1992).

[142] C. Tsai, K.H. Li, and J.C. Campbell, *Elec. Lett.*, **29**, 134 (1993).

[143] S. Lazarouk, A.A. Leshok, V. Borisenko, C. Mazzoleni, and L. Pavesi, *Microelectronic Engineering,* **50**, 81 (2000).

[144] E.S. Kolesar Jr, V.M. Bright, and D.M. Sowders, *Thin Solid Films*, **270**, 10 (1995).

[145] W. Lang, P. Steiner, A. Richter, K. Marusczyk, G. Weimann, H. Sandmaier, *Sens. Actuators A*, **43**, 239 (1994).

[146] W. Lang, P. Steiner, H. Sandmaier, *Sens. Actuators A*, **51**, 31 (1995).

[147] C.S. Lee, J.D. Lee, C.H. Han, *Sens. Actuators A*, **84**, 181 (2000).

[148] T.E. Bell, P.T.J. Gennissen, D. DeMunter, M. Kuhl, *J. Micromechanics and Microengineering*, **6**, 361 (1996).

[149] J. Zi, J. Wan, and C. Zhang. *Appl. Phys. Lett.*, **73**, 2084 (1998).

[150] C. Zhang, F. Qiao, J. Wan, and J. Zi, *J. Appl. Phys*, **87**, 3174 (2000).

[151] P. Yeh, *Optical Waves in Layered Media*, Wiley, New York (1988).

[152] S. Guo, *Plane Wave Expansion for Photonic Band Gap Calculation Using Matlab*, PWM Manual.

[153] J.D. Joannopoulos, R.D. Meade, and J.N. Winn, *Photonic crystals: Molding the flow of light*, Princeton University press, New Jersey (1995).

[154] K. Sakoda, *Optical Properties of Photonic Crystals*, Springer, Berlin (2001).

[155] S. Guo, and S. Albin, *Opt. Express*, **11**, 167 (2003).

[156] K.S. Yee, *IEEE Trans. on antennas and propagation,* **AP-14**, 302 (1966).

[157] A. Taflove and S.C. Hagness, *Computational Electrodynamics: The Finite-Difference Time-Domain Method*, Artech House Inc., Boston, (2000).

UNIVERSITAT ROVIRA I VIRGILI
DESIGN, FABRICATION AND CHARACTERIZATION OF POROUS SILICON MULTILAYER OPTICAL DEVICES
Elisabet Xifré Pérez
ISBN:978-84-691-0362-3/DL: T.2181-2007

[158] S. Noda, and T. Baba, *Roadmap on photonic crystals*, Kluwer (2003).

[159] E. Palik, and G. Ghosh, *Handbook of Optical Constants of Solids*, Academic Press, Orlando (1998).

[160] T. Lohner, M. Fried, P. Petrik, O. Polgar, J. Gyulai, W. Lehnert, *Mat. Sci. Eng. B*, **69**, 182 (2000).

[161] J. Lekner. *J. Opt. A: Pure Appl. Opt*., **2**, 349 (2000).

[162] R. Sauleau, P. Coquet, T. Matsui, and J.P. Daniel. *IEEE Trans. Antennas Propag.*, **51**, 3171 (2003).

[163] L. Pavesi, and P. Dubos, *Semicond. Sci. Technol*., **12**, 570 (1997).

[164] H.F. Arrand, T.M. Benson, T. Anada, M. Krüger, M.G. Berger, R. Arens-Fischer, H.G. Münder, H. Lüth, A. Loni, and R. Bozeat, *Tech. Dig. on Integrated Photonic Reasearch*, **6**, 311, (1996).

[165] B.E.A. Saleh, and M.C. Teich, *Fundamentals of Photonics*, Wiley, New York (1991).

[166] A. Yariv, *Optical Electronics in Modern Communications* (Oxford University Press, New York) 1997.

[167] T. Kawanishi, and M. Izutsu, *Opt. Express,* **7**, 10 (2000).

[168] M. Bloemer, G. D'Aguanno, M. Scalora, and N. Mattiucci, *Appl. Phys. Lett.*, **87**, 261921 (2005).

[169] A.G. Barriuso, J.J. Monzón, L.L. Sánchez-Soto, and A. Felipe, *Opt. Express*, **13**, 3902 (2005).

[170] M.L. Povinelli, M. Ibanescu, S.G. Johnson, and J.D. Joannopoulos, *Appl. Phys. Lett.*, **85**, 1466 (2004).

[171] S.G. Johnson, M. Ibanescu, M. Skorobogatiy, O. Weisberg, T.D. Engeness, M. Soljacic, S.A. Jacobs, J.D. Joannopoulos, and Y. Fink, *Opt. Express*, **9**, 748 (2001).

[172] M. Ibanescu, Y. Fink, S. Fan, E.L. Thomas, and J.D. Joannopoulos, *Science*, **289**, 415 (2000).

UNIVERSITAT ROVIRA I VIRGILI
DESIGN, FABRICATION AND CHARACTERIZATION OF POROUS SILICON MULTILAYER OPTICAL DEVICES
Elisabet Xifré Pérez
ISBN:978-84-691-0362-3/DL: T.2181-2007

[173] Z.H. Xiong, S. Yuan, Z.M. Jiang, J. Qin, C.W. Pei, L.S. Liao, X.M. Ding, X.Y. Hou, and X. Wang, *J. Luminescence*, **80**, 137 (1999).

[174] E. Xifré-Pérez, L.F. Marsal, J. Pallarès, and J. Ferré-Borrull, *J. Appl. Phys.*, **97**, 064503 (2005).

[175] J. Chilwell, and I. Hodgkinson, *J. Opt. Soc. Am. A,* **1**, 742 (1984).

[176] M. Ghulinyan, C.J. Oton, G. Bonetti, Z. Gaburro, and L. Pavesi, *J. Appl. Phys.*, **93**, 9724 (2003).

[177] S.T. Frohnhoff, M.G. Berger, M. Thönissen, C. Dieker, L. Vescan, H. Münder and H. Lüth, *Thin Solid Films,* **255**, 59 (1995).

[178] L. Pavesi, C. Mazzoleni, R. Guardini, M. Cazzanelli, V. Pellegrini, and A. Tredicucci, *Il Nuovo Cimento*, **18 D**, 1213 (1996).

[179] G. Vincent, *Appl. Phys. Lett*., **64**, 2367 (1994).

[180] K. Kordás, S. Beke, A.E. Pap, A. Uusimäki, S. Leppävuori, *Opt. Mat.*, **25**, 257 (2004).

[181] Y. Park, Y.G. Roh, C. Cho, H. Jeon, M. Sung, and J.C. Woo, *Appl. Phys. Lett*., **82**, 2770 (2003).

[182] M. Deopura, C.K. Ullal, B. Temelkuran, and Y. Fink, *Opt. Lett.,* **26**, 1197 (2001).

[183] A. Arena, S. Patane, G. Saitta, S. Savasta, R. Girlanda, and R. Rinaldi, *Appl. Phys. Lett.,* **72**, 2571 (1998).

[184] R. Guerrero-Lemus, F.A. Ben-Hander, L. Vazquez, C. Hernandez Rodriguez, and J.M. Martinez-Duart, *Phys. Stat. Sol (a),* **97**, 409 (2003).

[185] Z.C. Feng, and R. Tsu, *Porous Silicon,* World Scientific, Singapore (1994).

[186] G.E. Jellison, V.I. Merkulov, A.A. Puretzky, D.B.Geohegan, G. Eres, and D.H. Lowndes, *Thin Solid Films,* **377**, 68 (2000).

[187] R. Prabakaran, G. Raghavan, S.T. Sundari, R. Kesavamoorthy, and F.P. Xavier, *Physica E*, **15**, 243 (2002).

[188] J. Volk, M. Fried, O. Polgár, and I. Bársony, *Phys. Stat. Sol. (a)*, **197**, 208 (2003).

[189] T. Lohner, M. Fried, P. Petrik, O. Polgár, J. Gyulai, and W. Lehnert, *Mater. Sci. Eng. B,* **69-70**, 182 (2000).

[190] U. Rossow, U. Frotscher, C. Pietryga, D.E. Aspnes, W. Richter, *Appl. Surf. Sci.*, **102**, 413 (1996).

[191] M. Garriga, M.I. Alonso, and C. Domínguez, *Phys. Stat. Sol.,* **215**, 247 (1999).

[192] E. Vazsonyi, E. Szilagyi, P. Petrik, Z.E. Horvath, T. Lohner, M. Fried, G. Jalsovszky, *Thin Solid Films,* **388**, 295 (2001).

[193] G. Binning, C.F. Quate, and Ch. Gerber, *Phys. Rev. Lett.,* **56**, 930 (1986).

[194] O. Ben-Younes, M. Oueslati, and B. Bessais, *Appl. Surface Science.*, **206**, 37 (2003).

[195] C.S. Solanki, R.R. Bilyalov, J. Poortmans, G. Beaucarne, K. Van-Nieuwenhuysen, J. Nijs, and R. Mertens, *Thin Solid Films,* **451**, 649 (2004).

[196] J. Lee, K. Chakrabarty, and J. Yi, *Appl. Surface Science,* **211**, 373 (2003).

[197] S. Stolyarova, A. El-Bahar, Y. Nemirovsky, *J. Phys. D,* **33**, L90 (2000).

[198] K.P. Hong, and C.M. Lee, *J. Korean Phys. Soc.,* **42**, S671 (2003).

[199] A. Tsargorodskaya, A.V. Nabok, A.K. Ray, *IEE Proc. Circuits, Devices and Systems*, **150**, 355 (2003).

[200] T. Toyoda, T. Takahashi, and Q. Shen, *J Appl. Phys.,* **88**, 6444 (2000).

[201] V. Baranauskas, B.B. Li, M.C. Tosin, J.G. Zhao, H.J. Ceragioli, A.C. Peterlevitz, and S.F. Durrant, *Surface and Coatings Technology*, **133**, 325 (2000).

[202] F. Hassen, R. M'Ghaieth; H. Maaref, and R. Madar, *Mater. Sci. and Eng. C*, **15**, 113 (2001).

[203] D.J. Blackwood, and Y. Zhang, *Surf. Rev. Lett.*, **8**, 429 (2001).

[204] M. Born, and E. Wolf, *Principle of Optics*, Pergamon, Oxford (1980).

[205] S. Bosch, J. Ferré-Borrull, N. Leinfellner, A. Canillas, *Surf. Sci.,* **453**, 9 (2000).

[206] J. Sancho-Parramon, J. Ferré-Borrull, S. Bosch, and M.C. Ferrara, *Appl. Opt.*, **42**, 1325 (2003).

[207] S. Bosch, J. Ferré-Borrull and J. Sancho-Parramon, *Solid-State Electronics*, **45**, 703 (2001).

[208] M. Thönissen, and M. Berger, *Multilayer Structures of Porous Silicon* (in Properties of Porous Silicon), L. Canham, Ed., Short Run Press Ltd., London (1997).

[209] R.M.A. Azzam, and N.M. Bashara, *Ellipsometry and polarized light*, Nord-Holland, Amsterdam (1989).

[210] S. Zangooie, M. Schubert, C. Trimble, D.W. Thompson, J.A. Woollam, *Appl. Opt.*, **40**, 906 (2001).

[211] E.V. Astrova, V.B. Voronkov, A.D. Remenyuk, V.B. Shuman, and V.A. Tolmachev, *Semiconductors*, **33**, 1149 (1999).

[212] L.A.A. Pettersson, L. Hultman, H. Arwin, *Appl. Opt.*, **37**, 4130 (1998).

[213] C.A. Wang, S.H. Ma, H. Zeng, J. Li, L.Y. Chen, W.C. Wang, H. Tian, *Colloids and Surfaces A,* **284**, 414 (2006).

[214] T. Tsuru, T. Tsutou, T. Hatano, A. Yamamoto, *J. Electron Spectrosc. Relat. Phenom.*, **144**, 1083 (2005).

[215] E. Garcia-Caurel, J. Nguyen, L. Schwartz, and B. Drevillon, *Thin Solid Films*, **455**, 722 (2004).

[216] H. Arwin, *Thin Solid Films,* **313**, 764 (1998).

[217] F. Ferrieu, A. Halimaoui, and D. Bensahel, *Solid State Commun.*, **84**, 293 (1992).

[218] P.C. Wu, T.H. Kim, A.S. Brown, M. Losurdo, G. Bruno, and H.O. Everitt, Appl. Phys. Lett., **90**, 3119 (2007).

[219] R. Seitz, R. Brings, and R. Geiger, *Appl. Surf. Sci.*, **252**, 154 (2005).

[220] S. Strehlke, S. Bastide, O. Polgar, M. Fried, and C. Lévy Clement, *J. Electrochem. Soc.*, **147**, 636 (2000).

[221] T.H. Ghong, T.J. Kim, Y.D. Kim, D.E. Aspnes, *Appl. Phys. Lett.*, **85**, 946 (2004).

[222] J. Lekner, *Pur. Appl. Opt.*, **3**, 307 (1994).

[223] G. Bader, P.V. Ashrit, F.E. Girouard, and V.V. Truong, *Appl. Opt.*, **34**, 1684 (1995).

[224] B. Drévillon, J. Perrin, R. Marbot, A. Violet, and J.L. Dalby, *Rev. Sci. Instrum.*, **53**, 969 (1982).

[225] UVISEL Phase Modulated Spectroscopic Ellipsometer brochure (HORIBA Jobin Yvon).

[226] S. Zangooie, R. Jansson, and H. Arwin, *Mater. Res.*, **14**, 4167 (1999).

[227] C. Wongmaneroda,, S. Zangooie, H. Arwin, *Appl. Surf. Sci.*, **172**, 117 (2001).

[228] D.A.G. Bruggemann, *Ann. Phys.*, **24**, 636 (1935).

[229] W.H. Press, B.P. Flannery, S.A. Teukolsky, and W.T. Vetterling, *Numerical Recipes in C: The Art of Scientific Computing,* Cambridge University Press, Cambridge (1988).

[230] G.E. Jellison, Jr., Thin Solid Films, **313**, 33 (1998).

[231] S. Billat, M. Thönissen, R. Arens-Fischer, M.G. Berger, M. Krüger, and H. Lüth, *Thin Solid Films*, **297**, 22 (1997).

UNIVERSITAT ROVIRA I VIRGILI
DESIGN, FABRICATION AND CHARACTERIZATION OF POROUS SILICON MULTILAYER OPTICAL DEVICES
Elisabet Xifré Pérez
ISBN:978-84-691-0362-3/DL: T.2181-2007

[232] L. Dal Negro, C.J. Oton, Z. Gaburro, L. Pavesi, P. Johnson, A. Lagendijk, R. Righini, M. Colocci, and D. S. Wiersma, *Phys. Rev. Lett*. **90**, 055501 (2003).

[233] M. Thönissen, M.G. Berger, S. Billat, R. Arens-Fischer, M. Krüger, H. Lüth, W. Theiss, S. Hillbrich, P. Grosse, G. Lérondel, and U. Frotscher, *Thin Solid Films*, **297**, 92 (1997).

[234] H. Krzyzanowska, M. Kulik, J. Zuk, *J. Luminescence*, **80**, 183 (1999).

[235] B. DeBoo, J. Sasian, and R. Chipman, *Opt. Express*, **12**, 4941 (2004).

UNIVERSITAT ROVIRA I VIRGILI
DESIGN, FABRICATION AND CHARACTERIZATION OF POROUS SILICON MULTILAYER OPTICAL DEVICES
Elisabet Xifré Pérez
ISBN:978-84-691-0362-3/DL: T.2181-2007

UNIVERSITAT ROVIRA I VIRGILI
Departament d'Enginyeria Electrònica, Elèctrica i Automàtica
Avda. Països Catalans 26, Campus Sescelades, 43007 Tarragona, SPAIN

Design, fabrication and characterization of porous silicon multilayer optical devices

Thesis presented for the qualification of Ph.D.

by

Elisabet Xifré Pérez

Directors:

Dr. Lluís F. Marsal Garví
Dr. J. Pallarès Marzal

Tarragona 2007